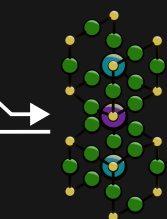
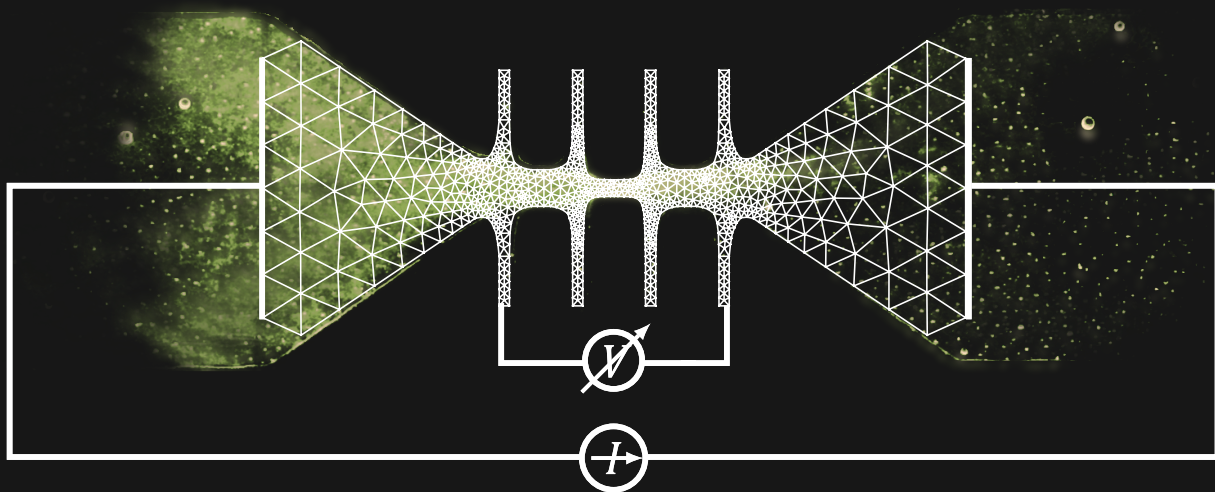

All-electrical oxygen doping in perovskites



PhD Thesis
Stefan Marinković
Academic Year 2023-2024



FACULTY OF SCIENCES

QUANTUM MATERIALS RESEARCH UNIT

EXPERIMENTAL PHYSICS OF NANOSTRUCTURED MATERIALS

All-Electrical Oxygen Doping in Perovskite Oxides

AUTHOR:

Stefan Marinković

SUPERVISOR:

Prof. Dr. Alejandro V. Silhanek

Professor, Head of Research Group,
Experimental Physics of Nanostructured Materials EPNM,
Université de Liège, Belgium

PRESIDENT:

Prof. Dr. Jean-Yves Raty

Associate Professor, Senior Research Associate,
Condensed Matter Simulation CSG,
Université de Liège, Belgium

JURY MEMBERS:

Dr. Javier E. Villegas

Senior Scientist,
Laboratoire Albert Fert, CNRS, Thales,
Université Paris-Saclay, France

Prof. Dr. Oleksandr Dobrovolskiy

Professor, Head of Research Group,
Cryogenic Quantum Electronics,
Technische Universität Braunschweig, Germany

SECRETARY:

Prof. Dr. Rudi Cloots

Full Professor, Director,
Group of Research in Energy and Environment from
Materials GREENMAT,
Université de Liège, Belgium

Prof. Dr. Jean-Pierre Locquet

Full Professor, Chair,
Leuven Nanoscience and Nanotechnology Research Centre,
KU Leuven, Belgium

PHD. THESIS PRESENTED IN PARTIAL FULFILMENT OF THE
REQUIREMENTS FOR THE DEGREE OF DOCTOR IN SCIENCE

ACADEMIC YEAR 2023-2024

PhD. thesis committee

President:

Prof. Dr. Jean-Yves RATY, Université de Liège (Belgium)

Secretary:

Prof. Dr. Rudi CLOOTS, Université de Liège (Belgium)

Jury members:

Dr. Javier E. VILLEGAS, Université Paris-Saclay (France)

Prof. Dr. Oleksandr DOBROVOLSKIY, TU Braunschweig (Germany)

Prof. Dr. Jean-Pierre LOCQUET, KU Leuven (Belgium)

Supervisor :

Prof. Dr. Alejandro V. Silhanek, Université de Liège (Liège, Belgium)

Dissertation presented in partial fulfilment of the requirements for the degree of Doctor in Science. The manuscript was defended by **Stefan Marinković** during a public oral examination on the August, 29th 2024.

Thesis realized with support of FNRS ASPIRANT Grant n° 1.A.320.21F.

©Copyright by Université de Liège - Faculté des Sciences, Place du 20 Août, 7, B-4000 Liège, Belgium.

Tous droits réservés. Aucune partie de ce document ne peut être reproduite sous forme d'imprimé, photocopie ou par n'importe quel autre moyen, sans l'autorisation écrite de l'auteur ou d'un des promoteurs.

All rights reserved. No part of this publication may be reproduced in any form by print, photo print or any other means without permission in writing from the author or the supervisor.

Acknowledgments

The work that follows would not have been possible without the financial support of FNRS, the facilities of EPNM and the hard work of numerous people and the generous support I received both professionally and personally. I have no hopes of capturing the extent of how much I owe to these people but will nevertheless try to express my deepest gratitude.

To my supervisor Alejandro I owe the incalculable debt of learning and all of my respect. I am grateful you chose to reply to my email when I wrote you all those years back as a bachelor student in Bosnia, and I hope that you got what you hoped to gain from helping me come abroad. I know I did, and I hope I also gain a friend and colleague as this chapter of my life and career comes to a close. Thank you for your patience and guidance, I hope we can remember this time fondly.

Whole swaths of this work would not be possible without the support, creativity and cleverness of my colleagues at EPNM and SPIN. The lasting support of Duy, who while not my supervisor, was always there as the second adult in the lab and has contributed to our work in many way is deserving of thanks. When I arrived as a master student, it was Sylvain, Joseph and Simon who showed me the ropes and taught me most of the useful skills I can boast today. Their great company was a privilege to enjoy. Simon, you have been around me for even longer, and provided your valuable skills both in experiment and theory to participate in all the publications that collectively are this thesis. I will always be in your debt. I wish you and Adele all the best. Also there to see me through the whole of it were Thomas and Emile. Emile, we have had many discussions about matters of both world and physics

and please know I appreciate you a lot. You are one of the key cogs of our machine at EPNM and are a great person. Thomas, you and I are graduating at the same time so I feel like we know each others suffering very closely. We have not worked on publications together, but I think the time we spent in these corridors amounts to a more profound solidarity.

Amaury and Nico, even though you joined a bit later, I could not imagine the lab without you. I am envious of both of your knowledge and am excited to see how far you can take it. Nico I am proud to see all the improvements you are providing in your iteration of our cryolabs.

No less important are the colleagues that spent time with us in the lab and moved on, like Francisco, Naama and Suraj. I am grateful for our time together and, in Suraj's case, for the company in our office. Francisco you have been one of our warmest additions. I welcome our new arrival Abhishek as warmly as I can in the last miles of my journey. My latest "student", who taught me at least as much as I taught him (including how to wrangle git), Daniel deserves a special thanks. Your contributions made the last experimental chapter of this thesis possible. I am very sure of your potential and you have a fan in me.

Francois, you and I have been both colleagues and students together. I consider you one of my oldest remaining friends here and admire you in your work. I am so happy we got to study, work, play and celebrate and I hope we never loose sight of each other. I still remember and keep other friendships from my student days, including Alex and Lin who have a special place in my heart.

Not all scientific work in this thesis is internal to our little band at EPNM-SPIN. The sample contributions of Anna Palau's group at ICMAB in Spain were half the effort of the project at hand. This includes the work of Alejandro Fernández-Rodríguez and Jordi Alcalà. I still have fond memories of my visit in preparation for the work in the first experimental chapter. I would like to further thank our other Spanish collaborators, including Narcís Mestres, Hailin Wang, Mariona Cabero, Jaume Gazquez as well as the team of Antonio Badía-Majós. Closer to home and also deserving of praise are our Belgian collaborators, including the group around Joris Van de Vondel, and especially Lukas Nulens. In the same vein I am grateful to the dear colleagues in Louvain-la-Neuve around Sorin Melinte, including Diego Jaramillo and Fernando Massa. I would be remiss not to thank our collaborators in Sweden lead by Floriana Lombardi, with Thilo Bauch and Edoardo Trabaldo, or our colleagues in China and Brazil. Special warm wishes to Lu Jiang and Elijah Abbey who have been here on prolonged stays where I had the privilege of

working with them. Special thanks also to Maycon Motta for our recent work together. The most recently deserving have been the members of Wolfgang Lang's group in Vienna, Fridrich Egyenes and Bernd Aichner.

With a special place in my heart, I want to say thanks to wonderful Benedetta, whose love and support have been key in keeping me afloat the last almost-two years. Thank you for helping me keep the course and for being my place of respite in the tumult. You have all of my soul.

It would be completely bizarre to connect my life in Bosnia to my life in Belgium were it not for Željko, the pioneer. The first who came from our town of Šamac and broke ground in Belgian academia is a dear friend of mine from way back. Thank you dearly, were it not for your recommendation and support none of this would come to pass. Ti si veza s kućom i uzor u ovom našem polju. Hvala ti za sve što si uradio, bez tebe ja ne bih mogao.

Prijatelji, hvala vam što ste vjerovali u mene i što ste i dalje tu za mene. Posebno hvala kolegama s fakulteta, Dini, Azri i Arminu za očuvano prijateljstvo, i hvala vam za razbibrigu u dokonim trenutcima.

Starim prijateljima hvala. Vesna, ti si sila gdje god si bila. Strašno mi je drago što smo prijatelji i što mogu da te pratim u tvojim putešestvijama. Slične puteve pratimo po bijelom svijetu, a znaš kako slične muke povezuju. Vladane, nismo se vidjeli predugo. Mnogo toga se promijenilo, ali neka prijateljstva ostaju stalna. Računajte na mene gdje god da odete.

Hvala porodici, prije svih bakama Jaki i Mari za ovaj život koji su mi omogućile. Hvala svim Šamčanima koji su bili uz mene i moje.

Moji najbliži, pišem vam na kraju iako je vaša podrška počela prva. Tata Zorane i mama Jasna, vama dugujem najviše. Dugujem vam život i sve što sam postigao, uključujući i ovu disertaciju. Hvala za sav trud i rad i muku, oče, hvala za sve što si pretrpjela, mama. Znae šta ste sve prošli, i znajte da su vam djeca zahvalna. Naša porodica je građena na ljubavi i uvijek ćete biti baza. Posvećujem ovu disertaciju vašim očevima, morao sam ih oponašati obojicu da bih ovo postigao.

Brate Filipe, znaj da te volim kao nikog na Zemlji. Uvijek želim biti tvoj oslonac i podrška. Hvala ti za prijateljstvo, za slušanje i savjete, i hvala ti za tvoje uspjehe. Ti si moj ponos, i u mojim očima te nikada neću prevazići.

*To the spirit of my two grandfathers,
Jovan and Tadija.*

Preface

To the solid ground of nature
trusts the Mind that builds for
aye.

William Woodsworth

In his seminal work on the philosophy of science "The Structure of Scientific Revolutions", [1] American philosopher Thomas Kuhn introduced the concept of the "paradigm shift". He observed that in the whole process of science as it evolves through history, new systems of belief and understanding of nature (paradigms) are adopted by scientists, then tested, expanded and pushed to their limits until breaking. These significant moments where the whole web of systems needs to shift to accommodate new understanding are, however, exceedingly rare. For the most part, scientific activity is a labor of puzzle solving, where the puzzle is already laid out and it is the scientists job to find out how the piece they are holding fits in the greater picture. He terms this "normal science".

The advent of quantum mechanics was one such paradigm shift, as was Onnes' discovery of electrical transport without resistance in elemental Hg [2] (what we refer to as superconductivity) and the implementation of the semi-conducting transistor as one of the first microelectronic components, among many other such discoveries. Indeed, the development of superconductivity science has already experienced another such break, with the discovery of "high temperature" superconductivity (one of physics' great misnomers) in cuprate oxides [3] rejuvenating the field that considered its puzzle solved,

all the way back in 1986. We have seen new paradigms arise in the field of electronics, with in-memory computing via memristive materials and brain-inspired artificial neurons being currently *en vogue* as candidates for components in futuristic computer systems. One may also envision new fabrication technologies and characterization techniques as their own paradigm shifts, considering how they redefine the possibility space in what we can make and study.

It is in this context that we find ourselves studying the property modulation of complex oxides, trying to fit our pieces in the puzzle of modern solid state science with its complex models of superconductivity and ferroics.[4] We justify this research not only with pure curiosity but with the prospect of using these materials in computing and sensing technologies of some future paradigm that we are certain, as always, is just around the corner. In this effort we are not disheartened by how frustratingly "normal" (in Kuhn's words) this science is, proudly filling in the small gaps left open by the legion of peers doing similar things in similar materials.

I invite You, dear reader, to join us in looking at the puzzle as we push through one more paradigm, continuing in our everlasting quest for knowledge.

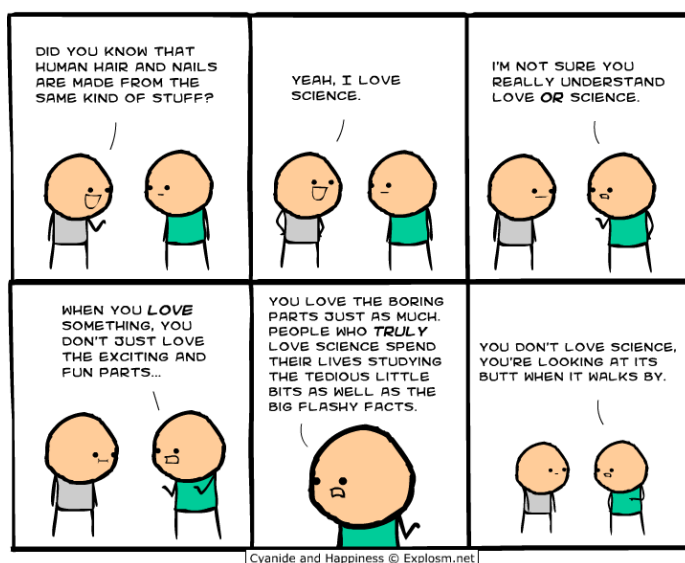


Figure 1: Comic by Kris Wilson, taken from <https://explosm.net/comics/kris-same>

Abstract

Complex oxides are at the heart of modern functional material developments. In particular, the perovskite ABO_3 structure is seen in compounds used in oxide solar cells, resistive memories, fuel cell catalysts, superconducting tapes, quantum bits and programmable magnets, making it one of the most studied material families. One important advantage of these systems is that their properties may be controlled *in situ* to change between various electronic states, usually by means of thermal or electric conditioning. In this thesis, the modulation of the properties of some perovskite oxides is demonstrated using simple electrical controls. The model material employed to this end is $YBa_2Cu_3O_{7-\delta}$ (YBCO) but results in ferroic manganites indicate that the behavior might be general to the material family. We have unambiguously demonstrated that oxygen vacancies located in the CuO chains in YBCO can be displaced several μm scale distances through a biased diffusive process known as selective electromigration. The rearrangement of these oxygen chains and the change in relative concentration δ , leads to a related shift in hole carriers in the CuO_2 planes. The final outcome is the possibility of tuning the numerous electronic phases displayed by this compound, all via electric actuation. The methodologies discussed, based on current driven oxygen diffusion in planar films, offer the advantage of easy fabrication and control comparable to common gated sample designs that require multi-step patterning. Reflectivity changes as a consequence of changing levels of oxygenation in the material are used to map the evolution of the phenomenon in real time and to validate a phenomenological finite element method (FEM) model, providing adequate descriptions of the effect as it occurs in these

practically useful materials. The understanding generated in this manner allows for reversible resistance switching and tuning of superconducting critical temperature T_c , as demonstrated in YBCO.

Résumé

Les oxydes complexes sont au cœur du développement des matériaux fonctionnels modernes. En particulier, la structure pérovskite ABO_3 se retrouve dans des composés utilisés pour de nombreuses applications telles que les cellules solaires, les mémoires résistives, les catalyseurs de piles à combustible, les rubans supraconducteurs, les bits quantiques ou encore les aimants programmables, ce qui en fait l'une des familles de matériaux les plus étudiées. Un des avantages majeurs de ces systèmes réside dans le fait que leurs propriétés physiques peuvent être contrôlées *in situ*, permettant le passage entre divers états électroniques, généralement par des moyens de conditionnement thermique ou électrique. Dans cette thèse, la modulation des propriétés d'une sélection d'oxydes pérovskites est rendu possible en se basant uniquement sur des contrôles électriques simples. La démonstration est principalement réalisée sur un matériau modèle, le YBCO, mais les résultats obtenus dans les manganites ferriques indiquent que le comportement expérimenté pourrait être général à cette famille de matériaux. Nous avons démontré de manière non équivoque que les lacunes d'oxygène situées dans les chaînes de CuO du YBCO peuvent être déplacées sur des distances de l'ordre de plusieurs μm grâce à un processus diffusif induit par un courant électrique et connu sous le nom d'électromigration sélective. La réorganisation de ces chaînes d'oxygène et le changement de concentration relative δ , provoque le déplacement des trous porteurs de charge dans les plans de CuO_2 . Par conséquent, le résultat final est la capacité de sélectionner l'une des nombreuses phases électroniques possible pour ce composé, le tout via une action électrique. Les différentes méthodologies étudiées dans cette thèse, toutes basées sur la diffusion d'oxygène induite par le courant électrique dans les films minces

nanostructurés, offrent l'avantage d'une fabrication simplifiée et d'un haut niveau de contrôle comparé aux dispositifs à grille couramment utilisés qui nécessitent une nanofabrication en plusieurs étapes. Le changement de réflectivité, conséquence directe des niveaux d'oxygénation variables dans le matériau, sont utilisés pour cartographier l'évolution du phénomène en temps réel et pour valider un modèle phénoménologique par éléments finis, fournissant des descriptions adéquates de l'effet tel qu'il se produit dans ces matériaux à intérêts industriels. La compréhension générée de cette technique permet, entre autres, un changement réversible de résistance et le réglage de la température critique supraconductrice T_c , comme démontré dans le YBCO.

Acronyms

AFM atomic force microscopy.

API application programming interface.

BNC Bayonet Neill–Concelman.

CCD charge coupled device.

CSD chemical solution deposition.

EBL electron-beam lithography.

EPNM Experimental Physics of Nanostructured Materials.

FEM finite element method.

GPIB general purpose interface bus.

HTS high temperature superconductor.

IC integrated circuit.

ICMAB Institut de Ciència de Materials de Barcelona.

LAO LaAlO_3 .

LSAT $(\text{La}_{0.18}\text{Sr}_{0.82})(\text{Al}_{0.59}\text{Ta}_{0.41})\text{O}_3$.

LSMO $\text{La}_x\text{Sr}_{1-x}\text{MnO}_{3-\delta}$.

MIT metal-insulator transition.

MOI magneto-optical imaging.

PAD polymer assisted deposition.

PCB printed circuit board.

PID proportional-integral-derivative.

PLD pulsed laser deposition.

PPMS physical property measurement system.

PVD physical vapor deposition.

QDPL Department of Microtechnology and Nanoscience, Quantum Device
Physics Laboratory, Chalmers University of Technology.

SCPI Standard Commands for Programmable Instruments.

SEM scanning electron microscopy.

SMU source-measure unit.

SQUID superconducting quantum interference device.

STEM scanning transmission electron microscopy.

STO SrTiO_3 .

UV ultra-violet.

XRD X-ray diffraction.

YBCO $\text{YBa}_2\text{Cu}_3\text{O}_{7-\delta}$.

Contents

I	Introduction	19
1	State of The Art	21
1.1	Introduction	22
1.2	Classification and Mechanism	23
1.2.1	Vacancy Diffusion	28
1.3	Doping Control in Transition Metal Oxides: A Family Picture	31
1.3.1	Simple Transition Metal Oxides	33
1.3.2	Perovskite Oxides	34
1.4	Field-Induced and Current-Induced Vacancy Diffusion	43
1.5	Summary	48
2	Methods	49
2.1	Sample Fabrication	49
2.1.1	Pulsed Laser Deposition	51
2.1.2	Chemical Solution Deposition	53
2.1.3	Substrate Selection	54
2.1.4	Thin Film Patterning	55
2.1.5	Sample Design	58
2.1.6	Film Characterization	58
2.2	Transport and Low-T Measurements	60
2.2.1	Electrical Test Equipment and Automation	60
2.2.2	Electromigration Protocols	62
2.2.3	Cryogenic Measurements	66
2.3	Imaging	69

2.4	Modeling	76
II	Current Driven Oxygen Electromigration for Doping Control in YBCO	79
3	Direct Visualization of Current-Induced Oxygen Electromigration in YBCO	81
3.1	Introduction	82
3.2	Results and Discussion	83
3.2.1	Electromigration process	83
3.2.2	Direct visualization of oxygen migration	85
3.2.3	Photoexcitation	91
3.2.4	Anti-electromigration	92
3.3	Samples	94
3.4	Modeling	94
3.5	Summary	95
4	Electrically-driven oxygen vacancy aggregation and displacement in YBCO films	97
4.1	Introduction	98
4.2	Results and Discussion	100
4.2.1	Optical and electrical probing of oxygen vacancy migration	100
4.3	Samples	113
4.4	Modeling	114
4.5	Summary	115
5	Oxygen Ordering in Untwinned YBCO Films Driven by Electrothermal Stress	117
5.1	Introduction	119
5.2	Results and Discussion	119
5.2.1	DC electromigration	119
5.3	Samples	127
5.4	Modeling	128
5.5	Summary	129

III	Electrical Oxygen Doping Control in Related Perovskites	131
6	From Electric Doping Control to Thermal Defect Nucleation in Perovskites	133
6.1	Introduction	134
6.2	Results and discussion	136
6.2.1	Directional migration of oxygen in $\text{La}_x\text{Sr}_{1-x}\text{MnO}_{3-\delta}$ (LSMO)	136
6.2.2	Generation of Crystallographic Defects in the LSMO/SrTiO ₃ (STO) System	139
6.3	Samples	148
6.4	Summary	148
IV	Reversible Switching Behaviour	151
7	Electromigration-driven weak resistance switching in high-temperature superconducting devices	153
7.1	Results and Discussion	155
7.1.1	Numerical results	158
7.2	Samples	161
7.3	Modeling	161
7.4	Summary	161
V	Conclusions	163
8	General Conclusions	165
8.1	Perspectives	167
VI	Appendices	169
A	Appendix to Ch.3	171
A.1	Inhomogeneous temperature distribution along the bridge before electromigration	171
A.2	Resistance changes after irreversible electromigration	171
A.3	Raman Spectra	173
A.4	Scanning Electron Microscopy Imaging	173
A.5	Realtime tracking of the electromigration process	175

B Appendix to Ch.4	177
B.1 Realtime tracking of the DC electromigration process	177
B.2 DC electrical stress under switching polarity	177
B.3 Realtime tracking of the AC electromigration process	178
B.4 Oxygen concentration, temperature, current density and electric field maps during AC electromigration process	179
B.5 Influence of x_{max} , x_0 and δx_0 on the oxygen diffusion	179
C Appendix to Ch.6	181
C.1 Finite Element Modeling	181
C.2 Realtime tracking of the electromigration process	184
C.3 STEM images	185
D Annex to Ch.7	189
D.1 Initial Thermalization Phase	189
D.2 Simulated Time Evolution of the Resistance, Doping and Temperature	191
D.2.1 Symmetric Mesh	191
D.2.2 Asymmetric Mesh	192
VII Curriculum Vitae and Publication List	243

Part I

Introduction

State of The Art

Layman's Overview: **Switching Oxides**

The difference between a simple binary oxide and a complex oxide (one which includes two or more non-oxygen ions) may seem small, but these more intricate oxygen-containing crystals exhibit more complex and fascinating physics. Adding just one more type of atom to the structure of an oxide crystal changes how the crystal arranges itself, how it behaves magnetically and electrically, how it vibrates and handles strain and imperfections. This intricacy is why complex oxides are used to find materials that can conduct electricity with zero resistance at low temperatures, change their electrical properties with magnets, and keep electric charges without needing a battery, among other exciting and useful phenomena.

Some oxides are special because one can change the amount of oxygen in them,

which changes their properties. It is possible to do this using external knobs like electric field, temperature, or strain. Because of this tunability, oxides are ideal for creating materials tailored to specific applications. In this thesis, we focus on materials whose functionalities can be controlled with electric field and current.

The simplest feature that can be controlled in this way is electrical resistance, an application studied under the moniker of resistive switching. While resistive switching is not exclusive to oxides, it is highly relevant to our discussion of property control in these materials. In oxides, this mechanism revolves around the oxygen atoms in the crystal and the various ways they can be moved back and forth.

In this chapter we lay the groundwork for studying electrical oxygen doping control in functional perovskite oxides. This doping control is in its simplest form well understood under the umbrella of resistive switching, and is first presented in that context before we attempt a heuristic theoretical description of the forces at play during vacancy diffusion in oxide materials, and its parametric control. Then the necessary understanding of oxide

physics is delivered, with special attention to perovskite oxides, covering some notable examples and their functionalities and presenting arguments for them as candidates for doping control technologies. Finally, we present an overview of the current state of oxygen doping control in perovskites for simple, electrical-only implementation schemes.

1.1 Introduction

Switching processes involve reversibly changing a property of interest, usually resistance R , in a device by an externally controlled parameter, such as an electric field E or current I . Historically, these effects were first described in disordered semiconductors[5] and simple oxides,[6, 7] with chalcogenide glasses[8] becoming a popular research subject soon after. Connecting a vertical stack of such material between two electrodes in a simple two-terminal device produces systems[9] with "memory",[10] meaning their resistance depends on the history of applied electrical controls. This application positions resistive switching at the forefront of future non-volatile memory technologies.[11] Additionally, systems with more than just binary ON and OFF states, known as multi-state devices, allow for the integration of logic and memory functionalities within a circuit. This is referred to as the in-memory computing paradigm.[12] Such systems bypass the von Neumann performance bottleneck of classical computing, a theoretical limit to computation efficiency due to the separation of logic and memory.

Inspired by living brains (biomimicry), ongoing efforts are aimed at developing artificial neurons using these systems, a field known as neuromorphic computing.[13–15] This is made possible by addressing the state of the device *in situ*, which can be used to tune the response of such an artificial neuron to stimuli. This is an ideal technology to address the demands of specialized circuitry for machine learning - a matrix of such neurons can serve as the hardware equivalent of the weight nodes in a model during training or operation. While fabrication and application of these systems remains nascent, a clear interest in the market exists for application-specific integrated circuit (IC) systems to service machine-learning systems.[16] In cases where other properties are modulated in addition to R , similar devices can function as programmable photo-detectors, micro-electromechanical machinery, or components in advanced quantum computing systems.[10, 17]

1.2 Classification and Mechanism

Several classifications of resistive switching are reported in literature,[18, 19] with the distinction criteria to highlight here being switching polarity (unipolar and bipolar systems), and number of states (binary and multi-state systems). Bipolar and unipolar resistive switching are illustrated in Fig.1.1(a) and Fig.1.1(b), respectively, through IV curves. Such curves show the current for a given voltage drive in the device, and their slope is the device resistance. Both (a) and (b) include an initial forming step where the driving mechanism is somehow initialized, and which has a starting resistance state different from the working low resistance state of the device in operation. These devices differ in whether the reset control must be applied in the opposite polarity of the original set control (bipolar), or if the system is set and reset without changing polarity (unipolar). Unipolar mechanisms are indicative of more thermally controlled processes, while bipolar switches tend to be determined by the charged nature of carriers and ions in the material.

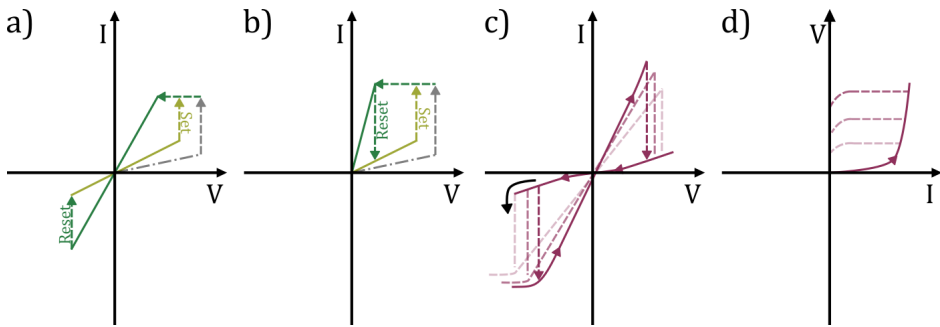


Figure 1.1: Characteristic IV behavior in devices displaying resistive switching. Bipolar resistive switching (a) is shown in devices where the polarity of the electrical stimulation is important, while devices where the effect is primarily thermally driven show unipolar resistive switching (b). Both of these cases (a,b) are shown as having an initial forming step in which the given switching mechanism is set (gray dash-dotted line), e.g. the initial crystallization of phase-change material or the formation of the filament channels in a metallization cell. These devices are binary switches that only have one ON and one OFF state accessible in operation. (c) An idealized switching oxide[20–23] IV , where the positively charged oxygen vacancies V_O^{2+} move in response to an electric field and control the resistance in the material. The dark-to-bright shadings show the effect of sweeping rate or temperature on the IV . [24, 25] The vacancy diffusion switching mechanism allows for multi-state memory in these devices, presumably allowing one to select different states as a function of electrical control, as shown by the various dashed lines in the VI curve in (d). [26]

Fig.1.1(c) shows idealized, slightly non-linear current-voltage (IV) curves characteristic of bipolar switching oxides,[25, 27] including functional perovskite oxides, which are at the core of our review. The transparent dashed lines illustrate the known effects of changing sweep rate or temperature on the low resistance state, showing the accessibility of multiple states in these devices. Their driving mechanism, understood to be centered around the diffusion of oxygen vacancies V_O^{2+} , allows for multiple non-volatile resistance states to be accessed reversibly, as illustrated by the dashed lines in Fig.1.1(d). This latter diagram corresponds to a perovskite constriction, in a low resistance state, being swept in increasing DC current[28, 29] until the electrical control induces vacancy accumulation. This redistribution of oxygen in the crystal locally creates a zone of higher resistance and may then be interrupted at will, leaving the device in one of the represented high resistance states. In view of this, we can regard oxide switches based on V_O^{2+} diffusion as multi-state switches.

Reversible resistivity change, potentially by orders of magnitude, is facilitated by one of the three comprehensive mechanisms illustrated in Fig.1.2. The phase change mechanism (PCM) shown in Fig.1.2(a), wherein the switch undergoes an amorphous-crystalline transition due to heating, is common in chalcogenide materials. The current induced temperature rise induces the phase change in both directions of the process. One should note that the temperature profiles of the same device in the OFF and ON states may differ a lot due to the changing resistance and precise process geometry, so transitions at wildly different temperatures can be accessed by heating. PCM are some of the leading candidates in terms of technological development,[30–32] with multiple implementations as binary switches based on it having been presented (for instance the rewriteable compact disc). These devices tend to behave in an unipolar fashion, as the temperature of the device determines the phase change. The second mechanism presented in Fig.1.2(b) that takes place in metallization cells (MC), where the ions of an active electrode diffuse into the changing material, has been implemented in numerous amorphous or crystalline materials[33] including both binary and perovskite oxides.[34] The limitations of such switches are in the stochastic nature of the filament growth and their limited cyclic stability. They tend to be bipolar binary switches, as the diffusion of metal ions depends on the polarity of the applied field. It should be noted that the opening and closing of the filament gap in the insulating matrix compliments the well understood electromigrative gap manipulation in metals.[35–37]

Vacancy diffusion (Fig.1.2(c)), hugely important in complex transition

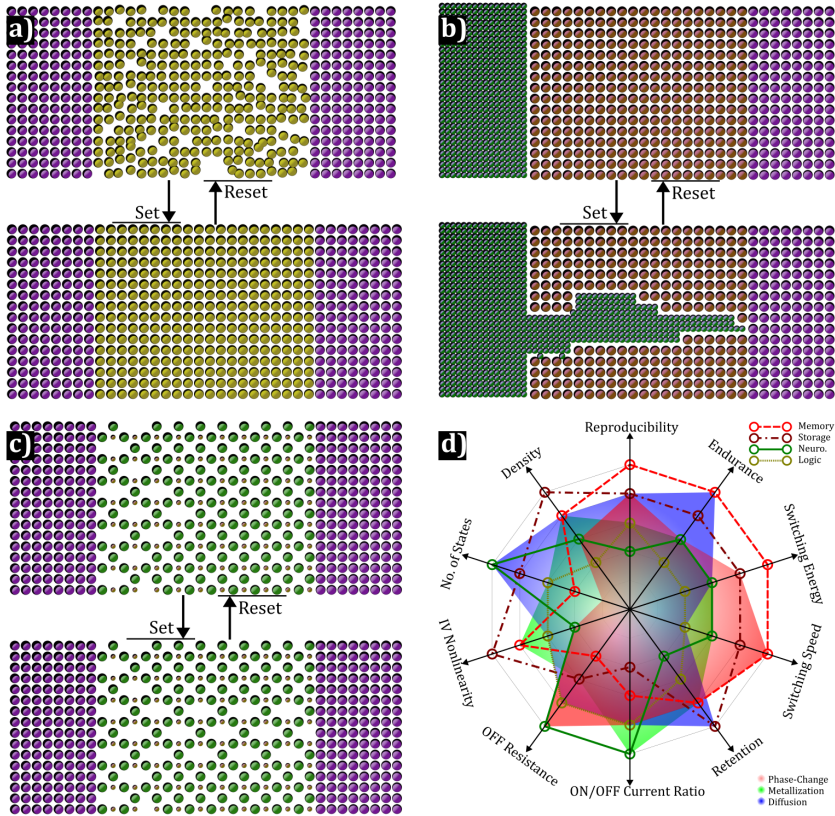
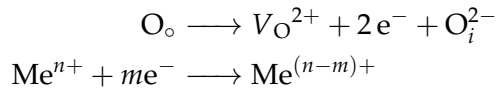


Figure 1.2: Illustration of common switching mechanisms. a) Phase-change materials undergo a glassy transition between an ordered (ON) and a disordered (OFF) state. b) Metallization cell systems function by intercalating metal ions in an insulating matrix, the device is in the ON state when the filament is connected. Metal ions can come from an active electrode (olive green) or from impurities/dopants (as in doped oxide switches). c) Metal oxides switch as their doping is controlled by oxygen vacancy distribution in the film - the device is ON when doped, i.e. when vacancies connect both electrodes. Shared color code: Magenta spheres are passive electrodes, yellow is phase-change material, green is active metal electrode, bronze is an insulator matrix, green and gold are the oxide. d) Schematic radar graph showing important characteristics for switching devices in computing. The lines and circles indicate the characteristics for the four main computing applications being studied - RAM memory, long term storage, neuromorphic (analog) computing and logic circuits. The shaded areas represent the current standards of the three families of switching materials in a-c). Radar graph and device demands based on Ref.[19], switch behavior adapted from Ref.[38].

metal oxides and focus of this study, is characterized by a rearrangement of ion-vacancy pairs of the material itself,[11] thus modulating the properties of the device under study. The correlated nature of the various physical orders in such materials have the effect of translating oxygen concentration and structuring into material doping. This effect is notably important in switching the properties of perovskite oxides,[20] a family of materials that includes some of the most exciting functionalities in modern material science. These include, but are not limited to, superconductors, magnetoresistive and multiferroic materials of many different compositions.[39–42]

Vacancies are in oxide materials more mobile than cations,[22] and their movement may lead to local accumulation that results in metal ion reduction[43]:



where O_o is a regular site-oxygen ion, O_i^{2-} an interstitial one and Me is a metal. If the metal reduction that occurs here facilitates electrical transport, as is the case in filling the $3d$ band of Ti^{4+} when switching in TiO_2 or SrTiO_3 ,[44, 45] the oxide exhibits increasingly metallic conduction due to deoxygenation by V_{O}^{2+} diffusion. Note however that, some oxides, including those discussed in the main text body, will become more resistive with increased V_{O}^{2+} concentrations. Vacancy diffusion as the basis for oxide switching physics is discussed below.

All these different mechanisms have advantages and disadvantages with respect to the varied possible applications of switching materials, as presented in Fig.1.2(d). While complex, some important trends to note are that memory and storage applications rely on highly non-linear IV characteristics, fast switching speed and low energy consumption, with reliability, endurance and retention being other very important qualities. Considering the requirements on non-linearity and switching speed, it is to no surprise that PCM devices have gotten further in those applications,[31] but similarly to metallization cells,[33] do not offer the necessary multi-state functionality and have limitations in endurance and retention.[38] Oxygen diffusion based systems, on the other hand, offer exactly the sought multi-state function in addition to being able to retain information over very long periods of time, thus garnering a lot of favor in the search for analog computing techniques.[14]

Oxides represent a special technological case, having a very high dielectric constant ϵ making them favorites in the semiconducting industry for the

production of dynamic random access memories (DRAM) or as gate insulators.[46] This means that a substantial understanding of their deposition and growth has been developed even without resistive switching effects being the drive of that research. This gives oxides a crucial advantage over both chalcogenide glasses and non-oxide metallization cells, in the form of a greater willingness and lower cost for adoption in the microelectronic industry.[47]

Beyond just resistance switching for memory cells, in-situ doping modulation has further applications in device fabrication. Possibilities of applying current and field control as compliments to standard fabrication techniques have been demonstrated in electromigration-driven constriction thinning[48, 49] in a number of metals, including among many others Au,[50], Nb[37, 51], Al[36] and alloys.[52] In these materials the strong momentum transfer from charge carriers to lattice ions causes atomic drift, a mechanism known as electromigration. This displacement of mass creates voids and hillocks (and heat) in the structure along the direction of carrier momentum and is a common failure point and a long standing concern in microconductor design, but it can be harnessed for purposeful creation of nanogaps, and other structural modifications.[53] In its simplest form, a nanogap can act as a bipolar binary switch, or can be used as building blocks in molecular electronics and nanophotonics. Ion drift in an ionic compound induced by similar electromigration effects[54, 55] is thus selective, as the increased mobility of one atomic species in the crystal causes its movement to be preferred. Through this approach, it is possible to devise techniques to apply high current densities to oxide structures with the objective to modulate their doping, as we create accumulation and depletion zones for V_O^{2+} while the remaining crystal retains one, albeit non-stoichiometric phase.

Compound material studies depend on growing our understanding of their phase diagram, which traditionally requires fabrication of many different samples with different compositions in comparable conditions. This method presents a severe limitation in terms of workload for any individual research effort and is prone to problems as individual sample batches may be non-comparable and thus may obscure important features of the material study. More modern approaches include fabricating materials with inbuilt composition spread (combinatorial studies)[56, 57], but the notion of using *in situ* modification methods has great promise in supplementing these works. Doping modulation in switching oxides, as shown in Fig.1.1(d)., where one uses electrical stimulation to change the material's resistance only to the desired extent before performing a measurement or characterization. In the example the drive is by current I . The steps can then be repeated, allowing

one to potentially measure a whole material phase diagram on a single device. In fact, pioneering studies following this approach have already been presented in perovskite materials.[58, 59]

1.2.1 Vacancy Diffusion

The dynamics of the switching processes observed in perovskite oxides, [60, 61] more than in other oxides,[62] hinges on the diffusion of V_O^{2+} , and we will thus be interested in formalizing it. For a mathematical treatment of the flux of V_O^{2+} in an oxide on a macroscopic level, we may utilize Fick's laws[63] of diffusion:

$$\bar{J}_V = -D_V \nabla c_V \quad (1.1)$$

$$\frac{\partial c_V}{\partial t} = \nabla \cdot (D \nabla c_V) \quad (1.2)$$

with J_V [$\text{m}^{-2}\text{s}^{-1}$] as the vector flux and c_V [m^{-3}] the concentration of the vacancies in the crystal. The diffusion coefficient D_V [m^2s^{-1}] is a tensor whose value depends on a preexponential factor D_V^* and temperature T [K] as per:

$$D_V(T) = D_V^* \exp\left(\frac{-E_a}{k_B T}\right) \quad (1.3)$$

for k_B [JK^{-1}] being the Boltzmann constant and E_a [J] is the activation energy of diffusion. T [K] is temperature. Considering that for every diffusing V_O^{2+} there must be a diffusing O atom $D_O c_O = D_V c_V$, and that the solid solution is very dilute in terms of vacancies $n_V \approx \frac{c_V}{c_O} \ll 1$, c_O being the oxygen concentration, we observe:

$$D_O = D_V \frac{c_V}{c_O} \approx D_V n_V \quad (1.4)$$

From here one can see that the diffusivity will necessarily be larger for vacancies and that their mean displacements will be orders of magnitude larger than atoms. D_V depends only on temperature as long as we consider the solution dilute.

One should consider all forces acting on V_O^{2+} as possible sources of J_V in order to fully implement Eq.1.1. Local differences in heat or strain and other parameters may contribute, as illustrated in the Tab.1.2.1.

Taking all this into account, one may formulate[68] a more complete

Box 1.1: Electromigration: What is the effective valence Z^* ?

In an effect similar to erosion of waterways through flowing water, electrical conductors can be affected by the electric current they carry through electromigration (EM). The phenomenon is seen in ionic diffusion occurring due to momentum transfer between charge carrier and lattice ions. The principal motivator for the study of this effect is the fact that it is a major failure mechanism in microelectronics,[64] as even small current densities may incur void formation or mass accumulation under prolonged operation. More recently, however, the effect is studied as a method for manufacturing extremely thin (atomic scale) constrictions and nanogaps.[53]

A microscopic description of the phenomenon is given by considering the forces acting on a charged particle (ion) in a crystal lattice, as per:

$$F = F_w + F_d = (Z_1 - Z_2)eE = Z^*eE$$

for e the electron charge, E the electric field and the difference of Z_1 and Z_2 describing the effective valence Z^* being acted on by the electrostatic force. Here Z_1 is the proportionality constant for the wind force F_w and represents the momentum transfer between carrier and defect, while Z_2 is the same for the direct force F_d originating from the electrostatic interaction, including the screening of the ion.[65] In the case of a common metal that is a cation in a crystal (Au, Al, Ag...) F_w and F_d oppose each other and F_w is dominant resulting in a mass transfer along the direction of the current flow. It is, however, possible to find Z_2 to be negative, especially for impurities in metallic matrices. Some numerical results can be found in Ref.[66].

Conclusive models of either force (F_w and F_d) are hard to come by, but numerous proposals have been put forward, including some that treat them in unison.

For an individual treatment of F_w a simple entry level model for metals can be constructed by considering the interaction between the electron and a cation defect or vacancy in the crystal lattice. Drawing a classical picture, the momentum transfer rate is equal to mv_d/τ_i where m is the mass of the charge carrier, v_d the drift velocity and τ_i the collision time for electrons scattering at an impurity. By introducing the densities of carriers n and defects N_i we can express the wind force F_w as a function of the current density j as:

$$F_w = -\frac{j/m}{e\tau_i N_i} = -e\frac{n\rho_i}{N_i\rho}E$$

where $\rho = E/j$ is the total resistivity and $\rho_i = m/(ne^2\tau_i)$ the resistivity originating from the defects. Other approaches have produced self-consistent definitions for F_w from the electron wavefunction, but we will point to literature[53] for this treatment in the interest of brevity.

It is important to note at this point that the wind force varies dramatically for various atomic positions in the lattice, with atoms on grain boundaries, surfaces and other positions with lowered binding energies having an easier time moving.

The direct force used to be treated as the simple electrostatic force $F_d = ZeE$ (for Z the charge of the ion), but screening effects add layers of complexity on this definition. A modern definition includes the screening effects, manifested in an increase in carrier density in vicinity of an impurity, by combining the electrostatic force and electron non-equilibrium states in a Boltzmann equation:

$$F_d = \frac{ZeE}{1 + (1/3)\beta\Delta n/n_0}$$

with Δn is the local increase in carrier density due to the impurity, n_0 the average carrier density and β is a parameter of order unity.

Table 1.1: Overview of vacancy diffusion effects.[67] σ is the strain.

Driving Force	Diffusion Gradient	Example
Electromigration	∇E	IC failure
Thermomigration	∇T	Soret effect
Chemical diffusion	∇c	Kirkendall effect
Strain	$\nabla \sigma$	Diffusion creep

expression for the vacancy flux as:

$$\bar{J}_V = -D_V \left(-c_V \frac{eZ^*}{k_B T} \nabla E + \nabla c_V + c_V \frac{f\Omega}{k_B T} \nabla \sigma - c_V \frac{Q^*}{k_B T^2} \nabla T \right) \quad (1.5)$$

Here e is the elemental charge and Z^* is the effective valence,[48, 69] representing the momentum exchange interaction between the charge carriers and the ions in the lattice. The meaning of this variable is discussed in Box.1.1. f is the adimensional vacancy relaxation factor (corresponding to the fraction of the atomic volume occupied by the vacancy, $0 < f < 1$), Ω is the atomic volume [m^{-3}] and Q^* is the heat of transport [J].

An illustration of the electrically-driven to thermally-driven diffusion in the terms in Eq.1.5 is given in Fig.1.3. In this work the full extent of this equation is not modeled, both because of computational intensity as well as because occasions where all forces play a major role are seldom. Electrical doping control in perovskite oxides will be based on those diffusion processes of V_O^{2+} that are controlled by the first term $-c_V \frac{eZ^*}{k_B T} \nabla E$.

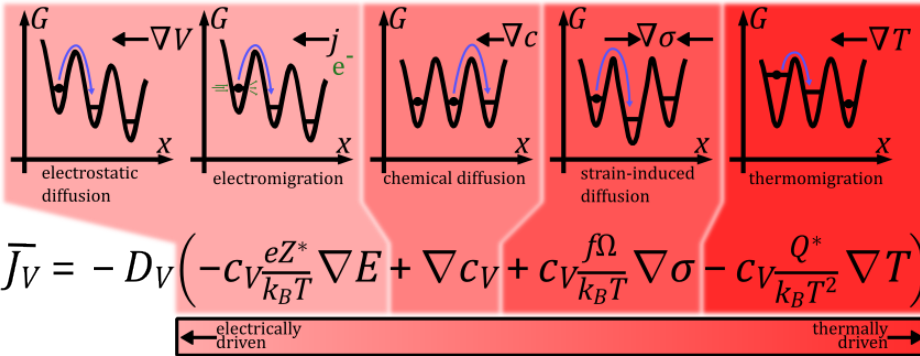


Figure 1.3: Illustration of the relative thermal and/or electrical influences on the free energy of diffusion G . x is the position of an ion. [19, 70]

Chemical diffusion, described in Eq.1.5 through the gradient ∇c_V , refers to diffusion due to local concentration inhomogeneities of the species in

the same manner one may observe it in gaseous or liquid solutions. This diffusive force is thus a minor contribution in well homogenized samples. Under the effect of the interaction energy in the crystal lattice coming from local strain or lattice mismatch, a species may diffuse as described by the strain-induced diffusion term $c_V \frac{f\Omega}{k_B T} \nabla \sigma$. This effect is notable, naturally, in samples with severe internal strain or great external pressure. Finally, thermomigration $c_V \frac{Q^*}{k_B T^2} \nabla T$ refers to that atomic movement affected by local temperature differences, and can be avoided in samples with homogeneous heat transfer.

Limiting ourselves to the electrically controlled term in the described diffusion process, we may choose to combine Eq.1.5 with Fick's law in Eq.1.2 and macroscopically describe electrically induced oxygen vacancy diffusion as:

$$\frac{\partial c_V}{\partial t} = \nabla \left(D_V \nabla c_V + c_V e Z^* \frac{D_V}{kT} \nabla V \right) \quad (1.6)$$

As we will show ahead in this thesis, this dependence has been successfully applied for describing both electric field[71] and current[72] driven vacancy diffusion and has been translated into empirical models of property control in both superconducting cuprate and magnetoresistive manganate samples.[73] Notably, it has been shown to be fully sufficient to describe experimentally observed oxygenation maps in current switching samples.[74]

Vacancy diffusion in oxide materials has been under intensive study,[75] and one may find both empirical models[60, 76] and full microscopic descriptions of the effect in literature.[43] It is crucial to apply proper care in selecting the diffusion model and customize it, as not only electrical,[77] but also heat transport[78] and strain[79] effects may become relevant at times.

1.3 Doping Control in Transition Metal Oxides: A Family Picture

Mathematical description of insulating oxide transport behavior was one of the driving forces in the development of correlated electron models of conduction.[80] Before this, the distinction between insulating and conducting materials was made by considering the highest occupied band in the structure. Conductors have unfilled bands, and insulators have filled bands, with the Fermi level lying in a band for conductors and in the gap for insulators. Pure metals, alloys, and other conductive crystals were described by conduction models based on non-interacting charge carriers on a periodic lattice. These

models, developed by Drude, Bloch, and Sommerfeld, allowed scientists to predict semiconductors more than a decade before Shockley and his team at Bell Labs presented the first transistor. Materials with small gaps were expected to be conductors at sufficiently high temperatures.[81]

However, these descriptions ran short when considering the electrical nature of transition metal oxides.[82] The non-interacting electron models did not provide satisfactory explanations for materials with overlapping orbitals.[83] To address this, conduction models based on electron-electron interactions, also known as correlations, were introduced by Mott[84] and then developed further by Hubbard[85] and others.[83, 86] Such compounds generally have a set of filled low lying orbitals and a set of half-full, commonly degenerate,[81] hybrid orbitals near the Fermi surface. The hybrid orbitals arise from the interaction of metal *d*-orbitals and the oxygen *p*-orbitals. Their conductivity is limited as a function of the exact position of their Fermi surface which in turn, is controlled by their doping. Because of these correlations the material exhibits transitions between conductive and insulating states, so called metal-to-insulator transitions (MIT). Correlated models explain the MIT[81, 87, 88] and cuprate superconductivity[89, 90], centering on electron-electron and electron-phonon correlations, and we now understand the importance of the interplay of magnetic, structural and electrical orders in all oxide properties. Pioneering work in recording the metal-insulator transitions in oxides has begun in the first half of the 20th century,[91] and continues to this day. Currently, a substantial effort is put in studying the metal-to-insulator and superconductor-to-insulator transitions (SIT) in complex oxides as a function of not only temperature,[92] but strain,[93, 94] pressure,[95] doping,[96] optical excitation[97, 98] and electrical stimulus.[99, 100] These reversible transitions in the electronic and structural phases of the material present a natural opportunity for study and application in resistive switching.

Initially, oxides as electrically switching materials were studied in the context of negative differential resistance[23] in oxides of metals commonly used as complementary metal-oxide semiconductor (CMOS) gates (Al, Ti, Nb, Ta, Zr). In these materials one could observe a drop in current increasing voltage, for voltages above a certain threshold,[6, 101] the same feature that is illustrated by the vertical drops in Fig.1.1c). Researchers covering the topic provide the initial explanations in terms of space-charge effects at the metal-oxide interface,[102] or in terms of avalanche-like effects, where initial charge injection close to the electrode causes further field amplification and therefore even further charge injection. While this interpretation still rings true for

numerous oxide systems experiencing a threshold switching effect,[103, 104] it does not cover all switching behaviors experienced in oxides. Further studies[11, 41] have then expanded the observations to a very wide family of oxide materials, forcing the conclusion that the effect may be more structural than purely electronic.

The presence of electrons in hybrid (Hubbard) bands determines the conductivity of these oxide materials,[80] creating a self-doping system[104] in the crystal centered around the presence of V_O^{2+} . Continuing the analogy to semiconductor physics, we thus may choose to consider the oxygen content of an oxide to represent its doping. As is shown for functional, often complex oxides below, this doping may control more than just the resistivity of the material as all oxide functionalities (ferroelectricity, magnetoresistance, optical behavior, magnetic and superconducting transitions) depend on the values of this doping.[105] It has been shown, for instance, that doping can induce solid-solid phase transitions[106] and tune the optical gap[107] properties of VO_2 .

1.3.1 Simple Transition Metal Oxides

The key features[11] of oxides that show a tendency to switch between multiple electronic states are mixed-valence metal ions and mobile oxygen vacancies. Both of these features are most prominent in transition metals. Their d -shell electrons allow multiple oxidation states of the same element and lower the bond strength of their Me-O bonds compared to more metallic elements in comparable compounds.[108] An excellent example of this is VO_2 [109] - V is a 5th group element with outer shell structure $[Ar]3d^34s^2$. The metal may take on oxidation states +2, +3, +4, +5 allowing for a great number of phases in the VO_x phase diagram as a function of oxygen content.[102, 110] The element effectively has an easy time coordinating with varying numbers of oxygen ions (and V_O^{2+}), and the reduced

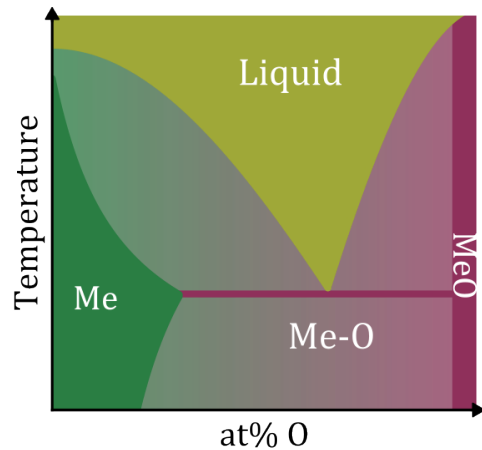


Figure 1.4: Generic oxide phase diagram in terms of atomic percentage of oxygen. The phase diagram includes an eutectic point and a melting line is indicated. The Me-O segment with the gradual coloring represents the metal-oxygen solid solution. Recreated from Ref.[19].

energy cost of restructuring facilitates the necessary anion diffusion.

Considering the phase diagrams of many such materials in terms of distinct phases of stoichiometric composition is probably inaccurate, due to numerous local defects and changes in crystal structure (see Box.1.2). Depending on the composition change, we may consider four kinds of defects[111] that facilitate non-stoichiometric[41, 112, 113] behavior: i. oxygen vacancies V_O^{2+} for easily reduced cations, (e.g. PrO_{2-x} and CeO_{2-x}), ii. interstitial oxygen O'' for easily oxidized ones (UO_{2+x}) iii. metal vacancies V_M^{n-} also with easily oxidized metal ions (e.g. Fe_{1-y}O , Mn_{1-y}O and Co_{1-y}O), and iv. interstitial metal, which follows V_M^{n-} . A better illustration of such metal oxide phase diagrams is presented in Fig.1.4, where the extremes in composition are the metal on the left and its highest oxidation state oxide on the right, with a solid oxygen solution describing most of the central part of the diagram. These materials conserve charge neutrality either through coupled defect pairs of opposite charge, or by changing the valence of the transition metals in the structure.

Other binary transition metal oxides have been studied under the auspice of resistance switching, with some notable examples being indicated by the red vertical bands in Fig.1.5. Note that the behavior is common among lighter transition metals and only the heavier group 4 and 5 elements. These elements have less-than-half filled d -orbitals, which hybridize with oxygen p -orbitals to form hybrid bands and are easily doped by vacancies. The prevalence of the effect in heavier elements is easily explained by the weaker bonding of the electrons in their atoms as they belong to less energetic, better shielded outer shells. Resistive switching in binary oxides, such as TiO_2 , [9, 114, 115], CoO_x [116], VO_2 [15] and HfO_x [117] is a common topic, and much literature exists summarizing the findings. [118]

1.3.2 Perovskite Oxides

We narrow our attention to perovskites, some of the most functionally iconic complex oxides. [119] Complex oxide here indicates that the material has two or more cations in the structure, and the family is so named for sharing its structure with a mineral form of calcium titanate. The perovskite ABO_3 structure is shown above the periodic table in Fig.1.5. [80, 120, 121] The A-site cation is a large, fully ionized metal and the B-site cation is the crucial, smaller cation forming hybridized orbitals with the oxygen atoms on the edges of the unit cell. The structure, with the parent compound BaTiO_3 (a cubic crystal), usually takes either an orthogonal or tetrahedral form, [120] and can feature mixed valence cations of great variety [122] and mobile V_O^{2+} . [75, 123, 124] The

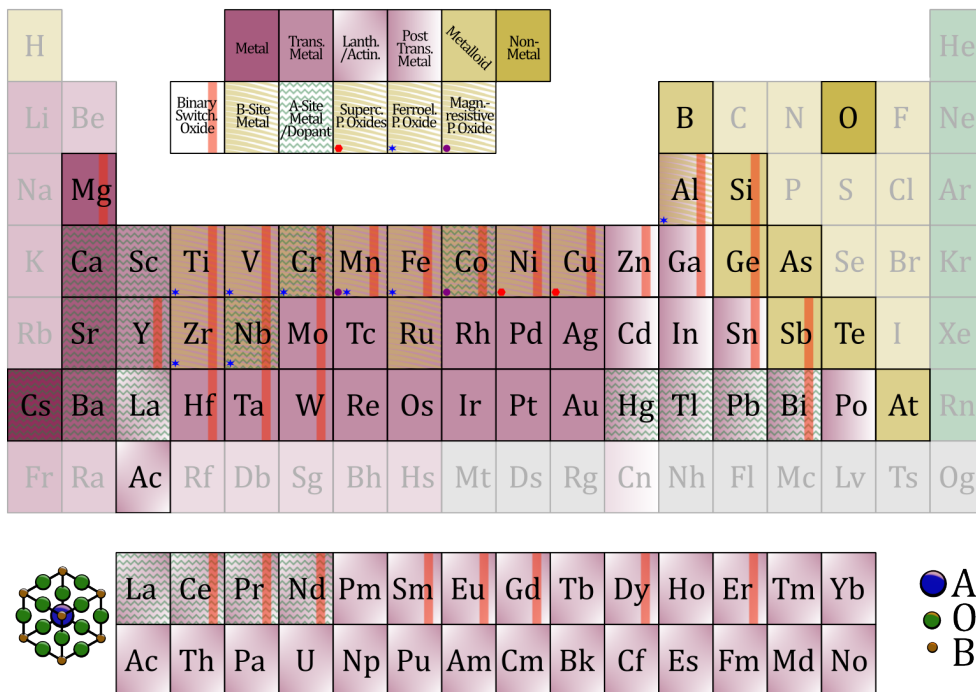


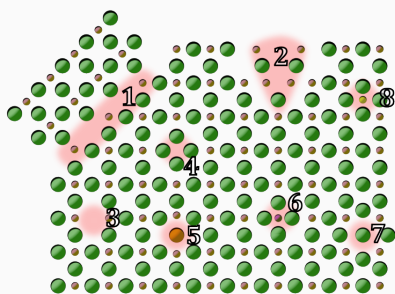
Figure 1.5: Switching oxides distributed across the periodic system. Alkaline metals and non-metals of little relevance are grayed out. Metals that have binary switching oxides are indicated by red vertical lines. A-site cations in perovskite oxides are indicated by the green horizontal zig-zag lines, while B-site cations are shown with golden waves. Additional symbols indicate the functionalities present in a any given family of perovskites based on their B-site cations.[80] The parent structure of the perovskite family is shown in the bottom left, the sizes represent ionic radii.

B-site cation function can be filled by all period 3 transition metals considering their available oxidation states and similar sizes, with some examples found in period 4. The A-cation is usually a heavier metal set lower and more left in the periodic table, with either the heavy earth-alkaline, early lanthanoid or, more rarely, heavy post transition metals filling the position. Common perovskite cations are indicated in Fig.1.5 with the semi-transparent overlays on the elements. Yellow waves and green ramps for B-site and A-site cations, respectively. Limiting our consideration to the cations in the oxide, we may say that the B-site cation controls the functionality physics of the material family and the selection of A-site tunes them.

Strong electronic correlation[125–127] effects result in a changing valence state of the crystal ions in such materials as they undergo charge injection,

Box 1.2: Crystal Defects in Oxides

No crystal is perfect, and the differences from ideal periodicity are called crystal defects. They are a natural consequence of growth conditions and the presence of impurities during crystal growth. Defects can have profound effects on the properties of any material. The whole semiconductor industry is built on the idea of influencing the properties of semiconducting crystals through inclusion of impurity phases, and the concept of "monocrystals" is defined by the avoidance of granular changes in growth direction of a crystal. Oxides are no exception to the presence of defects, as illustrated in the figure below.



In non-stoichiometric crystals, some defects allow the material composition to vary greatly (see main text). However, the term defect also includes the presence of

elements foreign to the compound itself and departure from the crystal periodicity. The defects, illustrated in the figure, are:

1) **Grain boundaries** are planes along which the crystal changes orientation of its periodicity. Each area of fixed orientation is considered a grain, and it is often advantageous to grow crystals with fewer grains if one aims to study purely the properties of the crystal itself.

2) If the crystal includes an irregularity in its periodic structure, like a sudden change of direction in the organization of the crystals which strains the surrounding crystal that is considered a **dislocation**.

3) & 4) Certain crystal positions may be left vacant during crystal growth due to a number of reasons, including lack of appropriate atoms. In oxides, these vacancies include **oxygen vacancies** V_O^{2+} (3) and **metal vacancies** V_M^{n-} (4).

5) & 6) Elements of similar charge and ionic radii can be substituted for each other in crystals. These defects include **anion substitutions** (5) and **cation substitutions** (6).

7) & 8) It is possible for small amounts of ions or atoms to be "locked" in the crystal outside of the common equilibrium positions in the crystal lattice, at the cost of strain in the material. These inclusions are usually referred to as **interstitial oxygen** (7) and **interstitial metal** (8).

subsequently changing the carrier density and resulting in Mott-type MIT.[34] This change of metal valence tends to be accompanied by a restructuring[128] of the crystal across its nonstoichiometric composition and a consequent modulation of various functionalities.[39] Common special functions of the oxides are indicated in Fig.1.5 with the corresponding B-site cations with whom they appear.

Notable examples of particular interest in the framework of our research include the ferroelectric ferrates and titanates akin to STO,[129] high critical temperature superconductors like $YBa_2Cu_3O_{7-\delta}$ (YBCO)[42] and related compounds and $La_{1-x}Sr_xMnO_3$ (LSMO)[40, 130] representing the magne-

toresistive manganites. Closer inspection of their functionalities, electronic phases, and structural features provides insight[41] in the importance of the various correlations of these oxides.

STO is a perovskite noted for its ferroelectric[131] and piezoelectric[132, 133] behavior. Its tetragonal, low temperature phase retains a spontaneous dipole as a consequence of applied electric field, while the high-temperature cubic form does not. It is in common use in solid state laboratories as one of the main epitaxial substrates for perovskite growth, together with LaAlO_3 (LAO). Oxygen defect structuring[44, 45, 134–136] has been well understood to be key to resistive switching and to fine-tuning the oxygen diffusivity[137] and the ferroelectric response of the material. Additionally, doping control by cation substitution, interstitial metal and other impurities has been studied in-depth in this material facilitated by its well understood growth parameters and use in epitaxial deposition of other perovskites.[34, 138]

LSMO represents manganate perovskites and is also a product of systematic cation substitution studies tuning its properties. It is common wisdom in recent times that $x = 0.3$ gives a material with the highest magnetization.[139] The phase diagram in Fig.1.6(a) is a schematic representation of the various phases of LSMO as a function of x . [139] The doping control in LSMO is commonly achieved by tuning the ratio of earth-alkaline to rare earth cations, although high V_O^{2+} mobility has been observed to control it on its own vector.[140, 141] The inset shows a ball-and-stick representation of the tetragonal LSMO unit cell. At low doping, the material is insulating, while being metallic at higher values. The spin-canted insulator phase is one with highly non-linear electric transport due to special topological features of the bands. LSMO is a great example of Giant Magnetoresistance (GMR), an extremely useful material property tunable by doping, discussed further in Box.1.3.

The tetragonal LSMO structure shown in Fig.1.6(a),[40] is considered the $n = \infty$ Ruddlesden-Popper phase, corresponding to $(A,A')_{n+1}\text{Mn}_n\text{O}_{3n+1}$. With decreasing n this sequence consists of an increasing number of MnO layers intercalating between the MnO_2 ones, and many such compounds are known in the manganite family. An additional layer of complexity exists in the material family as the V_O^{2+} defects form supercells in what is known as a brownmillerite crystal.[143]

YBCO is a very popular model material for the family of cuprate superconductors, due to its high- T_C and large body of literature surrounding it. Cuprate superconductivity is expanded upon in Box.1.4. The compound has seen use in commercial high temperature superconductor (HTS) tapes

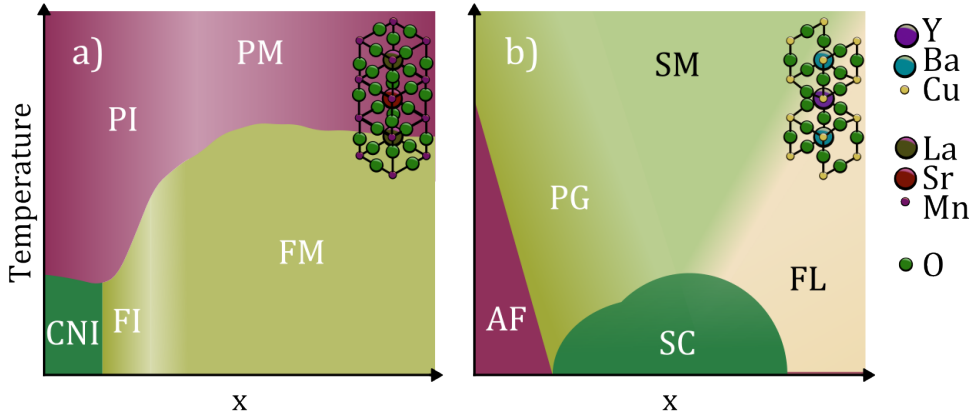


Figure 1.6: Generic perovskite oxide phase diagrams. a) LSMO phase diagram as shown in Ref.[139] as a function of x , indicative of hole doping in the material. PI is paramagnetic insulator, PM is paramagnetic metal, CNI marks the spin-canted insulator phase, FI the ferromagnetic insulator and FM the ferromagnetic metal. b) Idealized YBCO phase diagram, as presented in Ref.[42], as a function of hole doping, a function of the deoxygenation δ . AF is antiferromagnetic insulator, PG is the pseudogap phase, SM is the strange metal phase, FL represents Fermi liquid and SC is the superconducting phase. The insets represent the respective crystal structures.

and in other places where a cheap superconducting material is needed. The structure of YBCO is discussed in Box.1.5, and its phase diagram is shown in Fig.1.6b) as a function of the doping x .

The doping value x in Fig.1.6b) is reflective of the value of δ , the deoxygenation.[154] Both in terms of oxygen exchanged with the environment[155] as in samples with varying oxygenation levels,[58, 156] the resistivity ρ and the T_C strongly couple to oxygen content in the material. An orthorhombic-to-tetragonal transition that corresponds with a decrease in metallic character is observed as δ approaches 0.45. Optimal doping for the material ($T_c = 93$ K) is observed for $\delta = 0.05$. Underdoped YBCO in the pseudo-gap phase has been known to be susceptible to photodoping, where the superconducting T_C and normal state resistivity are modulated by illumination.[70, 157–159] This effect is also observed in other cuprate superconductors.[98] Additionally, V_O^{2+} restructuring seems to be another phenomenon that follows after light exposure YBCO.[160, 161]

Structural determination[120, 121] elucidated the interlaced perovskite-rock salt-perovskite structure, shown in the inset of Fig.1.6(b) and discussed in Box.1.5 consisting of the crystal layers:

Box 1.3: Colossal Magnetoresistance in the Manganite Family

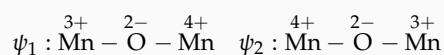
The resistivity of some materials depends on externally applied magnetic fields. Termed "magnetoresistance", this effect exists at low temperature even in metallic systems, where applied magnetic fields may influence the mean free path of electrons. Giant magnetoresistance (GMR), on the other hand is observed in multilayers of spin-polarized metals, where the change in resistance is caused by field induced spin alignment occurring at layer interfaces. Devices based on this phenomenon have already found their way to commercial applications, but a number of technological challenges remain. Essentially, as electrons travel through the lattice of a conductor, one of the causes of scattering events is due to misalignment of the spin states of neighboring metal ions and the charge carriers themselves. As the spin alignment of the ions in a lattice can be affected by an external field, this allows for another "knob" for property control.

Cobaltate and manganate oxides[41, 130] have the peculiar characteristic of exhibiting magnetoresistive behavior in single crystals and across grain boundaries,[142] and the amplitude of the induced resistivity change has lead researchers to term the effect colossal magnetoresistance (CMR).

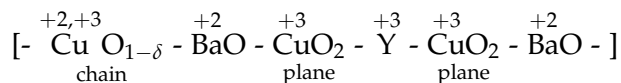
In the specific case of LSMO[40] the magnetic and conducting characteristics of the material are intimately linked to each other and to doping levels through the spin alignment of the metal ions in the Mn – O – Mn hybrid bonds. The *d*-orbitals of the Mn ions experience electrostatic repulsion from the *p* orbitals of the oxygen atom and loose their degeneracy. This band splitting causes electrons to populate bands of lower energy which distorts the shape of the orbitals (Jahn-Taller distortions). Suppression of these structural distortions (e.g. through dop-

ing, temperature or pressure) can cause the material to drastically change behavior, for example by exhibiting a metal-insulator transition (MIT) or changing from ferromagnetic to antiferromagnetic ordering (see Fig.1.6).

The electronic structure of manganites is intricate. Mn ions can exist in the +4 or +3 states and the metal is overall reduced with deoxygenation. If two Mn ions connected via an O ion have antiparallel spin alignment, electron transfer can only occur via a superexchange mechanism (electron changes spin orientation during the transfer), and the material behaves as a covalent, insulating crystal as is the case for LaMnO₃ and SrMnO₃. By mixing the cation ratios in LSMO (doping) we induce a mixed valence state of the Mn ions. One can then consider conduction in such manganites by imagining a crystal section of structure Mn – O – Mn in transport:



The two states ψ_1 and ψ_2 are degenerate and commutable via a double-exchange matrix element. Because of Hund rule coupling of the two metal ions of different valence this matrix only has finite values if the metal ions transferring electrons via the non-magnetic oxygen have aligned spin states. This mechanism allows for metallic transport in the ferro- or paramagnetic LSMO compound and is different from superexchange mechanisms seen in the simpler manganites.[125] As we can align the spin states of the Mn ions by external field, we may observe magnetoresistance. A review of the history of the double-exchange and later, more sophisticated models is given by Salamon and Jaime in Ref.[40].



Box 1.4: High T_C Superconductivity in Cuprates

High critical temperature T_C superconductivity has been first observed in cuprate perovskites in 1986 by Bednorz and Müller,[3] for which they shared a Nobel prize. They were not the first oxides with zero resistance transport and perfect diamagnetism, the hallmarks of superconductivity, as that honor goes to spinel titanates with T_C 's below 15 K.[144] The initial barium-copper-oxide perovskites already broke the previous theoretical maximum T_C of 30 K.[145] The YBCO system would become well known for its 93 K superconducting transition,[146] a firm 16 K above the boiling point of nitrogen, and today we know of other cuprate perovskites[147] with T_C 's up to 130 K under atmospheric pressure.[148]

The YBCO phase diagram is approximated in Fig.1.6b), and one should note the superconducting dome nested be-

tween the low doping, insulating antiferromagnetic phase and the semi-metallic/metallic regions of differing electronic descriptions. This amazing complexity has long been a nexus of research in the solid state community,[42] showing the tight linkage between oxygenation and doping in these materials. In the briefest, low doping YBCO exhibits numerous symmetry breaking behaviors, described as the pseudo-gap region,[149, 150] including charge-, spin- and pair-fluctuations as the temperature is lowered. It is more metallic with increased doping, where it is well described by Fermi liquid models.

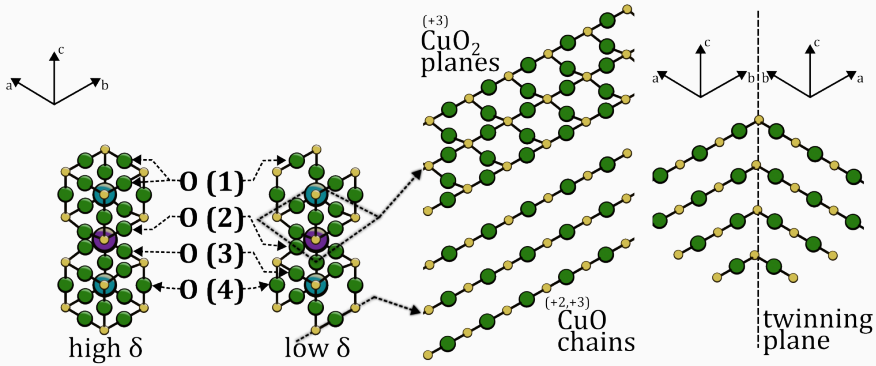
The microscopic carrier coupling mechanism that gives rise to cuprate superconductivity has not been elucidated yet and is a matter of active investigation.

The assigned oxidation states correspond to oxygen rich YBCO as reported in literature.[122] The structure is shown in the inset of Fig.1.6(b), for the superconducting, highly oxygenated[152] orthorhombic form of the material.[120, 121] It should be noted that there are two distinct positions for the Cu atoms to take, the basal Cu-O chains and the equatorial CuO_2 planes. These features are common to all cuprate superconductors,[120] and it is understood in literature that the superconducting Cooper pairs are localized in the plane, while the copper-oxygen chain function as charge reservoir layers.[162] The formal valence of the cations in the structure is indicated in the chain above, and one should consider the values for the copper ions a functions of δ .

Transport in YBCO is known to be highly anisotropic,[163, 164] with $\sim 60\%$ of the normal state conduction happening along the Cu-O chains.[165] This is understood as a consequence of the layered structure of the material and the electronic distinction of the layers. Cuprate superconductors are hole conductors in the normal state,[166] with the holes primarily existing in the chains and from there modulating the state of the electrons in the plane layer. The O(4) oxygen on the $[0,0,1/2]$ position (apical oxygen) is then the link between these two distinct parts of the crystal.

Perovskites have highly mobile V_O^{2+} [43, 167, 168] whose diffusivity de-

Box 1.5: Structure of YBCO



YBCO is among the most studied early cuprate superconductors,[120, 121, 151, 152] being one of the first ones with a T_C above N_2 boiling temperature. The compound has an interlaced perovskite-rock salt-perovskite structure as illustrated above (see Fig.1.6 for color code). The perovskite section are the basal regions with the Y atoms surrounded by (reduced) copper-oxygen tetrahedra, and the rock salt form is seen in the central Ba atom with copper-oxygen pyramids surrounding it.

It is now accepted in literature that YBCO occurs in two crystallographic symmetries, depending on the level of oxygen content: orthorhombic for low δ ($a \neq b \neq c$, space group $Pmmm$) and tetragonal for high δ ($a = b \neq c$, space group $P4/mmm$). The orthorhombic, well oxygenated form is the superconducting one and corresponds to compositions with δ below ~ 0.65 . Both forms of YBCO are illustrated in the figure above, and the values of their cell parameters[121] are listed in the table below.

	a [Å]	b [Å]	c [Å]
$\delta \approx 0$	3.82	3.88	11.68
$\delta \approx 0.45$	3.83	3.88	11.72
$\delta \approx 0.66$	3.86	$= a$	11.77

The oxygen atoms can be described as having distinguished functions in the

crystal and are labeled according to Jorgensen et al.[121] While both structures include the CuO₂ planes that contain O(2) and O(3), they are distinguished in the orthorhombic (low δ) form as hosting the superconducting Cooper pairs in the structure. This is a common feature of all superconducting cuprates.[120] The apical O(4) atom facilitates charge transfer from the basal Cu-O layer in the orthorhombic form, a function that is suppressed in the tetragonal crystal due to weaker Cu-O(4) interactions. In fact, it is this charge transfer that allows doping of the CuO₂ planes with holes from the CuO chains, which is key to both normal and superconductivity.[153] It has been shown that in approach of the orthorhombic-tetragonal transition (as δ increases) the site occupancy of O(1) drops while the $[1/2,0,0]$ position becomes increasingly populated, indicating a clear preference of V_O^{2+} to the CuO chains over the CuO₂ planes.

A common headache in characterizing the notoriously anisotropic YBCO crystal is its tendency to formation of twinning planes, that is crystallographic defect planes along which the a and b cell directions flip. The anisotropy has been characterized over the years (see main text) and today we have growth techniques which allow one to grow nearly untwinned films by means of substrate-induced anisotropic strain.

depends on oxygen non-stoichiometry[169, 170] and A-site cation.[171] Diffusion of V_O^{2+} is thus a prime target for research and nanofabrication efforts,[172] especially in a material as potentially useful as a high- T_C superconductor. Similar to how the electronic transport is anisotropic in YBCO, with $\rho_{ab} \ll \rho_c$, previous work has confirmed a diffusivity D_V of V_O^{2+} much larger in the ab plane $D_{ab}(V_O^{2+}) \gg D_c(V_O^{2+})$, with a preference for the b direction $D_b(V_O^{2+}) > D_a(V_O^{2+})$. [173] This can be approximated as being a consequence of the channeling through the $[1/2,0,0]$ positions.[174] This position is usually filled in the perovskite ABO_3 structure, and the vacant slot in cuprate superconductors is key to many of its properties.[175] The distinction between a and b values of either ρ or D are hard to distinguish due to the similarity of these cell parameters for YBCO. While the crystal is orthorhombic in its most interesting, superconducting phase, the distinction between the two cell parameters is very small (see Box.1.5, $\sim 0.3\%$). This allows the crystal to form twinning planes during growth. These planes then delineate areas where adjoining regions turn by 90° .

Furthermore, one should consider that strain[176] and dislocations in the structure may affect V_O^{2+} mobility in these materials. Fortunately, this may also be useful as it allows one to align certain perovskites, like YBCO and its Cu-O chains, along substrate terrace edges on substrates of certain cell parameters with proper chemical treatment.[177] Using this approach, one may create YBCO films and crystals that strongly disfavor twinning, allowing for better detection of physical properties. This feature is utilized for the work presented in Ch.5.

The microscopic origin of the resistance switching behavior in perovskites remains a contentious topic. Different mechanisms have been used to work out the minutiae of the origin of the changing ρ and Table 1.2 is a selected overview of these effects from the larger discussion of switching mechanisms by Bagdzevicius et al.[104] Specifically ferroelectric materials like ferrates[78, 178] are well described by invoking a depletion region originating from charge injection into the material.[179] Flipping the polarization of the ferroelectric causes a reversal of the positions of the depletion region and the associated band distortions in respect to the electrodes, being referred to as Schottky-type metal-semiconductor interfaces. This allows for diode behavior, specifically by making one electrode metallic and the other semi-metallic or insulating. Space-charge-limiting is a band conductivity model[180] built around charge injection from metal into an insulating layer, built around the introduction of trap levels in the energy bands in such systems, which may originate from dopants or defects (including V_O^{2+}). This model has seen some

success in describing the conductivity of some doped perovskite switches supported by the influence of choice of metal for the electrode.[181] Filament growth mechanisms additionally present valid models for the switching of certain systems,[182] especially certain doped perovskites in which the set and reset voltages do not depend on polarity. For thin films of several unit cell thickness, it has been demonstrated[183] that purely electronic mechanisms may explain switching tunneling resistance through ferroelectric films.[184]

For more complex perovskites we observe a tendency to invoke vacancy diffusion directly or through its implied doping effects. There are solid studies in the $\text{La}_{1-x}(\text{Sr,Ca})_x\text{MnO}_3$ system that support ionic displacement of both cations and anions,[185] but the diffusion of V_{O}^{2+} remains of central concern.[186] Switching in superconducting cuprates is starting to become more common, but devices presented so far had low OFF/ON ratios and slow writing speeds compared to manganites, although remaining a viable testing ground[24] for the V_{O}^{2+} induced redox mechanisms in the perovskite family. YBCO devices are being studied more intently recently and have a special place in the modulation of the superconducting transition of the oxide.

Vacancy diffusion yet remains the principal feature of switching oxides in many systems. It is especially important for systems with no metal diffusion from the electrode and no oxygen exchange between layers in some heterostructure where all of the change is kept internal. We will then address a number of such studies done in recent years in the section below in order to properly introduce the great promise of simple electrical controls in functional perovskites.

1.4 Field-Induced and Current-Induced Vacancy Diffusion

Oxygen diffusion may be electrically induced in perovskites both by very large current densities j and electric fields E using appropriate sample design. To achieve very high j , a device needs to be fabricated in such a way that its source-drain channel includes a constriction. This is easily achieved by standard patterning techniques, but large j can also be achieved through electron impingement in a scanning electron microscopy (SEM) or scanning transmission electron microscopy (STEM) setups, as well as with conductive atomic force microscope (cAFM) tips. Elevated E is, on the other hand, commonly achieved using gating, with a wide array of possible switching material-gate stacks being reported in literature.

Table 1.2: Perovskite oxide switch implementations and associated switching mechanisms.[104]

Perovskite Material	Special Functionalities	Switching Model	OFF/ON Ratio	Ref.
BiFeO ₃	Ferroelectricity	Schottky Barrier Modulation	10 ³	[78]
Co:BiFeO ₃	Ferroelectricity	Filament Growth (Unipolar)	10 ⁵	[182]
BaTiO ₃	Multiferroicity	Ferroelectric Tunnel Junction	10 ²	[183]
Cr:SrTiO ₃	Multiferroicity	Space-Charge-Limiting	10 ⁵	[181]
Nb:SrTiO ₃	Multiferroicity	Schottky Barrier Modulation	10 ³	[178]
YBa ₂ Cu ₃ O _{7-δ}	Superconductivity	Redox, V _O ²⁺ Diffusion	10 ²	[24]
La _{0.7} Sr _{0.3} MnO ₃	Magnetoresistivity	Redox, Ion Diffusion	10 ²	[185]
La _{0.7} Ca _{0.3} MnO ₃	Magnetoresistivity	Redox, V _O ²⁺ Diffusion	10 ³	[186]

With the understanding of both the physics of the observed processes and the material family we are considering, we will present an overview of some reported doping control measurements from literature. The examples are summarized in Table.1.3. We will limit our view to experiments that aim to control the doping by either current or field, and focus on those examples where vacancy diffusion is well attested.

Field induced doping control draws from a long tradition of semiconductor-gated transistors. Parallel devices consisting of oxide single crystals with metallized gates have been achieved in STO in the last decades.[187, 188] Similar to TiO_2 ,[115] STO has been shown to form metallized filaments by severe electroreduction.[189] Other studies have studied the effect in both doped and undoped STO single crystals with planar and lateral electrode geometries, reiterating the role of V_{O}^{2+} diffusion.[55] Beyond just metallic gates, some studies have harnessed the V_{O}^{2+} structuring effects in titanates to induce nanosized dislocations by applying fields via cAFM tips.[190] STO samples tend to be resistive, so that most switching experiments both by larger gates and AFM tend to be described as field switching.[44]

YBCO has seen much attention due to its tunable superconductor-to-insulator transition with possible applications in superconducting quantum interference devices and components in quantum computing. Metallic gating has been achieved in many configurations,[191, 192] including multiple gate geometries with OFF/ON ratios on the order of 10^3 . [71] Alternative gates implemented in YBCO films including solute electrolytes,[193] ferroelectric films[194] and ionic liquids,[195, 196] with the last two offering good retention performance and very high field densities in the active oxide film, respectively. Both resistive switching and superconducting T_C modulation are now well documented in YBCO as a consequence of field induced V_{O}^{2+} diffusion.[24] Very high ratios OFF/ON $> 10^5$ have been recently demonstrated for samples with micrometric metallic gates,[197] indicating that effective switches might still be possible.

Current driven switching was studied in cuprate superconductors since their initial appearance on the stage in the 90s, with specific interest always being given to the modulation of the superconductivity itself.[61] Particularly the studies of Moeckly et al., originally centered on current injection via STEM tip[198] and later by sample constriction[199] were the first ones that made the link between discoloration and deoxygenation which has been elaborated upon by other authors.[72, 200] We discuss the cAFM experiments in a current driven context here (contrast to the discussion in STO) simply because of the lower resistivity of the material. Oxygen depleted YBCO is

more reflective under visible light,[159] in a manner similar to V_2O_3 , and this feature represents a qualitative map of V_O^{2+} content in YBCO as supported by Raman spectra measurement.[74] This approach, together with the single-step fabrication of electromigration samples allows some of the simplest phase-diagram mapping protocols available.[58, 59]

It is worth noting that field and current driven approaches to perovskite switching show significant difference in timescale and oxygen ordering after accounting for device size and geometry. Field driven devices generally perform much faster ($\sim 10 - 100$ ms)[71] compared to simple current driven ones[73] (~ 1 s), even though significantly shorter switching times have been reported for specific materials and geometries.[58] Additionally, the exact nature of the oxygen ordering occurring in these devices is strongly dependent on the sample geometry and switching system, and remains a contested topic.

The specific anisotropy of YBCO films due to twinning tendencies imposed the question of the effect on electric doping control. This can only be answered by fabricating untwinned samples, a field that has seen recent development.[177] Building on this, we have shown in untwinned samples that diffusion remains thermally activated and thus dominated by the higher resistance of conduction for samples aligned orthogonally to the Cu-O chains.[201]

Electromigrative doping control in superconducting cuprates has been demonstrated to be usable in fabricating the weak links of superconducting quantum interference devices,[202] the best magneto-sensors, in an application parallel to that shown in superconducting metals.[37, 203] Some research effort has recently been put towards demonstrating actual resistive switches based on this principle, with the results pending.

Similar current driven control was also achieved in cobaltates[204] and manganites.[205–207] Manganites show similar optical behavior with deoxygenation as the cuprates in some experiments.[73] This application has long been considered for its potential uses in memory, as doping control in this manner allows for magnetic memories with very non-linear OFF/ON IV s, which is a very important feature for memory devices.[208]

The manganite switching mechanism is still being studied with notable recent studies showing unipolar behavior with clear distinctions between current and voltage drive.[209] LSMO switches driven in field configuration are much more commonly used in practice and one can find them mentioned together with common binary oxide switches in summaries.[104]

Table 1.3: Electrical Doping Control Methodologies Based on V_O^{2+} Diffusion in Functional Perovskite Oxides

Perovskite Material	Working Stack	Doping Control	Note	Ref.
Er(Mn,Ti)O ₃	Me:EMTO:Me	E	Field induced by cAFM tip.	[190]
SrTiO ₃	Me:STO:Me	E	Gated wafer experiment.	[187, 188]
SrTiO ₃	Me:STO:Me	E/I	Lateral vs. planar electrodes.	[55]
Fe:SrTiO ₃	Me:STO:Me	E/I	Lateral vs. planar electrodes.	[55]
YBa ₂ Cu ₃ O _{7-δ}	Me:YBCO	E	Metallic gating.	[71, 191, 192]
YBa ₂ Cu ₃ O _{7-δ}	E:YBCO	E	E - Electrolyte	[193]
YBa ₂ Cu ₃ O _{7-δ}	IL:YBCO	E	IL - Ionic liquid	[196]
YBa ₂ Cu ₃ O _{7-δ}	FEG:YBCO	E	FEG - Ferroelectric gate	[194]
YBa ₂ Cu ₃ O _{7-δ}	YBCO	I	Current by STM Tip	[198, 199]
YBa ₂ Cu ₃ O _{7-δ}	YBCO	I	High <i>I</i> by sample geometry.	[29, 72, 74, 210]
YBa ₂ Cu ₃ O _{7-δ}	YBCO	I	High <i>I</i> by sample geometry.	[201]
La _{1-x} Sr _x MnO ₃	LSMO	I	High <i>I</i> by sample geometry.	[73]
La _{0.8} Ba _{0.2} MnO ₃	LBMO	I	High <i>I</i> by sample texture.	[207]
La _{1-x} Sr _x MnO ₃	Me:LSMO	E	Metallic gating.	[209]
La _{0.7} Sr _{0.3} CoO ₃	LSCO	I	Thermal cycling with applied <i>I</i> .	[204]
Pr _{0.7} Ca _{0.3} MnO ₃	PCMO	I	Thermal cycling with applied <i>I</i> .	[204]
Bi ₂ Sr ₂ CaCu ₂ O _{8+δ}	BISCCO	I	Current by 3D sample geometry.	[58]

1.5 Summary

Doping control in perovskite oxides, understood as a function of the oxygenation of the non-stoichiometric oxide, is the control property we have to master to achieve tunable superconductors, multiferroic transistors, bits and memristive devices. Extensive studies over the last decades have shown time and time again that the diffusion of the mobile oxygen vacancy is the mechanism of this control, and it is now common to utilize a number of external parameters, like temperature, pressure and electric/magnetic field to control the oxygenation of oxide samples. While most of these methods require implementation during fabrication, electrical switching is special in that it allows the modification of devices *in-situ*. This is of interest both in phase-diagram studies as well as for tunable functional devices, of whom the simplest one is the resistive switch. State-of-the-art evidence is presented that all model perovskite systems whether that be multiferroic titanates, magnetoresistive manganites or superconductive cuprates share the key features of switching oxides in multi-valent cations and mobile oxygen vacancies. We emphasize the simplicity and individual advantages of field and current control in such systems, and highlight the exceptional usefulness of the geometric constriction in achieving electrical doping control in perovskite oxides. These methods already show promise in fabrication and study, and are one more argument for wide-spread oxide electronics in the future of technology. This seems a safe assumption considering that no other material family has shown the same diversity in physical functionalities while having a pre-existing manufacturing pipeline in standard CMOS technology, which already uses oxides. The wide spread of both device design and material composition is highlighted, in order to justify the research effort presented in this thesis and to urge further study of different combinations for a complete model of the switching behavior of such compounds.

Study of electrically induced diffusion in thin films relies on electrical feedback control and appropriate visualization. The former permits both reading the device resistance state and the application of stimuli to achieve the desired diffusion. While the electrical resistance of perovskite thin films is already a good proxy for their oxygen doping, we can reinforce our findings on the material changes with a wide range of microscopic observations. In this chapter, we will examine the methodologies used in the presented research, starting with sample fabrication (substrate selection, patterning and deposition), before showcasing the instrumentation and software control used in the electromigration experiments and taking a look at the indispensable microscopy techniques that inform our conclusions on the nature of the selective oxygen diffusion in the perovskite oxides. Finally, we shall discuss the finite element models employed in explaining the observed sample behavior.

2.1 Sample Fabrication

Condensed matter research hinges on our ability to deposit high quality films with precise deposition parameters, ensuring reproducibility. In the scope of our investigation of oxygen diffusion in the perovskite material family, we have utilized thin films of YBCO and LSMO. Considering the complex nature of such oxides, deposition of thin films of sufficient quality requires precise control of multi-element stoichiometry and a sufficient control of the growth kinetics for guaranteeing homogeneous and epitaxial film deposition. Commonly, these two issues are approached separately, with precursor chemicals used to synthesize a coarse-grain, relatively inhomogeneous oxide material that can then be used to produce high quality films in a number of

Layman's Overview: Methodologies in Solid State Studies

This thesis focuses on the principles and techniques of solid-state physics and material science, particularly in the fabrication and characterization of thin films. These methods are crucial for advancing our understanding of material properties and developing new applications in microelectronics and other high-tech industries. These films are grown on monocrystalline substrates. These substrates are near-perfect crystals, typically purchased from industry vendors. Nowadays the production of these materials is rather common in the microelectronics industry. However, laboratory in-house production is also diffuse. One ubiquitous fabrication method is evaporation: the material is simply evaporated under low pressure and directed towards the substrate for controlled growth. Many other methods are available, each with its advantages and disadvantages.

To achieve the sensitivity and precision required for characterization and application, thin films only become useful if shaped into devices. This is why we often carve out thin films into constrictions, junctions and the like. We create these patterns in the thin films using lithography. This method, like its namesake artistic discipline, centers on covering a "canvas" with a mask to hide a part of the substrate allowing us to deposit material in the desired shapes. The opposite might also be true, we can cover a complete thin

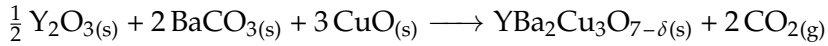
film and etch away the undesired parts. The patterns created by scientists and engineers are numerous, but in our work, we use a simple constriction: a line of material is deposited on substrate, with a narrowing at a certain point.

Besides fabrication, solid-state laboratories focus on characterization. In this thesis we will mostly use electrical measurement equipment, various microscopes, and spectrometers. Electrical test equipment for thin films is similar to that used in other disciplines but differs in sensitivity and the amplitude of stimuli and signals. Spectrometers are a large family of instruments that measure the sample's response to varying stimuli. For example, by shining X-rays onto a sample and varying their angle, we get amplified responses where the X-rays diffract on the periodic crystal lattice. This technique provides information about atomic distances in a film. Microscopic methods provide detailed images of the thin films. Optical microscopes offer a broad overview, while more advanced techniques like SEM and STEM provide high-resolution images of the film's surface and internal structure. These methods are invaluable for identifying defects and understanding the film's morphology.

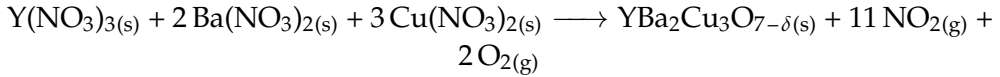
The following chapter describes the methods used in fabricating and characterizing our samples.

evaporation based deposition techniques, physical vapor deposition (PVD) techniques being the most common. This compartmentalization allows researchers to outsource the production of adequate targets to industry, freeing up resources to focus on film growth in-house.

Synthesis of complex oxides for deposition targets and other applications which are not highly dependent on crystallinity and film homogeneity proceeds by a solid-solid reaction with heating.[143, 211] Here oxides or salts of the metals are powdered and combined in the expected ratios to produce the desired compound, as in the example of YBCO:



Barium carbonate is very insoluble and tends to cause inhomogeneities and phase separation in the above reaction, leading to the use of nitrates instead of oxides, as below.



Any synthesis of a non-stoichiometric oxide requires special care in respect to the oxygen partial pressure in the surrounding, doubly so for a reaction where oxygen factors both as a product and as the non-stoichiometric component of YBCO. This procedure, and related synthesis methods for other perovskite oxides, results in bulk substances that can be processed by heating,[212] pressing and recrystallization methods to achieve better material qualities, including single crystal films.[213, 214] Alternatively, synthesis products with relatively low crystallinity and homogeneity may be used as targets for thin film deposition techniques as described in the following sections. For the purposes of the research at hand, targets were purchased from industrial suppliers and used in-house by our collaborators for thin film fabrication.

2.1.1 Pulsed Laser Deposition

Thin films in solid state physics are achieved by deposition in vacuum or near-vacuum environments, by transitioning the material whose thin film we desire to deposit from a condensed phase at the target, to gas or plasma in the chamber and back to solid at the substrate. This final deposition step is where we introduce changes in morphology and crystallinity, or affect chemical changes like oxidation in relevant materials. The sublimation of the solid target can be achieved in a number of ways, from thermal evaporation to plasma sputtering, and we classify these methods as PVD. This principle can be taken further, by using multiple targets or gas injection to achieve chemical reactions on the substrate, or by combining multiple evaporation techniques, leading to a truly wide range of possibilities.[215]

The YBCO thin films that we have used in our work (Ch.3, Ch.4, Ch.5) were grown by pulsed laser deposition (PLD). In this PVD method the target evaporation is achieved by laser ablation (out-of-equilibrium emission of material after etching), where short (\sim ms), energetic laser pulses evaporate the surface of a rotating target. Target preparation includes cleaning and polishing steps as surface texturing can lead to uneven depositions. The

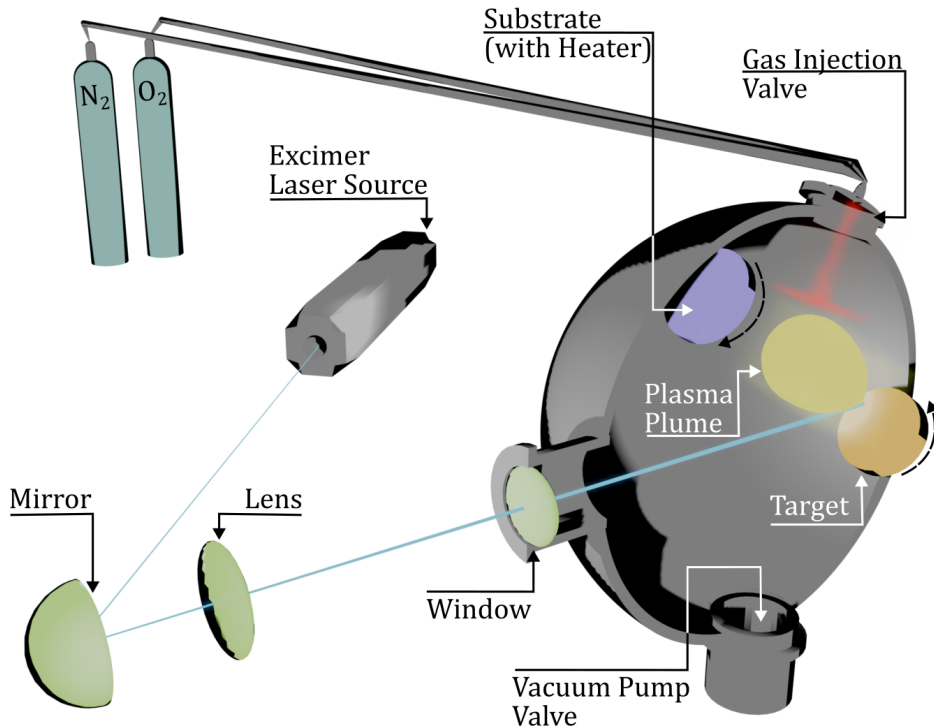


Figure 2.1: Simplified working principle of thin film deposition by pulsed laser. The chamber is vacuum sealed and pumped to low pressure, and the oxide film properties are controlled by substrate heater temperature and oxygen partial pressure. Deposition thickness is calibrated in laser pulses per nm. A piezoelectric scale (not shown) is used to measure the real film thickness.

substrate is mounted on a heater at a 52.5 mm distance from the rotating target, and kept at 800 °C to encourage proper crystallization. The ultra-violet (UV) laser usually originates from a excimer laser source $\lambda = 248$ nm, is operated at 5 Hz (200 ms pulse) and is focused using a system of mirrors. The laser has an illumination spot of 1 to 2 mm² and is tuned to a fluence of 2 J/cm². In the PLD setup at Institut de Ciència de Materials de Barcelona (ICMAB) 26 laser pulses correspond to 1 nm of film thickness for the range 10-250 nm. The chamber is pressurized with 0.3 mbar of O₂. The oxygen gas serves both for phase stability and to reduce the energy of the plume particles. A simplified illustration, containing some basic elements of a PLD system is shown in Fig.2.1.

2.1.2 Chemical Solution Deposition

Alternative paths to thin film deposition are numerous in both academia and industry. chemical solution deposition (CSD) is a relatively low cost method that requires no PVD setups and allows great control of composition of the deposited material, as the constituent elemental materials are deposited on the substrate from soluble metallo-organic precursors which can be purchased or synthesized in chemical laboratories. Such precursor mixtures are pyrolyzed to remove the organic, leaving the inorganic components in solid state on the substrate, ready for thermal recrystallization and oxygenation steps. The method is scalable[216] and versatile and has seen use in semiconductor[217] and oxide manufacture.[218]

We have used samples prepared by CSD for the work presented in Ch.3 and Ch.4. For their preparation, the chosen route was via a low-F organo-metallics. These organic compounds, namely acetates (for introducing Ba and Cu) and trifluoroacetates (for Y) are good chelating agents for a number of metallic ions, and are easy to pyrolyze and to remove from the system. The low amount of fluorine content also ensures good yields with the Ba-ions, which tend to otherwise serve as sources of phase impurities. In fact, the methodology implemented uses a reduced Ba content in the precursor (Y:Ba:Cu = 1:1.5:3) as it has been shown to give the best results.[219]

It should be noted that a major concern in these methodologies is that the organic precursor molecules pyrolyze to water, among other reaction products, which can have detrimental effects on the perovskite nucleation. Laboratories performing these depositions are thus humidity controlled (<10%).

The precursor chemicals used to achieve proper stoichiometry are mixed in organic methanol with 30% propionic acid at 30 °C, and then dried to dehydration in a vacuum rotary evaporator at 131 mbar and 70 °C to reduce the water content below 1%. This produces a gelatinous material that is dissolved in minimal amounts of methanol and stirred for 24 h before being diluted to the required concentration for spincoating. The solution is coated on an appropriate perovskite epitaxial substrate, and baked on a hotplate to evaporate most of the organic solvents and remnant water.

The coated substrate is then treated in a programmable pyrolysis chamber, and the reaction speed and film quality obtained depends strongly on the implemented temperature profile and atmosphere in the chamber. Notably, after initial heating above 110 °C (above water boiling point) the atmosphere is humidified to avoid sublimation of copper salts. The temperature is important to avoid incorporating the water in the nascent metal-oxide crystals. The pyrolysis reaction is simply the heat driven decomposition of the or-

ganic agents, mostly to CO_2 and H_2O and other volatiles, and reaches peak temperatures $\sim 300^\circ\text{C}$. Commonly the temperature profile also includes a calcination process to generate a homogeneous and nanocrystalline film of the separate oxide or fluoride phases CuO , Y_2O_3 and BaF_2 .

The nanocrystalline film produced in pyrolysis is taken to a tubular furnace in which the temperature and atmosphere gas mixture can be controlled. As for the pyrolysis, the exact temperature profiles are discussed in literature, but the important part are an initial high temperature ($\sim 800^\circ\text{C}$) growth and sintering step, performed mostly in wet atmosphere to avoid copper oxide sublimation (which is replaced with a dry N_2 and O_2 atmosphere for the sintering step). Finally, an oxygenation step is implemented in a pure O_2 atmosphere at lower temperature ($\sim 450^\circ\text{C}$) to optimize the doping levels in the material. In conventional thermal annealing, both of these temperature/gas regimes are maintained for hours on end and include finely controlled heating and cooling rates in between, more on which is provided in references. Recently, there has been work on using faster, so-called "flash heating" methods to mimic the above procedure in a fraction of the time, which are discussed in Ref.[197].

Polymer Assisted Deposition

For the LSMO samples discussed in Ch.6 the thin films were deposited via a more involved CSD method that replaces the short-chain carbohydrates with large-chain polymers - polymer assisted deposition (PAD).[220, 221] The compounds used (polyethyleneimine of average molecular weight $M_w = \sim 25000 \text{ gmol}^{-1}$ as the polymer and ethylenediaminetetraacetic acid (EDTA) as the chelating agent) serve the function of the acetates in the previous section but only decompose at higher temperatures, temperatures that are in fact very close to the equilibrium for the formation of the perovskite crystal. Thus, the pyrolysis and growth phases are combined as the metal oxides are not dropped from the solid solution until conditions are ready to achieve B-cation ordering. This simplifies the process in regards of the number of annealing steps and setups necessary and produces films with excellent epitaxial and magnetic properties.

2.1.3 Substrate Selection

The principal driver in PLD, CSD, PAD and other deposition techniques is achieving epitaxial growth and large grain size. Epitaxiality indicates that the respective orientation of the unit cells of substrate and thin film are aligned.

Naturally, substrates of matching cell parameters tend to be found in the same structural family.

The usual application of epitaxy is to align the substrate and film crystals along the c crystallographic direction, meaning that substrate choice is usually dictated by a tendency to reduce the lattice mismatch in terms of a and b . Several industry standard perovskite materials are commonly used as substrate platforms for such growth, with LAO and STO being the most accessible. Despite the parent compound of the perovskites, BaTiO_3 , being cubic ($a = b = c$) most of the complex derivatives tend to be tetragonal ($a = b \neq c$) or slightly orthorhombic ($a \neq b \neq c$), so the choice of the tetragonal substrates is not surprising. Single crystal wafers of these oxides are available for purchase in supplier catalogs (ours being supplied by CrysTec GmbH, Germany) and are paired with complex oxides for the specific deposition needs.

The YBCO films discussed in Ch.3, 4 and 7 are grown on LAO, which offers epitaxy with little mismatch. For the YBCO films studied in Ch.5, the substrate choice is of special importance, as the terraced MgO film creates directional strain YBCO that disfavors twinning during PLD deposition of the perovskite.[177] This is a special interest we pursue to study the effect of the a/b orientation of our constrictions on the oxygen diffusion, and is discussed in detail in Ch.5.

The LSMO films we study in Ch.6 are deposited on STO wafers. This combination induces slight lattice strain due to mismatch, as shown in Fig.2.2. In the interest of studying strain effects on diffusion one could compare films deposited on LAO and $(\text{La}_{0.18}\text{Sr}_{0.82})(\text{Al}_{0.59}\text{Ta}_{0.41})\text{O}_3$ (LSAT), giving us a wide range of strain situations to compare in regards of effect on the oxygen diffusion.

2.1.4 Thin Film Patterning

Lift-off and chemical or plasma etching are conventional techniques for achieving micro- and nanometric film patterning in solid state physics. All modern patterning techniques begin with a lithography step, where the desired pattern is written into a sacrificial mask layer coated on the substrate. While optical lithography is standard in industry-scale applications, smaller lab-scale lithographies that require ever-changing designs favor modular techniques and apply electron-beam based techniques alongside them.

The samples deposited in ICMAB (Ch.3,4,6, and 7) were patterned via optical lithography, by changing the solubility of a photoresist by laser irradiation and subsequently etching the perovskite film in acid or plasma. The

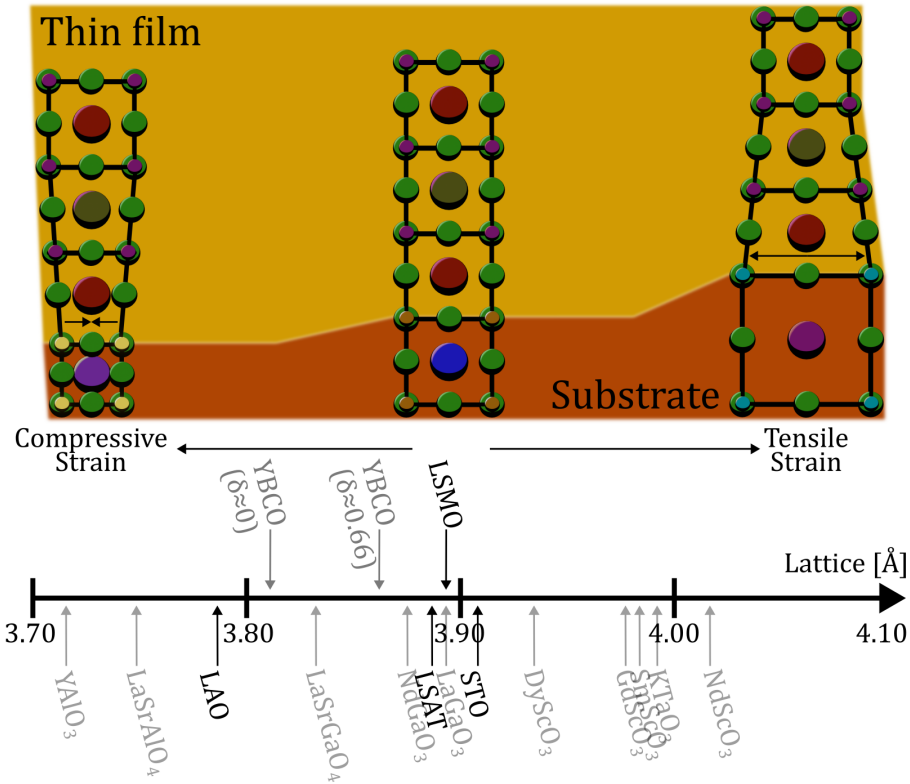


Figure 2.2: Schematic representation of compressive and tensile strain induced in a perovskite thin film by substrate lattice dimension mismatch. The axis in the bottom shows approximate values of lattice parameters for a number of common perovskites. On the example of LSMO, compressive strain may be induced by growing the film on LAO and tensile by growing on STO, while the best match is provided by $(\text{LaAlO}_3)_{0.3}(\text{Sr}_2\text{TaAlO}_6)_{0.7}$ (LSAT).

two etching procedures are differentiated by their anisotropy: chemical etching is fairly isotropic and can produce more rounded film edges, while being cheaper and less resource intensive; plasma etching is fairly anisotropic but requires specific equipment to be employed. A schematic illustration of the process is shown in the top arm of Fig.2.3. The patterns used in Ch.5, fabricated by our collaborators in Department of Microtechnology and Nanoscience, Quantum Device Physics Laboratory, Chalmers University of Technology (QDPL) were achieved by electron beam lithography and dry ion beam etching.

Either of the employed methods is based on lithographic patterning.

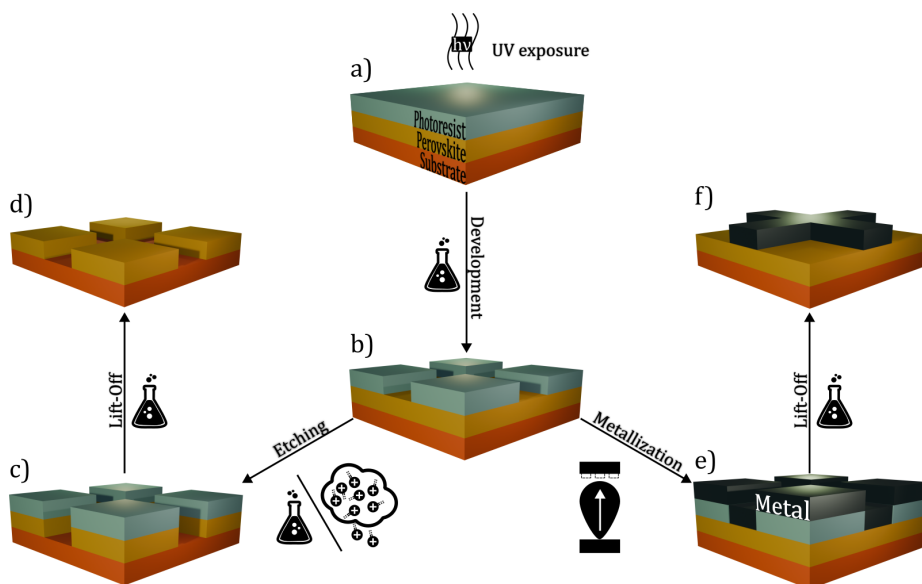


Figure 2.3: Schematic representation of thin film patterning and metallization processes used in this work. Starting sample consists of an unpatterned perovskite film covered with a photoresist. Using laser photolithography, the desired pattern is written into the photoresist (a). Areas exposed to the laser light become more soluble and dissolve in the development step when exposed proper solvents (2% $C_4H_{12}N^+$ in water), creating the pattern in the photoresist (b). If the patterning is being performed on the perovskite film itself, the stack is etched either via chemical (H_3PO_4) or Ar plasma etching (c). The photoresist in this setup protects the perovskite film underneath from the etch and can be freely lifted with organic solvents (like acetone) revealing the patterned perovskite underneath (d). A procedure without etching is used for metallization as the metal films are reserved for electrodes and have a larger thickness and less demand for precision film edges. Here the developed substrate-film-resist stack is metallized via PLD (e) and the final metal pattern is remnant after chemical lift-off (f).

The sample design is first written into the photo- or electron-beam resist, depending on the patterning technology employed. If a positive resist is used the exposed parts of the resist turn soluble, revealing the substrate/thin film below in lift-off. Negative photoresists are those where all but the exposed regions stay soluble to the developer. The choice of depends on the specific needs of the process.

It should be noted that we use metallized electrodes for ensuring metallic

contact between bonding wires and thin films, and these are patterned and deposited with a simplified procedure as the requirements on edge quality is lowered. This procedure is illustrated in the bottom arm of Fig.2.3.

Overall the patterning process starts from a thin film covering all of the substrate on which a photoresist is patterned to expose the undesired sections of the perovskite. The film is then etched, and the photoresist is lifted. In the next step a new resist is applied exposing the parts that are meant to be metallized. Metal is deposited and liftoff is performed leaving the metallic electrodes.

2.1.5 Sample Design

The sample design philosophy centers on the idea of simple planar constrictions which condense the current flow to a region of elevated current density j . This, in turn, causes the constriction to act as a nucleation point for electromigration phenomena, i.e. the current induced flow of oxygen ions in the crystal.

The implemented designs are shown in Fig.2.4, the first one (a) being a legacy design from previous work reported in Ref.[51] by Baumans et al. and is a simple geometric constriction in a bow-tie shape. This design offers a single resistance reading which allowed the authors to inspect the interplay of electromigration current and superconducting critical current T_c in YBCO thin films. We use these samples for the initial studies discussed in Ch.3. Similar, single-resistor designs were used in Ch.5 but were updated into a Dayem bridge design (b). The simplified electric schematic of these sample designs is shown in panel (c). For most of our works we utilize a triple-Dayem bridge design, illustrated in panel (d). This design is a key feature of our efforts as it allows us to electrically monitor the directional evolution of the oxygenation profile in the sample - the narrow bridge in the center guarantees the highest current density and flux divergence and serves as the triggering point for all electromigrative effects. Resistance (R) readings from the wider constrictions allow us to electrically infer the oxygen- V_O^{2+} counterflow identifiable by their opposite trends. The corresponding schematics are shown in (e). An illustration of an individual device (f) and device packaging on a chip (g) is shown in the bottom panels.

2.1.6 Film Characterization

Film quality is confirmed after deposition by our collaborators in charge of the fabrication. The principal structural analysis technique is X-ray diffraction

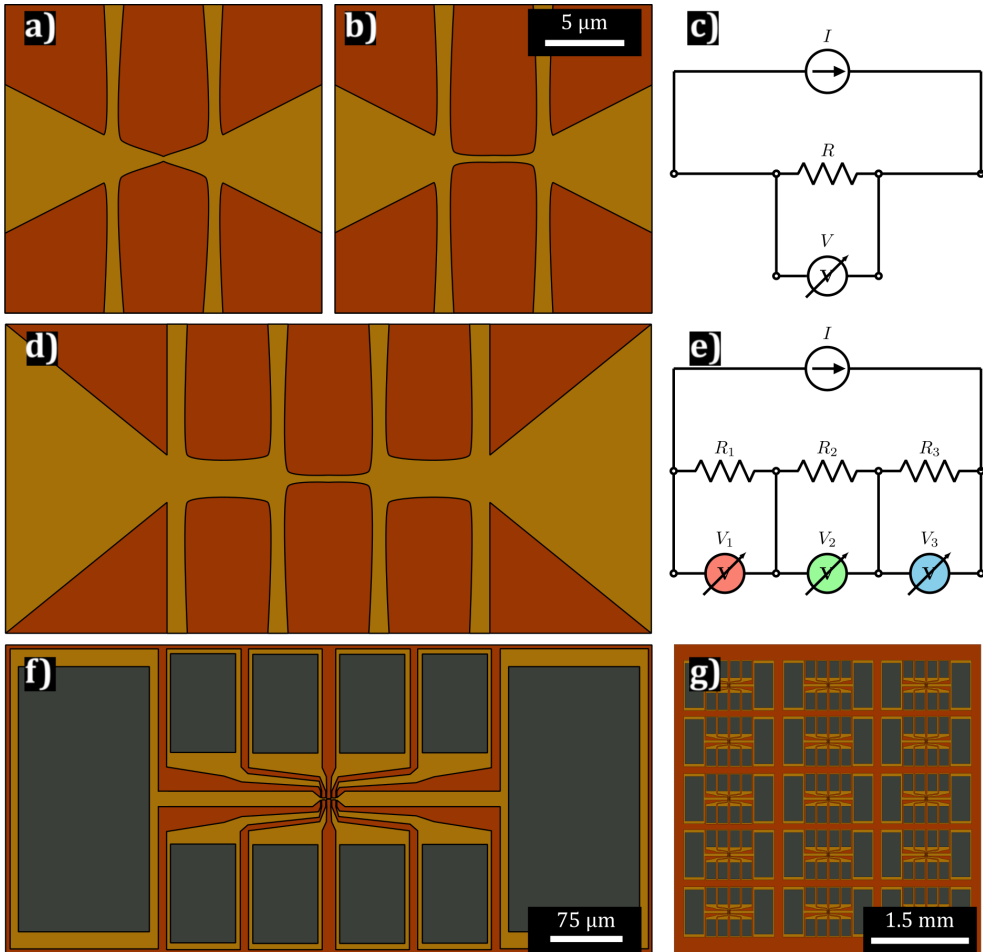


Figure 2.4: Illustration of the sample designs used in the context of this thesis. Color code is same as in Fig.2.3 and Fig.2.2: substrate is orange and thin film is yellow, metallized sections are dark gray. The important distinction between the sample designs in a,b) and d) is the number of resistances individually accessible, as shown in the panels c) and e). We will stick to the colors indicated on the voltmeters in e) for the remainder of the thesis to indicate the left-center-right constrictions by red-green-blue, and define positive current polarity as having the positive arm of the circuit on the right. A single device will have the source/drain lines (horizontal) connected to large metallized electrodes and the voltmeter terminals (vertical) to smaller ones, as shown in f). Single chips are patterned in a matrix of identical devices, commonly in a 3×5 array. Every device is individually accessible by wire bonding, as shown in g).

(XRD), a technique that returns a response spectra to film irradiation with X-rays as a function of the incident angle. This method is especially important in CSD deposited films where the sample composition needs to be confirmed, and in the untwinned samples where the degree of twinning can be deduced from the diffraction patterns. Details of this standard technique are discussed elsewhere in literature.[197]

Film thickness was periodically measured to confirm the calibration of the deposition techniques, commonly using optical profilometry or X-ray reflectometry. These techniques offer a fast solution to measure height variations along a line profile. We have additionally performed atomic force microscopy (AFM) measurements (discussed below) where complementary thickness characterization was deemed necessary.

Critical temperature and transport characterization was performed after deposition using a commercial physical property measurement system (PPMS), and magnetic characterization, was done using a superconducting quantum interference device (SQUID) setup.

2.2 Transport and Low-T Measurements

2.2.1 Electrical Test Equipment and Automation

The cornerstone of our research work is electrical transport measurements, be that at room temperature or in a cryogenic environment. For this purpose samples need to be mounted on testing stages, wirebonded using fine wires and stressed and tested using appropriate equipment.

Received samples are manufactured as described in Sec.2.1, an example of such a chip with 15 YBCO devices on LAO is given in Fig.2.5a). The sample chip is glued to an oxygen-free copper sample base using silver paste. The silver serves as both electrical and thermal link in cryogenic equipment. The gold base is then fit and screwed into a PCB collar with its own gold pads feeding through to standard Mill-Max pin connectors. Using a wirebonding system, the metallized pads of a single device are connected to the pads of the PCB with Al-Si wires of 25 μm diameter. An assembled sample-on-gold base-in-PCB collar is shown in panel (b). The Mill-Max pin connectors have receptacles in home-made testing stages (c), accessible by BNC cables that are used for most electrical testing in the lab, either directly or by being adapted into from other connectors.

DC electrical measurements are performed using programmable source-measure unit (SMU) and voltmeter systems with suitable operating ranges.

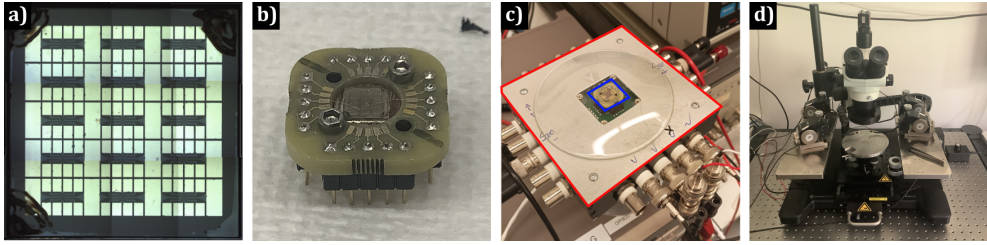


Figure 2.5: a) Sample under optical microscope. b) Sample chip glued to a gold-plated oxygen-free copper base with silver paste, mounted in a printed circuit board (PCB) with vertical metallic connectors. The sample is bonded to the gold pads of the PCB with fine wire, and the pads themselves feed through to the vertical connectors. c) Individual sample testing stage (red square), the sample PCB envelope is visible in the center (blue square), while the Bayonet Neill–Concelman (BNC) coaxial connectors are visible on the sides. The stage includes a $240\ \Omega$ resistance between the connectors and the pins of the PCB board and is grounded. d) Probe station for bondless testing, with low magnification microscope.

Our device-stage or device-cryostat feed-through circuits tend to bear $k\Omega$ resistances, thus requiring 10-100 V drives for electromigration (mA currents). For noisier measurements with low drives, like for $R(T)$ measurements, the more sensitive AC lock-in measurement systems is used. Programmable current driven signal generators link via trigger cable to the lock-in amplifiers allowing one to use the voltage readings at trigger time to calculate resistances in our sample. The lock-in systems allow us to separate the low amplitude signal from noise contributions, by amplifying the signal component in interfering constructively with the trigger.

All these controllable instruments are issued commands and queried for readings using manufacturer specific application programming interface (API) code or the Standard Commands for Programmable Instruments (SCPI) ("skippy") protocol. Using these in conjunction with other general purpose programming languages (python) or more specialized testing/automation languages (LabVIEW) allows experiment automation. For this purpose the instruments are connected with each other and a computer using general purpose interface bus (GPIB) cables and appropriate adapters.

If room temperature measurements are sufficient, the procedure can be simplified by directly contacting the on-chip devices via metallic probes in a probe station (d), omitting the need for wirebonding.

2.2.2 Electromigration Protocols

Electromigration experiments have been performed at Experimental Physics of Nanostructured Materials (EPNM) for about 8 years at the point of writing of this thesis, which brings with itself significant experience in performing such testing. While the previous works were mostly focused in elemental metals and binary alloys, some experience has been gained in perovskite ceramics before this project took it further.

The main problem in performing electromigration, an intrinsically stochastic phenomenon, is control: sample heating and material diffusion cause resistance increases which further increase Joule heating and diffusion leading to a positive-gain feedback loop. In order to avoid sample destruction, more or less sophisticated protocols need to be employed.

Proportional-Integral-Derivative (PID) protocol

Particular process control is required in applying electromigration for the fabrication of nanosized gaps or constriction thinning, as previously presented in Ref.[37, 51]. A proportional-integral-derivative (PID) protocol was thus previously developed and implemented in LabVIEW by Zharinov and collaborators[28] to optimize process control in electromigration experiments. We utilize this protocol primarily in the work presented in Ch.3.

PID designates a standard process optimization method in which the value of a control variable (in our case applied current or voltage) is adjusted based on the relationship between a measured process variable e obtained in comparison with predetermined setpoint value (here conductance change over time $p_{setpoint}$), in $e(t) = p - p_{setpoint}$ for $p = \frac{dG}{dt}$. The algorithm for this kind of process control is schematically illustrated in Fig.2.6.

The condition $e(t) > k \cdot \epsilon(t)$ (with $\epsilon(t)$ the root-mean-square noise) is implemented to stop the algorithm from responding to noise and to identify rapid, uncontrolled change in the process variable. Exponential change in the process variable is traditionally hard to control via PID, which is why the left-hand side of the algorithm is implemented. Here, when the process variable becomes much larger than the $k \cdot \epsilon(t)$ term, the program activates a non-linear correction to the applied voltage in the form of $f_{nl}(N) = -\delta U_{0\downarrow} \cdot a^N$, for $-\delta U_{0\downarrow}$ and a being constants tuned to the system. The exponential dependence on check iteration N serves to rapidly counteract resistance increase. Otherwise, if the process remains well controlled and within the range of change of the process variable defined by the constant k , the control variable (voltage U) is adjusted. The adjustment is done using the

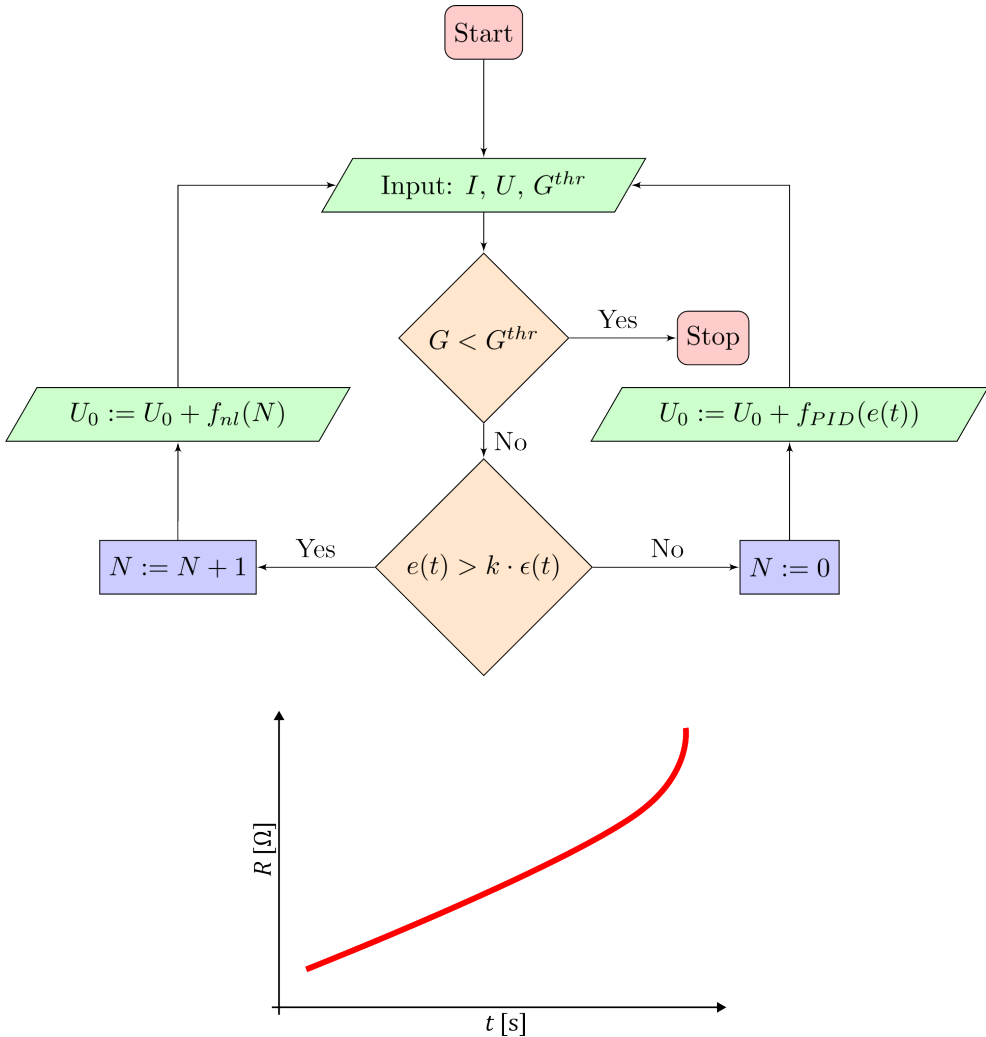


Figure 2.6: PID algorithm and the resulting $R(t)$ dependence. Red rounded rectangles are terminators, green parallelograms are inputs/outputs, orange squares are decisions and blue rectangles are processes. I is starting current, U is starting voltage, G^{thr} is the threshold conductance, $e(t)$ is the process variable, k is a constant, $\epsilon(t)$ is the root-mean-square noise, N is an iterator. The functions f_{nl} and f_{PID} are the non-linear and PID response, addressed in the main text body.

PID function f_{PID} which includes the respective proportional, integral and derivative terms responding to the process variable. These terms can and should be tuned for different materials and terms. The speed at which all this can be performed suffers a bottleneck in the minimum time it takes to communicate with the instrument which depends on the NPLC value and is usually on the order of \sim ms. Additionally, the protocol is implemented in a rather complex LabVIEW virtual instrument whose loop time is on the order of \sim s.

Applying this control protocol ideally yields $R(t)$ curves as the one shown in the lower part of Fig.2.6. The continuous monitoring of the control variable, i.e. the applied voltage provides us with a mostly stable value of $\frac{dR}{dt}$, which is very useful for utilizing electromigration for nanofabrication purposes like constriction thinning and gap manufacturing.

Pulsed-excitation protocol

One important question that is often front and center in electromigration studies is the value a threshold current density that can trigger the effect in a given system, even if the definition of such a threshold may seem arbitrary. We have developed a simple protocol for investigating the value of this threshold, based on applying a series of pulses of linearly increasing amplitude, similarly to the results shown in Ref.[222]. The resistance of the constriction is measured between the pulses with low current to separate the resistance increase originating from heating, and allowing for more reliable insight into the persistent system changes. The protocol is illustrated in Fig.2.7.

By distinguishing between the resistance measured under electric stress (pulse resistance, R_{max}) and the resistance value of the sample with low excitation (probe resistance R_{min}), we can clearly define the threshold electromigration current I_{EM} . This is made possible by setting the pulsing time $t_{pulse} \sim 1$ s to a value significantly lower than the probing time $t_{probe} \sim 10$ s, in addition to controlling the current density. The current applied during the pulsing is in the MAcm^{-2} range, while it is orders of magnitude lower for the probing (kAcm^{-2}). Importantly, the period between two subsequent pulses is in the range of 30 s to 1 min, as it also includes the time to take optical images and a short safety period. This allows us to separate thermal effects from electrical measurements, and can allow us to limit the destructive nature of electromigration experiments. The simple protocol can then be further expanded by doing other characterizations during the probing, beyond the optical imaging being done. We apply this protocol broadly in Ch.4,5 and 6.

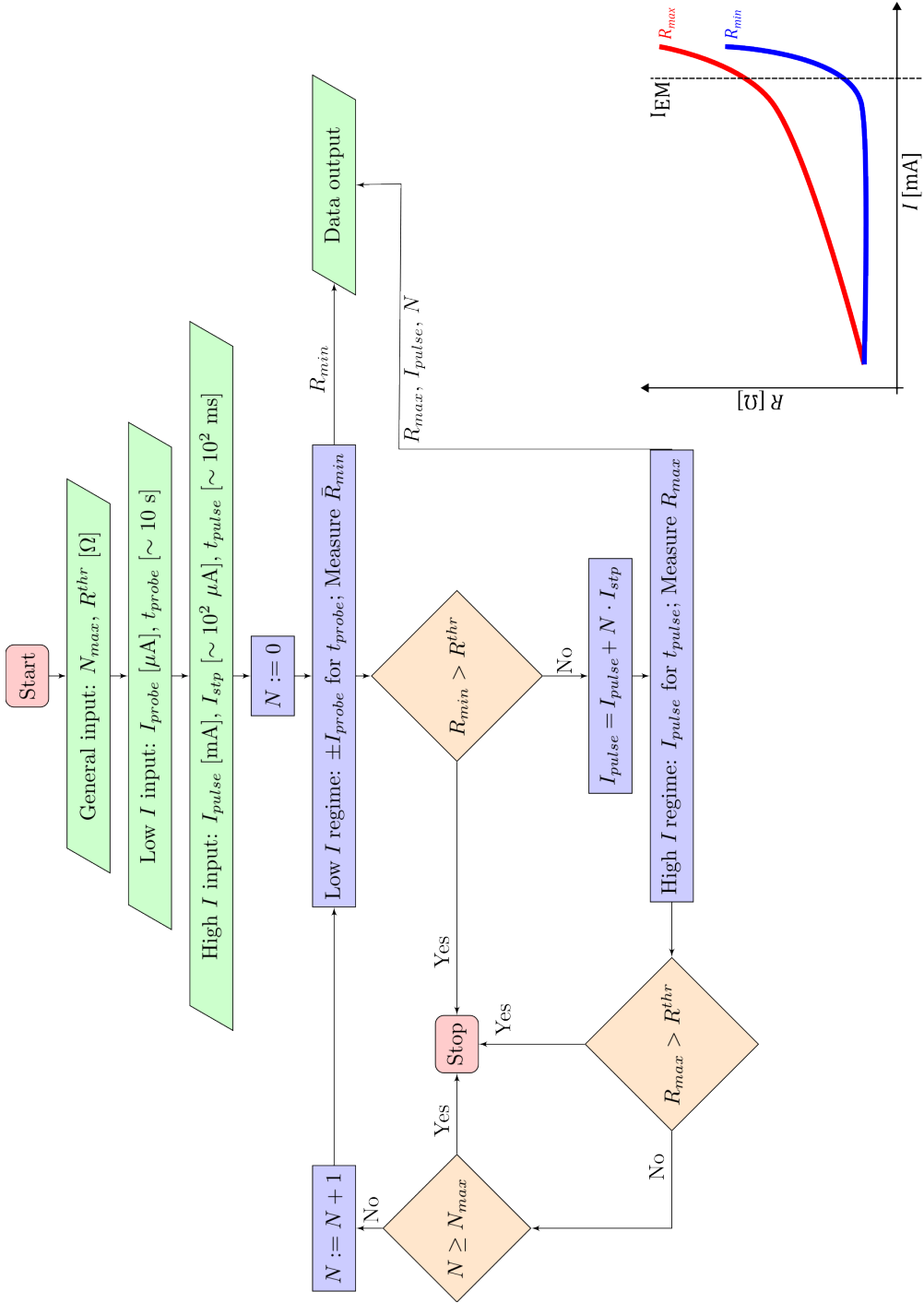


Figure 2.7

Figure 2.7: Pulsed-excitation protocol algorithm and the resulting $R(I)$ dependence. Same illustration convention as in Fig.2.6. I_{probe} and t_{probe} are the current and duration values in the low I part ("probe") of the protocol which produces R_{min} , i.e. the resistance isolated from the influence of Joule heating. I_{pulse} and t_{pulse} are the current and duration of the high I regime ("pulse"), where only the starting value of I_{pulse} is directly controlled by the user and is then linearly increased for every cycle. R^{thr} is the threshold resistance which triggers the algorithm to stop, in order to prevent sample destruction. We calculate the mean resistance \bar{R}_{min} measured for positive and negative I_{probe} during t_{probe} , and correlate the value to the previous R_{max} , i.e. the resistance measured during the pulse. Additionally, we may employ optical or other imaging techniques during the probe phase to track the visible changes in the system. Note that the R_{min} curve is flat until a threshold value of current is reached. We denote this as the electromigration threshold current I_{EM} .

Continuous switching protocol

For experiments in which the main goal is to reversibly switch the resistance state of a device, we apply a protocol that periodically switches the polarity of a current with fixed amplitude. In fact, we apply two distinct but related protocols for this, as shown in Fig.2.8.

The protocol produces a characteristic, dome shaped, resistance curve in perovskite samples which is a consequence of the oxygen- V_O^{2+} front passing through the constriction. The continuous switching protocol is either applied with a fixed switching period where the user inputs the switching time δt , or by determining a threshold resistance R_0 that triggers the polarity flip. The two modes show slightly different behaviors - the time-logic paradigm allows the overall resistance to drift if the given δt is far from the equilibrium value, while the resistance-logic one maintains an overall unchanging resistance trend giving a more reversible effect. Ideally, the resistance-logic method will equilibriate to a fixed switching time after a sufficient number of switching cycles. Essentially, by applying the resistance-logic method one may find a suitable value of δt to impose on the system for future experiments.

This method was employed in obtaining the reversible switching data shown in Ch.7.

2.2.3 Cryogenic Measurements

Characterizing the electric or magnetic response of a device at low temperature is an essential tool in order to gain further understanding of the different

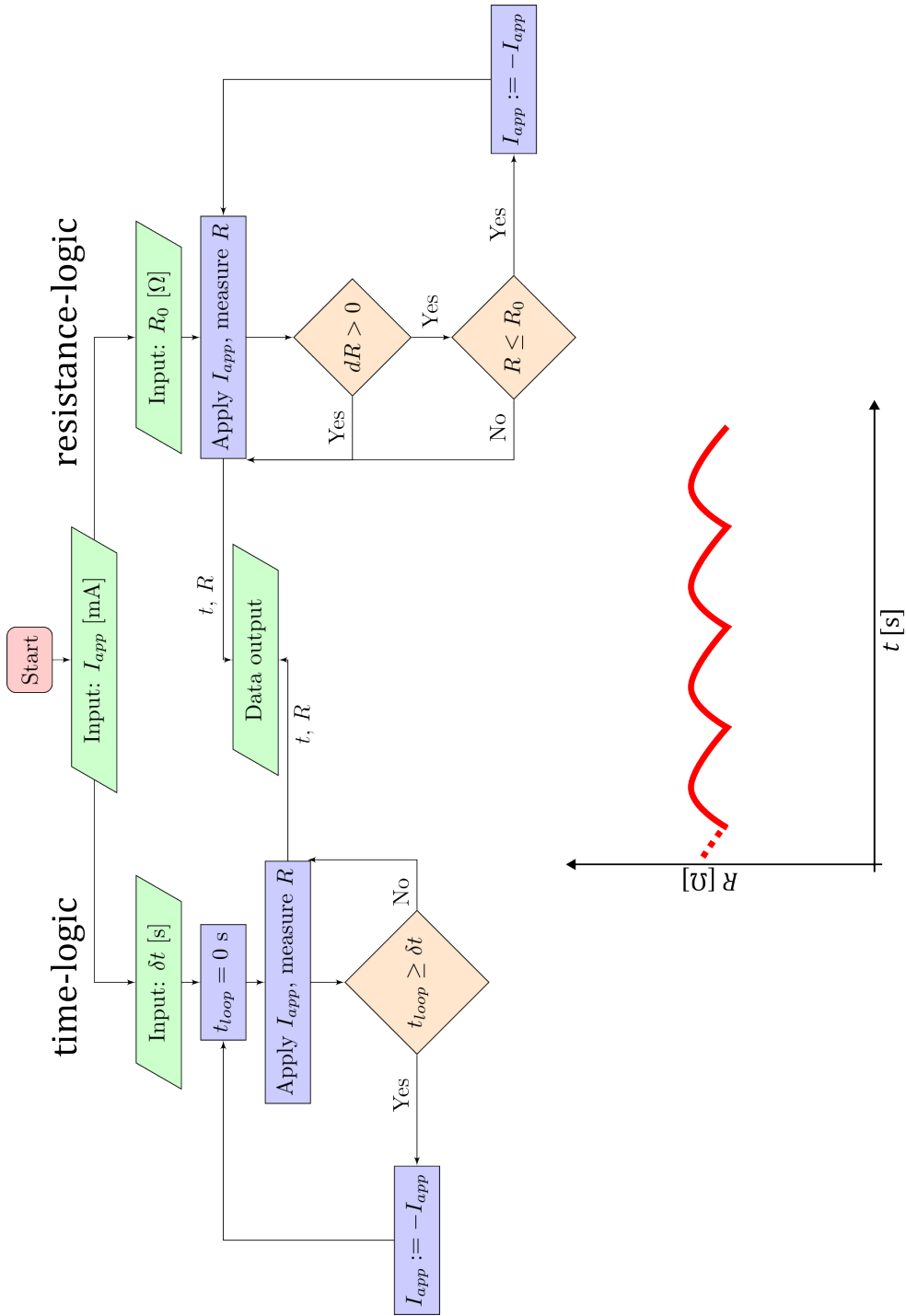


Figure 2.8

Figure 2.8: Continuous switching protocols and the resulting $R(t)$ curve. Same illustration convention as in Fig.2.6. The left-hand side of the diagram represents switching with a fixed period for the polarity flips (time-logic) and the right-hand side is switching at a predetermined threshold resistance (resistance logic). Both are executed using a fixed current amplitude I_{app} , but also take their respective control variables as inputs. The two-step decision process in the resistance-logic algorithm prevents unwanted polarity switches due to small fluctuations at the polarity inversion. Note the characteristic domed resistance curves in the bottom panel, every dome corresponds to one current polarity, two domes together make a whole period.

microscopic mechanisms at play.

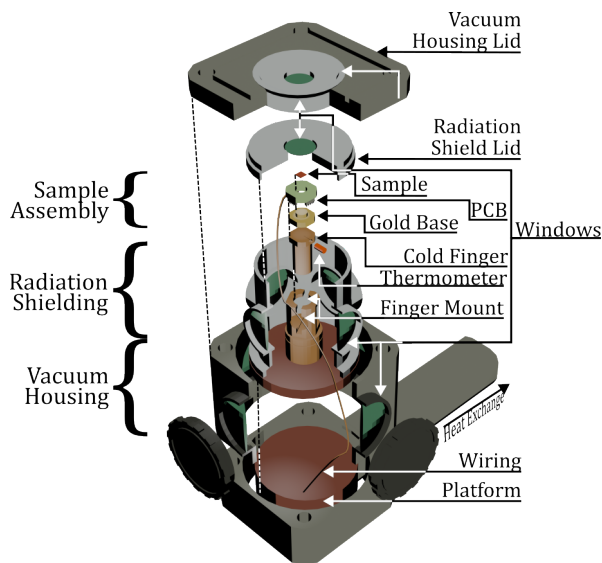


Figure 2.9: Schematic illustration of the tabletop cryogenic chamber of the Montana Instruments Cryostation used at EPNM. The sample assembly, which consists of the sample on top of a PCB envelope with a metallic base is mounted on top of an oxygen-free copper cold finger. The finger is mounted on the platform from which the heat extraction is performed. The chamber has two layers of shielding, an outer vacuum housing and a radiation shield. The key feature of this assembly is the optical access and the configurable electrical access via wiring.

The Montana Instruments Cryostation housed at EPNM was the main workhorse for the presented work. Besides the low maintenance costs and ease of use, the system has the advantage of having the samples optically accessible during cooling. The system utilizes a Gifford-McMahon refrigeration cycle to maintain a closed He loop. It offers a of cooling power ~ 100 mW at base temperature, thermal cycling speed of ~ 2.5 h for a complete cooldown and minimum temperature of ~ 3.7 K. The principal use of this system is for magneto-optical imaging but allows us to also image our samples during low- T electromigration experiments. Samples fit into the PCB envelopes (see Sec.2.2.1) are neatly mounted on a cold finger centered under the opti-

cal access window and connected with wiring, allowing for a great range of customizable experiment designs. The instrument is responsible for all cryogenic measurements discussed in the text barring the Hall effect and some of the $R(T)$ measurements in Ch.3 which were acquired using the Quantum Design physical property measurement system (PPMS) housed by ICMAB.

PPMS systems are one-stop solutions for a number of electric and magnetic measurement problems in solid state physics. They offer much higher cooling power and are fit with multiplexed voltmeters and powerful magnets with maximum fields of up to 18 T. The system has a lower minimum temperature (~ 1.5 K) and a much faster thermal cycling speed (~ 10 min), which allows for more measurements to be done in sequence.

2.3 Imaging

In this work we utilize numerous imaging techniques for characterizing our samples and for revealing some of the phenomena under investigation. The images produced through the various microscopies discussed here are processed using both commonly available applications and home-made programs and scripts. Raw tiff images such as those from optical microscopes or SEM systems are loaded into ImageJ for length measurements and alignment in multi-image series. Gwyddion was used for processing AFM images. Automated image processing is mainly done in python, images are loaded using the pillow package while the numpy and scipy packages are used for mathematical image treatment (image subtraction, convolution and filtering). Image presentation (like most data presentation) is done using the matplotlib package, as is animation frame generation, later rendered using Kdenlive. Further raster processing is done in GIMP and vector graphics are worked with in Inkscape. 3D representations of the techniques are generated in Blender.

Optical Microscopy

Throughout this text we will be discussing results relying on the changing reflectivity of perovskite thin films as a function of their oxygenation. In effect, this means that we may utilize simple optical imaging to gather the oxygen distribution maps of our samples. Such results are discussed in Ch.3,4,5 and 6.

For these purposes we utilize a modular Olympus BXFM microscope, whose kit includes a polarizer-analyzer pair, a Bertrand lens and a bright

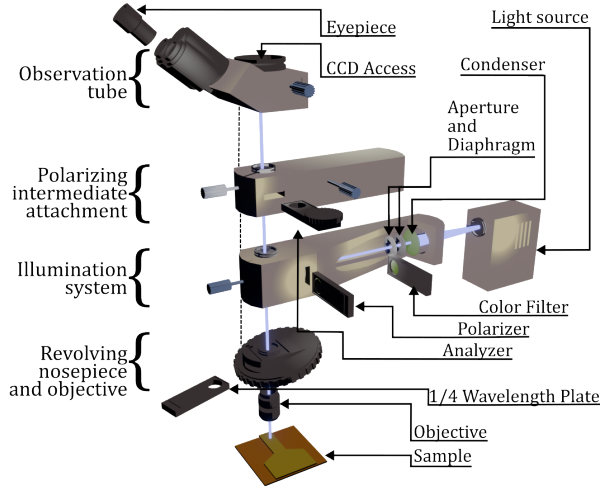


Figure 2.10: Schematic illustration of the Olympus BXM modular microscope assembly at EPNM. The light from the source passes through a condenser lens to parallelize the light rays, before passing through configurable apertures. The light is filtered with a green filter and passed through a polarizer and a quarter-wave plate. Image magnification is controlled by the objective. After reflection the light passes through an adjustable analyzer. The analyzer operates like a second polarizer to select the polarization of the collected light. The analyzer is mounted in a Bertrand lens.

field/dark field switch. The assembly is illustrated in Fig.2.10. We employ objectives with magnifications up to $50\times$ (numerical aperture 0.5 and polar angle 30° for a working distance of 10.6 mm). A Qimaging Retiga 4000R charge coupled device (CCD) is mounted on the microscope and used to produce 16 bit grayscale images (usually in the tiff format). The CCD can be controlled via LabVIEW or python.

Magneto-Optical Imaging (MOI)

Magneto-optical imaging (MOI) is a family of visualization techniques that draw contrast from the local magnetic field generated in a sample being studied. The EPNM toolkit includes both Faraday-effect based as well as Kerr-effect based techniques. Such imaging can be immensely useful in studying materials with magnetic functionalities, such as our superconductors and ferromagnetic materials. As magneto-optical techniques see limited application in the text, we will limit our discussion to a brief overview of Faraday-effect based magneto-optical imaging (MOI), which was used in Ch.3 and Ch.6.

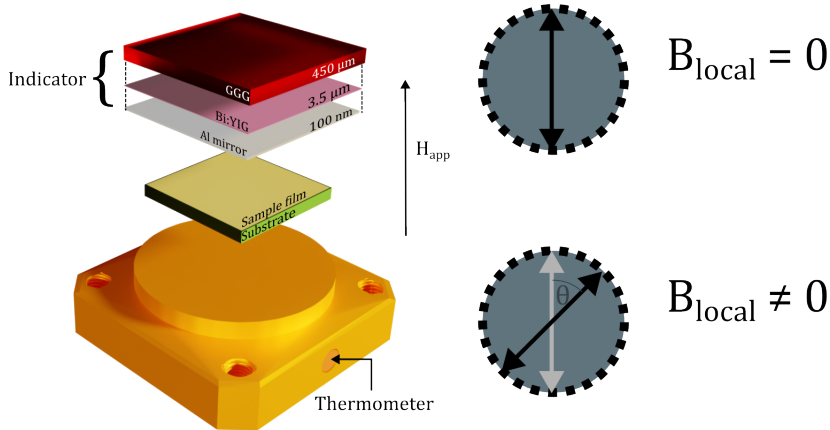


Figure 2.11: Cryostat cold finger - sample - indicator stack for Faraday-effect based magneto optical imaging. The change in the light polarization is illustrated on the right hand side.

The polarization of light can be affected by magnetic fields. If the polarization of light is changed in transmission through a medium by a field parallel to the direction of incidence, we denote this the Faraday effect. In practice, this means that linearly polarized light traveling through certain crystals will experience rotation of its polarization plane as a function of the local magnetization. A related but distinct phenomenon is dubbed the Kerr effect, where polarization changes on reflection from a material and can be influenced by magnetic fields both perpendicular and parallel to the angle of incidence. MOI makes use of these effects to generate contrast images based on the local magnetization in a sample. For Faraday based techniques, an optically active indicator stack is placed on top of a studied sample to facilitate the necessary rotation, as illustrated in Fig.2.11.

As most effects of interest (superconductivity, intense ferromagnetism, etc.) occur at low temperatures, the sample is usually placed in an optical cryostat as the one shown in Fig.2.9. The indicator stack consists of a gadolinium-gallium garnet (GGG) as the substrate, a Bi-doped yttrium-iron garnet as the optically active material and an Al-mirror. The stack is placed directly on the sample (mirror towards the sample). The indicator has in-plane magnetic domains. Polarized light travels through the stack, rotates at the indicator as a function of the local out of plane magnetic field of the sample below, and reflects off the mirror. Since the rotation of polarization is proportional to the local magnetic field component B_z normal to the sample plane, the use of an analyzer oriented perpendicularly to the initial direction of polarization

results in images where the intensity is proportional to B_z . Our polarized light microscope is illustrated in Fig.2.10. The images are acquired with a CCD camera and have a pixel size of $1.468 \times 1.468 \mu\text{m}^2$. Post-image processing was done to remove the inhomogeneous illumination and field-independent background, using the ImageJ software. More information about the setup can be found in Ref. [223]. By adjusting exposure times and analyzer angle, and performing a calibration at elevated temperatures (above T_c for superconductors) one can then obtain quantitative images of the local magnetic field in the sample.

The optical images were obtained in cryogenic conditions with up to 50x magnification objective followed by a x2 magnification lens and collected in bright field mode with a continuous green illumination filtered from a Hg lamp. The objective has a numerical aperture $\text{NA}=0.50$ and working distance of 10.6 mm, which corresponds to a polar angle of $\theta=\arcsin(0.5) \approx 30^\circ$, meaning that the largest component of the electric field is in the plane of the film (i.e. the ab -plane in YBCO films).

μ Raman spectroscopy

μ Raman spectroscopy is, as the name suggests, a combination of optical imaging and Raman spectroscopy, that is spectroscopic measurements in the range of Raman-active phonon modes in a crystal. This can allow for chemical mapping in materials where appropriate phonon modes can be found, such as in YBCO where a single phonon mode may persist across a range of δ values. μ Raman microscopes can sometimes acquire full rasters of Raman spectra, or may be limited to single points in an otherwise common optical microscopic image, such as the results presented in Ch.3.

Raman scattering experiments were performed at room temperature in the backscattering geometry using an Xplora Horiba Jobin-Yvon micro-Raman spectrometer equipped with a high sensitivity air cooled CCD (charge-coupled device) as the detector. The 532 nm laser line was used for the measurements. The incident laser beam was focused to a $1 \mu\text{m}$ spot using an $\times 100$ microscope objective on the sample. The laser power was kept below 1.0 mW to avoid laser-induced heating. The spectrometer resolution was 2 cm^{-1} . The polarization of the electric field of the incident and scattered light was kept parallel to the crystallographic ab -axis of the YBCO layer.

Scanning Electron Microscopy (SEM)

By sweeping a focused beam of keV electrons impinging on a conductive material and detecting electrons ejected from the interaction volume, we can resolve 2D images of our sample surface. The technique based on this, SEM is used for its nanometric resolution allowing one to distinguish single grains of epitaxial films. We utilize a combined SEM-electron-beam lithography (EBL) Pioneer TWO system commercially offered by the German company Raith GmbH, and the working principle is illustrated in Fig.2.12.

The interaction of the impinging electrons with the sample volume and the resulting signal sources are illustrated on the side of Fig.2.12. The electrons in SEM have energies up to $\tilde{30}$ keV. Auger electrons can be useful for learning the surface atomic composition but are used more rarely. Secondary electrons (<50 eV energy) are generated by inelastic scattering. They provide topographical information while backscattered electrons, coming from elastic scattering deeper in the sample, show contrast based on atomic number and phase differences. The produced X-ray radiation includes characteristic X-rays of the elements in the volume. The presented work will use two detectors for secondary electrons, the InLens detector located within the objective lens collects secondary electrons of higher energy, while the Everhart-Thornley detector in the sample chamber collects most lower energy secondary electrons.

The choice of detector can alter the nature of the generated images. Images resolved with the InLens detector are generated by electrons which originate from a region close to the beam focus point (secondary electrons of first generation - SE1) and their contrast reflects the surface topography, with phases of a lower work function appearing brighter. Another detector (Everhart-Thornley) collects secondary electrons that originate in a more extended region around the beam focus point defined by backscattered electrons (SE of second generation - SE2), giving a contrast more strictly dependent on the surface topography.

Scanning Transmission Electron Microscope (STEM)

STEM is another electronic imaging technique based on electron-matter interaction, but focused on electron transmission through a thin sample wedge. The instrument operates similarly to a SEM with the caveat of using a much more energetic electron beams, in the 100 - 300 keV range. The electron beam-sample volume interaction is similar to Fig.2.12. STEM generates transmitted and backscattered electrons, secondary electrons and

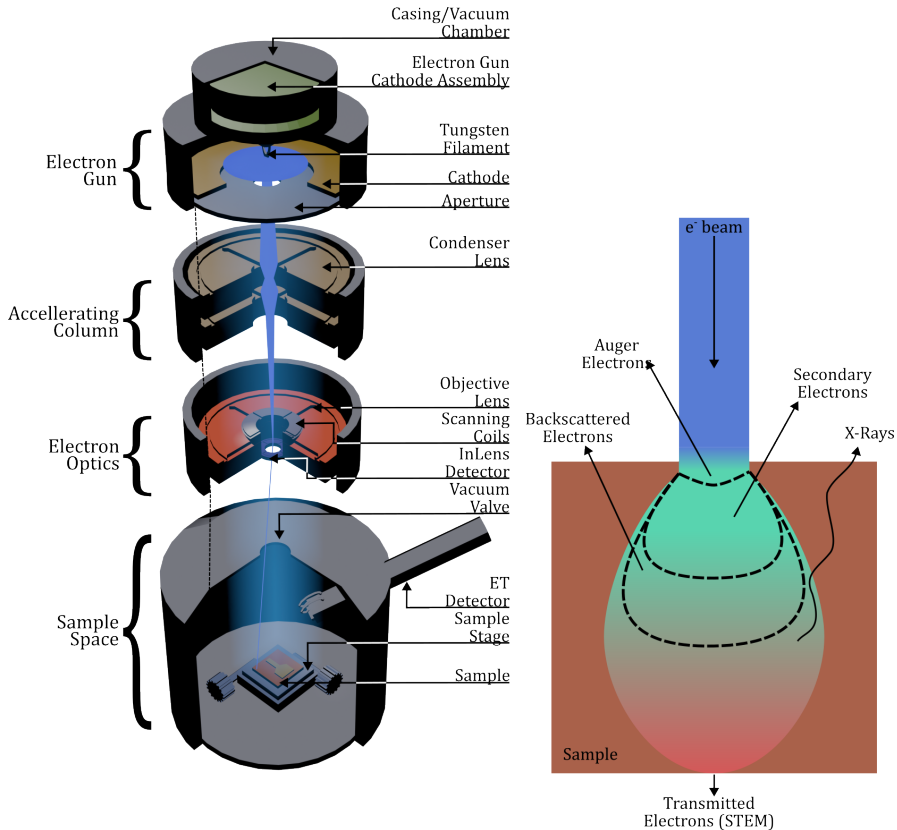


Figure 2.12: Schematic illustration of working principle of a SEM. The electron beam originates from a hot tungsten filament of the electron gun, by means of hot field effect. The extractor anode is mounted below it. A part of the emitted electrons passes the aperture and enter the acceleration column where condenser lenses form the beam and provide acceleration set by the operator. The beam passes through an electrostatic lens and a set of deflection coils for scanning the sample surface before entering the sample chamber. The sample is mounted on a stage with very fine mechanical controls for positioning. The InLens detector is positioned in the objective lens, and the Everhart-Thornley detector is mounted on the side of the sample chamber. The interaction of the impinging electrons and the sample volume is shown on the right. Electrons are only transmitted in very thin samples by very energetic electrons, usually in STEM setups.

characteristic X-rays. Appropriate detectors can then collect these signals, with the most interesting ones for our application being the ones collecting transmitted and scattered electrons that give a contrast based on the height of the atomic stack they pass through and the mass of the atoms. When acquired

in high-angle annular dark-field imaging mode (HAADF), the STEM images show the so-called Z-contrast, where the intensity of the atomic columns scales with the atomic number Z .

Additionally, other detectors can be used, including an electron energy loss spectroscopy (EELS) detector which characterizes the energy lost by the electrons in transmission which provides chemical and electronic information.

STEM offers truly atomic resolution, where single atoms can indeed be resolved, such as in the examples given in Ch.6. The technique requires destructive ion-beam milling techniques to cut out a lamella of the sample, but is uniquely useful in obtaining images of crystal defects in the sample cross-section.

Samples were characterized using a JEOL JEM ARM200cF operated at 200 kV, equipped with a CEOS aberration corrector and GIF Quantum ER spectrometer, at the Universidad Complutense de Madrid, Spain. The STEM specimens were prepared using a FEI Helios nanolab 650, at SEM-FIB microscopy service of the Universidad de Málaga.

Atomic Force Microscopy (AFM)

AFM and its derivative techniques like conductive AFM (cAFM), Kelvin-probe AFM (KPFM) and others, all are based on the principle of interactions between the sample surface and a probe on an oscillating cantilever brought into close proximity (or direct contact) with the sample.

In an AFM microscope, the cantilever is mounted with a piezoelectric element. Using the contraction of the piezoelectric, the cantilever is oscillated at a given frequency measured by shining a laser into the cantilever tip and measuring its deflection with a photodiode. The extremely sharp tip at the end of the cantilever is brought close to the sample surface and can then act as a probe for numerous interactions, as illustrated in Fig.2.13. Alternatively, the tip is brought in contact with the surface and the signal is measured directly, like conductance in cAFM.

The oscillation frequency of the cantilever is directly responsive to the measured interaction - in the case of standard AFM this is the Van der Waals force, for cAFM it is conductance and for Kelvin-probe AFM it is the local work function at the surface. Derivative techniques are usually coupled with standard AFM techniques, and one usually obtains a topographic image with nanometric resolution in the z -scale and a slightly weaker resolution in plane.

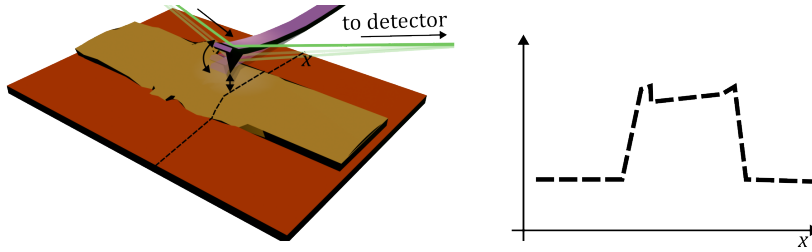


Figure 2.13: Simplified view of AFM. The deflection of the oscillating tip changes as a function of an unspecified interaction as it is driven across the surface. The measured response is produced on the right.

2.4 Modeling

We utilize FEM to investigate the oxygen concentration and temperature profile of our samples during the experiment. We employ the proprietary software suite COMSOL, with or without a dedicated MATLAB controller, to make a 2D model of the perovskite film as a continuous, isotropic material whose oxygen concentration may vary between $c_{min} = 3.41 \times 10^{28}$ and $c_{max} = 4.01 \times 10^{28}$ ions m^{-3} . We introduce a more convenient derived parameter $x = (c - c_{min}) / (c_{max} - c_{min})$ representing the doping.

The temporal evolution of x depends on the electric field as well as on the temperature as described in Ch.1 and in Eq.2.4 below. We omit terms relating to thermomigration and stress-induced migration as these are not pertinent for our studies.

$$\frac{\partial x}{\partial t} = \nabla \cdot (D \nabla x + zuFx \nabla V) \quad (2.1)$$

with D the temperature-dependent diffusion constant that is governed by the Arrhenius expression $D = D_0 \exp(-E_a/k_B T)$. We consider E_a the activation energy (in eV) and k_B the Boltzmann constant, while z is the charge number of the oxygen ions, u the Nernst-Einstein ratio ($u = \frac{\mu D}{k_B T}$, with μ the mobility) and F the Faraday number. The charge number of oxygen $z = -2$ is an approximation of Z^* (see Box.1.1). Setting it to a negative value determines the direction of the mass transfer in respect to the field.

The first term on the right-hand side of Eq.2.1 describes thermally activated diffusion along concentration gradients, whereas the second one addresses diffusion due to potential gradients and carrier momentum transfer. The resolution of these equations with interdependent parameters is implemented in an iterative segregated algorithm, either using MATLAB to

mediate between iterations in COMSOL, or directly as a segregated solver in COMSOL.[224]

First, the heat equation is solved accounting for Joule heating using an x -dependent resistivity and considering heat evacuation through the substrate, to obtain the temperature distribution in the system. Then, the Poisson equation is solved to determine the electric potential distribution in the sample alongside with the diffusion of oxygen according to Eq. 2.4. An example of a 2D finite element mesh representing the device is illustrated in Fig.2.14.

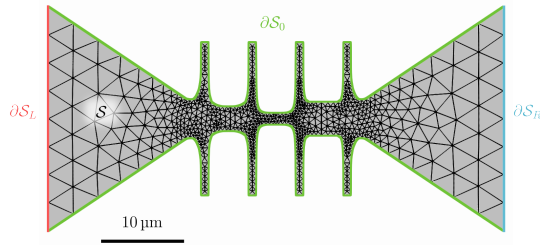


Figure 2.14: Representation of a finite element mesh, S used for modeling the electrically driven oxygen diffusion. δS_L and δS_R are domain boundaries used to define the electrical control, with δS_L usually being the ground. Both are given fixed values for oxygen content. δS_0 is the model edge. The mesh geometry is taken from SEM images of a real device.

Part II

Current Driven Oxygen Electromigration for Doping Control in YBCO

Direct Visualization of Current-Induced Oxygen Electromigration in YBCO

Based on: S. Marinković, A. Fernández-Rodríguez, S. Collienne, S. B. Alvarez, S. Melinte, B. Maiorov, G. Rius, X. Granados, N. Mestres, A. Palau, and A. V. Silhanek, “Direct visualization of current-stimulated oxygen migration in $\text{YBa}_2\text{Cu}_3\text{O}_{7-\delta}$ thin films”, *ACS Nano* **14**, 11765–11774 (2020) 10.1021/acsnano.0c04492

Main Contributions: experiment design, electromigration experiments, photoexcitation measurements, cryogenic transport measurements, optical, MOI and SEM imaging, data interpretation and presentation and writing

Auxiliary Contributions: PPMS Hall effect measurements and finite element modeling

Layman's Overview: Reflectivity as a Proxy for Oxygenation

Optical reflectivity is one of the properties modulated in perovskite oxides when changing oxygenation under electrical stress. It can be defined as the amount of light reflected off the material surface under illumination. Effectively, this means that deoxygenated (larger δ) YBCO is brighter.

In this chapter, we take advantage of optical reflectivity to map the movement of oxygen in and out of a constriction under stress, by combining spectro-

scopic and electrical characterization techniques. We confirm that this is indeed the oxygen moving through the bulk, and demonstrate how it correlates to changing resistance R and superconducting critical temperature T_c . Our findings demonstrate beyond doubt that the directional movement of oxygen in the material is a consequence of the applied electrical stimuli, and provide a solid basis to understand the phenomenon of selective oxygen electromigration in perovskite oxides.

In this chapter, we focus on the visualization of changing oxygen doping in an extended region through current-stimulated oxygen migration in $\text{YBa}_2\text{Cu}_3\text{O}_{7-\delta}$ superconducting bridges. For this, we use samples as described in Sec.2.1.5 and apply the methodology described in Sec.2.2.2. The emerging, propagating front of current-dependent doping δ is probed *in situ* by optical microscopy and scanning electron microscopy. The resulting images, together with photo-induced conductivity and Raman scattering investigations reveal an inhomogeneous oxygen vacancy distribution with a controllable propagation speed permitting us to estimate the oxygen diffusivity. These findings provide direct evidence that the microscopic mechanism at play in electrical doping of cuprates involves diffusion of oxygen atoms with the applied current.

3.1 Introduction

As discussed in Ch.1, the physics of copper oxide superconductors continues to be one of the most fascinating scientific topics since their discovery in the late 80's.[3] This notoriety can be arguably attributed to a superconducting transition temperature greatly exceeding those of any known superconductor at room pressure, the plethora of unconventional electronic phases and the yet unsettled origin of the pairing mechanism.[42] It is not uncommon that slight changes in the stoichiometry of complex oxides lead to large variations of its properties. The interplay between various electronic orders can account for the reported sensitivity of these materials to parameters like composition, temperature, magnetic field, and pressure.

In particular, it has proven to be a challenge to precisely control the oxygen stoichiometry and consequently to establish an accurate phase diagram.[57]

More specifically, it has been difficult to attain particular critical chemical compositions separating two distinct quantum ground states, which are important for the studies of quantum critical points in condensed matter. In addition, traditional methods consisting in synthesizing and characterizing samples one composition at a time may become an inefficient workload with questionable results when comparing different samples. Therefore, developing new technologies with high efficiency and accurate synthesis are becoming a leading priority in superconductor science.[56]

In this chapter, we explore the possibility to tune the oxygen content in $\text{YBa}_2\text{Cu}_3\text{O}_{7-\delta}$ (YBCO) by mass-selective migration of oxygen atoms induced by large electrical current densities. The material choice is primarily motivated by the fact that YBCO lies among the most investigated high- T_c superconductors and for which it is well documented that oxygen stoichiometry has a dramatic effect on its properties.[121] For instance, the crystalline structure of YBCO changes from orthorhombic to tetragonal, while the c -axis lattice parameter increases by lowering the oxygen content.

3.2 Results and Discussion

3.2.1 Electromigration process

The investigated superconducting samples are YBCO thin films, patterned to form narrow bridges with two different designs as shown in Figure 3.1(a,b). In all cases the narrowest section of the transport bridges was $\sim 1\text{-}2\ \mu\text{m}$ wide. Figure 3.1(c) shows an optical microscopy image of an entire device and Figure 3.1(d) shows the associated magneto-optical image for the same device obtained at $T = 4.5\ \text{K}$ and $\mu_0 H = 0.95\ \text{mT}$. This image evidences the magnetic flux expulsion from the superconducting parts of the sample with bright blue areas corresponding to high magnetic fields and dark regions representing low magnetic fields. The homogeneity of the magnetic flux expulsion is a strong indication of the high quality of the YBCO film, confirming its excellent superconducting behavior and absence of macroscopic defects.

The electromigration (EM) process in the constrictions was induced by ramping up the voltage bias while simultaneously monitoring the change in conductance dG/dt (see Sec.2.2.2). A typical resistance-current curve, $R(I)$, obtained at $T = 105\ \text{K} > T_c$ for the sample of Figure 3.1(a) is shown in Figure 3.2(a). At low currents, *i.e.* within the range between point pristine and point A, the $R(I)$ exhibits a smooth nearly reversible increase mainly due to Joule heating effects. At about 12 mA, corresponding to a current density

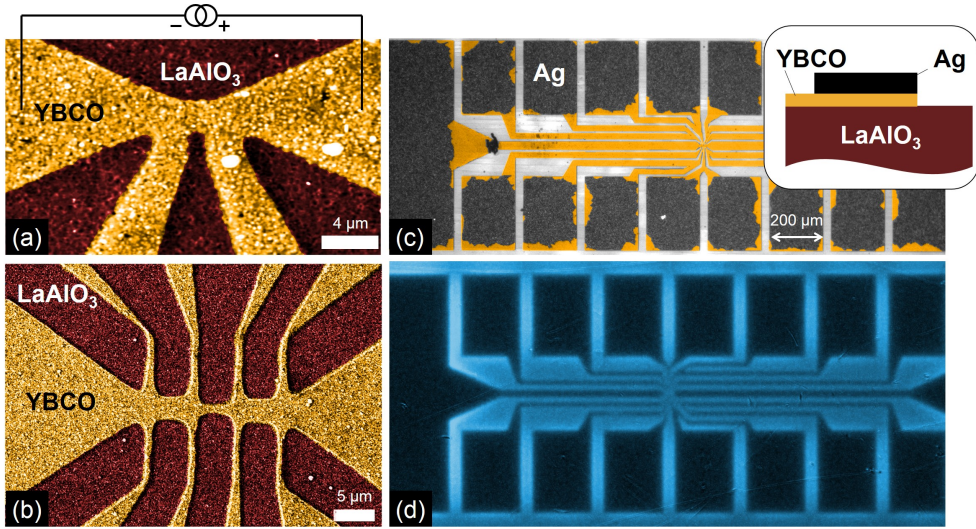


Figure 3.1: Scanning electron microscopy images of a single YBCO constriction (a) and a symmetric three-bridges structure (b). Electromigration takes place in between voltage contacts where the current density reaches its maximum value. In (a) the narrowest point of the bow-tie structure is $1 \mu\text{m}$ wide. In (b) the central bridge is $0.8 \mu\text{m}$ wide and the two symmetrical arranged side bridges are $3 \mu\text{m}$ wide. Panel (c) shows an optical microscopy image of the entire device. Inset: cross-section at the voltage pad showing the epitaxial $\text{YBa}_2\text{Cu}_3\text{O}_{7-\delta}$ film grown on a LaAlO_3 single crystal substrate and Ag electrodes. In panel (d) a magneto-optical image obtained at $T = 4.5 \text{ K}$ and $\mu_0 H = 0.95 \text{ mT}$ for the device in panel (c) is shown.

$J \approx 8 \text{ MAcm}^{-2}$, a change of sign in the slope indicates that electromigration has been launched, as suggested by the fact that less current is needed to increase the resistance. The inset in Figure 3.2(a) shows the time evolution of the circulating current through the sample which takes place on the scale of several hours.

Note that although these measurements have been done at constant bath temperature, the local temperature at the constriction can be substantially higher. Using finite element simulations we can estimate the local temperature at point A as $T_{\text{loc}} \sim 525 \text{ K}$ (see Annex A.1). This value represents an estimation reliable only for currents lower than point A. Above this point the stoichiometry of the sample changes and a new calibration would be needed for each data point. For the sake of comparison, YBCO decomposition temperature, *i.e.* the onset of melting, takes place around 1273 K , [225] recrystallization is observed ca. 1073 K , [216, 226] oxygen loss starts at around 673 K [227] while oxygen movement and ordering is present at even lower

temperatures.[228] Therefore, the combination of high temperature and high current density is expected to induce directed diffusion of oxygen atoms.

Using neutron diffraction on samples with varying δ , Jorgensen *et al.*[121] and others [128] have shown that the vacancies in the orthorhombic superconducting $\text{YBa}_2\text{Cu}_3\text{O}_{7-\delta}$ system clearly prefer the O(1) position in the copper chains, thereby tuning the Cu(1)-O(4)-Cu(1) bond lengths and the doping levels in the CuO_2 planes (see Box.1.5). This means that $\text{YBa}_2\text{Cu}_3\text{O}_{7-\delta}$ can be described as two lattices, one hosting all the truly periodic atomic positions (Y, Ba, Cu(1, 2), O(2, 3, 4)) and another one hosting the O(1)- V_O^{2+} lattice, where V_O^{2+} are the vacancies at the O(1) site position. It is known that vacant sites, rather than interstitials, are involved in the diffusion of oxygen atoms most likely following a O(1)- V_O^{2+} -O(1) hopping path. More details on the vacancy mechanism of oxygen diffusion in the CuO chains can be found in Ref.[229]

3.2.2 Direct visualization of oxygen migration

In order to unveil the directed migration of oxygen atoms, we resort to optical imaging at cryogenic conditions. Figure 3.2(b) shows false colored differential optical microscopy images obtained at 105 K, revealing the evolution of the area affected by the electromigration (darker region). The labels correspond to the points indicated in Figure 3.2(a). The superposed white curve delineates the borders of the transport bridge. The electromigrated region can also be evidenced in bright-field optical images since the creation of oxygen deficient zones in YBCO films results in increased reflectivity (see text below).[199, 230] Note that the change of optical response is directional towards the cathode side, and therefore cannot be attributed to the symmetrically spread Joule heating. The majority charge carriers (holes) flow from right to left in the same direction as oxygen vacancies (*i.e.* towards the cathode). A close inspection of the optical intensity from the affected area actually shows a mixture of high intensity and low intensity spots indicating a rather inhomogeneous redistribution of oxygen vacancies.

In order to confirm that oxygen atoms are displaced out of the constricted region and correlate optical images with electrical measurements, we have redesigned the device geometry as presented in Figure 3.1(b). This structure consists of a narrow central bridge symmetrically surrounded by wider bridges, each bridge individually addressable by corresponding voltage contacts. In Figure 3.3(a) we plot the normalized resistance $R(T)/R(200\text{ K})$ as a function of temperature for the three bridges when the sample is in its pristine state. For the sake of clarity, we have indicated with red color the

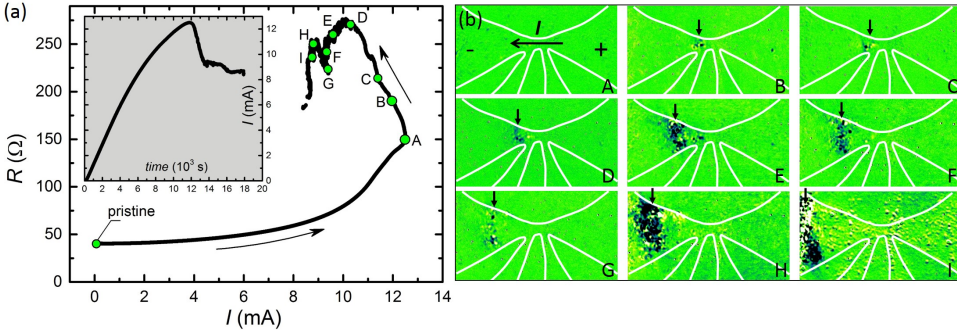


Figure 3.2: (a) Resistance of a YBCO device similar to the one in Figure 3.1(a) as a function of the circulating current during an electromigration process. The time evolution of the measurement is indicated by the black arrows. The initial temperature in the pristine state is 105 K and increases up to ~ 525 K at point A. Controlled feedback operates from point A on avoiding thermal runaway. Inset: current circulating through the sample as a function of time during the electromigration process shown in the main panel. (b) Differential images showing the evolution of the front of the affected region for an applied current running from right to left as indicated in panel (a). Positively charged oxygen vacancies move towards the cathode (-) and negatively charged oxygen atoms move towards the anode (+). The labels correspond to the points indicated in panel (a). The superposed white curve delineates the borders of the transport bridge and the vertical black arrows indicate the mean position of the propagating front.

left bridge, green for the central bridge, and blue for the right bridge. The normalized resistance allows us a direct comparison between the central and side bridges, being the absolute resistance of the central bridge a factor 3.25 higher than the side bridges as expected from geometrical considerations. The perfect overlap of the normalized resistance curves demonstrates that the lateral structuring of the YBCO film has no effect on the superconducting transition and the resistivity of the film. In other words, the pristine sample behaves as a monolithic structure with uniform composition and electrical response. In the rest of the manuscript we will keep $R(200\text{ K})$ of the pristine sample as the normalization factor.

A strikingly different electrical response is observed after electromigrating the sample as shown in Figure 3.3(b). Similarly as for the device in Figure 3.2, the polarity of the voltage bias during electromigration corresponds to cathode (-) on the left side and anode (+) on the right side. In order to facilitate the observation of the induced relative change, in Figure 3.3(b) we replot the universal $R(T)/R(200\text{ K})$ for the pristine sample with black

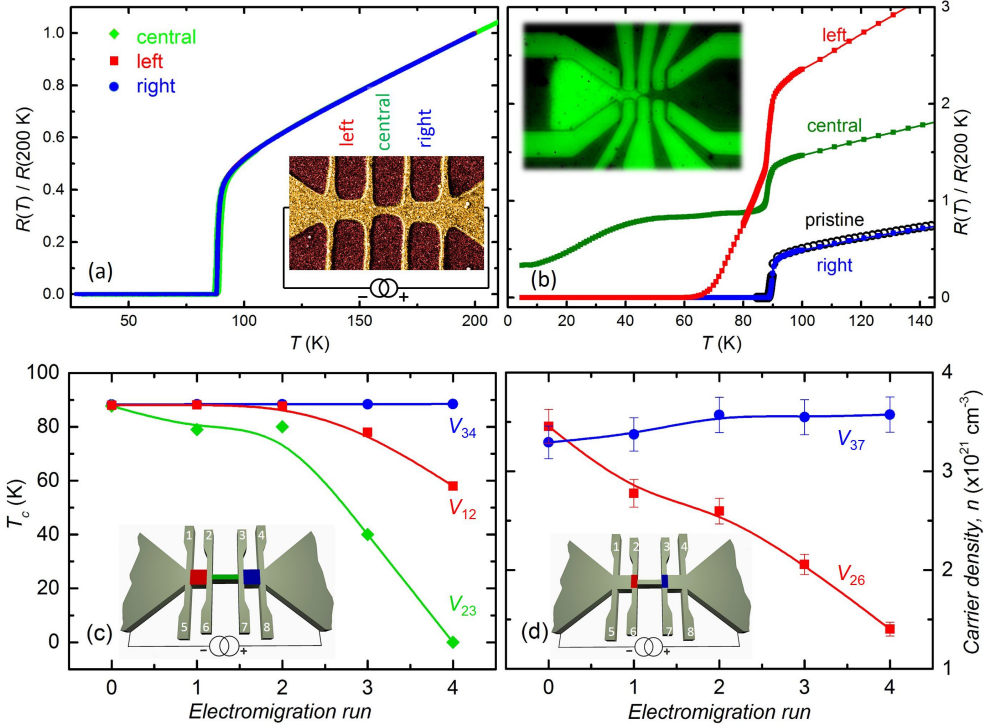


Figure 3.3: Normalized resistance $R(T)/R(200\text{ K})$ as a function of temperature for the central bridge (green), left bridge (red), and right bridge (blue) for the sample in the pristine state (a) and after electromigration (b). The inset in panel (a) shows a scanning electron microscopy image of the three bridges connected in series, indicating the color code of the voltage signal acquired and the polarity of the current source. In panel (b), the universal response for the pristine sample is replotted with black open circles. Inset in panel (b): optical microscopy image obtained after electromigration process. The affected area on the cathode side is clearly visible as a bright region starting from the central bridge and extending deep into the current leads to the left. Evolution of the critical temperature T_c (c) and the carrier density, n (d) at different regions of the YBCO constriction. The color code of the data points corresponds to the signal picked up at the colored regions in the insets. For the sake of clarity the numbering indicates the voltage contacts addressed in each measurement.

data points. The left and central bridges exhibit a radically different trend after electromigration. The left bridge shows a substantial increase of the normal state resistance and a clear decrease of the superconducting critical temperature as well as a broadening of the transition width. Interestingly, the central bridge still exhibits a superconducting transition at $\sim 30\text{ K}$ with

a low temperature phase corresponding to a dissipative state and a higher normal state resistance with respect to the initial state. The right bridge remains nearly unaffected with respect to the initial state. Further electromigration (See Annex A.2.) leads to a full suppression of the superconducting condensate in the left bridge and, more interestingly, to a decrease of the normal state resistance in the right bridge without affecting T_c . Note that the superconducting transitions at the left and central bridges exhibit broad distributions $\delta T_c \sim 20$ K reinforcing the idea of a highly inhomogeneous state, as proposed in Ref. [198] In addition, a clear transition at 90 K remains visible for the affected bridges, indicating that part of the bridge has not been modified by the electromigration process.

An optical microscopy image taken at the end of an extended electromigration process is shown as an inset in Figure 3.3(b). This image was taken at 105 K in bright field with the analyzer adjusted to optimize the contrast. The affected area on the cathode side is clearly visible as a bright region starting from the middle bridge and extending deep into the current leads to the left. The optical properties of YBCO have been investigated in Ref. [199, 230–233]. Kircher *et al.* [230] reported a decrease of reflectance with increasing oxygen content for the electric field parallel to the crystallographic a -axis, whereas an increase in reflectance occurs for the electric field parallel to the c -axis. In addition, far field measurements of c -axis normal films show an increase of reflectivity where oxygen content has been depleted.[199] According to this interpretation, higher reflectivity on the cathode side is indicative of an increase in oxygen vacancies, in agreement with the scenario proposed above.

Precise tuning of the oxygen diffusion through the sample may be achieved by applying subsequent electromigration runs in order to progressively increase the oxygen vacancies concentration on the central and left bridges. Figure 3.3(c) shows the evolution of the critical temperature obtained with a low voltage criterion of 100 nV for the three bridges (right, left and central with data points colored according the sketch in the inset) and after four sequential electromigration runs. In addition, Figure 3.3(d) shows the evolution of the carrier density, n , obtained from Hall measurements at 105 K using transverse voltage contacts located at the edges of the central bridge as illustrated in the inset.

The observed dependence of both T_c and carrier density is fully consistent with the interpretation corresponding to oxygen atoms diffusing towards the anode and oxygen vacancies flow towards the cathode during the EM process. In other words, the doping level δ increases on the cathode side and decreases on the anode side. This scenario naturally accounts for the suppression of T_c

and reduction of the carrier density on the cathode side. Note that the carrier density exhibits a slight increase on the anode side (blue points) consistent with the scenario where oxygen atoms replenish some vacancies and with the observation of a decrease of normal state resistance on the anode side after several EM steps.

It is interesting to use the information presented in Figure 3.3 in order to estimate the hole doping p , *i.e.* the number of holes per copper atom in the CuO_2 planes. Hole doping is a parameter of paramount importance determining the critical temperature of the cuprates for which the $T_c(p)$ and $p(\delta)$ dependences have been experimentally estimated in Ref. [162]. In Figure 3.4 we reproduce the data from Ref. [162] together with the $T_c(n)$ obtained from the electromigration measurements presented in Figure 3.3(c,d). In view of the fact that T_c and n have been probed at different parts of the bridge, in Figure 3.4 we plot the average critical temperature between left and central bridges as a function of the carrier density inferred from the left Hall cross. The fair agreement between the two independently determined experimental data points encourage us to propose the present method as an appealing approach to fine tune the doping level in cuprates for eventually obtaining a detail mapping of the electronic phases in these materials. Nevertheless, care must be exerted in comparing our data obtained in thin films and with carrier density estimated from 105 K measurements, to those of Ref. [162] corresponding to single crystals and with hole doping obtained at 300 K.

Compelling evidence that EM selectively displaces oxygen atoms can be obtained from μ -Raman spectrometry. This technique enables the local quantification of oxygen content along the YBCO constriction after different electromigration runs.[234] Green points in Figure 3.5(a) show the spots where the micro-Raman signal has been collected. The Raman shift in the 500 cm^{-1} mode accounts for the c -axis motion of the apical oxygen atoms

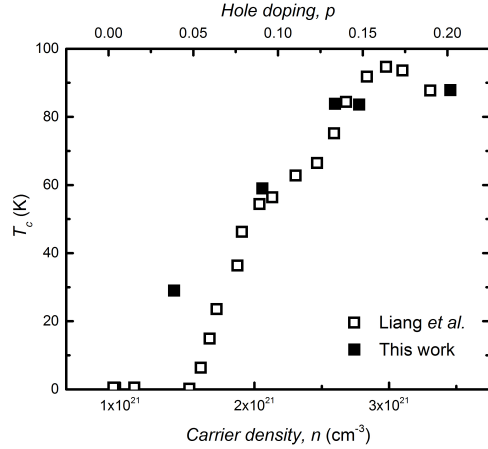


Figure 3.4: Superconducting critical temperature as function of the carrier density and hole doping estimated from the current-induced oxygen migration (filled squares). For the sake of comparison, we reproduce the data from Ref. [162] (empty squares).

[O(4)] bridging the CuO chains and CuO₂ planes [235, 236] (see Annex A).

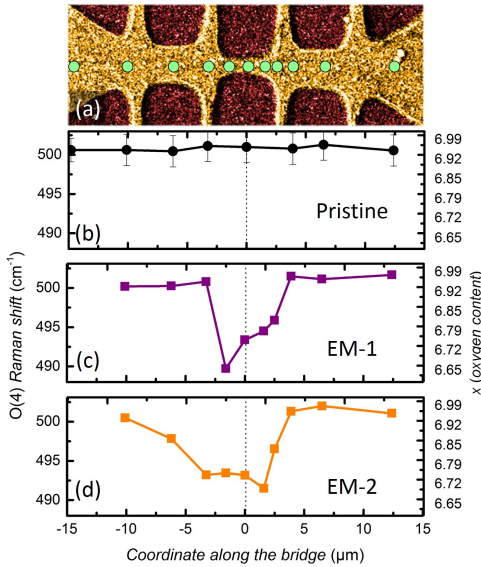


Figure 3.5: O(4) phonon mode frequency measured along the linear scan displayed in panel (a), for the pristine state and after reaching two different EM states (applied current 16 mA), together with the extracted oxygen content. The center of the constriction is marked with a dotted line. The error bar in the phonon frequency is 2 cm^{-1} and displayed only for the pristine sample.

This relationship originates from the variation of the c -cell parameter with δ . Indeed, an expansion of the unit cell occurs (increase of the c -parameter) when the oxygen content $x = 7 - \delta$ decreases and therefore the frequency of the O(4) phonons is shifted downwards with a linear dependence on x , as a result of bond softening [152, 236]. Figure 3.5(b-d) display the evolution of the O(4) phonon frequency measured for three different cases corresponding to the pristine state (b) and after two successive EM runs (c-d). For the pristine state (black points) a phonon frequency value of 502 cm^{-1} is observed, consistent with an optimal doped homogeneous track with an oxygen content of $x = 6.95$.

After performing controlled electromigration up to 16 mA (EM-1 state) the linear Raman scan across the constriction shows a large down shift of the apical oxygen mode frequency from 502 cm^{-1} to 490 cm^{-1} , at the central and part of the left side of the bridge. This shift is consistent with a region of depleted oxygen content, $x \sim 6.65$ towards the cathode. A slight increase in the O(4) phonon frequency is observed at the right side of the bridge confirming a reduction in the amount of mobile oxygen vacancies and consequently, a possible enhancement in the oxygen doping. After subsequent electromigration process with the same current amplitude (EM-2 state), the Raman scan (orange squares), indicates an enlargement of the oxygen depleted region towards the left side of the bridge, consistent with an enlargement of the region where oxygen vacancies are created.

After performing controlled electromigration up to 16 mA (EM-1 state) the linear Raman scan across the constriction shows a large down shift of the apical oxygen mode frequency from 502 cm^{-1} to 490 cm^{-1} , at the central and part of the left side

3.2.3 Photoexcitation

An elegant way to probe the induced inhomogeneous oxygen distribution can be achieved through photoexcitation effects. Indeed, it has been previously shown that illuminating oxygen deficient YBCO films, (i) decreases the normal state resistivity and increases T_c , and (ii) changes the carrier density as well as the carrier mobility. In addition, a long relaxation time, of the order of days at room temperature, is observed once the illumination is turned off.[237] There is a clear correlation between the oxygen content and the relative change in the resistivity produced by the photoexcitation. More precisely, the lower the T_c of the sample, the larger the relative change in the resistivity.[97] The essential mechanism behind this effect implies the photodoping of the CuO_2 planes by electron-hole pair excitation involving two possible scenarios for the electron trapping mechanism, namely photoassisted oxygen ordering[157] and trapping at oxygen vacancies.[158]

Figure 3.6(a-c) summarizes our findings after continuous illumination with 550 nm wavelength on an already electromigrated sample (similar to the state shown in the inset of Figure 3.3(b)). A direct comparison with the response of the sample without illumination shows that during continuous photoexcitation the transitions at ~ 90 K remain unchanged while the broad transitions at lower temperatures are enhanced. Indeed, photoexcitation leads to a slight increase of T_c (the white curve shifts to the right) and to a reduction of the normal state resistivity at the left and central bridges, consistent with the premise of oxygen depletion in these zones. In contrast to that, for the oxygen rich side (right bridge), the critical temperature remains unchanged whereas the normal state resistivity increases. Note that sample heating due to the illumination process cannot explain a decrease of resistance as observed in the central and left bridges.

Let us now investigate the time evolution of the photo-induced changes in conductivity in the central bridge before and after electromigration. Figure 3.6(d) shows the percentage change of the central bridge resistance with respect to the initial value R_0 as a function of time. Note that the pristine sample exhibits no resistance change during illumination at 200 K (yellow squares) whereas after creating an oxygen-deficient region by electromigration, a clear photodoping is observed (green circles). At this temperature, the induced photoconductivity is persistent and no relaxation is observed. By increasing the temperature to room temperature (inset Figure 3.6(d)) and turning off the illumination, the photo-enhanced state undergoes a very slow relaxation process. All these findings are in agreement with the investigations performed in oxygen-deficient YBCO samples by Markowitsch *et al.*[159] and

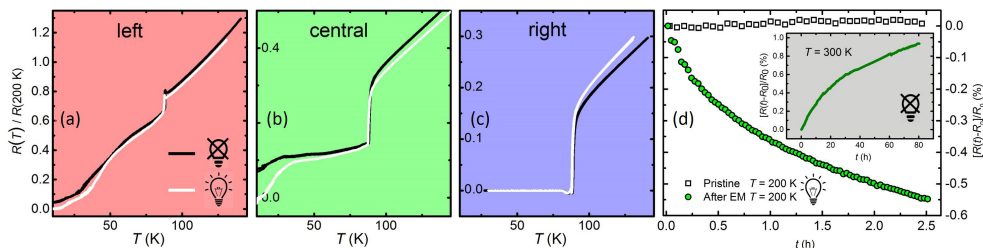


Figure 3.6: Normalized resistance $R(T)/R(200\text{ K})$ for the left (a), central (b), and right (c) bridges before (black) and after (white) illumination. Note the different vertical scale range in each panel. Panel (d) shows the percentage change of the central bridge resistance with respect to the initial value as a function of time. The pristine sample exhibits no resistance change during illumination at 200 K (empty squares) whereas after electromigration clear photodoping is observed (green circles). Inset: At room temperature and switching off the illumination, the photoexcited sample can relax back to the original state in a much longer time scale.

others.[98, 160]

3.2.4 Anti-electromigration

One particularly appealing aspect that could situate voltage-controlled electromigration as a privileged tool of choice for tuning the oxygen content, is the possibility to heal a previously electromigrated sample, by simply inverting the direction of the electrical drive (anti-electromigration). Although this technique seems to work fairly well for elemental materials,[35, 36, 50, 52, 210, 238] its success in YBCO has shown to be rather limited.[29] In order to illustrate this effect, starting from the EM sample (inset of Figure 3.3(b)) we invert the polarity of the voltage in such a way that now the right bridge corresponds to the cathode side and the left bridge to the anode side. Subsequently, we run an anti-electromigration while simultaneously acquiring optical images. A selected set of these images is presented in Figure 3.7(a-f) while panel (g) shows the evolution of $R(I)$ during the EM process. A complete video can be found in Annex A. At first sight, these images confirm that the previously affected areas due to the EM are not recovered by the anti-EM process. Instead, a new affected region of depleted oxygen extends toward the right (cathode) side. A closer look into the data actually reveals some partial healing effect. By taking differential images, *i.e.* subtracting consecutive images (Figure 3.7(h-i)), one can clearly see a pair of dark (oxygen rich) and bright (oxygen depleted) zones. In other words, the initial affected area caused by the EM shows partial healing during anti-EM.

The fact that this healing effect takes place in a restricted zone might indicate loss of oxygen from the sample.

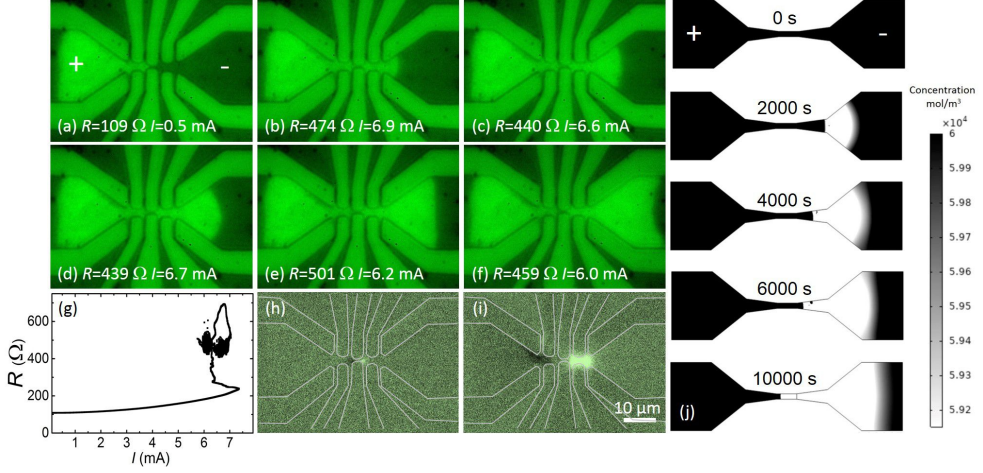


Figure 3.7: (a-f) Optical microscopy images showing the progression of the oxygen depleted zones (bright) during the anti-electromigration process. The time elapsed between consecutive images is about 15 minutes. (g) Resistance of the central bridge of a YBCO device as a function of the circulating current during the anti-electromigration process. The labels (R, I) in panels (a-f) correspond to the coordinates along the $R(I)$ curve shown in panel (g). (h-i) Differential images illustrating the partial healing (black spots) due to anti-electromigration on a previously affected area by electromigration. The gray curve is a guide to the eye delineating the transport bridge. Panel (j) shows simulation images of the evolution of the oxygen concentration starting from the pristine state, as the voltage is ramped up with time.

Experimental measurement of oxygen tracer diffusion in the $a - b$ plane of single-crystal YBCO [170] suggests an activation energy $E_0 = 0.97 \pm 0.03$ eV for the oxygen atoms whereas the in-plane oxygen diffusion constant has been measured to be $D = 1.4 \times 10^4 \exp(-E_0/k_B T) \mu\text{m}^2\text{s}^{-1}$ with k_B the Boltzmann constant. Finite element simulations of the heat transport indicate that the local temperature during the EM can be as high as 700 K for which $D \sim 1.45 \times 10^{-3} \mu\text{m}^2\text{s}^{-1}$. For the images in Figure 3.7 the sample was exposed to electrical stress during $\tau = 5000$ s, thus giving a diffusion length $L = \sqrt{D\tau} \sim 2.6 \mu\text{m}$ whereas the actual experimental progression in the time scale of the experiment is about 30 μm . Several effects can be invoked to justify this discrepancy. Firstly, complementary measurements [173] have indicated that the diffusion constant D_b for oxygen motion along the crystallographic b -axis is at least 100 times larger than the diffusion constant in the a direction which could account for the observed rapid diffusion. Secondly, a higher diffusion

has been reported in Ref. [71] resulting from an applied electric field. Thirdly, oxygen motion is accelerated by defects such as twin boundaries and/or grain boundaries.

Figure 3.7(j) shows FEM results of the evolution of the oxygen concentration as the voltage is ramped up with time on the left contact whereas the right one remains grounded. A complete video of the process is published online.[72] As experimentally observed, oxygen vacancies flow from left to right thus generating an oxygen depleted region spreading from right part of the current leads to the middle bridge.

3.3 Samples

Epitaxial 100 nm thick $\text{YBa}_2\text{Cu}_3\text{O}_{7-\delta}$ films were grown with the c -axis aligned perpendicular to the film plane, either by chemical solution deposition[219] or by pulsed laser deposition on LaAlO_3 single crystal substrates. For both type of deposition methods, similar results were observed and therefore no distinction have been made here. For ensuring ohmic electrical contacts, 200 nm thick Ag electrodes were sputtered and annealed by heating in an oxygen-rich environment. Films were patterned to form narrow bridges with a 4-point geometry, for both resistivity and Hall-measurements, by photolithography followed and dry ion-beam etching. More than 20 samples with sharp superconducting transitions at $T_c \sim 90$ K, were analyzed for the work in this chapter.

3.4 Modeling

Simulation of the oxygen diffusion process has been modeled by using the partial differential equation solver developed by COMSOL Multiphysics® modeling software, as discussed in Sec.2.4. We used a 2D domain with a three-bridge structure, mimicking the experimental geometry considered in the experimental pattern shown in Figure 3.1(b). Two top contacts were located at both ends of the simulated domain in order to electrically polarize the sample. The right contact (anode) was grounded while a step function from zero bias voltage was applied to the left contact (cathode).

In the oxygen diffusion framework we are considering two driving forces, a first one associated to the gradient of the chemical potential depending on the concentration of diffusing oxygen ions ($D\nabla c$, with D the diffusion coefficient and c the oxygen concentration) and a second one associated to the

electrical field ($-\nabla V$). Note that in this iteration we employ a simpler model without the variable x :

$$\dot{c} = \nabla \cdot (D\nabla c + zuFc\nabla V), \quad (3.1)$$

with $z=-2$ the oxidation state of oxygen ions, u the Nernst-Einstein ratio ($u = D/RT$ with R the gas constant), and F the Faraday constant. We assume a diffusive regime in a continuous medium approximation with oxygen redistribution within the closed system but without external exchange. The effective diffusion coefficient has been considered isotropic although varying in space through the dependence of the temperature induced during the electromigration process. We assume a typical thermally activated process $D=D_0\exp(-E_0/k_B T)$, with $D_0= 1.4 \cdot 10^4 \mu\text{m}^2\text{s}^{-1}$ and $E_0 = 0.97 \text{ eV}$. [170] The temperature distribution along the bridge has been evaluated according to the values obtained during the electromigration process as shown in Annex A. The oxygen concentration limits have been established according to the maximum ($\delta=0$) and minimum ($\delta=1$) oxygen doping, considering the volume of the limiting structures, being 66910 mol m^{-3} and 56616 mol m^{-3} , for the orthorhombic and tetragonal phases, respectively. We have started the simulations with an initial underdoped homogeneous oxygen concentration of $c_0 = 60734 \text{ mol/m}^3$ to better visualize the effect of oxygen diffusion through the channel. The electric potential is determined from the constitutive relation $\mathbf{E} = -\nabla V = \mathbf{J}/\sigma$ and the charge conservation equations $\nabla J = q$, with \mathbf{J} the electric current density, σ the electric conductivity and q the electronic charge density. The electric conductivity has been directly correlated with the local oxygen concentration, using a linear function $\sigma(c) = 10^2 \text{ Sm}^{-1}$ if $c < c^*$ and $\sigma(c) = 10^2 + 632(c - c^*) \text{ Sm}^{-1}$ otherwise, which phenomenologically describes the change between the optimally doped and underdoped states. Here $c^* = 61614 \text{ mol m}^{-3}$.

3.5 Summary

To summarize, we have demonstrated the possibility to locally deoxygenate $\text{YBa}_2\text{Cu}_3\text{O}_{7-\delta}$ by applying high current densities in the normal state. The proposed approach complements the widely investigated gate-induced electric field effect in this material. Progressive current-stimulated oxygen diffusion is shown to enable tuning of $\delta(J)$ resulting in rather inhomogeneous distributions of oxygen vacancies. We provide experimental evidence through Hall measurements, micro-Raman and photoconductivity investigations, that the electromigration process allows a selective placement of oxygen atoms. The

induced stoichiometry modulations become more stable (*i.e.* irreversible) as the excess current with respect to the onset of electromigration, increases. The affected areas can be directly visualized by optical and electronic microscopy. This method represents a powerful alternative to locally fine tune the charge carrier density in cuprates.

Electrically-driven oxygen vacancy aggregation and displacement in YBCO films

Based on: S. Collienne, S. Marinković, A. Fernández-Rodríguez, N. Mestres, A. Palau, and A. V. Silhanek, "Electrically-driven oxygen vacancy aggregation and displacement in $\text{YBa}_2\text{Cu}_3\text{O}_{7-\delta}$ films", *Advanced Electronic Materials* **8** (2022), 10.1002/aelm.202101290

Main Contributions: experiment design, electromigration experiments, cryogenic transport measurements, optical and SEM imaging, data interpretation and presentation and writing

Auxiliary Contributions: finite element modeling

Layman's Overview: Modeling Oxygen Diffusion

Having demonstrated the link between the reflectivity of a YBCO film and its oxygenation in Ch.3, in this chapter we focus on testing the reversibility of the process and refining and validating a phenomenological finite element model. The interest here lies in the straightforward comparison between experimentally obtained optical images and the oxygen concentration distribution obtained from our model.

In this chapter we will debut the pulsed excitation protocol (See Ch.2), where we stress our thin films by applying a current stress in short pulses. This contrasts with the previous approach where the stress was applied continuously. By allowing the sample to cool before characterization, we can avoid biases stemming from Joule heating seen in the continuous PID protocol of Ch.3.

Combining direct visualization of current-induced oxygen migration through optical microscopy and finite element modeling of driven oxygen diffusion, in the previous chapter, we were able to estimate the average activation energy of oxygen motion in the crystallographic ab -plane of c -axis oriented polycrystalline $\text{YBa}_2\text{Cu}_3\text{O}_{7-\delta}$ films. In this chapter, experiments and modeling are compared side-by-side for the case of constant current electromigration as well as for a train of current pulses of varying amplitude (see Fig.2.7). The simulations reproduce the induced resistance changes after electromigration and confirm a high degree of spatial inhomogeneity in the stoichiometry. Assuming a temperature and oxygen concentration dependent resistivity, we are able to capture the change of superconducting critical temperature, normal state resistance, and the development of multistep transitions as a function of the electromigration history. The simulations are then applied to scrutinize the influence of activation energy, disorder in oxygen content and initial oxygen concentration on the electromigration process.

4.1 Introduction

The variation of oxygen concentration in YBCO mostly occurs in the O(1) sites of the CuO chains along the crystallographic b -axis. In the superconducting orthorhombic phase ($\delta \approx 0$), if the O(1) atom migrates to a neighboring vacant O(5) site, it will find a channel along the b -axis direction with essentially no diffusion barrier. [174] It is expected that the associated activation energy E_a will depend strongly on the amount of oxygen atoms per unit cell, with E_a lowering as the number of available sites (i.e. δ) increases. This has been indeed experimentally confirmed in YBCO crystals for which it was reported $E_a = 1.3$ eV for $\delta = 0$ and $E_a = 0.5$ eV for $\delta = 0.38$. [229] Concomitant isotopic

^{18}O tracer diffusion measurements by Rothman *et al.*[170] indicated a value of $E_a = 0.97$ eV in the ab -plane of bulk YBCO pellets. Similar value was reported for YBCO single crystals with stoichiometry $\delta = 0.5$ by Veal *et al.* [228] through thermal annealing process. Soon after, Choi *et al.* [239] calculated the oxygen tracer diffusion coefficients using the cluster variation method in conjunction with the path probability method for a perfect lattice and showed that activation energies are significantly dependent on the oxygen density and the degree of long-range order, with $E_a = 0.8$ eV in the tetragonal phase and $E_a = 1.2$ eV in the orthorhombic phase. The fact that the activation energies for the oxygen diffusion decrease with decreasing oxygen content was also confirmed in laser ablated thin films by Krauns and Krebs.[240] In Ref.[241] a migration energy as low as 0.3 eV has been calculated for oxygen ions in the ab -plane using a shell model for the orthorhombic phase. A more in-depth investigation of oxygen tracer diffusion in untwinned single-crystalline YBCO showed that the diffusion along the b direction can be at least 100 times faster than diffusion along the a direction.[173] In all cases, diffusion along c axis was reported to be substantially slower than within the ab plane.

The dispersion observed in the reported values of the activation energy can be partially accounted for by the fact that a distribution of activation energies depending on the local environment is to be expected.[198] More importantly, several paths of oxygen diffusion may coexist with diffusion along the surface, the grain boundaries, and twin boundaries dominating over lattice diffusion as demonstrated by comparing single crystals to polycrystalline YBCO.[155] This has been recently demonstrated via molecular dynamics simulations by Wang *et al.* [242] where it was shown that oxygen diffusion in YBCO can be enhanced in grain boundaries with an activation energy exponentially decreasing with the grain boundary angle.

In general, the experimental investigations presented above rely on diffusive processes induced by thermal annealing under controlled environmental conditions. The current driven diffusion presented in Ch.3 allows doping modulation in YBCO *in situ*.[72] This technique has been implemented to scan the entire temperature-hole concentration phase diagram one and the same sample. [59] In this case, the agglomeration of oxygen vacancies manifests itself as a zone of higher reflectivity thus permitting to track the temporal evolution of the affected area by optical microscopy.

In this chapter, we provide optical microscopy inspection of oxygen vacancy migration stimulated by high current densities and complement this study with finite elements modeling in order to quantitatively assess the

effect of effective activation energy for oxygen diffusion. We demonstrate that the oxygen disorder induced by electromigration can take place simultaneously in several spots along the transport bridge. Low frequency AC electromigration illustrates a limited reversibility process which is accentuated if a concentration-dependent activation energy is introduced. The modeling is able to capture the evolution of the superconducting transition after electromigration as well as the oxygen vacancy mapping.

4.2 Results and Discussion

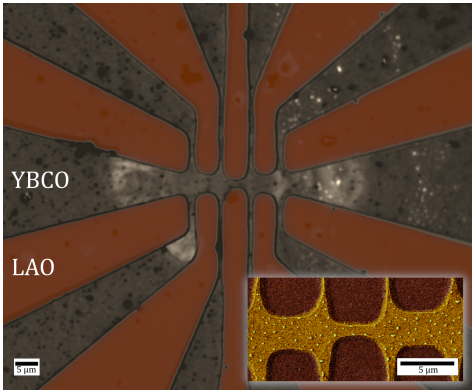


Figure 4.1: Optical microscopy image of the entire device after electromigration. The inset shows a scanning electron microscopy image of the three central bridges.

The investigated superconducting samples are YBCO thin films patterned into a multiterminal bridge shape as shown in Figure 4.1. Eight voltage probes are used to individually assess the electrical response of the three bridges connected in series. The length \times width of the two side bridges is $5 \mu\text{m} \times 3 \mu\text{m}$, whereas for the inner bridge the dimensions are $3 \mu\text{m} \times 1 \mu\text{m}$. All films exhibited superconducting critical temperatures $T_c \sim 85 \text{ K}$ consistent with $\delta \sim 0.2 \pm 0.05$ defined as the maximum slope of the resistance vs temperature $R(T)$ curve.

4.2.1 Optical and electrical probing of oxygen vacancy migration

The electromigration process was achieved through two different approaches, namely (i) constant current measurements and (ii) amplitude-dependent current pulses as those discussed in Sec.2.2.2.

DC electric stress

For the constant current measurements, a DC current is maintained by the source and the resistance R of each of the three bridges is independently monitored as a function of the time elapsed t . The inset in the left panel of Figure 4.2 shows a scheme of the current polarity imposed and the color code used to indicate the response of each bridge. At 3 mA (corresponding

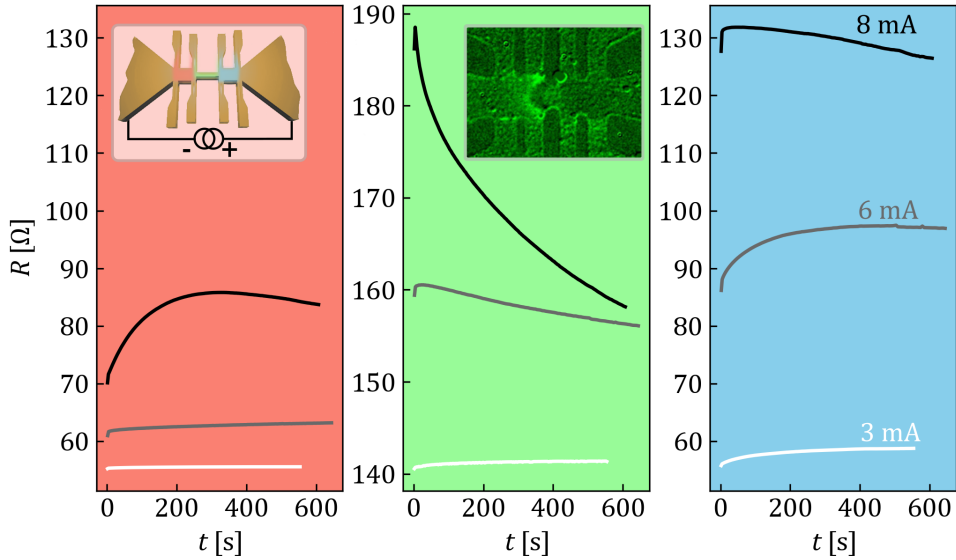


Figure 4.2: Experimental evolution of the resistance as a function of time under continuous electrical stress for the left, central, and right bridges. The inset in the left panel shows the polarity of the current source and the color code associated to each bridge. An optical microscopy image of the electromigrated YBCO device is shown as inset of the central panel. Higher reflectivity (brighter zone) reveals the region with oxygen deficiency. Measurements performed at room temperature and in ambient conditions.

to 3 MA cm^{-2} in the central bridge), a small increase of the resistance as a function of time is observed in the three bridges. When the current is increased to 6 mA the initial resistance increases substantially due to Joule heating. Surprisingly, while the left and right side bridges exhibit an increase of resistance with time, the central bridge shows a progressive decrease. Further increasing the current to 8 mA, shows that all three bridges reached a regime of decreasing resistance with time. A real time evolution of the optical microscopy images is published online[74] for a similar device. In order to understand this behavior, it is necessary to invoke the displacement of oxygen vacancies from right to left and a simultaneous counterflow of oxygen ions. Within this scenario, the increase of the resistance with time corresponds to the propagation of the front consisting of an area of depleted oxygen in between the corresponding voltage probes. Eventually, the trail of that front is reoxygenated and leads to a decrease of resistance. An optical image of the oxygen-poor front (brighter color) obtained few seconds after

applying 8 mA is shown in the inset of the middle panel. The origin of the observed increase of reflectance when the oxygen content decreases has been investigated by Kircher et al.[230] by measuring the dependence of the dielectric tensor on the oxygen stoichiometry. Additional experiment with lower, alternating DC polarity are available in Annex.B.2.

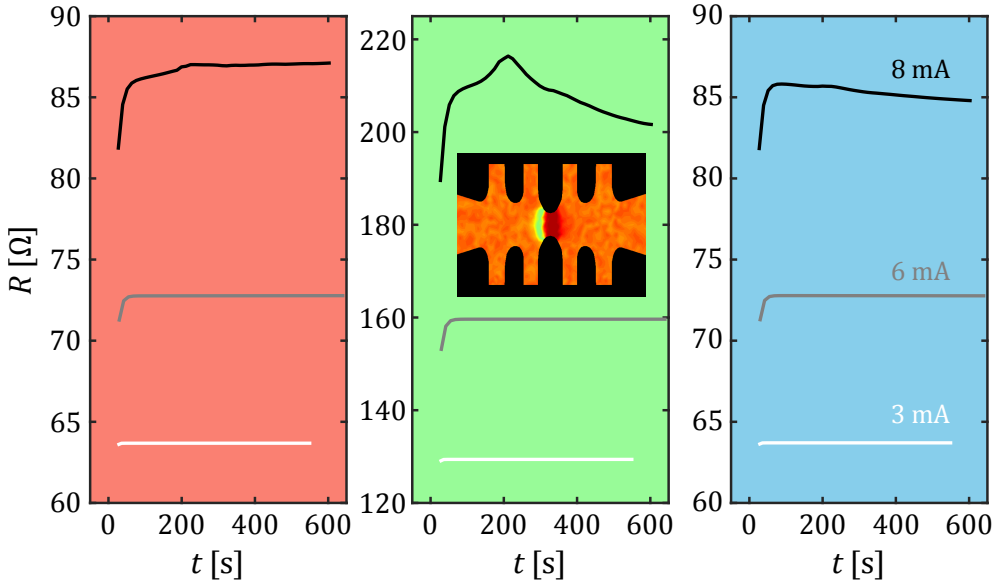


Figure 4.3: Evolution of the resistance as a function of time under continuous electrical stress for the left, central, and right bridges as obtained by finite-element modeling with $E_a = 0.7$ eV, $x_0 = 0.76$, $x_{min} = 0.5$, $x_{max} = 0.95$ and $\delta x_0 = 5\%$. Inset in the middle panel shows a mapping of the oxygen distribution (yellow / green color indicates the oxygen depleted zone and red color the oxygen rich zone).

Figure 4.3 shows the results obtained from numerical simulations for similar continuous current stress. The initial reduced concentration (see Sec.4.4) $x_0 = 0.76$ has been chosen so as to approach the experimentally determined $R(T)$ of the bridges. In addition, a disorder in oxygen distribution of $\delta x_0 = 5\%$ with respect to the mean value x_0 , has been assumed. In Ch.3 it has been shown that after electromigration part of the bridge becomes deoxygenated down to a certain minimum value x_{min} whereas other zones are oxygenated up to an upper value x_{max} . This can be understood as a consequence of a concentration-dependent activation energy $E_a(x)$. In the present case, we have taken $x_{min} = 0.5$ and $x_{max} = 0.95$.

For 3 and 6 mA the simulations show an initial resistance increase fol-

lowed by a very stable state. The fact that this stability plateau is reached in much shorter time-scale than in the experimental measurements, suggests that in the experiments the entire substrate is heated by the current whereas in the simulations we assume that the bottom of the substrate is at a fixed temperature. For 8 mA DC current, the simulations reproduce the observed experimentally trend and confirm that the initial increase of resistance produces a propagating front of depleted oxygen distribution, whereas the resistance decrease is caused by an oxygenation process. The inset in the middle panel of Figure 4.3 shows a mapping of the oxygen distribution obtained under the same conditions as the snapshot shown in the inset of Figure 4.2. The similarities are apparent: a bright arc-shaped front corresponding to the oxygen depleted zone emerges from the central bridge, with a counter-propagating red color front indicating excess oxygen. Note that the optical images clearly reveal the oxygen depleted zone, but are less sensitive to the zone where oxygen content has increased.

AC current stress

The above described approach consisting of a constant bias current suffers from uncontrolled modifications to the sample and eventually by thermal runaway causing permanent damage to the bridges. In addition, it is inconvenient for imaging since the oxygen diffusion proceeds during the acquisition time of the CCD camera. To avoid these drawbacks, we resort to current pulsed measurements following the protocol shown in Figure 4.4(a) and previously described in Sec.2.2.2. Two consecutive probe current pulses of constant amplitude ($I_{probe} = 10 \mu\text{A}$) and opposite polarity of 10 s duration are averaged to obtain the total resistance of the sample, i.e. in between the external voltage contacts as shown in Figure 4.4(b). The probe pulses are followed, after 5 s, by 10 s pulsed current of variable amplitude I_{PLS} . After each pulse, the current is cut off for 5 s, much longer than the characteristic time of thermal relaxation ($\sim \mu\text{s}$), [243, 244] to allow the sample to cool down to bath temperature. The panel (c) shows the oscillating I_{PLS} with a maximum amplitude of 8 mA. In the panel (d) the evolution of the total resistance of the device resulting from the oscillating train of pulses is shown. Black circles correspond to the total resistance after the current pulse has been applied, i.e. remanent resistance (left axis) whereas the white circles correspond to the total resistance during the current pulse (right axis). The latter exhibits a parabolic shape resulting from the Joule heating and the temperature dependent resistance of the device whereas the former remains unaffected by the Joule heating and represents a more convenient tool for

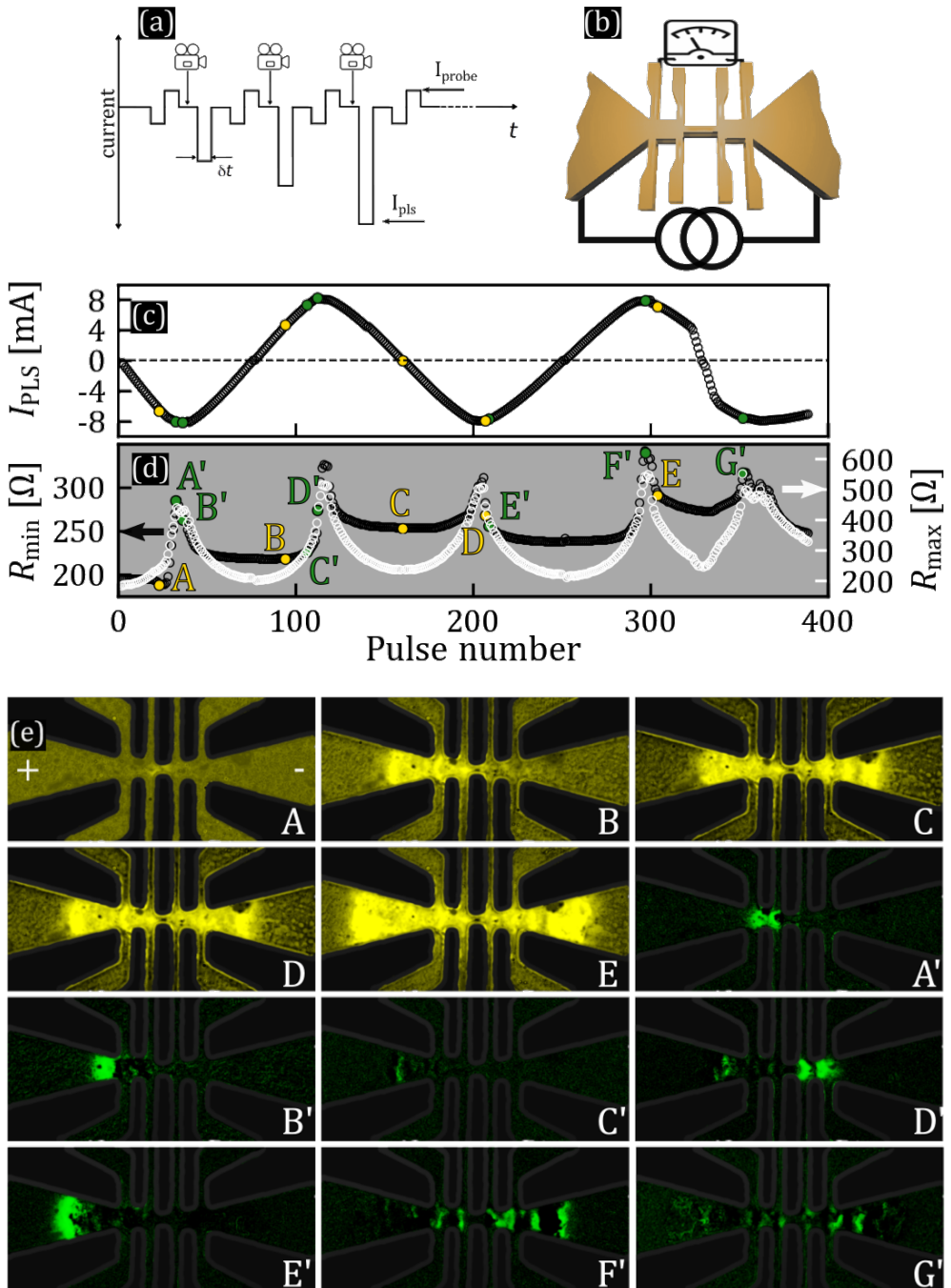


Figure 4.4: See next page.

Figure 4.4: (a) A bipolar I_{probe} pulsed current is used to monitor the sample resistance whereas a $I_{PLS} \gg I_{probe}$ of variable amplitude triggers the electromigration process. Optical microscopy images are acquired after each probe pulse. (b) The total sample resistance picked up by the external electrodes is monitored before and during the I_{PLS} excitation. The panel (c) shows the evolution of I_{PLS} and the panel (d) the resulting evolution of sample resistance before (black points, left axis) and during (white points, right axis) the application of I_{PLS} . Representative optical microscopy images at different stages of the electromigration process are shown in (e). Images labeled A-E acquired at the corresponding yellow points in panel (c), provide direct optical contrast of the affected areas. Images labeled A'-G' acquired at the corresponding green points in panel (c), provide differential optical contrast of the affected areas.

unveiling the irreversible changes induced by the electromigration process.

For current pulses up to $I_{PLS} \sim 6$ mA, the remanent resistance of the device remains invariable, meaning that the sample has not undergone any modification. For $6 \text{ mA} < I_{PLS} < 7 \text{ mA}$, a slight decrease of the sample resistance is observed. As demonstrated by Moeckly *et al.*[198] this effect cannot be solely ascribed to a thermal annealing process resulting from Joule heating but in addition, a current stimulated redistribution of chain oxygen vacancies needs to be invoked. This initial healing of the sample is followed by a rapid increase of the resistance associated to long-range oxygen migration. Interestingly, when I_{PLS} starts to decrease, the sample undergoes a healing process, even though the current flow does not change polarity. The maximum of resistance recovery is obtained for $I_{PLS} \sim 0$. Note that the recovery is incomplete, meaning that the sample experiences irreversible deterioration.[196] Inverting the current polarity does not provide much further healing but rather leads to another increase of resistance followed by a plateau. As current amplitude alternates, a similar sequence of resistance peak-plateau stages develops with the general trend towards an overall progressive deterioration of the device. This observation suggests that low frequency AC-excitations may represent an effective way to increase the resistance of the transport bridge in a controlled fashion.[59, 202]

Let us now analyze the induced inhomogeneous oxygen distribution as revealed by in situ optical microscopy. A selected set of images is presented in Figure 4.4(e) corresponding to different stages during the electromigration cycle process. A complete animation is published online in the Supplementary Information with Ref.[74]. For images A to E taken at the yellow points

indicated in panel (c), the image corresponding to the initial pristine state has been subtracted in order to improve the contrast. Point A corresponds to the onset of electromigration which becomes visible at the central bridge, where the current density and the local temperature are the largest. Point B, taken at the plateau of resistance, shows the extent of the oxygen depletion zone (brighter region) obtained after reaching the maximum current amplitude. At this point the resistance of the device has decreased as a consequence of a partial replenishing of oxygen atoms in between the outer voltage probes. Point C is obtained after inverting the current direction and together with the image corresponding to point B, demonstrates the directional character of the electromigration process, with oxygen vacancies moving with hole carriers. In D and E, the affected area has further expanded outside the external voltage probes, and therefore it is not captured by the electrical measurements.

When the current direction is inverted, the change of oxygen content in already affected areas becomes nearly imperceptible in the bright microscopy images. A convenient way to unveil these changes is to subtract consecutive images as shown in frames A' - G' of Figure (e). The point A' is taken at the first maximum of resistance and shows that modification of the oxygen content takes place mainly on the left bridge. Point B' corresponds to the maximum current amplitude and shows that oxygen vacancies are mainly affecting the cathode side (-) which lies outside the outer voltage probes. The fact that the resistance has decreases indicates that in turn, oxygen ions are replenishing the previously oxygen-depleted zone in between the voltage probes. When inverting the current direction (C' and D') the oxygen content changes are rather minor in the already affected areas and more prominent in the unaffected right bridge zone. Images E', F', and G' show that further oxygen displacement in these previously modified regions does not happen locally as it would be the case for a single propagating front but in waves extending throughout the device. The reason for this effect lies on the multiterminal geometry of the sample which induces an inhomogeneous current distribution and hot spots of current crowding (see Annex B.3).

The results of finite element modeling of oxygen diffusion, for the case of pulsed electromigration are shown in Figure 4.5. The same train of current pulses and overall measurement protocol as in the experiment presented in Figure 4.4 are reproduced in the simulation. The parameters used for these simulations ($E_a = 0.4$ eV, $x_0 = 0.76$, $\delta x_0 = 5\%$, $x_{min} = 0.5$, $x_{max} = 0.95$) have been chosen so as to approach the experimentally determined initial $R(T)$ of the device and the extent of affected area. Panels A-E show the oxygen

concentration mappings and panels A'-G' indicate differential changes in the oxygen concentration at selected points during the electromigration process. The resistance oscillations before (black points) and during (white points) the pulse, qualitatively capture the features observed experimentally. The permanent changes in sample resistance start to happen for a current of 6 mA. The decrease of sample resistance at point A, results from the oxygenation of an initially less than optimally doped sample ($x_0 = 0.76$). Note that this reoxygenation takes place mainly at the central bridge where the current density is higher and which contributes the most to the total resistance (i.e. in the pristine state, $\sim 50\%$ of the resistance measured at the outer probes comes from the central bridge). This local minimum is followed by a rapid increase

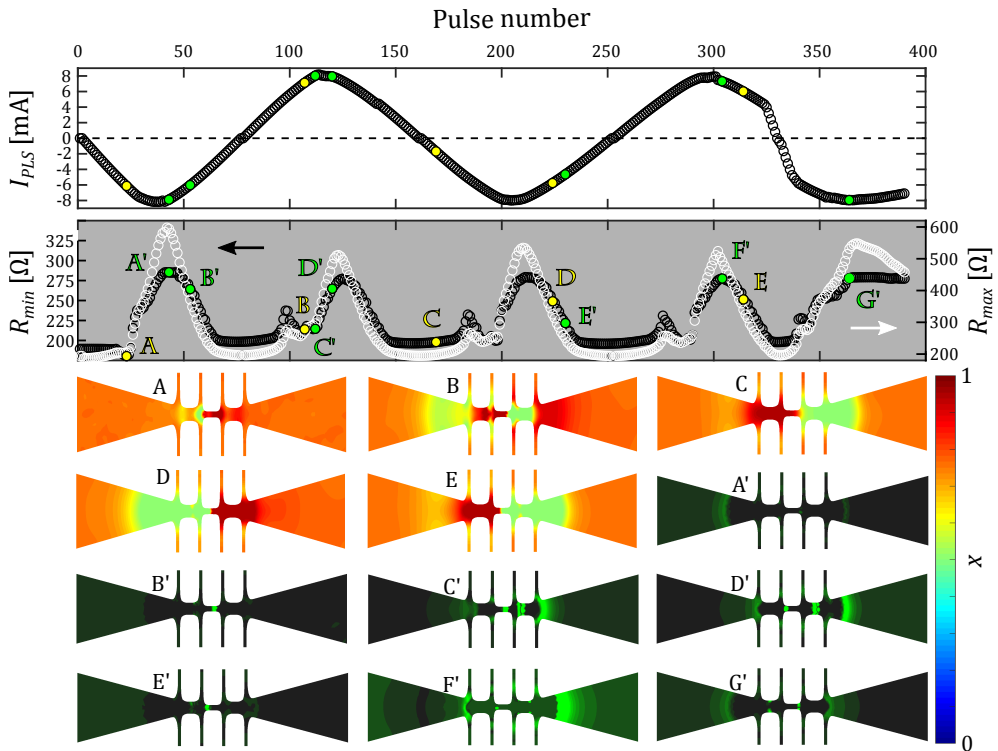


Figure 4.5: Finite element modeling of the resistance and oxygen cartography evolution as a function of an oscillating current pulse I_{PLS} . For the sake of convenience, the I_{PLS} as a function of pulse number already shown in Figure 4.4(c) is replotted here. The simulated R_{max} , R_{min} , oxygen concentration, and differential concentration mappings are to be directly compared with the experimental data presented in Figure 4.4.

of resistance as the oxygen depleted zone propagates to the left side. At the maximum of resistance, the local temperature reaches 671 K. Consistent with the experimental observation, a healing process evidenced by a decrease of resistance occurs when the pulsed current amplitude decreases. We attribute this effect to the thermally activated relaxation process. Indeed, even though the applied current is smaller than that needed to induce electromigration, Joule heating rises substantially the local temperature and induces a relaxation process driven by the pronounced gradient of oxygen concentration that will partially reoxygenate the central bridge. Below certain current threshold no further changes are observed (oxygen diffusion is halted) and a resistance plateau develops. This resistance plateau exceeds the initial resistance of the sample which, implies irreversibility in the electromigration process. Note that the modeling produces a lower irreversibility than the one observed experimentally. This is also visible in the oxygen concentration mapping. Indeed, when comparing points B and C, one can remark that at point C the previously deoxygenated region on the left side of the device has been replenished and reoxygenated. To explain this discrepancy between theory and experiment, one can invoke a concentration dependent activation energy (see discussion below for more details) or simply oxygen loss to the environment due to the high temperatures attained during the electromigration process. The modeling also shows local satellite maxima just before reaching the maximum current amplitude. The origin of this satellite peak is that the high temperature and electric field at the central junction generate a better oxygen mobility and consequently a higher oxygen flux than the neighboring junctions. In the case of a current moving oxygen to the right, this creates an oxygen defect on the left side of the central bridge that cannot be directly supplied with oxygen coming from the left. This temporarily produces an oxygen defect in the central bridge and thus gives rise to an increase in resistance. Interestingly the differential images A'-G' confirm that changes in the concentration during the current reversal take place simultaneously throughout the entire structure instead of in a single propagating front. The complete simulation showing maps of oxygen content, temperature, current density and electrical field of the results discussed in this section is available as an animation in the Supplementary Information of Ref.[74].

Thus far we have investigated the global response of the entire device as the train of pulses oscillate in amplitude driving oxygen vacancies back and forth. We can obtain further insights by analyzing the local modifications operating in each individual bridge. Figure 4.6 shows the $R(T)$ response at the left (salmon panel), central (green panel) and right (blue panel) bridges for

the initial (pristine) state (white dots), after reaching the maximum applied current (point D, gray dots) and after reversing the polarity of the current up its maximum value (point F, black dots). Some representative optical microscopy snapshots for the points indicated as A,B,...,F are shown. As evidenced by the snapshot D, the maximum applied current (from right to left) gives rise to a substantial diffusion of oxygen vacancies, way beyond the outer voltage contact. After this electromigration run, we observe that the right bridge exhibits a reduction of the normal state resistance and a slight increase of the superconducting critical temperature. The central bridge also exhibits a decrease of the normal resistance which is concomitant with a slight increase of T_c , whereas the left bridge shows increased normal state resistance and a double step transition. By inverting the applied current polarity, thus replenishing of oxygen at the left bridge and inducing oxygen vacancy displacement towards the right bridge, a healing of the resistance of the left bridge and a clear deterioration of the conducting properties at the right bridge are observed. This is consistent with the optical image shown in panel F.

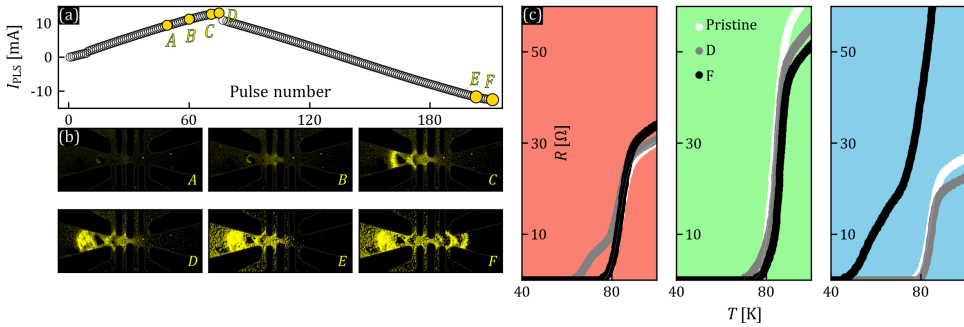


Figure 4.6: (a) Amplitude of the current pulse I_{PLS} as a function of pulse number. (b) Optical microscopy images corresponding to the points labeled in panel (a). The brighter yellowish zones correspond to oxygen depleted areas. (c) Resistance vs temperature showing the superconducting transition at the left (salmon panel), central (green panel), and right (blue panel) bridges, respectively. The response of the pristine sample is shown with white points, after reaching maximum current amplitude is shown with gray data points, and after reaching maximum current of opposite polarity is shown with black points.

As shown in Figure 4.7, the numerical modeling, assuming similar conditions as in the experiment, is able to qualitatively capture most of the features and trends observed experimentally. Note that the simulations predict that

both central and left bridges should be severely affected by the electromigration process, exhibiting a double-step transition. This is in agreement with measurements obtained by controlled electromigration as reported in Figure 3.3 and Figure A.2. Nevertheless, some discrepancies between the experiment and the model can be pointed out. Namely, (i) the amplitude of the resistance and critical temperature changes differ and (ii) the observed healing effect upon current polarity reversal is less pronounced than predicted numerically. As we have stressed above, these discrepancies might arise from important ingredients that are not taken into account in the present model, such as the effect of oxygen chain ordering, oxygen content-dependent activation energy and loss of oxygen into the environment.

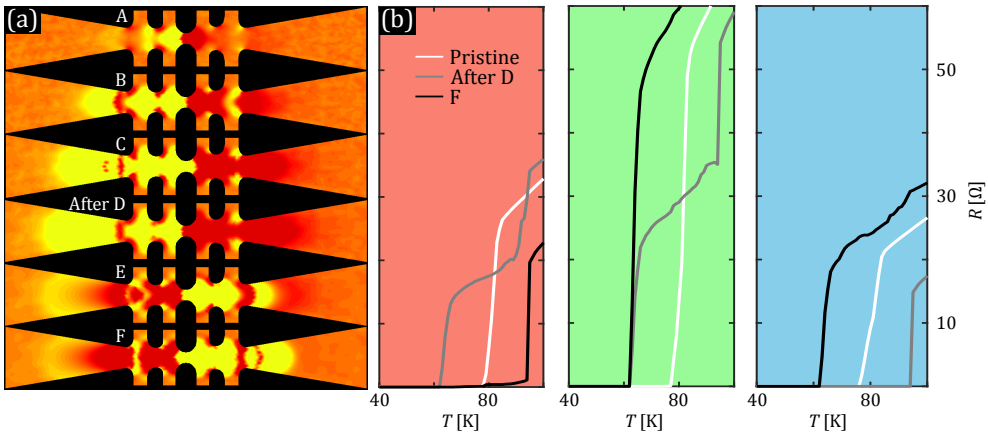


Figure 4.7: Panel (a) shows the simulated oxygen maps for the same points A \rightarrow F as shown in Figure 4.6(a) except for the fourth point (formerly D) which is now taken after D. The red and yellow colors correspond to oxygen-rich and oxygen-poor areas respectively. (b) $R(T)$ curves for the left, center and right bridges. The color convention used is the same as in Figure 4.6(c). The parameters for these simulations are $E_a = 0.7$ eV, $x_0 = 0.76$, $x_{min} = 0.5$, $x_{max} = 0.9$ and $\delta x_0 = 5$ %.

Effect of modeling parameters

Now that we have validated the proposed numerical model through direct comparison with experiments, it is interesting to further scrutinize the influence of the different parameters involved in the model on the electric response of the device and the spatial extent of oxygen diffusion. To that end, in Figure 4.8 we monitor the resistance at remanent (i.e. after each current pulse) R_{min} and during the pulse R_{max} as a function of a pulsed

current amplitude that increases linearly from zero and reaching a maximum value of 8 mA at pulse 40 and then decreasing linearly down to zero at pulse number 80. Panels (a) and (b) along with snapshots A-E show the influence of the activation energy E_a . For $E_a \geq 0.4$ eV the electromigration first induces a small resistance drop before leading to a resistance increase, consistent with the experimental findings. As expected the larger E_a the higher the current density needed to trigger electromigration. In addition, as E_a decreases the maximum resistance achieved increases and consequently so does the Joule heating. Therefore, for lower E_a the attained highest temperature along the bridge increases (panel (b)) and the oxygen diffusion further expands into the leads (snapshots A-E).

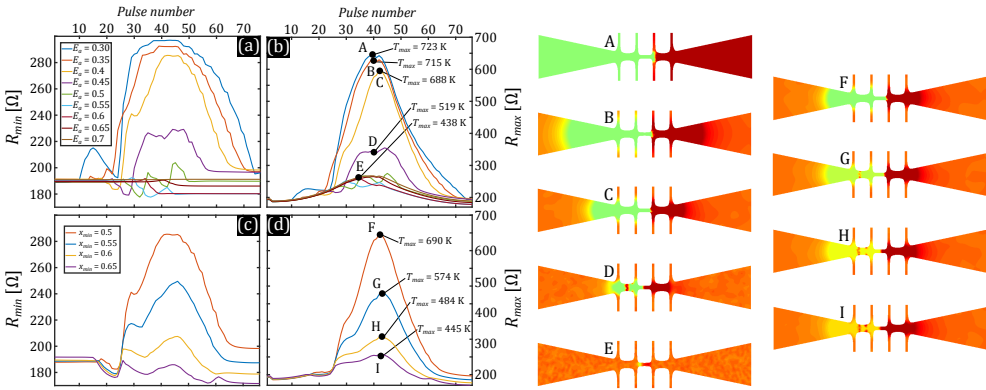


Figure 4.8: The evolution of R_{min} and R_{max} for different activation energies are given in panels (a) and (b) respectively (E_a is given in eV). The other parameters remain unchanged: $x_0 = 0.76$, $x_{min} = 0.5$, $x_{max} = 0.95$ and $\delta x_0 = 5\%$. Panels (c) and (d) show R_{min} and R_{max} for several x_{min} and constant activation energy $E_a = 0.4$ eV. The snapshots on the right show the oxygen distribution for the corresponding points A - I indicated in panels (b) and (d). The maximum attained temperatures are shown in panels (b) and (d).

Figure 4.8 (c) and (d) show the resistance change when x_{min} is varied while the rest of the parameters remain constant. As a reminder, limiting the amplitude of the reduced concentration x is a zeroth-order approximation to account for a concentration-dependent activation energy. Allowing to access smaller values of oxygen concentration leads to more pronounced modifications of the resistance and higher temperatures (panel (d)) although not major modifications are observed in the spatial extent of the diffusion (snapshots F-G). Interestingly, we have found that modifications on the parameters maximum oxygen concentration x_{max} , the initial oxygen concentration x_0 , and

the amplitude variation around the mean value δx_0 have minor impact on the final state (see Annex B.5). In brief, the activation energy and the lowest achievable oxygen concentration are the key parameters ruling the extent of the oxygen diffusion. This finding suggests that the activation energy should depend on the actual oxygen concentration.

Oxygen concentration dependent activation energy

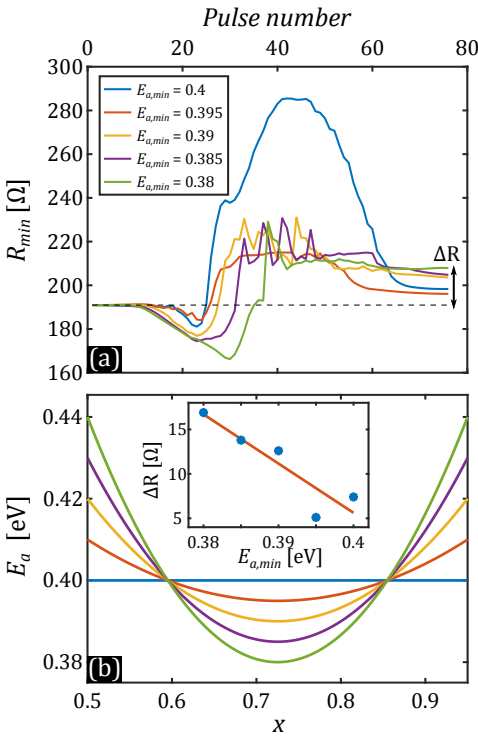


Figure 4.9: Panel (a) shows the temporal evolution of R_{min} for the different $E_a(x)$ profiles given in panel (b). The observed correlation between the irreversibility parameter $\Delta R = R_{final} - R_{init}$ and the lowest value of the activation energy is given as the inset of panel (b). The others parameters are $x_0 = 0.76$, $x_{min} = 0.5$, $x_{max} = 0.95$ and $\delta x_0 = 5\%$. The value of the applied current corresponds to the first 80 pulses of the Figure 4.5.

The extended mobility of oxygen in YBCO is, as mentioned above, greatly due to the presence of vacant sites in close proximity to the moving atoms, allowing for a less energetic diffusion mechanism by interstitials in comparison to substitution mechanisms.[245, 246] This can aid in understanding why many reports, including those mentioned in the introduction, show a smaller diffusivity of O with lesser oxygen content. A good indicator of the oxygen ordering in many complex oxides are the elastic properties, accessible via acoustic relaxation measurements as shown in the work of Cannelli *et al.*[247] The elastic energy loss of YBCO with variable δ is shown to be distinct and to include separate structural phase transitions, that occur at varying temperatures. The same authors show that, as a function of oxygen content, the intensity of the three identified structural phase transition peaks shift,[167] with two of them, appearing at 400-600 K being characteristic of orthogonal YBCO and tetragonal YBCO having its characteristic peak at significantly lower temperatures. The observed elastic energy loss is due to oxygen diffusion and ordering in the orthorhombic lattice, and the activa-

tion energy of this process (~ 1.1 eV) is higher than expected as one must take into account the restructuring of the whole orthorhombic oxygen chains to accommodate further oxygen into the lattice. This is in agreement with the idea that twinning in optimally-doped YBCO is a way to relieve strain from the highly non-stoichiometric structure of the material. Seeing the increase in E_a for both lower (as diffusion by substitution is more energetically demanding) and higher oxygen levels (due to orthorhombic oxygen chain restructuring), one could make an argument for a parabolic shape of the oxygen diffusivity in the material, as has been seen for similar perovskite oxides by Yoo *et al.* [169] Looking for a good first approximation to model the experimental data, we will now assume that our mobile oxygen has a peak diffusivity somewhere in the non-stoichiometric region. Therefore, we propose in this section to investigate the effect of a parabolic $E_a(x)$ by imposing that the average value over the allowed range of x is constant and equal to 0.4 eV. The lowest value of the activation energy $E_{a,min}$ allows to label the different profiles.

Figure 4.9(a) shows the evolution of R_{min} versus time for the profiles of $E_a(x)$ given in Figure 4.9(b). We observe that the final resistance increases as $E_{a,min}$ decreases. This result can be interpreted as follows: in the initial state the homogeneity of the oxygen concentration also implies homogeneity of the activation energy (close to the minimum of the parabola). The central bridge, where the electric field and temperature peak, will quickly generate an asymmetric distribution of oxygen and consequently increase the activation energy in the left and right bridges which will have a reduced mobility when the current changes polarity. This difference in mobility implies different oxygen concentrations and therefore different resistances between the final and initial states. We therefore define the parameter $\Delta R = R_{final} - R_{init}$ (see Figure 4.9(a)) as an indicator of irreversibility. The evolution of this parameter as a function of $E_{a,min}$ shown in the inset of Figure 4.9(b) indicates that an inhomogeneous activation energy accentuates the irreversibility for the oxygen transport. This finding suggests that in order to explain the observed irreversible response of the electromigration process a concentration-dependent activation energy should be invoked. Nonetheless, other effects such as oxygen loss could also play an important role.

4.3 Samples

Epitaxial 50 and 100 nm thick $\text{YBa}_2\text{Cu}_3\text{O}_{7-\delta}$ films were grown with the c -axis aligned perpendicular to the film plane, by pulsed laser deposition

on LaAlO₃ single crystal substrates. For ensuring ohmic electrical contacts, 200 nm thick Ag electrodes were sputtered and annealed by heating in an oxygen-rich environment. The films were patterned via photolithography and dry ion-beam etching into multiterminal triple constrictions.

4.4 Modeling

The oxygen diffusion model is mostly constructed as described previously in Sec.2.4. The heat equation takes the form:

$$\rho_m C \frac{\partial T}{\partial t} = \kappa \nabla^2 T + \rho(x, T) \mathbf{j}^2 \quad (4.1)$$

where ρ_m is the density in kg m⁻³, C the specific heat capacity in J kg⁻¹ K⁻¹, T the temperature in K, κ the thermal conductivity in W K⁻¹ m⁻¹. The second term on the right-hand side of equation (4.1) represents the Joule heating and involves the resistivity of the material which depends on both the concentration and local temperature. The functionality $\rho(x, T)$ imposed in the model is taken from experimental values reported in Ref.[156] (see Figure 4.10(a)). For $T > 300$ K, we assume a linear dependent resistivity $\rho(x, T) = [1 + \alpha(T - T_{ref})]\rho(x, T_{ref})$ with $\alpha = 5 \times 10^{-3}$ K⁻¹ determined by $R(T)$ measurements and $T_{ref} = 300$ K.

Finally, the Poisson equation is solved to obtain the electric potential distribution in the sample:

$$\nabla^2 V = 0 \quad (4.2)$$

Note that the right-hand term of the equation is set to zero in order to guarantee charge neutrality throughout the device. The electric field $\mathbf{E} = -\nabla V$ is related to the current density \mathbf{J} by Ohm's constitutive equation $\mathbf{J} = \mathbf{E}/\rho(x, T)$ and does not take into account the ionic current whose contribution is negligible.[71] The solution of the system of equations with proper boundary conditions is obtained for the exact geometry of the real sample, using the finite element software COMSOL.[224] A top view of the layout and the mesh used for FEM simulations is shown in Figure 4.10(b). Due to the small thickness/width aspect ratio, the equations are only solved for 2D for the YBCO layer while only the heat equation (4.1) is solved for the substrate. The values of the thermal coefficients are listed in the Table 4.1. Slightly different thermal coefficient as reported in refs.[248, 249] lead to similar results.

Having a system of coupled equations combined with logarithmic behavior of resistivity with concentration makes simultaneous resolution particularly demanding. In order to speed up the numerical calculations, an iterative

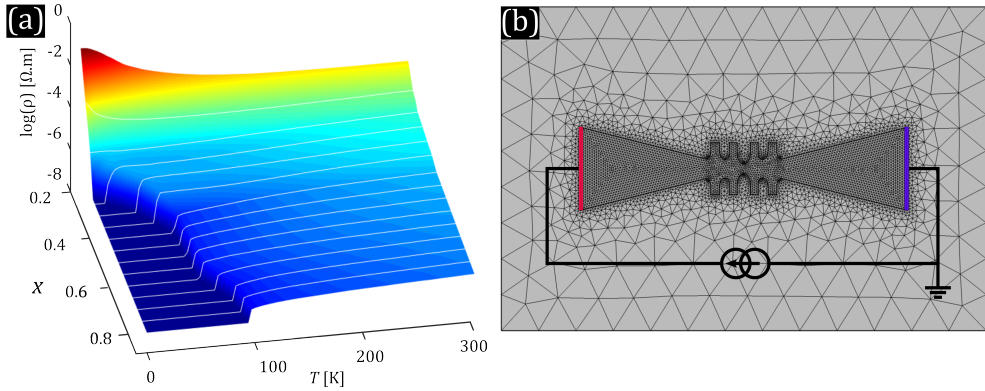


Figure 4.10: (a) Linear interpolation of $\rho(x, T)$ data extracted from Ref.[156]. For values of T above 300 K, a single α value is derived from an $R(T)$ curve for all oxygen concentrations. (b) Top view of the layout and the mesh used for FEM simulations. The positive (red) terminal is simulated as a current source while the negative (blue) terminal is connected to ground. The value of the current injected at each time step of the simulation is dictated by the experimental values.

	ρ_m [kg m ⁻³]	C [J kg ⁻¹ K ⁻¹]	κ [W K ⁻¹ m ⁻¹]
LAO	6520 [250]	450 [250]	11.7 [250]
YBCO	6300 [251, 252]	520 [164, 253]	10 [164]

Table 4.1: Thermal coefficients used as input parameters in COMSOL simulations.

time process with two steps per iteration is used. First, the temperature and potential profiles are evaluated at iteration i assuming x to be constant as determined in the previous iteration $i - 1$. During this step, the temperature dependence of the resistivity is assumed to be the temperature profile from previous iteration. Second, the new spatial distribution of the concentration x is calculated assuming T and V constant. The values T , V and x at the first iteration are given by the initial conditions of the problem. It is worth noting that the model is improved from the iteration in Ch.3 by the fact that the resistivity is temperature and concentration dependent, and that the mesh matches the sample geometry more closely.

4.5 Summary

To summarize, in this chapter we have performed continuous DC and pulsed electromigration on YBCO while simultaneously recording the electrical sig-

nal in a multiterminal bridge and monitoring the oxygen displacement by optical reflectometry . These results are compared to finite element modeling for which current-induced oxygen diffusion is coupled to heat transport, including a temperature and concentration dependent resistivity. The simulations are able to qualitatively and to certain extent quantitatively capture the general trend observed in the experiments (electrical response and oxygen concentration mapping) and allow to estimate the local temperature during the electromigration process and the activation energy associated to the diffusion process. In addition, the model permits us to explore the influence of different parameters such as initial oxygen concentration, oxygen disorder, and activation energy, which would require a colossal effort to address experimentally. These findings might shed light on the recent investigation of DC and AC electromigration in YBCO[59, 202] and could be extended to explore the memristive properties of this material[191] or the electrical doping of $\text{Bi}_2\text{Sr}_2\text{CaCu}_2\text{O}_{8-\delta}$. [58] The close correlation between experiments and theory may encourage further research to explore the predictive power of the modeling to analyze the retention time and endurance of memristive devices based on oxygen motion and the effect of degassing caused by oxygen out-diffusion. Even though the proposed modeling substantially outperform previous attempts,[72] there are nevertheless further refinements that could be considered at expense of preventing accessible interpretation, such as 3D simulation structure, thermomigration, and a term in the model accounting for oxygen loss.

Oxygen Ordering in Untwinned YBCO Films Driven by Electrothermal Stress

Based on: S. Marinković, E. Trabeldo, S. Collienne, F. Lombardi, T. Bauch, and A. V. Silhanek, “Oxygen ordering in untwinned $\text{YBa}_2\text{Cu}_3\text{O}_{7-\delta}$ films driven by electrothermal stress”, *Physical Review B* **107**, 10.1103/PhysRevB.107.014208 (2023) 10.1103/PhysRevB.107.014208

Main Contributions: experiment design, electromigration experiments, cryogenic transport measurements, optical and SEM imaging, data interpretation and presentation, writing

Auxiliary Contributions: finite element modeling

Layman's Overview: Direction Dependent Diffusion

Any crystal is defined by the periodic arrangement of ions in a lattice. We define the smallest repeating unit of the crystal as its unit cell. Properties that behave the same way along any cell direction are called "isotropic", and we expect such behavior from symmetric crystals. YBCO is distinctly different in all three of its crystal directions and the diffusion of oxygen in the material is thus anisotropic.

Using a sophisticated deposition method we fabricate a YBCO film where the differentiation between the crystal directions is strictly maintained. This is important because the crystals, usually, tend to flip orientation along defect planes, in what is known as twinning. Our "untwinned" YBCO films can then be employed in studying the anisotropy in the oxygen diffusion under electrical stress.

By applying the same electromigration protocol and model as described in Ch.4 we show that the anisotropy in the crystal is dominated by the Joule heating effects that originate from the different (anisotropic) resistivities. Due to the much easier diffusion along the channels in one of the YBCO crystal directions we expect easier electrically-induced diffusion along it. However, the lower resistivity while stressing samples oriented along the easy diffusion direction means that the constriction remains cooler. Hence, the easy diffusion direction requires more stress to reach the temperatures needed for the process to start in any significant manner. We conclude that electrically-induced oxygen diffusion in our materials is thermally controlled.

After having validated our model of electrically driven oxygen diffusion in YBCO, in the following chapter we experimentally investigate the displacement of oxygen vacancies at high current densities in highly untwinned $\text{YBa}_2\text{Cu}_3\text{O}_{7-\delta}$ films grown on top of MgO substrates. Transport bridges oriented along the $\text{YBa}_2\text{Cu}_3\text{O}_{7-\delta}$ crystallographic directions [100] (*a*-axis), [010] (*b*-axis), and [110] (45° from principal axes) reveal that the onset of vacancy migration is mainly determined by the local temperature (or equivalently by the dissipated power) rather than the associated activation energy. If this threshold value is exceeded, a clear directional migration proceeds as evidenced by optical microscopy. Concomitant electrotransport measurements show that an intermediate phase, characterized by a decrease of resistivity, precedes long range migration of vacancies. We numerically demonstrate that this intermediate phase consists of a homogenization of the oxygen distribution along the transport bridge, a phenomenon strongly dependent on the activation energy and the initial degree of disorder. These findings provide some important clues to determine the level of order/disorder in $\text{YBa}_2\text{Cu}_3\text{O}_{7-\delta}$ films based on electric transport measurements.

5.1 Introduction

Most studies in oxygen diffusion in YBCO and related perovskites have been performed on non-uniform crystallographically oriented samples which are polluted by twin boundaries regularly exchanging the a and b crystal axes. This condition masks the fact that oxygen diffusion is expected to be largely favored along b than along a -axis. In other words, the activation energy E_a associated to oxygen migration should be strongly dependent on the in-plane direction. Thus far, little is known about the influence of an anisotropic activation energy on the migration phenomenon.

In this chapter, we address this question by investigating the current-stimulated oxygen migration process in 80 % untwinned films with electric current flowing along different in-plane crystallographic orientations. The preferential alignment of the CuO chains along one of the in-plane directions of the substrate results from the large mismatch between the MgO substrate and the YBCO layer[177]. There are two competing mechanisms determining the onset of electromigration. On the one hand, the activation energy is lower along b , thus favoring oxygen diffusion in that direction. On the other hand, migration onset is a thermally activated process triggered by Joule heating first along a direction due to its higher resistivity. We demonstrate that the latter effect sets the onset of electromigration, whereas clear hints of an anisotropic activation energy are seen in the propagation of the oxygen depleted front as well as in the degree of average oxygen ordering induced by the current. Finite elements modeling provide further insights permitting to link the electrotransport measurements with real space oxygen distribution maps.

5.2 Results and Discussion

5.2.1 DC electromigration

Early investigations of oxygen tracer diffusion in untwinned single-crystalline YBCO showed that the oxygen diffusion along the b direction (the direction of the CuO chains) can be substantially faster than diffusion along the a direction.[173] This fact suggests the possibility to achieve current-induced oxygen migration more easily if the transport bridge is oriented along the b -axis than along the a -axis. (see Ref.[74] and references therein). In order to address this question, we have fabricated transport bridges oriented along three crystallographic directions, namely [100] (a in Fig.5.1(a)), [110] (45°

off a in Fig.5.1(b)), and $[010]$ (b in Fig.5.1(c)). The lower row in Fig.5.1 shows the corresponding resistivity vs temperature response obtained at zero applied magnetic field. The fact that the resistivity along the b -axis is the lowest comes from the fact that CuO chains aligned along this direction provide an extra conductive channel absent along a direction. Friedmann et al.[163] reported a ratio $\rho_a/\rho_b \approx 2.2 \pm 0.2$ for untwinned single crystals in a broad temperature range. Assuming a similar value for a perfectly (100 %) untwinned thin film and considering that in our samples $\rho_a/\rho_b \approx 1.6$ (see inset in the lower rightmost panel), we estimate a $75 \pm 5 \%$ untwining within a linear approximation. This indirect estimation is consistent with the more direct XRD measurements but is somewhat less accurate due to the influence of anisotropic stress imposed to the atomic lattice by the substrate.

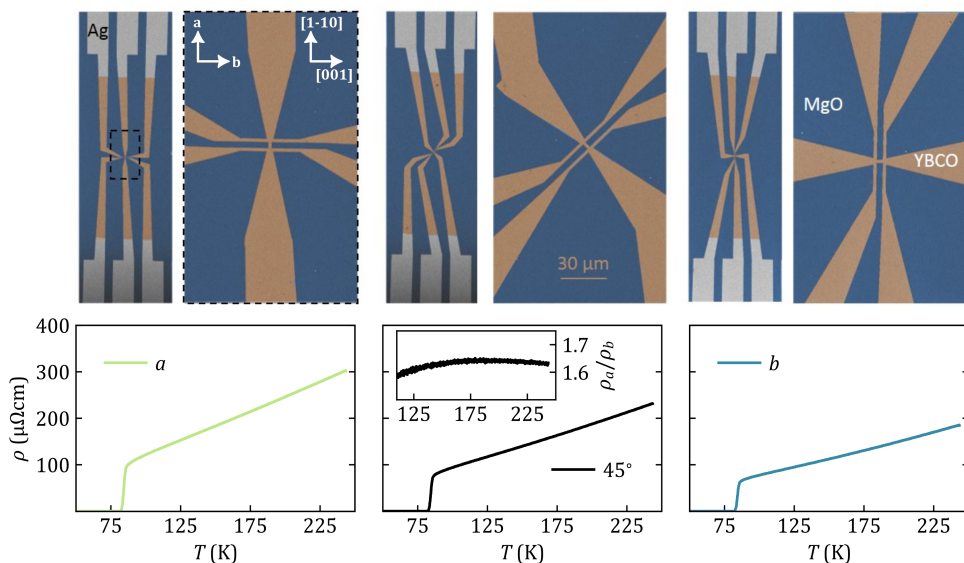


Figure 5.1: Low magnification and high magnification false-colored scanning electron microscopy images of transport bridges along the crystallographic directions a (left), 45° from a (top central panel) and b (rightmost panel). The lower row shows the associated resistivity vs temperature curves obtained at zero applied magnetic field. The inset in the lower central panel shows the ratio ρ_a/ρ_b in the whole temperature range.

The protocol used to achieve electrically-stimulated oxygen migration consists of applying 1 s pulses of DC current with linearly increasing amplitude (see inset in Fig.5.2(a) or Sec.2.2.2). The resistance of the sample is probed after every driving pulse with a small bipolar pulse of $10 \mu\text{A}$ (0.001 MAcm^{-2})

amplitude and 10 s duration. Samples are optically imaged after the resistance measurement is finished, once for every amplitude of the driving pulse. This experiment is performed under atmospheric conditions. Fig.5.2(a) shows the resulting evolution of the bridge resistivity as a function of the density of current during the electric pulse. Pulses of small amplitude lead to no modification of the sample resistance as manifested by the current independent resistivity. Beyond a certain threshold current density, a slight decrease of resistivity (less than 1 %) is systematically observed. As demonstrated by Moeckly et al.[198] this effect cannot be solely attributed to a thermal annealing process resulting from Joule heating but requires in addition, a current stimulated redistribution of chain oxygen vacancies. Interestingly, this improvement of the conductive properties is less pronounced when the current is along the a -axis which is consistent with the fact that oxygen diffusion (and thus ordering) is hampered along this direction. This initial improvement of the sample is followed by a rapid increase of the resistivity associated to long-range oxygen migration. Remarkably, even though the activation barrier is expected to be substantially lower for oxygen diffusion along the b -axis, the current density needed to stimulate the diffusion process is larger along b than along a . The reason for this effect can be traced back to the fact that for a given current, a higher resistivity along a implies a more pronounced Joule heating and consequently a higher local temperature. Since oxygen migration is thermally activated, this effect gives rise to an early oxygen diffusion along a as current density increases.

A possible way to discern thermally driven from electrically induced oxygen displacement is to compare the power dissipated at the onset of migration. Indeed, for an isotropic system for which the diffusivity does not depend on the in-plane direction, the diffusion should be triggered at the same temperature (proportional to the power applied) independently of the direction of the current. In other words, the onset of migration should take place at a constant power threshold for all in-plane current orientations. In Fig.5.2(a) we indicate the power density $\mathfrak{P} = \rho J^2$ at the onset of resistivity decrease, as well as at the onset of resistivity increase, for the three investigated current directions. The fact that \mathfrak{P} at the onset of resistivity decrease is nearly independent of the orientation suggests that the threshold for electromigration is determined by the local temperature rather than the activation energy. Indeed, for a given current, in the expression for diffusivity $D \propto \exp(-E_a/k_B T)$, the local temperature $T \propto \rho$. Both E_a and ρ are highest along the a -axis, and these two parameters have competing effects. If the angular variation of ρ is more pronounced than that of E_a , a minimum in the

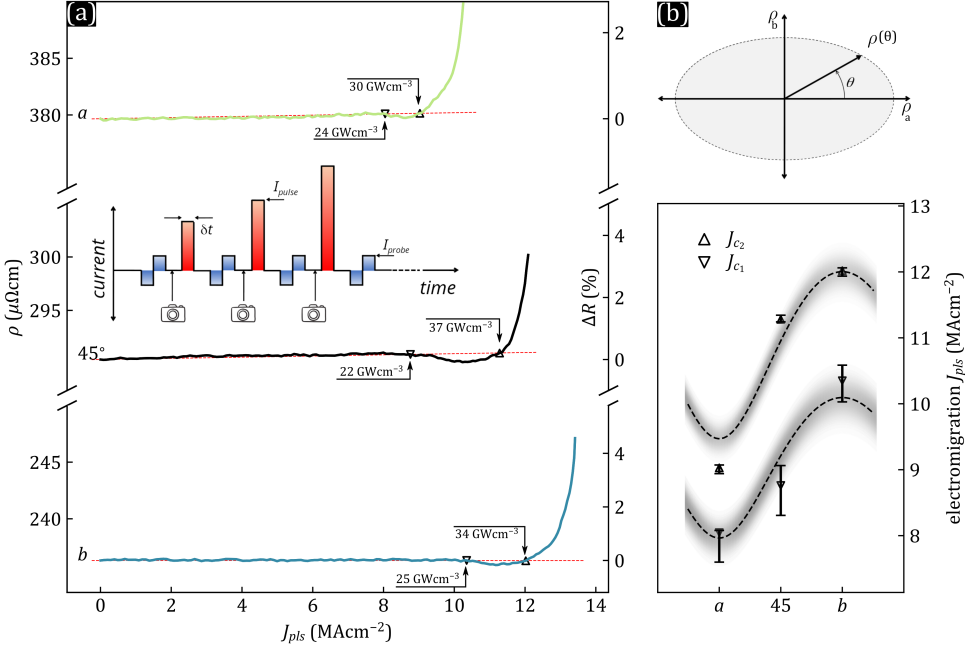


Figure 5.2: (a) Evolution of the sample resistivity as a function of the applied pulsed current density for bridges oriented along three crystallographic axes. The power dissipated in the bridges at the onset of the resistivity decrease (∇) and increase (Δ), is indicated with black arrows. The inset shows the measurement protocol using pump-probe current pulses and intercalated optical microscopy snapshots. (b) Schematic representation of the anisotropic $\rho(\theta)$ following an elliptic angular dependence (upper panel). The lower panel shows the experimentally determined onset of the sample resistivity decrease (∇) and the increase (Δ). The gray shadow covers a zone limited by the fittings to Eq. (5.1) for the extreme (minimum and maximum) power p_0 inferred from the experimental data points.

threshold current density for electromigration is expected along a -axis, as observed experimentally.

Assuming that the onset of electromigration is defined by a power density threshold p_0 and considering an anisotropic resistivity $\rho(\theta)$ of elliptic shape as schematically shown in the upper panel of Fig.5.2(b), it is possible to deduce a current density threshold of electromigration,

$$j(\theta) = \sqrt{\frac{p_0}{\rho_a \rho_b} \sqrt{(\rho_a \sin \theta)^2 + (\rho_b \cos \theta)^2}}. \quad (5.1)$$

The lower panel of Fig.5.2(b) shows the experimentally determined onset of the sample resistivity decrease (∇) and the onset of sample resistivity increase (\triangle), together with the prediction of Eq.(5.1) with a graded color intensity representing the error bar on p_0 . The fair agreement between the proposed model and the experimental data validates the scenario for which the electromigration onset is set by the local power density or, equivalently, by the local temperature.

In Fig.5.2 we have purposely limited the irreversible increase of resistivity to few percent of the initial value. After this first electromigration, no hint of sample modifications were observed by optical reflectivity. However, by further increasing the current density in such a way to induce $\sim 30\%$ increase of resistance, the oxygen deficient regions become visible by optical microscopy[230]. Fig.5.3 shows a selected set of snapshots of the diffusion process in which affected areas exhibit a higher reflectivity (i.e. brighter color). These images point to the existence of oxygen depleted spots at the sharp corners of the structure and propagating into the current leads, suggesting the importance of current crowding in the triggering process. The previous two chapters show this effect in fully twinned YBCO films on LaAlO_3 substrates.[72, 74] No major changes are observed on the central bridge itself. Note that the diffusion pattern observed along a and b axes is symmetric whereas the one observed along 45° is asymmetric, suggestive of an influence of the crystallographic orientation. Nevertheless, the affected area is clearly directional demonstrating the electric current/field drive on the displacement of atoms. Based on the above considerations, we

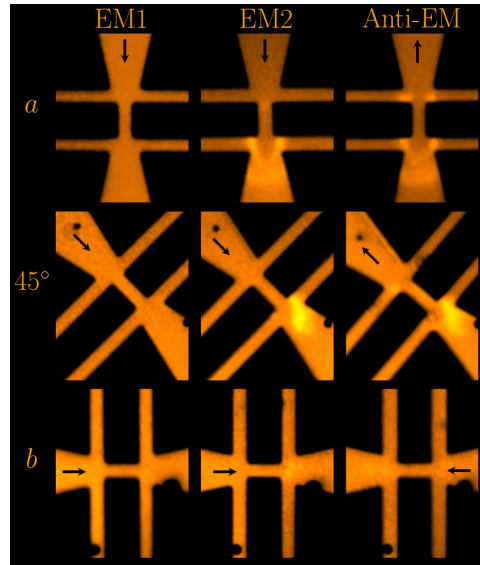


Figure 5.3: Bright field optical microscopy images for the bridges oriented along the a , 45° , and b crystallographic directions after (EM1) mild electromigration with $\sim 3\%$ increase in resistance, (EM2) severe electromigration with $\sim 30\%$ increase in resistance, and (Anti-EM) reversing the current polarity, so called anti-electromigration. All the images were acquired on the same sample in chronological order EM1, EM2, and finally Anti-EM under ambient conditions. The black arrows indicate the current direction.

Based on the above considerations, we

suggests a scenario in which the onset of electromigration is dictated by the local temperature at the transport bridge and the direction of electromigration is determined by the applied electric field and/or current density.

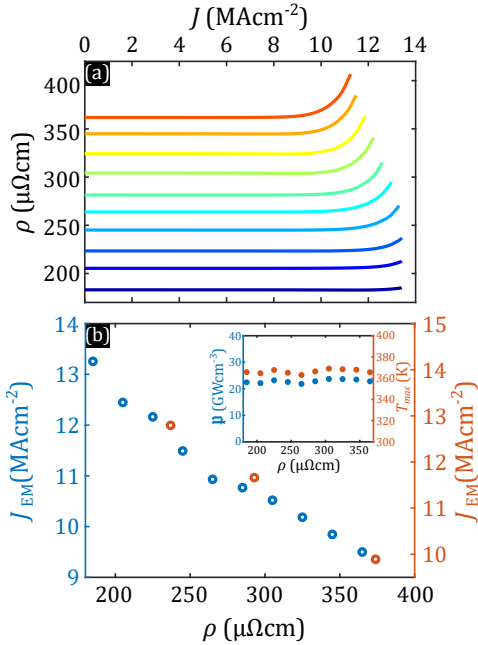


Figure 5.4: (a) Numerical simulation of the sample resistance for ρ varying from 185 to 365 $\mu\Omega\text{cm}$ in steps of 20 $\mu\Omega\text{cm}$. The following parameters have been used for these simulations: $E_a = 0.55$ eV, $\alpha = 5 \times 10^{-3}$ K^{-1} , $x_0 = 0.9$, $\delta x_0 = 5\%$, $x_{min} = 0.5$, and $x_{max} = 0.95$. (b) Electromigration current determined using a criterion of 1 % increase on resistance, as a function of the resistivity extracted from the numerical simulation (blue) and the experiments (orange). The inset shows the power density (left ordinate) and maximum temperature (right ordinate) at the onset of electromigration for samples of different resistivity.

Attempts to recover the initial resistance of the bridges by reversing the current polarity have proven unsuccessful unless the resistance changes are within few percent of the starting resistance. Transport measurements show that a minor healing effect takes place before a new increase in resistance develops. This minor healing process is also visible in the rightmost column of Fig.5.3 (labeled anti-EM) as the brightness of the oxygen depleted area decreases while new white spots appear on the opposite side of the bridge.

Let us now investigate the oxygen diffusion process by following the numerical model introduced above and considering the same exact geometry as for the sample investigated experimentally. Our first objective consists in demonstrating that the onset of electromigration is entirely determined by the power density and the local temperature, rather than the current density. To that end, we will assume that the activation energy for oxygen diffusion $E_{a_a} = E_{a_b} = E_a$ are independent of the crystallographic orientation whereas the an homogeneous resistivity ρ changing with angle as shown in Fig.5.2(b) is considered.

Fig. 5.4(a) shows the resistance as a function of the applied current for an ensemble of bridges with identical shape but different resistivity. The simulation parameters have been chosen in such a way to approach the

experimental data shown in Fig.5.2(a). The current threshold for electromigration determined using a 1 % increase of resistance is plotted in Fig.5.4(b) as a function of the sample's resistivity. In the same panel the experimental data has been added and shows a similar trend as for the simulation, i.e. the current threshold for electromigration decreases as resistivity increases. Simulations allow us to estimate the maximum temperature T_{max} attained at the onset of electromigration as shown in the inset of panel (b) for each of the curves in panel (a). One can observe that the local temperature triggering the oxygen migration process is rather independent of the sample resistivity thus confirming that T_{max} is the essential parameter controlling the onset of the migration process. In the same inset we have plotted the power delivered at the bridge at the onset of electromigration and, as expected, it shows a similar trend as T_{max} . In brief, the experimental trend shown in Fig.5.2(b) can be simply accounted for by an increase of resistivity without the need to invoke an angular dependent E_a .

Interestingly, as shown by the blue curve in Fig.5.5(a), the proposed numerical model is also able to capture the experimentally observed improvement of the conductive properties of the bridges in the vicinity of the onset of electromigration, as seen in Fig.5.2(a). In order to demonstrate that the origin of this resistance shallow minimum can be linked to the ordering or homogenization of the oxygen concentration, we computed the residual r defined by,

$$r = \sum_i \sqrt{(x_i - x_0)^2} \quad (5.2)$$

with i indicating each node of the simulation grid, x_i the local oxygen concentration, and x_0 the mean value of the concentration throughout the sample. In other words, $\delta x_i = x_i - x_0$ and r represent the degree of local and global oxygen disorder in the sample, respectively. In Fig.5.5(a) the red curve shows r as function of the applied current associated to the sample depicting the blue curve response. It can be clearly seen that the initial phase of the electromigration process consists in a homogenization of the oxygen content before a severe disorder sets in at higher currents. A more compelling evidence that the slight improvement of samples' conductivity arises from oxygen concentration ordering comes from Fig.5.5(b). In this panel we plot the normalized resistance $R_{min}(I)/R_{min}(0)$ for samples with increasing degree of concentration inhomogeneity δx_0 . For small values of δx_0 (i.e. rather homogeneous samples), the local minimum is absent, whereas as δx_0 increases the local minimum becomes progressively more pronounced. This is an interesting finding which could be implemented to quantify the degree of disorder in a

sample by measuring the depth of the shallow minima in $R(I)$. Furthermore, the process of current stimulated oxygen ordering should be also influenced by the activation energy barrier to overcome in order to displace the oxygen atoms. In Fig.5.5(c) we show that as E_a increases, the ordering is less effective and consequently, the local minimum becomes shallower. This result seems in agreement with the experimental data shown in Fig.5.2 where a higher E_a expected along a -axis exhibits a less pronounced local minimum.

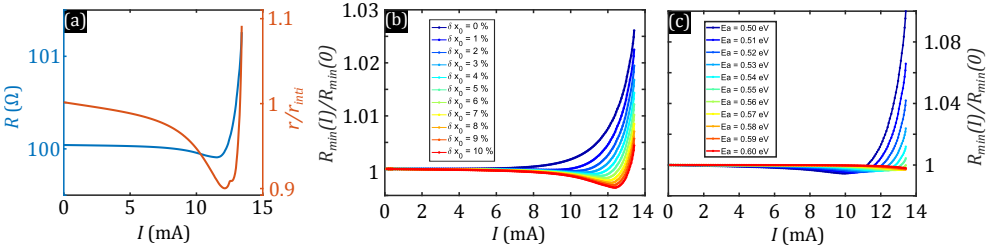


Figure 5.5: (a) Zoom in showing the numerically calculated initial change of resistance with current (blue line) of one of the curves in Fig.5.4(a) together with the evolution of the residual function r (orange line). (b) Evolution of the local resistance minima as a function of the degree of oxygen concentration disorder δx_0 . (c) Evolution of the local resistance minima as a function of the activation energy E_a .

In an attempt to numerically replicate the oxygen vacancy mappings revealed in Fig.5.3, the model must explicitly account for an anisotropic activation energy as described in section 5.4. The resulting map of oxygen concentration as determined by the numerical simulations with $E_{a_a} = 0.55$ eV and $E_{a_b} = 0.5$ eV, and reproducing the experimental conditions of Fig.5.3, are shown in Fig.5.6. Most of the features observed in the optical images of Fig.5.3 are also captured by the simulations. In particular, the nucleation of oxygen depleted zones at the location of maximum current crowding and the propagation of an arc-shaped front into the current leads. The lowering of the activation energy along the b direction naturally stimulates oxygen migration along this direction even if the bias current is along a (first row of Fig.5.6). Since the current streamlines diverge at the bridge's lower end, the oxygen vacancies migrate preferentially along the direction of the voltage pads and little along the bridge direction. The subsequent anti-EM step further reproduces the experimental findings, namely a reoxygenation of the previously depleted oxygen vacancy pockets and the formation of new pockets at the bridge's upper end. The second row of Fig.5.6 describes the situation for a 45° rotation of the bridge with respect to the a direction. Although the simulations show stronger effects for the center of the bridge

than for the current pads, we do find an asymmetric distribution of oxygen which is explained by an easier diffusion triggered by the current density component J_b with respect to J_a . Finally, the simulation along the b axis (third row of Fig.5.6) shows a strong migration almost exclusively along the bridge axis leaving the voltage pads intact.

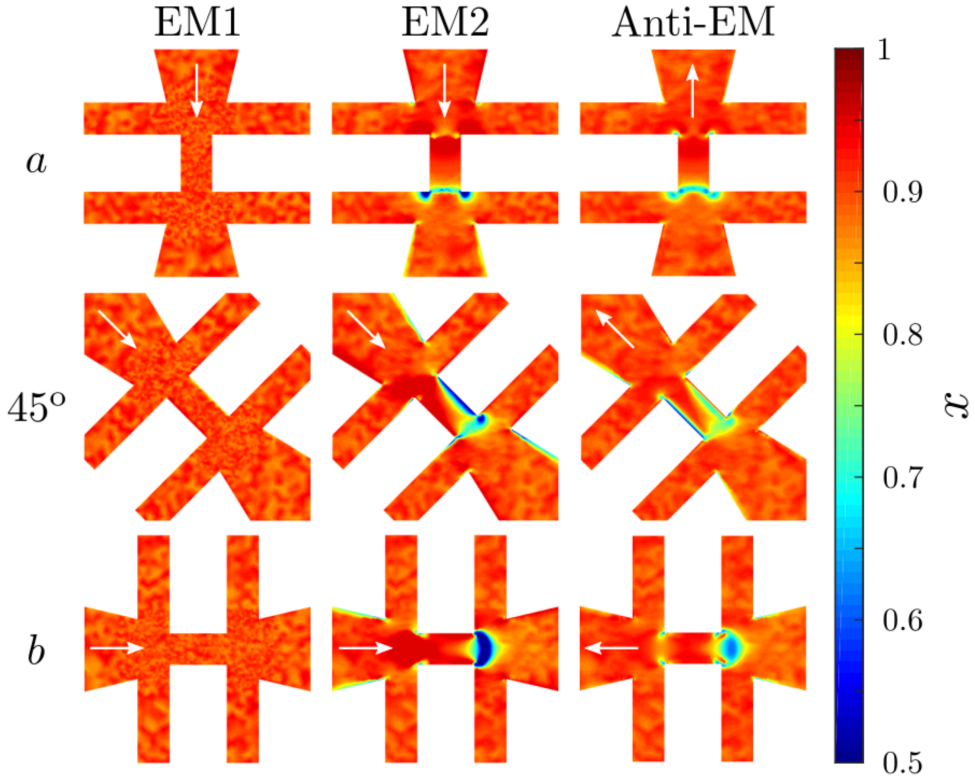


Figure 5.6: Numerical simulations reproducing the oxygen vacancy distribution of Fig.5.3 using the anisotropic model of section 5.4 with $E_{a_a} = 0.55$ eV, $E_{a_b} = 0.5$ eV.

5.3 Samples

Epitaxial 50 nm thick $\text{YBa}_2\text{Cu}_3\text{O}_{7-\delta}$ films were grown by pulsed laser deposition with the c -axis aligned perpendicular to the film plane on $\text{MgO}(110)$ single crystal substrates. For ensuring ohmic electrical contacts, Au electrodes were sputtered. The films were patterned via electron beam lithography[254, 255] and dry ion-beam etching into a bridge-type constrictions as shown in Fig. 5.1. The length \times width of the bridges is $5 \mu\text{m} \times 2 \mu\text{m}$. All films ex-

hibited superconducting critical temperatures T_c of ~ 87.5 K (corresponding to doping $p \sim 0.19$). The asymmetrical (038)-(308) reflections in 2θ - ω XRD maps reveal a 80% untwinning degree[177]. The measurements presented in this work have been tested in 4 full sets of samples (i.e. 12 bridges in total).

The optical microscopy images were obtained under atmospheric conditions with a $50\times$ magnification objective (NA=0.5) followed by a $2\times$ magnification lens and collected in bright field mode with a continuous green illumination filtered from a Hg lamp. The optical microscopy imaging is performed simultaneously with the electrotransport in order to be able to make a reliable comparison of the electromigration effects.

5.4 Modeling

The model is constructed like the ones in Sec.2.4 and the one in Ch.4. The key difference is that the diffusivity and resistivity are expressed as second order tensors depending on the orientation of the sample.

In this case $\mathbf{D} = D_0 \text{diag} [\exp(-E_{a_a}/k_B T), \exp(-E_{a_b}/k_B T)]$ is the temperature dependent diffusion tensor, $D_0 = 1.4 \times 10^{-8} \text{m}^2 \text{s}^{-1}$ [170], E_{a_a} and E_{a_b} the activation energies in eV along directions a and b respectively

The second term on the right-hand side of Eq.(4.1) represents the Joule heating and involves the resistivity tensor $\rho(x, T) = \text{diag}[\rho_a, \rho_b]$ of the material which depends on both the oxygen concentration and local temperature. The ratio $\rho_a(x_0, T_{ref})/\rho_b(x_0, T_{ref}) = 380/236$ at the initial oxygen concentration x_0 is determined from measurements at low current (see Fig.5.2). The functionality $\rho(x, T)$ imposed in the model is taken from experimental values reported in Ref.[156]. For $T > 300$ K, we assume a linear dependent resistivity $\rho(x, T) = [1 + \alpha(T - T_{ref})]\rho(x, T_{ref})$ with $\alpha = 5 \times 10^{-3} \text{K}^{-1}$ determined by $R(T)$ measurements and $T_{ref} = 300$ K.

We will first consider an isotropic version of the equations that satisfactorily explains the electrotransport properties and later on add a slight anisotropy of the oxygen diffusion in order to better account for the observed oxygen vacancy mappings. The values of the thermal coefficients are listed in the Table 5.1. Slightly different thermal coefficient as reported in Refs.[70, 248] lead to similar results.

Having a system of coupled equations combined with logarithmic behavior of resistivity with concentration makes simultaneous resolution particularly demanding. In order to speed up the numerical calculations, an iterative time process with two steps per iteration is used as in Ch.4. First, the temperature and potential profiles are evaluated at iteration i assuming x to be constant as

	ρ_m [kg m ⁻³]	C [J kg ⁻¹ K ⁻¹]	κ [W K ⁻¹ m ⁻¹]
MgO	3600 [256]	930 [256]	50 [256]
YBCO	6300 [251, 252]	520 [164, 253]	10 [164]

Table 5.1: Thermal coefficients for the MgO substrate and the superconducting YBCO film used as input parameters in COMSOL simulations.

determined in the previous iteration $i - 1$. During this step, the temperature dependence of the resistivity is assumed to be the temperature profile from previous iteration. Second, the new spatial distribution of the concentration x is calculated assuming T and V constant. The values T , V and x at the first iteration are given by the initial conditions of the problem.

5.5 Summary

In conclusion, we investigated the electromigration process on highly twinned $\text{YBa}_2\text{Cu}_3\text{O}_{7-\delta}$ films grown on MgO substrates. We demonstrate that the onset of oxygen migration is determined by the local temperature rather the activation energy associated to the atomic migration. Prior to long range electromigration, a current range for which the resistivity of the sample decreases is observed. Finite elements modeling suggests that this behavior is caused by a current-stimulated oxygen ordering. The maximum degree of oxygen homogenization being ruled by the initial level of oxygen disorder and the migration activation energy. The numerical model is able to reproduce the observed oxygen vacancy mapping provided that an anisotropic activation energy is taken into account. The proposed model could be further improved by incorporating some degree of twinning, implementing a three-dimensional representation of the $\text{YBa}_2\text{Cu}_3\text{O}_{7-\delta}$ sample, and including a thermomigration term in the modeling. These findings provide further understanding on the non-monotonous change of resistivity systematically observed in oxides samples before severe electromigration.

Part III

Electrical Oxygen Doping Control in Related Perovskites

From Electric Doping Control to Thermal Defect Nucleation in Perovskites

Based on: S. Marinković, A. Fernández-Rodríguez, E. Fourneau, M. Cabero, H. Wang, N. D. Nguyen, J. Gazquez, N. Mestres, A. Palau, and A. V. Silhanek, “From electric doping control to thermal defect nucleation in perovskites”, *Advanced Materials Interfaces* **9** (2022), 10.1002/admi.202200953

Main Contributions: experiment design, electromigration experiments, cryogenic transport measurements, optical, MOI and SEM imaging, data interpretation and presentation, writing

Layman's Overview: Electrical Oxygen Diffusion in Related Perovskite Materials

YBCO is by far not the only perovskite oxide with a very mobile oxygen atom. In fact, literature reports indicate that this feature is very common in the perovskite oxide material family, and it is thus expected that we can demonstrate electrical oxygen diffusion in these materials as well. We use the well studied ferroic material LSMO as an illustrative example.

In this chapter we apply the pulsed-excitation protocol (See Ch.2) to demonstrate electrically driven oxygen diffusion in LSMO. The results show many simi-

larities with YBCO including the possibility to use optical reflectivity to map oxygen diffusion. Some differences we find include a smaller necessary current amplitude for electromigration and more stringent conditions for obtaining in optical detection of the changes.

Notably, the electrothermal stress induced in the LSMO films are shown to be capable of creating defects in the STO substrate. These defects are shown to be insulating, and thus distinct from previously reported electroformed channels in the substrate material.

Motivated by the results in YBCO, we turn to manganites to study electrically driven oxygen diffusion in related perovskites. Simultaneous optical microscopy and electric transport measurements on $\text{La}_{0.7}\text{Sr}_{0.3}\text{MnO}_3$ (LSMO) nanobridges, grown on SrTiO_3 (STO), show direct evidence of directional oxygen vacancy migration under large voltage bias. Comparative study on discontinuous structures, with voltages applied across a micron-scale gap, demonstrates that high electric fields induce electrolytic modifications confined to the anode. Additionally, extensive electromigration is shown to induce the formation of linear surface scars on the STO substrate, following well defined crystallographic directions. We demonstrate the reproducible triggering of these surface dislocations, unveil their thermal rather than electrical origin and show that they do not represent electroformed conduction channels. High-resolution Scanning Transmission Electron Microscopy (STEM) imaging reveals that the scars correspond to nanometer scale steps caused by (101) gliding planes in the STO caused by the proliferation of edge dislocations and local lattice expansion.

6.1 Introduction

Amidst all perovskite-type oxides, $\text{La}_{1-x}\text{Sr}_x\text{MnO}_{3-\delta}$ (LSMO) occupies a privileged place as the most studied manganite, greatly due to its magnetoresistive and resistance-switching behavior (see Ch.1), as well as the close relationship of its conductive and magnetic response to crystal structure. Substituting La^{3+} by Sr^{2+} oxidizes Mn^{3+} into Mn^{4+} , resulting in a mixed valence of Mn

ions in the unit cell[139] and the material's non-stoichiometry. As x increases, a double exchange interaction between Mn ions bridged by oxygen[125] dictates the electronic distribution leading to the development of a ferromagnetic phase at low temperatures. This phase has a Curie temperature reaching a maximum of $T_C \approx 370$ K for $x \approx 0.33$. In this system, magnetism and conduction are intimately coupled: when the magnetic moments are misaligned (i.e. the material is in the paramagnetic state), electrons cannot be transferred by means of a double exchange mechanism, and hence a decrease of resistivity is associated with spin-alignment (see Box.1.3). With increasing oxygen deficiency δ , the average Mn oxidation state decreases and thus the average Mn ionic size increases. As a result, the lattice parameter of manganese oxide increases and both the Curie temperature and the magnetization decrease whereas the resistivity increases.[140]

After recognizing the importance of the oxygen distribution in the material and its anisotropic atomic mobility characteristic of perovskites, there were several attempts at demonstrating the thermoelectrically induced migration of vacancies in LSMO on STO. Balcells et al.[205] showed that at high current densities ($> 10^5$ Acm⁻²), the depletion of oxygen content promotes irreversible changes in the samples with a remarkable increase of resistance and a reduction of the ferromagnetic transition temperature. Recently, further evidence suggesting the displacement of oxygen vacancies under the combined effect of electric field and Joule heating has been reported.[204, 207, 257, 258] Even though voltage induced phase changes were observed at the microscopic level by means of Scanning Transmission Electron Microscopy (STEM) by Yao et al.,[259] unambiguous macroscopic evidence of electrically stimulated oxygen vacancy migration has not been provided as of yet.

In this chapter, we use concurrent optical microscopy and electrical transport measurements to assess the oxygen vacancy distribution in LSMO nanobridges, epitaxially grown on STO substrates, under controlled electrical stress in ambient and cryogenic conditions. Evidence is provided of directional oxygen flow under large voltage bias, which is then compared to the behaviors of discontinuous (gapped) structures. For the latter, a distinctly electrolytic behavior is observed. Strikingly, a peculiar structural feature suddenly emerges upon extended electromigration: superficial scars as linear defects spreading from the LSMO nanobridge outwards along the crystallographic directions of the substrate. Electrical characterization, scanning electron microscopy (SEM), atomic force microscopy (AFM), conductive AFM (c-AFM), as well as STEM are used to assess the effects of electrothermally driven oxygen migration on the structural stability of the system.

Our findings demonstrate the possibility to achieve all-electrical and targeted generation of dislocations in post-synthesized on-chip structures in the path towards new ionic functional devices.

6.2 Results and discussion

6.2.1 Directional migration of oxygen in LSMO

The 20 nm-thick LSMO films investigated in this work exhibit a metal-insulator transition and a Curie temperature above room temperature evidenced by the temperature dependent magnetization $M(T)$ and the resistance $R(T)$ shown in Fig.6.1(a,b). The presence of the low-temperature ferromagnetic phase is directly confirmed by the magneto-optical image shown in the inset of panel (a) obtained at 5 K with an in-plane field of 3 mT. Similar magnetic field landscape is obtained at room temperature. Two different geometrical sample designs have been measured: (i) a continuous, multi-probe structure consisting of a narrow central LSMO bridge symmetrically surrounded by wider bridges, each bridge individually addressable by corresponding voltage contacts as shown in Fig.6.1(c), and (ii) a discontinuous, mirror symmetric structure, as shown in Fig.6.1(d), separated by a gap of 3, 7, or 15 μm .

The multiterminal bridge shown in Fig.6.1(c) permits us to electrically unveil the directional displacement of oxygen. To that end, current pulses of 1 s duration at ambient conditions are applied across the entire device with the polarity as indicated by the sketch in Fig.6.2(b). Fig.6.2(a-c) show the relative resistance change ΔR at each junction with respect to the resistance of the pristine state, as a function of temperature. These panels are color-coded as indicated in the sketch in Fig.6.2(b). The first three pulses are of same amplitude, i.e. 0.5 mA, whereas the last one is doubled to 1 mA. The resistance as a function of temperature $R(T)$ is measured after every pulse for all junctions simultaneously with a current of 100 nA RMS, using a lock-in amplifier.

Although optical images taken before and after the pulses do not exhibit any hint of modification on the constrictions, the gathered electrical data shows evidence of directional mass transport. Electro-pulsing induces an increase of resistance on the left bridge and a corresponding decrease on the right one. This behavior is consistent with oxygen vacancies displacing from anode (+) to cathode (-) since increasing oxygen deficiency δ leads to an increase in resistivity.[140] Note that the central bridge remains mostly

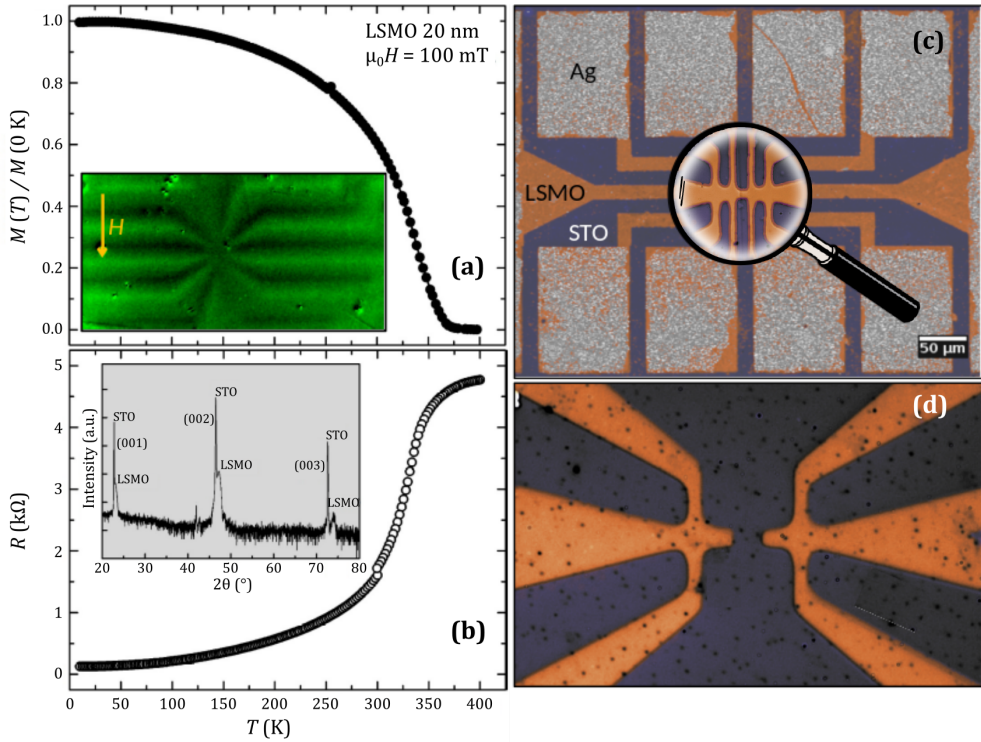


Figure 6.1: Normalized magnetization (a) and resistance (b) as a function of temperature for a 20 nm thick plain film of LSMO. The ferromagnetic-paramagnetic transition takes place at a Curie temperature $T_C \approx 370$ K and is accompanied by a metal-insulator transition. The inset in panel (a) shows a 5 K magneto-optical image of the stray field generated by the sample shown in panel (c) with an in-plane magnetic field $H = 3$ mT. The inset in panel (b) corresponds to the X-ray diffraction spectra of a plain LSMO film deposited on STO substrate. SEM images of the two investigated sample layouts (continuous and discontinuous) are shown in panels (c) and (d), respectively. The zoom-in in panel (c) with a magnifying glass shows an optical microscopy image of the three bridges, the central one being $1 \times 3 \mu\text{m}^2$. In panel (d) the gap separating the two mirror symmetric structures is $3 \mu\text{m}$.

invariant after the pulses and that for all three bridges the resistance changes are almost imperceptible below 50 K.

The previous chapters show that oxygen deficient $\text{YBa}_2\text{Cu}_3\text{O}_{7-\delta}$ offers the possibility to visualize vacancy distribution as they diffuse under electrical stress.[72] A similar phenomena could be expected in LSMO, considering the fact that both materials are perovskite-like structured ceramic oxides. In order to induce longer range oxygen vacancy displacements and image

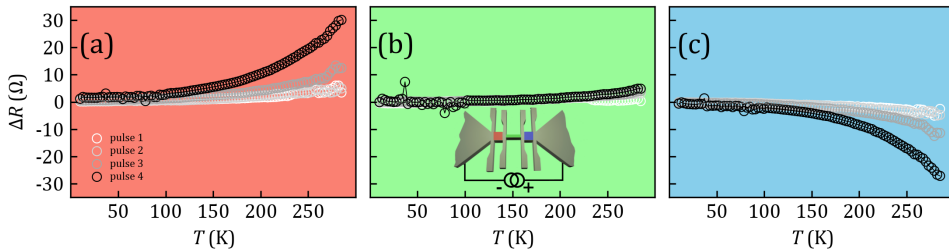


Figure 6.2: Relative change of resistance $\Delta R = R_i - R_0$, with R_i obtained after i -th current pulse and R_0 the resistance in the pristine state, as a function of temperature. The first three pulses are of same amplitude 0.5 mA whereas the fourth and last pulse increases to 1 mA. The background color of each panel indicates the corresponding transport bridge as illustrated in the sketch of panel (b).

the diffusion process in situ at 110 K, we submitted the sample to a series of voltage pulses of linearly growing amplitude as schematically shown in Fig.6.3(a). Before and after each pulse, the resistance of the sample is monitored and optical images are acquired. The voltage amplitude and the current circulating through the device in response to the voltage pulses, as a function of pulse number (or time) are plotted in Fig.6.3(b).

The current I_{PLS} initially increases linearly as a consequence of a nearly invariant resistance. For higher amplitude of voltage pulses the current seems to saturate in a plateau value of ~ 4 mA indicating a resistance growing roughly linearly with the applied voltage. The resistance of each bridge as a function of pulse number is shown in panels (c-e) with an excitation respecting the same polarity as shown by the sketch in Fig.6.2(b). Consistent with the previous observation, the resistance of the individual bridges remains constant up to pulse number 12 and undergo modification for higher pulse numbers. A selected set of optical images is shown in the lower two rows of Fig.6.3 in which the corresponding pulse number is indicated. Up to pulse number 14 no apparent changes in reflectivity are discerned. However, starting from pulse number 20, a clear progressing front of increased reflectivity advances towards the cathode. To the best of our knowledge, this is the first direct visualization of electrically-driven macroscopic migration of oxygen vacancies in LSMO.

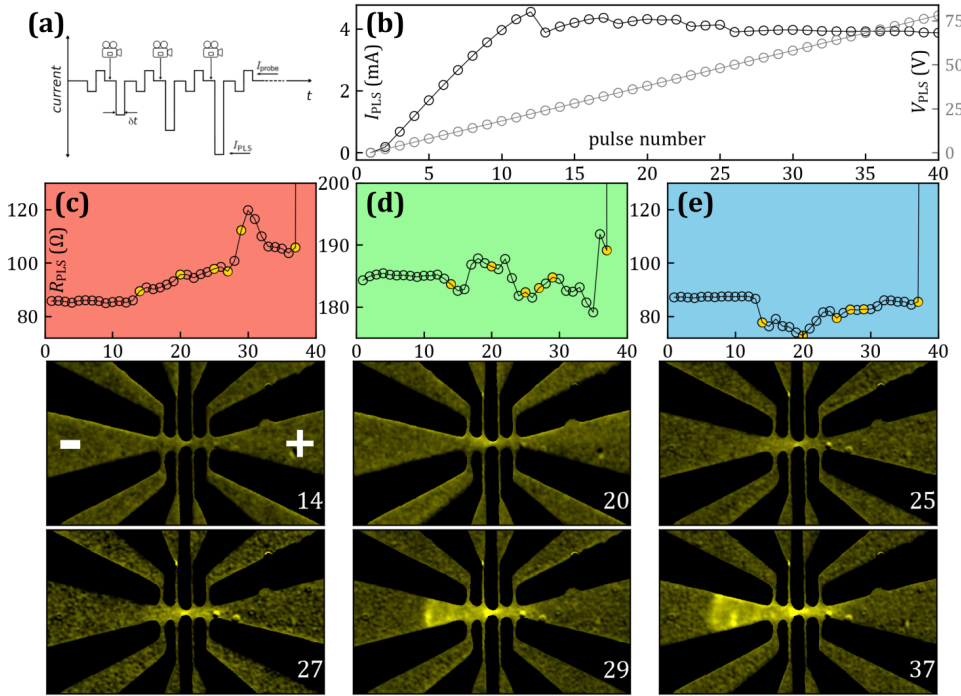


Figure 6.3: (a) A bipolar I_{probe} pulsed current is used to monitor the sample resistance whereas a $I_{PLS} \gg I_{probe}$ of variable amplitude resulting from linearly increasing voltage pulses (b) triggers the oxygen migration process. Resistance of the left (c), central (d), and right (e) bridges after the voltage pulse as a function of the pulse number. The lower two rows show optical microscopy images acquired after the pulse number indicated in the frame. Electric transport and microscopy imaging are acquired at a bath temperature of 110 K.

6.2.2 Generation of Crystallographic Defects in the LSMO/STO System

The resistance of the measured device increases abruptly around pulse number 37, as is shown in Fig.6.3(c-e). A close inspection of the optical images before (Fig.6.4(a)) and after (Fig.6.4(b)) this transition reveals the formation of lines extending across both the substrate and the LSMO nanobridges, notably along well defined crystallographic directions [100] and [010] of the STO. This effect has been observed in all samples under significant electro-pulsing stress. The pristine sample shown in Fig.6.4(a) is absent of lines, whereas for the electrically stressed sample in panel (b), two vertical lines and an horizontal line are indicated with white arrows. Inspection of the sample by scanning

electron microscopy shown in Fig.6.4(c) reveals further details. Indeed, this image has been acquired with a Everhart-Thornley secondary-electron detector, giving mostly topographic contrast. The fact that the vertical line at the left appears dark whereas the line at the right side appears bright, suggests that the left line is a step down and the right line is a step up. Step heights can be quantified with higher z-resolution by AFM, as shown in Fig.6.4(d-h). Panels (d) and (e) show two scan areas of $8 \times 8 \mu\text{m}^2$, and the line profiles **A-A'** and **B-B'** are shown in panels (f) and (g), respectively. The measurements indicate that the whole structure undergoes a decrease in height of about 15 nm in between the the vertical streaks shown in panel (b). The profile **B-B'** taken at the substrate shows that indeed this structural defect propagates and likely originates on the STO substrate. Panel (h) presents a tilted three-dimensional view of panel (e) for better visualization of the trench produced in the sample. The steps seemingly align well-defined crystallographic orientations of the STO substrate.

Electric-field triggered structural transformation in STO has been reported by Hanzig et al.,[260] who showed that the out-of-plane lattice parameter increases by increasing the electric field up to few MVm^{-1} . High electric field combined with high temperature induces migration of oxygen vacancies along the local chemical and electric potential,[55] which in turn causes a cation (Sr, Ti) counterflow maintaining charge neutrality. This redistribution of mobile species reduces the stability of the crystal structure. A reversible electric field-induced structural change in the near-surface region of STO has also been reported through X-ray absorption measurements by Leisegang et al.[188] using calculated Ti valence as a proxy for the oxygen vacancy distribution. More recently, Bobeth et al.,[187] Szot et al.,[44] Waser et al., [45] and Rodenbucher et al.[189] have shown via X-ray scattering measurements that well-oriented streaks along the [100] axis of the STO crystal, 1 to 10 μm in diameter, emerge from the cathode and propagate towards the anode during what is known as the electroformation process. These authors demonstrate that these streaks do not propagate on the surface, but are situated within a skin region 100 μm below the surface. Upon connecting the electrodes by these streaks, the resistance suddenly drops suggesting the development of a pipe diffusion conduction mechanism. In contrast to this, crystallographic edge dislocations in STO have shown no evidence of pipe diffusion and the consequent improvement of ionic transport.[136, 137]

The fact that the observed lines are crystallographically oriented superficial scars on the STO, rapidly developing irrespective of the voltage polarity, points to a different phenomena than the streaks reported in Ref.[44] Further

evidence can be obtained by using two separate electrodes (i.e. a well-defined anode-cathode system) and attempting to trigger streaks by increasing the electric potential difference between them. The sample layout shown in Fig.6.1(d) was used and exposed to a linearly increasing voltage bias regime as schematically shown in the top left panel of Fig.6.5 and discussed in Sec.2.2.2, while optical images were taken at each voltage step. A selected set of images for which the pristine state has been subtracted to improve the contrast, is shown in Fig.6.5. From zero up to a potential difference of 152 V no effect is observed in the structure. At 154 V, the sample changes its reflectivity (darkens) on the anode side (+) and remains unchanged on the cathode side (-). The affected area keeps growing as voltage increases until 172 V and by exceeding 172 V another zone of the anode starts to

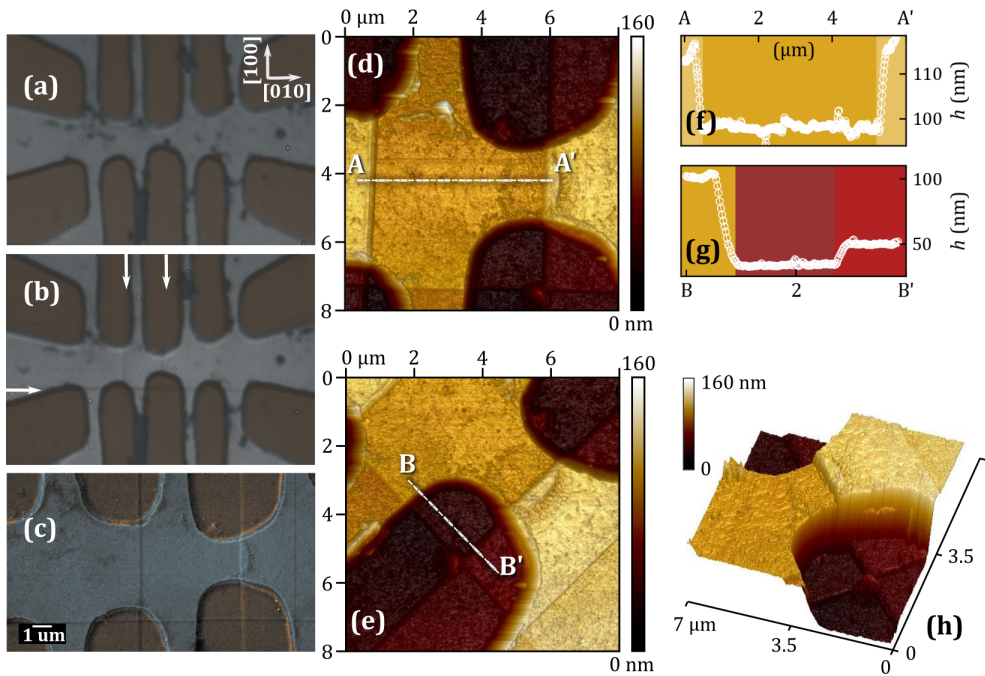


Figure 6.4: Bright-field optical microscopy images of the LSMO/STO sample in the pristine state (a) and after applying a high electro-thermic stress (b) at bath temperature of 110 K. In (b) the appearance of dark vertical and horizontal lines in the substrate are indicated with white and black arrows, respectively. In (c) a scanning electron microscopy image of the central and left bridges is shown. Atomic force microscopy images of the same sample are shown in panels (d), (e) and (h). The line profiles indicated by the segments **A-A'** and **B-B'** are shown in panel (f) and (g), respectively.

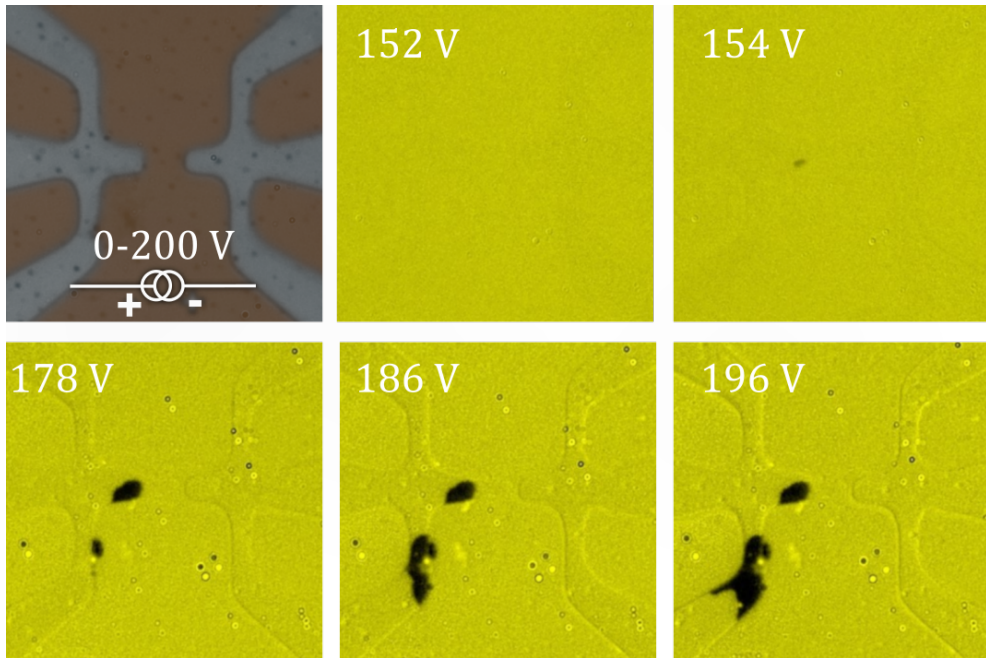


Figure 6.5: Upper left panel: Optical microscopy image of the measured device and the polarity of the sweeping voltage ranging from 0 to 200 V at ambient conditions. The narrowest gap between the two electrodes is $3 \mu\text{m}$. Yellowish background panels show differential images for which the image of the pristine sample has been subtracted to that of the indicated voltage. An area of electrolyzed LSMO can be observed developing above 154 V.

become affected and grows as voltage difference increases. The spread of the discolored area is roughly radial from the biasing voltage contact linking it to the field spreading across the dielectric substrate. Note that no streaks were generated in this experiment.

For the structure in Fig.6.5, the gap between the anode and cathode is $3 \mu\text{m}$, for which a voltage of 152 V corresponds to an electric field of $\sim 50 \text{ MVm}^{-1}$. This value is an underestimation ignoring the shape of the electrodes and is close the reported dielectric breakdown of STO.[77] Scanning electron microscopy images of the affected area clearly reveal evidence of gas bubbles developing under the anode, suggesting a solid-state electrolytic processes as reported by Szot et al.[44] More importantly, the absence of streaks as those reported in Ref.[44] confirms that the lines observed in Fig.6.4 have a different origin.

By changing the circuit configuration to that shown in Fig.6.6 in such a way to induce a circulating current in the right side of the sample, we can

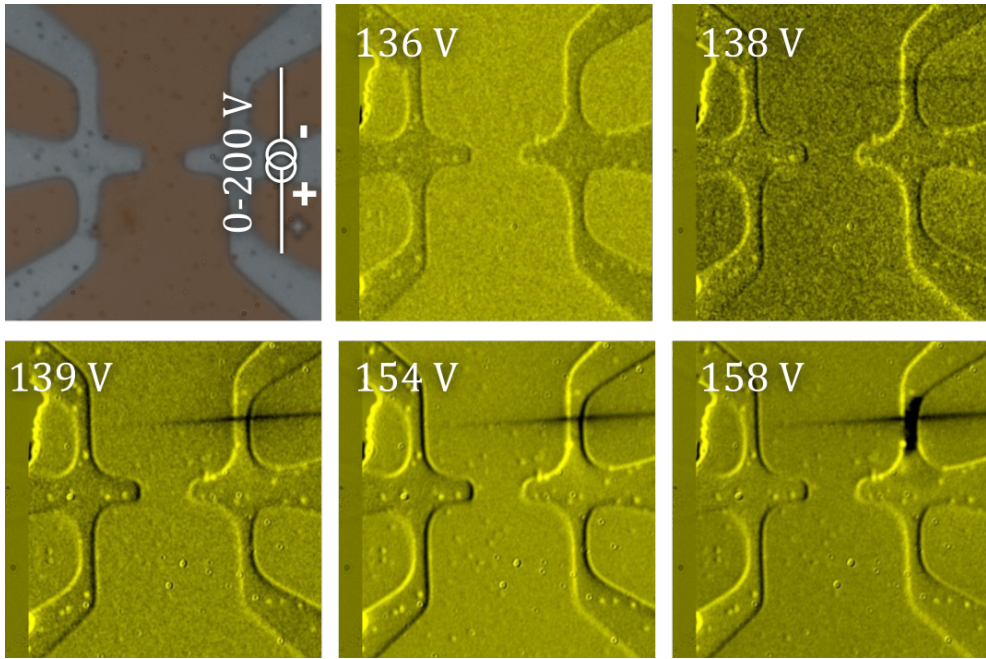


Figure 6.6: Upper left panel: Optical microscopy image of the measured device and the connection circuit used to sweep the voltage ranging from 0 to 200 V at ambient conditions. The narrowest gap between the two electrodes is $3 \mu\text{m}$. Yellowish background panels show differential images for which the image of the pristine sample has been subtracted to that of the indicated voltage. A singular linear crystallographic defect develops and grows in the system above 138 V, before the device is electrically damaged at 158 V.

reproducibly confirm the triggering of the linear structural defects at high applied voltages. A selected set of differential images acquired at the voltage labeled in each panel, shows that little happens to the sample up to 136 V and then from 138 V a linear structural defect develops and subsequently grows until 158 V, where the LSMO sample is locally damaged. Concomitant electric transport measurements along the current path show that the sudden appearance of the linear structural defect leads to a resistance jump. This is expected considering that the thickness of the LSMO is similar to the depth of the linear trench created in the substrate.

We have also simultaneously measured the leakage current through the gap by applying 1 V between the left and right side of the structure. Interestingly, within the noise level of the measurement, a nearly constant leakage current of 10 nA remains unaffected by the formation of the linear defect. This is yet another distinctive feature differing from the streaks reported

in Ref.[44] Furthermore, by performing conducting-AFM in the structural steps and plateaus we confirm that these defects do not represent conducting channels. It is also worth mentioning that we were unable to trigger the linear defects in a similar device made of 100 nm-thick Ag (instead of LSMO). In this case, the electromigration of Ag happens at high currents (~ 41 mA), but overall low dissipated power (about 50 times lower than in LSMO) thus unable to reach the high temperature gradients needed to induce the linear fractures (see Annex C).

The optical images shown in Fig.6.6 show that the imprinted signature of the linear defects fades away as the distance from the nucleation point increases. In order to unveil the underlying mechanism of this effect, we resort to complementary ex situ SEM and AFM investigations of a comparable device as the one shown in Fig.6.6. These results are summarized in Fig.6.7. In panel (a), a SEM image of the region of interest reveals the presence of additional lines not resolved by the optical microscopy. The extent of two notable trenches on this sample were measured by AFM. The lines correspond to height steps measured along the directions x_1 and x_2 indicated in panel (a). The resulting step-height profiles are shown in panel (b) for the direction x_1 and in panel (c) for the direction x_2 . These profiles show that the step-height decreases as the distance from the nucleation point (the LSMO nanoconstriction) increases, explaining the progressive fading of the lines observed optically in Fig.6.6. Another sample that underwent crystallographic deformation under electric bias was analyzed by AFM and is presented in panel (d). A zoom-in of the AFM images at a crossing point of several lines is shown in panel (e). These images evidence several step levels occurring on the STO substrate.

Considering the origin of the observed streaks, it is important to note that both LSMO and STO, as well as their interface are known to exhibit vacancy ordering driven phase transformations. Indeed, LSMO subjected to either heating, electric bias or epitaxial strain effects close to the substrate interface, shows vacancy ordering which leads to the formation of a new phase with a reduced unit cell[259] (brownmillerite[143] - $\text{La}_{0.7}\text{Sr}_{0.3}\text{MnO}_{2.5}$), while in STO, oxidizing conditions and electric bias are known to induce the formation of interwoven Ruddlesden-Popper phases (usually denoted $\text{SrO}(\text{SrTiO}_3)_n$ or $\text{SrTiO}_{2.5}$).[135, 187] All of these phase changes lead to alterations in the unit cell parameter of the material. Oxygen vacancy ordering can also occur between these two materials, mostly due to their shared, large oxygen mobility and similar unit cell constants,[141, 261] with some arguing for a limited oxygen exchange across the interface.[259] These previous results

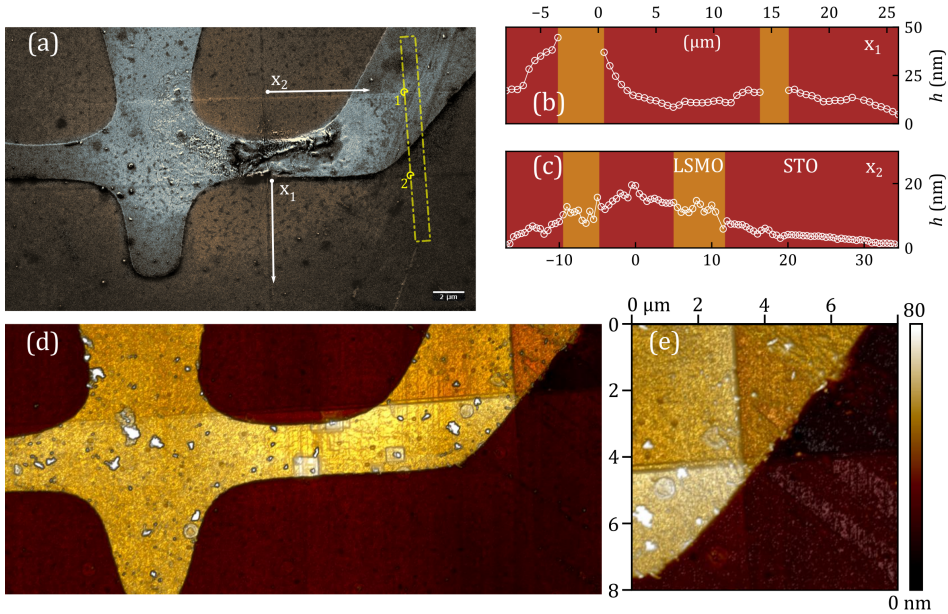


Figure 6.7: (a) Scanning electron microscopy of a LSMO/STO device evidencing several steps after severe electrothermal stress. Step-height along the x_1 (b) and along the x_2 (c) directions indicated in panel (a). Note that the profile along x_1 crosses two LSMO bridges, the one shown in (a) and one opposing it across the gap as shown in Fig.6.6. (d) Atomic force microscopy image of a device comparable to the one in (a) after triggering surface scars by applying electro-thermal stress. A zoom-in of the AFM images of the device in (b) at a crossing point of several lines is shown in panel (e). The rectangular box in panel (a) indicates the lamella cut-out by focused ion beam for subsequent STEM investigation presented in Fig.6.8 and Fig.6.9.

are, admittedly, hard to compare due to broadly varying sample history and methodologies, but it seems abundantly clear that both materials in our system can accommodate variable amounts of oxygen vacancies by making structural concessions. The importance of the epitaxial strain between the thin film and the substrate can not be ignored, as it can affect the phase composition close to the interface and has been shown to increase vacancy mobility in perovskites.[176] Investigating the heat diffusion and electric field distribution on the proposed system with specific regard to vacancy distribution and sample geometry might give more clues on the species mobility in the case under study and allow us to gain insight into the thermodynamics of the effect at hand (see Annex C).

In order to gain further insights on the crystallographic modifications

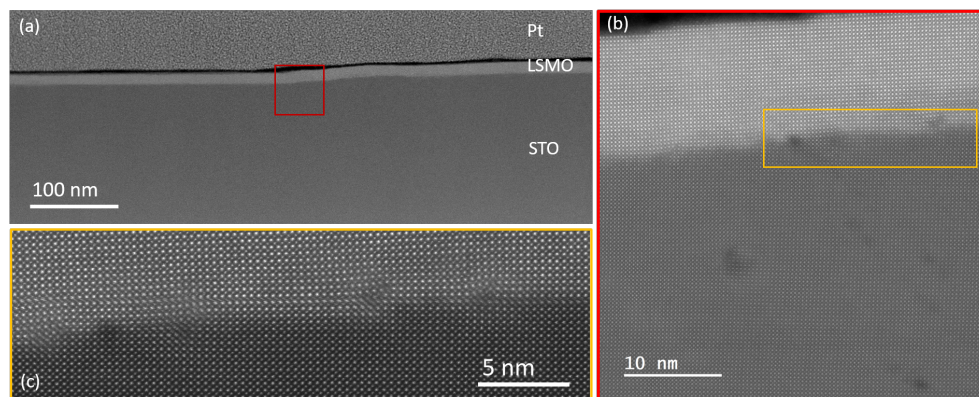


Figure 6.8: (a) Low magnification Z-contrast image of the FIB-cut lamella obtained from the zone indicated in Fig.6.7(a) around the step labeled 1. (b) Higher-magnification Z-contrast image of the red framed region marked in panel (a). (c) Atomic resolution image image of the yellow framed region marked in panel (b).

induced both by electrically stimulated oxygen migration as well as by the formation of the superficial scarring, we have carried out STEM investigations. To that end, a lamella was cut out using a focused Ga-ion beam (FIB) in the region indicated in Fig.6.7(a). This region of interest includes two steps triggered by the electro-thermal effect indicated with the labels 1 and 2. Fig.6.8 and Fig.6.9 summarize the most salient features observed in the vicinity of the surface scars 1 and 2, respectively. In Fig.6.8(a) a low-magnification Z-contrast image evidences the presence of a Pt top layer used to protect the LSMO/STO during FIB cutting process. The LSMO appears brighter than the STO substrate because it contains a heavier cation (La). Fig.6.8(b) shows a higher-magnification Z-contrast image of the red-framed region marked in panel (a) where the step 1 takes place. Note that in this region the LSMO/STO interface exhibits several defects and the nearby LSMO planes are highly tilted. Interestingly, dark spots running along the (101) crystallographic direction, and likely arising from dislocations, are embedded within the STO.[195] The darkish contrast of these defects suggests an increase of the unit cell around them (i.e. Sr-Sr distance) and therefore a contrast decrease. The proliferation of edge dislocation at the LSMO/STO interface is more apparent in panel (c) corresponding to the yellow framed region in panel (b). It is worth mentioning that the proliferation of these defects resulting from the electro-thermal stress is not visible away from the linear scars, where the LSMO layer shows a cube-on-cube epitaxial relationship with STO substrate

and a coherent and sharp interface absent of defects.

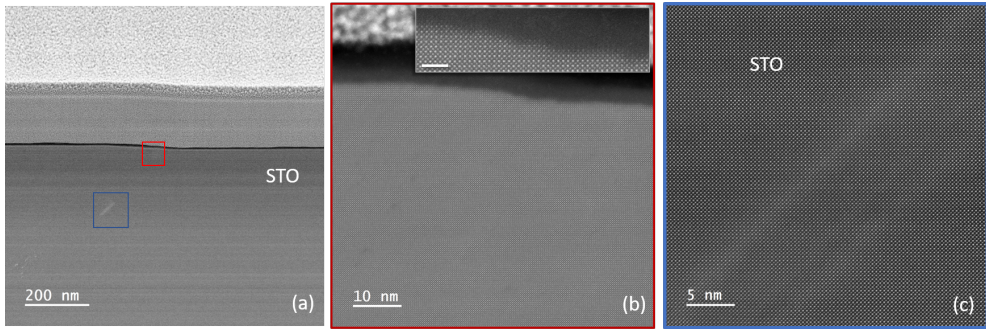


Figure 6.9: (a) Low magnification Z-contrast image of the FIB-cut lamella obtained from the zone indicated in Fig.6.7(a) around the step labeled 2. (b,c) Higher-magnification Z-contrast image of the red and blue framed regions marked in panel (a), respectively. Inset in (b) shows an enlarged image at the surface of the bare STO. Scale bar is 2 nm long.

In Fig.6.9(a) a low-magnification Z-contrast image of the step 2 is shown, along with a higher-magnification image taken at the red-framed region (Fig.6.9(b)) and blue-framed region (Fig.6.9(c)). Note that at this step there is no LSMO layer on top. The presence of dislocations embedded in the STO and emerging from the surface step is confirmed in Fig.6.9(b). In this panel, the Z-contrast image shows clear atomic scale steps at the surface. Faint contrast along the (101) plane likely related to a distortion of the STO matrix become apparent in Fig.6.9(c). The defects found within the STO substrate shown in Fig.6.8 and 6.9 run parallel to the (101) planes, which might correspond to the gliding planes, see Fig.C.4. Simultaneously acquired Electron Energy Loss Spectroscopy (EELS) reveals no significant changes in the fine structure of the Ti and Mn L-edges and the O K-edges of both the LSMO layer and the STO substrate when comparing regions at the steps/defects and far from them (see Annex C). This finding suggests that the scars do not involve oxygen vacancies far from the nucleation point.

We speculate that the pair of scars and the consequent proliferation of defects favor gliding planes along the (101) direction because of the shorter atomic distance along these planes (corresponding to lower activation energy for atomic diffusion). The fact that no correlated defects are observed in the manganite layer is consistent with a high temperature during the electro-thermal formation and the consequent plastic deformation of this layer. Nevertheless, the highest reached temperature does not seem to be enough to promote large diffusion of oxygen across the LSMO/STO interface. This

interpretation is consistent with the early report by Jiang et al.[78] on the thermo-mechanical plastic deformation in resistive switching devices made of vertical structures with Pt electrodes on oxygen depleted STO samples.

6.3 Samples

The $\text{La}_{0.7}\text{Sr}_{0.3}\text{MnO}_3$ thin films studied here were epitaxially grown by polymer-assisted deposition (PAD) on (001)- SrTiO_3 single-crystal substrates.[221] Individual solutions of the different metal ions were prepared by dissolving the corresponding La, Sr and Mn nitrates in water with ethylenediaminetetraacetic acid (EDTA, 1:1 molar ratio) and polyethyleneimine (PEI), Sigma Aldrich Ref. 408727, with an average molecular weight of 25.000 (1:1 mass ratio to EDTA). Each individual solution was filtrated using Amicon filtration units (10 kDa), and retained portions were analyzed by Inductively Coupled Plasma (ICP) Spectrometry (Optima 4300 DV ICP-OES Perkin-Elmer). Solutions were mixed according to the desired stoichiometry (La:Sr:Mn=0.7:0.3:1) and spin-coated on top of $5 \times 5 \text{ mm}^2$ (001)-STO substrates purchased from CrysTec GmbH, Germany. After the polymeric layer has been deposited, it is annealed in a horizontal tube furnace in oxygen flow at $950 \text{ }^\circ\text{C}$ for 90 min. The thickness of the grown LSMO epitaxial thin films was 12–20 nm as determined by X-ray reflectometry. The LSMO thin films were subsequently patterned by photolithography and dry ion-beam etching. The etching process etches away the uncovered LSMO film and a few tenths of nm of the STO substrate. For ensuring ohmic electrical contacts, 50-100 nm thick Ag electrodes were sputtered and annealed by heating in an oxygen-rich environment.

6.4 Summary

The main findings of this work is twofold. Firstly, we demonstrate, by means of concurrent optical imaging and electrical characterization, the directional nature of electrically stimulated oxygen displacement in LSMO. Evidence for this is found in the directional resistive switching noted around the nucleation point of electromigration and in real-time optical images which reveal a vacancy-rich propagating front spreading on the cathode side of a LSMO nanoconstriction. This observation goes along with the wealth of evidence for enhanced oxygen mobility in perovskite-like solid systems

and speaks for the potential electromigration holds to tailor the material properties.

Secondly, we show that at higher applied voltages, an interplay of vacancy ordering, electromigration and thermal effects causes extended changes in both the studied thin film and the STO substrate. This manifests as crystallographically aligned steps in the topography of the observed samples, originating at the conductive LSMO strip and extending along the STO wafer axes up to $\sim 30 \mu\text{m}$ away. HRSTEM imaging provides valuable hints to elucidate the origin of this superficial scarring and suggests a scenario where local electro-thermal stress generated under the narrowest section of the LSMO sample, is released by the generation of edge dislocations running along the crystallographic (101) direction of the STO substrate. We demonstrate that the observed linear steps are reproducible and precede dielectric breakdown of the system and do not correspond to electroformed conduction channels as reported in previous works.[44]

Controlled defect introduction into a material, separated or coupled with atomic migration effects could allow to surpass bulk doping limits when properly controlled, as shown in recent literature.[190, 262] In this sense, further study and mastery over the above reported defect generation procedure seems invaluable to attain further progress in device functionalization.

Part IV

Reversible Switching Behaviour

Electromigration-driven weak resistance switching in high-temperature superconducting devices

Based on: S. Marinković, D. Stoffels, S. Collienne, N. Mestres, A. Palau, and A. V. Silhanek, “Electromigration-driven weak resistance switching in high-temperature superconducting devices”, unpublished

Main Contributions: experiment design, electromigration experiments, data interpretation and presentation, writing

Auxiliary Contributions: finite element modeling

Layman's Overview: Continuous Low-Amplitude Switching

The ability to change the resistivity of any material with electrical control is limited in usefulness if we can only do it once and are constricted in our ability to reverse the effect on demand. In this chapter we demonstrate that using low amplitude electrical stimulation, it is possible to keep the changes in the resistivity of the material limited to a few percent. This gentle electromigration allows us to recover the original resistivity of the material. Interestingly, we observe

no change of the superconducting properties of YBCO, indicating that whatever change we are affecting in the film occurs in a separate region of the crystal from the bulk, leaving a percolative superconducting circuit throughout.

The oxygen diffusion through the material is validated via a phenomenological numerical model, and we observe clear evidence of a back-and-forth movement of the oxygen, evidenced by electrotransport measurements.

The preliminary results in reversible, current driven switching shown in Sec.B.2 illustrate that current driven memristive behavior in YBCO is achievable. In this chapter, we investigate the two-terminal resistive switching properties of YBCO when the system is driven by electric current. We perform all-electrical switching to characterize and control low-amplitude resistance changes, and we implement finite element modeling to explain how these effects can be properly accounted for by oxygen-vacancy counterflow induced by electric bias.

Introduction

This chapter aims to investigate low-amplitude resistance switching in YBCO. Most importantly, the method only relies on electrical current flowing directly through the material to modulate the oxygen doping, all via the phenomenon of selective electromigration. We explore the possibility of inducing a small resistance increase ($\sim 1\%$) followed by a recovery to the initial resistance by applying a bipolar bias current of constant amplitude. We unambiguously demonstrate that the resistance changes are associated with back-and-forth oxygen displacement over long distances ($\sim 10\ \mu\text{m}$) driven by a current-stimulated diffusive mechanism. This slow switching process ($\sim 1 - 20\ \text{s}$) can be repeated 10^4 times with high fidelity and little variation of the overall resistance of the device. This fact seems to point to a negligible oxygen loss from the device. Low-temperature measurements show that the procedure also works at 100 K but requires higher drives. The induced small resistance changes have no impact on the superconducting transition. The periodic albeit non-monotonous pattern displayed by the time evolution of the resistance can be properly captured by finite element modeling taking

into consideration the interplay between oxygen diffusion, heat equation, a resistivity which depends on the oxygen content, and the specific sample geometry.

7.1 Results and Discussion

In order to investigate the degree of control, reversibility, retention, and endurance of the resistive switching caused by selective current-induced oxygen vacancy (V_O^{2+}) electromigration, the following protocol was implemented (see Sec.2.2.2):

First, a constant amplitude current of $I_{app} = +5.8$ mA is applied across the constrictions while the resistances of each individual bridge are monitored simultaneously. After an initial training phase dominated by thermalization (see Annex I), we set a predefined base resistance R_0 as 1% above the low-current resistance of the central bridge. After that, the central resistance R_C starts exhibiting a dome-shape evolution (see green background panels in Fig. 7.2). The current polarity is reversed upon reaching R_0 on the falling slope of the dome-shaped curve of R_C .

The zooms on the middle column of Fig. 7.2 show the resistive response of the three bridges for one period of the square-wave excitation (highlighted with a darker background in Fig. 7.2(a-d)). The observed response is a direct manifestation of an oxygen-vacancy counterflow swaying from left to right and vice-versa. In the positive half-period ($I_{app} = +5.8$ mA), the dome-shaped curves of the resistance in the central junction (Fig. 7.2(b)) reveal a deoxygenation front passing through it. The left bridge exhibits a nearly linear increase of resistance as this region becomes progressively populated with oxygen vacancies (Fig. 7.2(a)). Concomitantly, oxygen atoms migrate towards the symmetrically opposite bridge on the right, which naturally explains its decrease in resistance (Fig. 7.2(c)). Upon inverting the current polarity (Fig. 7.2(d)) on the second half-period ($I_{app} = -5.8$ mA), the outer bridges reverse roles, and the central

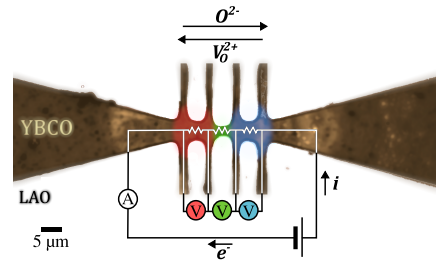


Figure 7.1: Sample layout in the form of a triple-constriction where each of the three bridge resistances can be accessed using two of the perpendicular terminals. The color code associated with the three bridges will be respected throughout the manuscript. The battery indicates what is defined as a positive voltage configuration.

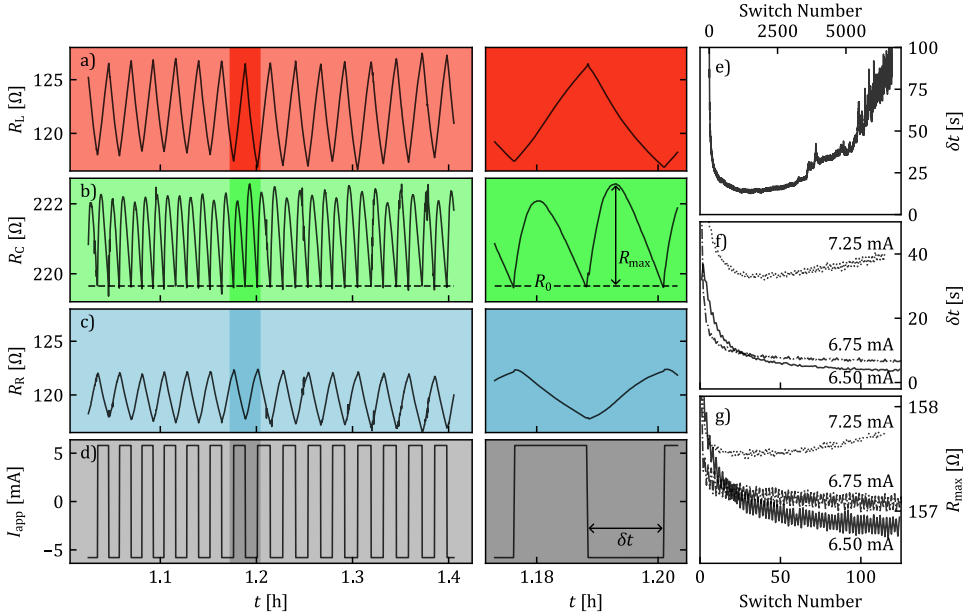


Figure 7.2: Reversible resistive switching in a micropatterned YBCO film via square wave current of 5.8 mA amplitude and varying period. The red, green and blue panels correspond to the negative electrode (left), center and positive electrode (right constriction) resistance vs time measurements, while the gray panel shows the applied current. The switching resistance criterion (R_0) is set manually after a short initialization phase and is shown with the dashed horizontal line. This criterion is only checked in the middle constriction and determines the position at which the current polarity is switched. Note that the resistances of the left and right constrictions follow opposing trends, while the central constriction has a dome-shaped $R(t)$ curve. This is explained by an oxygen-vacancy counterflow following the current direction where the deoxygenation front repeatedly passes through the central constriction during switching. The insets are zooms on the highlighted sections of the data set. Experiments are performed in ambient conditions. (e) Evolution of the half-period δt (see definition in panel (d)) for a sample switching in a bipolar square wave current bias for ~ 7000 switching cycles. Polarity is switched whenever R_C returns to a preset R_0 , corresponding to 1% increase of resistance from pristine state. (f) Evolution of δt for three different current amplitudes performed on the same sample, the corresponding R_{max} evolution is shown in (g). These measurements were performed in the same device in chronological order starting from the lowest current and progressively increasing the current.

bridge exhibits a new dome as the deoxygenated phase expands in the opposite direction. Note, however, that the resistance dome on the central

bridge reaches a different local maximum amplitude R_{\max} depending on the current polarity and that the R_C domes have a generally slanted shape with the rising side being steeper (positive skewness). This periodic resistance cycling can be repeated without any observed structural damage for a large number of cycles. The maximum number of switching iterations we have tested is $\sim 10^4$.

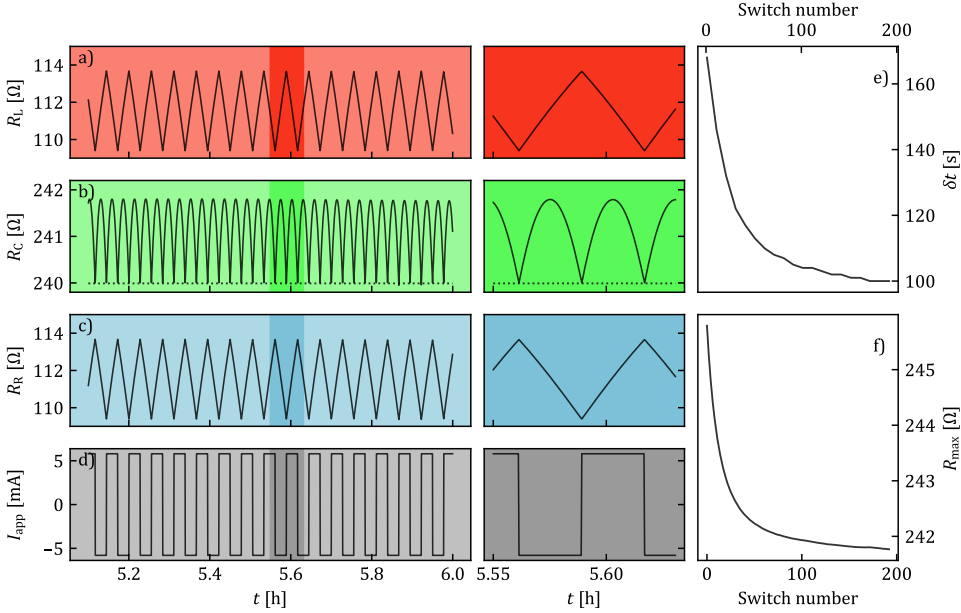


Figure 7.3: Finite element modeling of the experimentally observed switching behavior in YBCO thin film constrictions. The numerical model captures both the regular dome shape of R_C (b) and the opposite trends in R_L (a) and R_R (c), as well as the decreasing values of δt (e) and R_{\max} (f).

It is worth noting that the amplitude of the resistance oscillations in the left and right bridges are unequal, even though the number of vacancies/atoms swaying from one side to the other remains the same. This difference reflects an asymmetry in the affected volume between the respective left and right voltage contacts which could arise from uncontrollable inaccuracies in the patterning process or simply be imposed by the initial current polarity.

We should stress the fact that the criterion implemented for switching current polarity is not a fixed period but rather the condition that R_C returns to R_0 . In other words, neither the period of the square-wave nor the amplitude of the resistance modulations are controlled parameters. This is better illustrated by tracking the evolution of the half-period δt as a function of the

switching number, as is shown in Fig.7.2(e). Note that δt exhibits an initial sharp decrease before reaching a stable value. We speculate that this behavior may be caused by the formation of oxygen diffusion channels which, once established, are repeatedly reused during subsequent cycling, somewhat similar to the forming phase in filamentary memristive devices.[10] Eventually, after several thousand switches, irreversible modifications seem to clog the channels and δt tends to slowly rise.

Fig.7.2(f,g) show the evolution of δt and R_{\max} as a function of switch number for several current amplitudes. These measurements were sequentially performed on a single sample. For the highest current amplitude (7.25 mA) a rise in δt occurs after ≈ 25 switches, whereas for lower currents the initial decrease in δt and R_{\max} are much more pronounced and a subsequent rise is expected to occur later (i.e. at higher switch numbers). This is consistent with the interpretation, that higher drives induce more defects and thus lead to a premature failure of devices.[191]

Attempts to reproduce reversible resistance switching at low temperature ($T = 110$ K) show successful results, although the current needed to produce similar resistance change roughly doubles the one at room temperature. In all cases, the weak modifications induced in the normal state resistance by the switching process have no impact on the superconducting transition, confirming that the maximum induced displacement of oxygen atoms in these experiments represents a minor perturbation, which in turn ensures reversibility.

7.1.1 Numerical results

Let us now apply finite element modeling (FEM) of electrically driven oxygen diffusion in order to gain further understanding on the link between microscopic mechanisms and electro-transport measurements. To that end, we set up a simulation that mimics the experimental protocol presented above and implemented it to reproduce the data of Fig.7.2. As in the experiment, the two control parameters are the base resistance R_0 , corresponding to the R_C value at which the polarity switch is triggered, and the applied current I_{app} .

The resulting resistance evolution for the three bridges obtained from the FEM is presented in Fig.7.3. They clearly capture the most significant experimental features of the device shown in Fig.7.2, hence supporting the interpretation of oxygen- V_O^{2+} counterflow as the main mechanism at the origin of resistive switching. Panels (e,f) also reproduce the settling of the value of $R_{\max} \sim 242 \Omega$ and $\delta t \sim 100$ s after 200 switching events, in accordance with the initial trend reported in Fig.7.2(e-g).

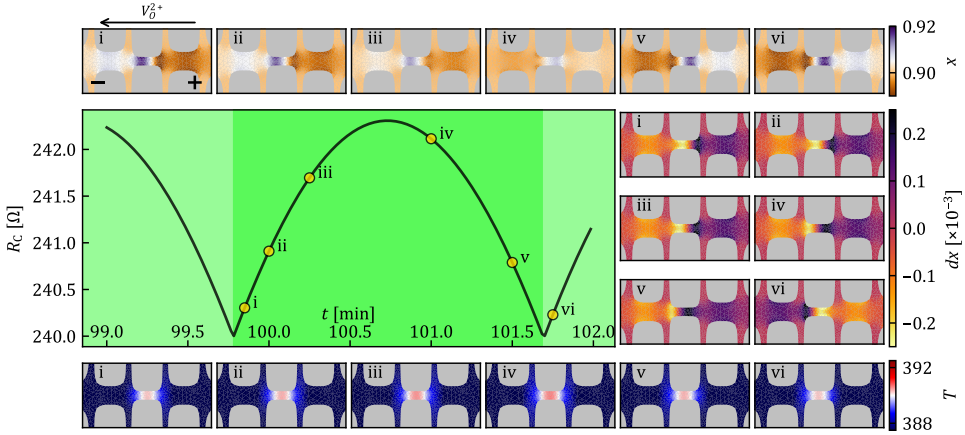


Figure 7.4: Close up of the evolution of a single dome $R(t)$ from the finite element model. Oxygen distribution maps (in x) are shown in the upper row, oxygen distribution differential maps (dx) are depicted to the right and temperature profiles (T) are shown in the lower row, for the points indicated by the yellow circles. The highlighted section corresponds to a positive current polarity pulse.

Let us now dig further into the time evolution of the oxygenation and temperature during the switching process, as described by the numerical modeling. To that end, in Fig.7.4 we display a single $R_C(t)$ dome obtained for $I_{app} = +5.8$ mA and $R_0 = 240 \Omega$, after ~ 1.5 h of periodic switching. The top row shows snapshots of the oxygen content as described by the variable x for specific times labeled (i-vi). Panel (i) indicates the polarity during the highlighted dome. This polarity is inverted upon reaching panel (vi). The right panels show dx (or similarly dx/dt), the local change of x between a given time-step and the previous one obtained 100 ms before. The bottom row shows the temperature maps for the same instances (i-vi).

The initial distribution of oxygen concentration x shown in panel (i), reveals a large zone of rich oxygen content (blue) at the central constriction coexisting with a small (white) stripe of slight oxygen depletion, naturally explaining the low resistance value. Note that the right bridge exhibits depletion of oxygen (brown) whereas the left bridge is oxygenated but less than the central bridge. The polarity indicated in panel (i) pushes the V_O^{2+} to the left and the oxygen ions to the right. This causes the white stripe at the central constriction to move towards the left, whereas the blue zone will tend to displace towards the right side, as shown in panels (ii-iv). At point (iv) the central bridge is more uniformly depleted in oxygen, which accounts for the

high resistance value. At point (v) the situation is nearly mirror symmetric to that of picture (i). In other words, in the rising branch of the dome (i-iii) the center constriction is mostly a vacancy sink, then it becomes relatively equally distributed in (iv) and finally an oxygen sink in (v). These features become more compelling by plotting the differential of x , that is the change in oxygenation level from one simulation step to the next.

The dx maps show the rate of change of the oxygen concentration, with yellowish color when the rate is negative (oxygen content decreases) and darker color when the rate of change is positive (oxygen content increases). Since the polarity is kept constant for the considered dome, this rate of change remains roughly the same for (i-v). Note, however, that changes operate along the central bridge, averaging to negative rate of change for (i-iii) and positive for (iv,v). When the polarity of the current changes in the next dome (vi), the rate of change changes accordingly. Note that the dome is perfectly symmetric indicating that the initial current polarity does not introduce any asymmetry in the migration process. Detailed animations showing the time evolution of the oxygenation and temperature are presented in the Supplementary Information (Annex II).

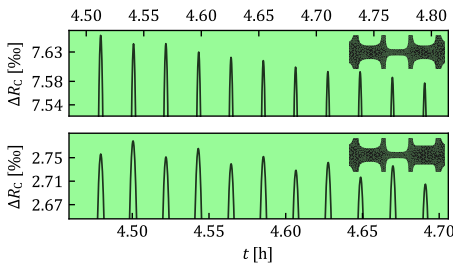


Figure 7.5: Section of a finite element modeling simulation on a symmetric (upper panel) and an asymmetric (lower panel) mesh where the right constriction is $1 \mu\text{m}$ wider than the left one (see inset). The asymmetry induces an alternating trend in the evolution of R_C where positive polarity periods show higher R_{max} . The low observed amplitude results from the relatively long time needed for the system to settle.

Fig.7.4 also reveals the presence of wave-like deoxygenation fronts in the x and dx images, similar to those previously reported in Ch.4. The wave nucleates at points of large flux divergence, that is, at the junctions of the constrictions and at the voltage lines. The bottom row shows that the temperature profile of the sample remains roughly homogeneous, with peak temperatures of ~ 90 K above room temperature, replicating the experimental observation elaborated upon in Annex I. As expected, close to the peak of the dome at point (iv) a higher resistance implies more Joule heating and consequently higher temperature.

Although the proposed model satisfactorily accounts for the experimentally observed behavior of the sample, the simulations do not seem to replicate all details such as the alternating

R_{\max} values. In order to explain the origin of the varying dome height for positive and negative bias, as shown in Fig.7.2, we ran FEM simulations on an intentionally asymmetric device and compared it to a symmetric one, as depicted in Fig.7.5. In the asymmetric structure (lower panel), the right constriction is $1 \mu\text{m}$ wider than the left one. Under this circumstance, the right constriction starts in a lower resistance state and never reaches the same peak oxygenation state as the left one, which is well illustrated in Annex II. During positive polarity, oxygen flows left to right, but the flow is limited due to reduced current density and lower temperature in the wider (right) constriction. On reversal, the wider constriction, which is colder and is comparably deoxygenated, traps vacancies and in this way extends the oxygen flow in the left constriction, leading to a larger reduction of R_C during negative pulses. Thus, the experimentally observed alternating R_{\max} values could be explained by invoking geometrical asymmetries or likely other sources of asymmetries in the microstructure.

7.2 Samples

Samples consist of 50-nm-thick films of *c*-axis oriented YBCO, epitaxially grown on LaAl_2O_3 (LAO) substrates and patterned into a triple-constriction design shown in Fig.7.1. The samples were grown by chemical solution deposition (CSD) and exhibited sharp superconducting transitions at 90 K (corresponding to $\delta=0.05$). The inner constriction (green) is $1 \times 5 \mu\text{m}$ and the outer ones (left-red and right-blue) are $3 \times 5 \mu\text{m}$. The samples were subjected to high current densities (up to 14 MAcm^{-2}) corresponding to colossal power densities ($P \sim 5 \text{ GW/cm}^3$).

7.3 Modeling

The FEM model was constructed like discussed in Sec.2.4. The crystal orientation dependent diffusivity and resistivity do not make a comeback, and the model is streamlined to calculate continuous change in the system. This iteration of the model is operated only by COMSOL, without a MATLAB intermediary script.

7.4 Summary

We investigated the reversible (low on-off amplitude) resistive switching by selective electromigration of oxygen in YBCO through a simple electrical

protocol. The methodology can be easily replicated and applied to a broad family of oxide materials.[73, 171] We study the resilience of these devices to cyclic stress and the evolution of the resistance of multiple constrictions in series. The observed oxygen-vacancy counterflow is validated via finite element modeling. The presented results provide insights into the nature of the wavelike movement of the deoxygenation front and local temperature under low-frequency AC current stress.

The presented research supports the interpretation of electrical oxygen- V_O^{2+} redistribution as the driving mechanism for switching. It has been demonstrated that electric field-induced transition to high resistance states occurs through the generation of $YBa_2Cu_4O_7$ (Y124) intergrowths with a large number of oxygen vacancies.[197] Although we expect that a similar mechanism applies when electromigration leads to large on-off amplitudes[72], it remains unclear in the present case if clusters of Y124 phase develop or a more uniform redistribution of oxygen takes place. Judging by the insensitivity of superconducting transitions to the actual normal state resistance, we believe that disconnected clusters or filaments of depleted oxygen concentration coexist with optimally doped regions. FEM simulations were able to qualitatively, and to a certain extent, quantitatively reproduce the experimental findings. In the present report, the period of the dome $\delta t \sim 20$ s and the propagation distance of the deoxygenated front $\sim 5 \mu\text{m}$ points to a very slow diffusion process. It remains to be explored the maximum switching speed either by electric gating or electromigration. The phenomena of electromigration at ns time scale is expected to generate little Joule heating thus requiring substantially higher current pulses to achieve similar resistances changes as the one explored in this work. As a last remark, it is instructive to point out that the trade-off between large amplitude switching and reversibility suggests that electromigration in YBCO may, at the μm scale investigated here, not represent a competitive alternative to memristive effect based on electric-field gating. The latter permitting much larger amplitude variations than the ones here reported and yet within a reversible regime. [192] Current-driven switching still offers advantages in ease of implementation through simpler fabrication and a lower number of terminals, as well as the possibility to more comfortably access a higher number of resistive states in the devices, which still may make them appealing for neuromorphic applications.

Part V

Conclusions

General Conclusions

The results presented over the course of this text provide ample evidence for the feasibility of electrical control as a methodology by which we may tune the oxygenation (and consequently the doping) of functional perovskite oxides. To this end, we demonstrate that a simple planar sample design, with appropriate electrical controls, is sufficient.

In Part II we study the mechanisms behind current driven oxygen diffusion in YBCO, the chosen model material. The key property that allows us to reveal the displacement of oxygen vacancies is the oxygenation-dependent reflectivity observed in YBCO. The initial findings discussed in Ch.3 in simple bowtie constrictions informs us of the necessary current densities needed to achieve the effect and provide justification for the study, motivating us to move onto a triple constriction design to study the directionality of the driven diffusion effect. The more intricate sample design shows that the oxygen- V_O^{2+} counterflow is dependent on polarity of the current, allowing for localized modulation of both the resistivity ρ and superconducting critical temperature T_c . The oxygen diffusion is confirmed beyond doubt by carrier density measurement, μ Raman spectroscopy and photoconductivity experiments, all of which nicely fit previously reported behaviors. Subsequently, a phenomenological description based on FEM is developed and validated in Ch.4. The proposed model captures all macroscopic features of the phenomenon of selective oxygen electromigration in the perovskite oxide, including both the changes of the transport and superconducting properties and the modulation of the oxygen levels. The theoretical results are readily compared with optical images captured during the experiment. The question of anisotropic oxygen diffusion in YBCO is addressed in Ch.5, where the importance and dominance of thermal effects is illustrated. Despite the

faster diffusion of oxygen along the b axis YBCO, we have shown that the more resistive transport along a lends itself to lower electromigration current amplitudes due to the dominant Joule heating.

Part III (Ch.6) unveils similar behavior in LSMO thin films, indicating a general trend. Transport measurements and optical imaging indicate a consistent directional, driven diffusion behavior, limited only by the more resistive nature of LSMO thin films. Interestingly, we find that the electrothermal stress in the LSMO films causes defect formation in the STO substrate. These defects are strictly distinct from previously reported electroformed conduction channels in STO and we characterize them as originating from edge dislocations. The reproducibility of this kind of defect formation is illustrated on a large number of samples and their orientation along known crystallographic directions offers interesting potentialities for nanofabrication and structuring.

Building on the finding of Part II, in Part IV (Ch.7) we show that by limiting the amplitude of the resistance change by only weakly modifying the oxygenation state of our film we may reversibly switch the resistance state of the devices up to $\sim 10^4$ times. The highly reversible behavior is easily implemented and controlled and may offer possible applications in analog and neuromorphic computing, while maintaining the pristine T_c of our films. Additionally, these findings mark the maturation of our phenomenological model, as we implement it in a streamlined and optimized manner that allows us to simulate thousands of individual switching events.

Throughout this thesis the electrically driven oxygen diffusion in perovskite thin films has been studied and applied in devices. The findings seem to be general to the perovskite oxide family and beyond, based on known behaviors in other oxides. While the amplitude of the resistance change we demonstrate in our devices is not competitive with reported binary oxide switches, the special functionalities offered by complex perovskites make them interesting for other applications like sensing and analog computing. Additionally, downsizing and alternative sample designs might still show them to be viable candidates in other applications. The conclusions we make also allow for implementations of diffusion based devices built from earth-abundant materials that can contribute to solving the technological challenges of the coming years. Finally, the phenomenological model validated throughout the studies collated in the text is now mature enough to be offered for predicting behaviors of other materials.

8.1 Perspectives

Open questions remain on the nature of the driven, selective diffusion process that has been studied in the course of this PhD thesis. For one, the temporal limitations of the diffusion process are not well understood, and one is to assume that there is a lower limit to how quickly the oxygen- V_O^{2+} exchange may be induced. For this purpose, very short pulse measurements are being executed with collaborators at the time of writing of this thesis. The current expectation, supported by preliminary findings, is that with decreasing pulse duration the necessary current density for electromigration should be increasing. It remains to be seen what the functionality of this relationship is and whether at short enough pulses (\sim ns) a new athermal regime develops.

Furthermore, while oxygen is by all indications the most diffusive species in most, if not all, perovskite oxides, the diffusion of the cations in the structure is ill understood. The contribution of this kind of diffusion and the possibility to change the nature of the diffusing species might have interesting technological implications, and would allow for very fine control in the phase composition of thin films.

Whether the selective nature of driven oxygen diffusion is truly a general property of perovskite oxides and other complex oxides is an interesting subject worthy of study both for its technological implications and fundamental interest. Preliminary results performed in cobaltates show that the same protocols discussed throughout this thesis are applicable at least in that class of materials, with similar behavior being expected in other oxide crystals.

The effect of substrate induced strain on perovskite thin films under electrothermal stress has been touched upon in Part III but remains an open topic. Preliminary results on manganite perovskites grown on a number of substrates show that electromigration current density indeed depends on the nature of the substrate-induced strain, but no conclusions can be made until further experimental measurements are in.

Recent reports in novel, multiterminal sample architectures have been demonstrated as being able to direct the effects of electromigration in a significantly more targeted manner, in metals.[264] Transitioning to a multi-terminal layout could thus prove to be a way to localize the effects of selective electromigration in perovskite oxides for better phase change control or more reliable switching.

With the current characterization it remains unclear whether the oxygen redistribution and the associated phase change occurs in filaments or through a moving phase interface. The filamentary mechanism,[23] is common in

many oxides including those of titanium and vanadium,[45] which would justify a more microscopic characterization of the effect observed in the complex oxides studied here. Following this, one may question whether the switching mechanism might be influenced by sample geometry or environmental conditions.

Finally, it remains difficult to distinguish the effects of current J and electric field E have on the diffusion ions in studied crystals. The oxides we present here are worse conductors than metals making it even harder to claim separation between these two effects. Even with this limited understanding, electrical drives have been utilized in studying the phase diagrams of perovskites.[58, 59] Full understanding of electrically driven doping modulation in perovskite oxides would be a leap forward in material science allowing unprecedented levels of phase control in single devices.

Part VI

Appendices

A.1 Inhomogeneous temperature distribution along the bridge before electromigration

The nearly parabolic increase of resistance as current increases $R(I)$ shown in Fig.3.2 2a is caused by Joule heating. This interval of the $R(I)$ curve is reproduced as a continuous blue line in Fig.A.1. By performing finite element simulations of the heat transport equation using the commercial software COMSOL[224] we are able to fit the $R(I)$ dependence and thus estimate the maximum temperature at the constriction. The layout of the modeled system consists of a transport bridge with the exact same geometry as the real sample and lying on top of a LAO substrate at $T = 105$ K. The resistance temperature coefficient $\alpha = 8.962 \cdot 10^{-3} \text{ K}^{-1}$ and the sample resistivity $\rho = 237 \mu\Omega \text{ cm}$ at $T = 105$ K have been experimentally determined, whereas the thermal conductivity of the sample and the substrate have been taken from Ref.[265] and Ref.[250], respectively. The results of the simulations shown by square symbols in Fig.A.1 nicely reproduce the $R(I)$ dependence followed by the experimental data. Figure S1b shows the inhomogeneous temperature distribution for an applied current $I = 12$ mA.

A.2 Resistance changes after irreversible electromigration

Fig.3.3 shows the change in resistance for the three bridges connected in series after a quasi-reversible electromigration process. When the electromigration

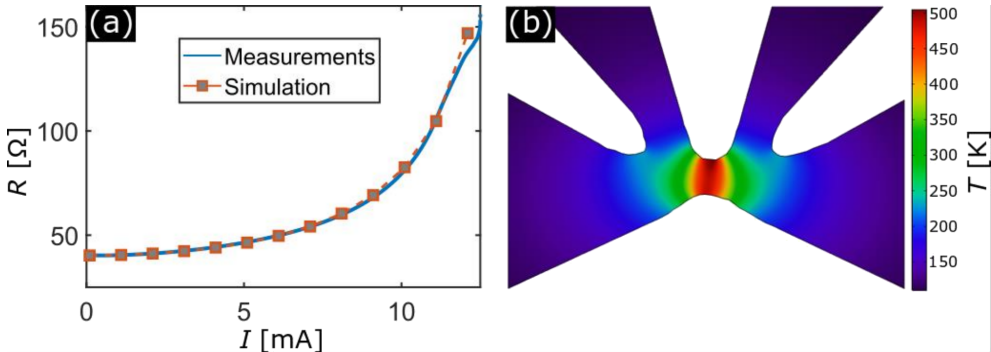


Figure A.1: (a) Non-monotonous resistance rise as a function of current during the first electromigration process. The continuous blue line represent the experimental data and square symbols connected by a dashed line correspond to finite element simulations. (b) Simulated temperature distribution of the bridge for an applied current of 12 mA.

is continued further, more radical changes are observed with respect to the pristine sample. Fig.A.2 shows the normalized resistance obtained in the left, central, and right bridges after irreversible electromigration. The inset shows an optical image of the final state after this electromigration process. Note that the resistivity of the right bridge has substantially decreased with respect to the pristine sample.

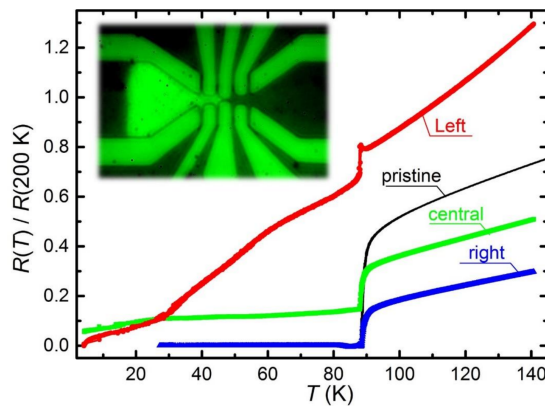


Figure A.2: Resistance $R(T)$ for the left (red), central (green), and right (blue) bridges, normalized by the $R(200 \text{ K})$ of the pristine sample. For the sake of comparison, the universal response for the pristine sample (shown in Fig.3.3) is replotted here with a black line. The inset shows an optical image of the final state after the electromigration process.

A.3 Raman Spectra

Fig.A.3 shows some representative Raman spectra, obtained for different oxygen doping levels. It is clearly observed that the O(4) phonon mode is shifted to lower frequencies as the oxygen content is reduced. The in-phase O(2,3) mode at 435 cm^{-1} is not easily observed in optimally doped spectra due to its temperature dependence, which makes it weak at room temperature.[266] However, its intensity increases in the oxygen deficient regions which allow disorder induced $q \neq 0$ scattering to be observed in the Raman experiments.[235]

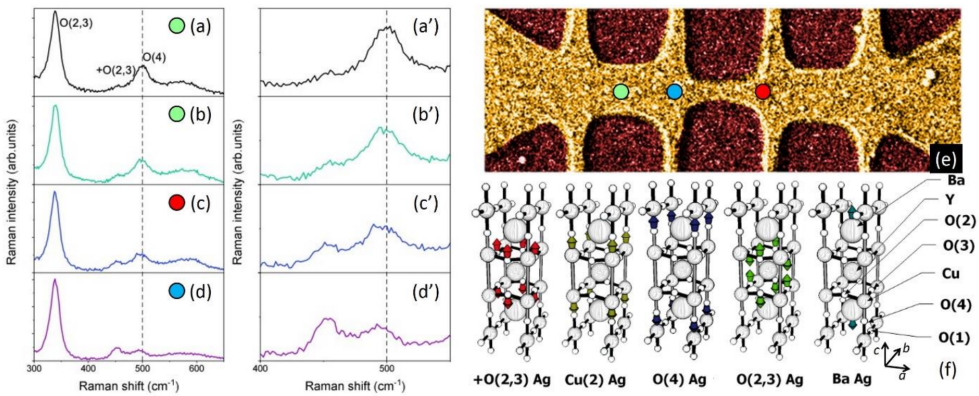


Figure A.3: (a-d) Typical room temperature μ Raman spectra obtained at different spots along the transport bridge as indicated by the colored circles in panel (e). Panels (a'-d') show a zoom in the data presented in panels (a-d). The spectrum in panel (a) corresponds to the pristine sample whereas those in panels (b-d) correspond to the electromigrated sample. (f) Optically active Raman modes along the crystallographic c-axis for YBCO. The apical O(4) Ag phonon mode occurs at 500 cm^{-1} .

A.4 Scanning Electron Microscopy Imaging

In order to further assess the changes produced by the electromigration process, we carried out *ex situ* optical and electron microscopy imaging. Fig.A.4 shows dark field (a) and bright field (b) optical microscopy images without analyzer and illuminated with polarized light. Dark field imaging permits to collect scattered light and thus reveals the surface roughness. The fact that the modification of the material is not evidenced by this method

seems to indicate that no morphological changes have occurred to the sample. In contrast to that, bright field imaging which is related to the reflectivity of the sample clearly unveils the change of conductivity of the affected regions.

Scanning electron microscopy images collected by InLens secondary electron (SE) and Everhart-Thornley (ET) detectors, are shown in panel (c) and (d), respectively. The InLens detector collects mainly secondary electrons which are generated near the upper region of the beam-sample interaction volume and therefore provide direct information on the sample's surface. No morphological changes are seen in these images. However, the region affected by EM is clearly revealed with bright contrast.[267, 268] It is worth emphasizing that the changes observed in the InLens SEM images cannot be ascribed to thermal effects due to Joule heating otherwise the voltage leads should have been also affected, which is not the case. More precisely, clear filamentary and highly inhomogeneous modifications of the material are observed in the InLens SEM images. The ET detector collects electrons which are also produced by backscattered electrons as they exit the specimen and therefore its inherent lower resolution make less prominent the inhomogeneity, as shown in Figure S4d.

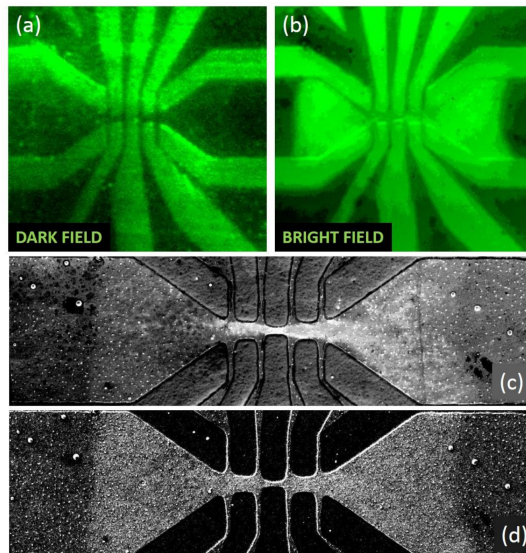


Figure A.4: Dark field (a) and bright field (b) optical microscopy images. Scanning electron microscopy images collected by InLens secondary electron detector (c) and Everhart-Thornley detector (d). For the SEM images an acceleration voltage 5 kV, aperture size 30 μm , and working distance 6 mm has been used.

A.5 Realtime tracking of the electromigration process

The video published with Ref.[72] shows the time evolution of the electromigration process as evidenced by a bright field optical microscopy imaging (upper panel), while monitoring the central bridge resistance (lower left panel) and the current flowing through the device (lower right panel). These measurements have been acquired at 105 K.

B.1 Realtime tracking of the DC electromigration process

The animation available in the supplementary information published with Ref.[74] shows the time evolution of the DC electromigration process as evidenced by a bright field optical microscopy imaging (upper left panel) and differential imaging (upper right panel), while monitoring the left, central and right bridge resistances (lower row). These measurements have been acquired at ambient conditions and constant current of 8 mA.

B.2 DC electrical stress under switching polarity

As a complement to the experiment of DC stress described in the Fig.4.2, we investigated the effect DC stress of opposite polarities on the oxygen diffusion. To that end, a device identical to the one used in unidirectional DC stress, is biased with a current of 5.8 mA which polarity changes every ~ 450 s as shown in Fig.B.1, where red, green, blue background indicates left, central and right bridge, respectively. The polarity + corresponds to current and oxygen vacancies flowing from right to left. The observed opposite behavior between left and right bridges can be naturally explained by the counterflow of oxygen vacancies and oxygen atoms. The central bridge exhibits local maxima related to an oxygen vacancy front propagating back and forth. Indeed, the rising part corresponds to an oxygen depleted zone entering the central bridge while getting re-oxygenated at its tail. When this train reaches the central bridge then the resistance starts dropping. The global tendency

observed in the red and blue panels compared to the green one indicates a progressive accumulation of oxygen in the central part coming from nearby bridges.

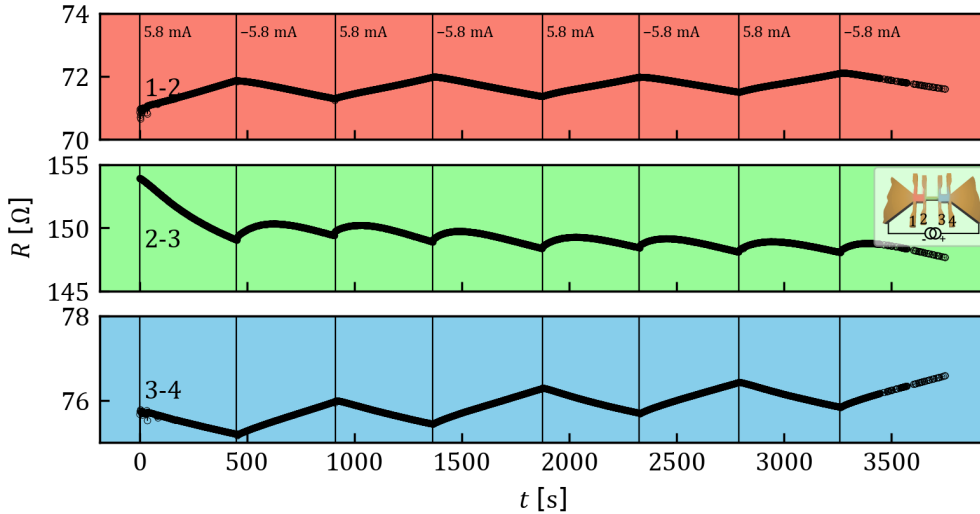


Figure B.1: Experimental evolution of the resistance as a function of time under DC stress of 5.8 mA of periodically switching polarity. The inset shows the polarity of the positive current and the color code associated to each bridge. These measurements were performed at room temperature and under ambient conditions.

B.3 Realtime tracking of the AC electromigration process

This animation, available in the supplementary information published with Ref.[74], shows the time evolution of the AC electromigration process as evidenced by a bright field optical microscopy imaging (upper panel right column) and differential imaging (middle and lower panels right column), while monitoring the current fed through the bridges (upper panel left column), the total resistance picked up at the outer voltage contacts after the pulse (central panel left column) and the total resistance during the pulses (lower panel left column). These measurements have been acquired at ambient conditions.

B.4 Oxygen concentration, temperature, current density and electric field maps during AC electromigration process

These videos (available with Ref.[74]) show the numerically modeled oxygen concentration (upper left), temperature (upper right), current density (lower left) and electric field (lower right) maps during AC electromigration process corresponding to Fig4.5, using a fixed and an adaptive color scales.

B.5 Influence of x_{max} , x_0 and δx_0 on the oxygen diffusion

Additional simulations were undertaken to investigate the effect of the parameters x_{max} , x_0 and δx_0 . To that end, in Fig.B.2 we plotted the resistance at remanence (i.e. after each current pulse) R_{min} and during the pulse R_{max} as a function of a pulsed current amplitude that increases linearly from zero and reaching a maximum value of 8 mA at pulse 40 and then decreasing linearly down to zero at pulse number 80. The results for x_{max} are shown in panels (a) and (b). As expected, a high value of x_{max} allows to reach higher oxygen concentrations and thus lower resistances (panel (a)). The Joule effect is therefore reduced as shown by the lower maximum temperatures reached for high values of x_{max} (panel (b)). Panels (c-f) show no differences in the final state reached and indicate that the influence of the parameters x_0 and δx_0 is minor in our model.

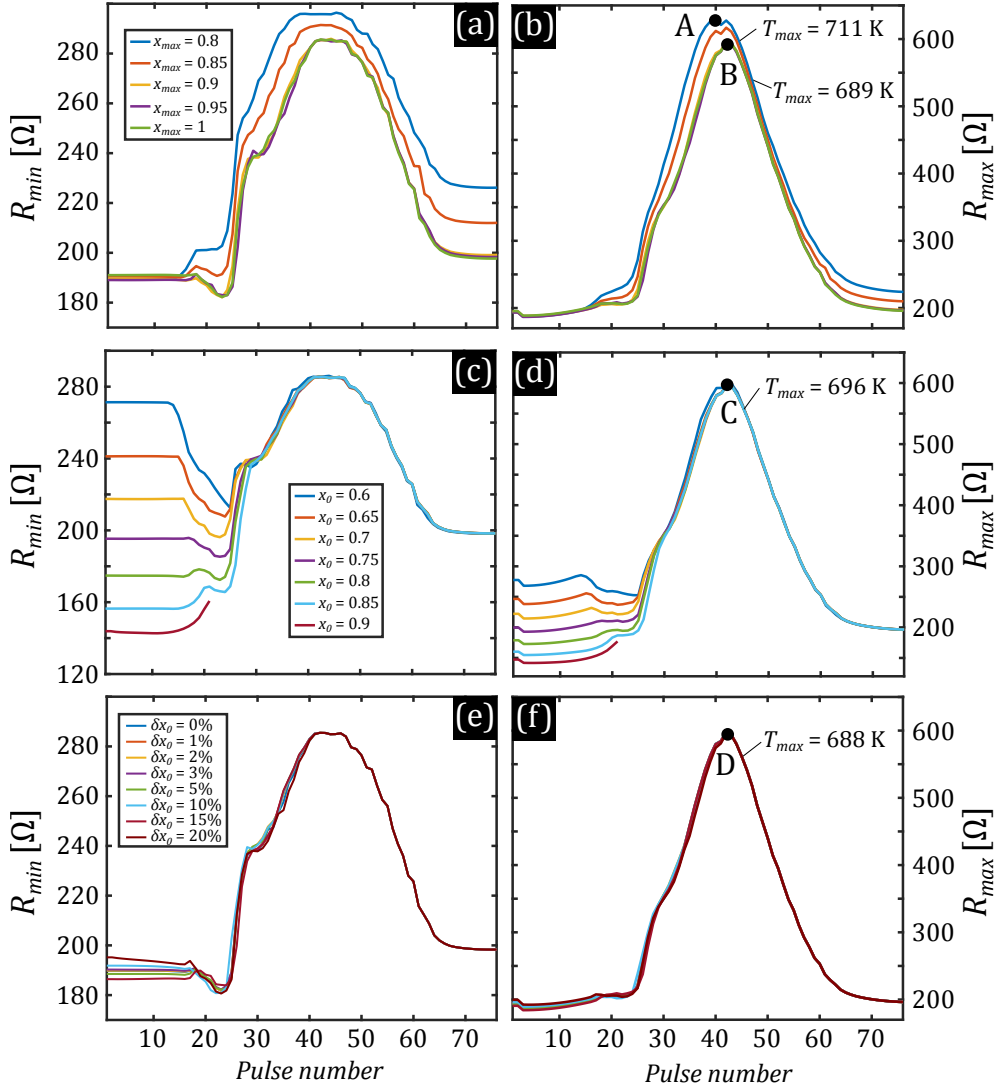


Figure B.2: Panels (a) and (b), (c) and (d), (e) and (f) show the evolution of R_{min} and R_{max} for different values of x_{max} , x_0 and δx_0 respectively. Unless otherwise stated, the values of the parameters are given by : $E_a = 0.4$ eV, $x_0 = 0.76$, $x_{min} = 0.5$, $x_{max} = 0.95$ and $\delta x_0 = 5$ %.



Appendix to Ch.6

C.1 Finite Element Modeling

The Poisson equation is solved to obtain the electric potential distribution in the sample:

$$\nabla^2 V = 0. \quad (\text{C.1})$$

Note that the right-hand side of equation (C.1) is set to zero in order to guarantee charge neutrality throughout the device. The electric field $\mathbf{E} = -\nabla V$ is related to the current density \mathbf{J} by Ohm's constitutive equation $\mathbf{J} = \mathbf{E}/\rho(T)$ and does not take into account the ionic current whose contribution is negligible.

In addition, the heat equation (C.2):

$$\rho_m C \frac{\partial T}{\partial t} = \kappa \nabla^2 T + \rho(T) \mathbf{J}^2, \quad (\text{C.2})$$

is solved in order to obtain the spatial distribution of temperature $T(x, y, z)$, where ρ_m is the density in kg/m^3 , C the specific heat capacity in $\text{Jkg}^{-1}\text{K}^{-1}$, T the temperature in K, κ the thermal conductivity in $\text{WK}^{-1}\text{m}^{-1}$. The right-most term on the equation (C.2) represents the Joule heating and involves the resistivity of the material which depends on the local temperature. The $\rho(T)$ dependence used in our model is taken from experimental values reported in Ref.[205, 269]. For $T > 400\text{K}$, we assume a constant resistivity.

The solution of the system of equations (C.1) and (C.2) is obtained using the finite element software COMSOL for a geometry reproducing the exact shape of the measured sample as extracted from the analysis of SEM images.

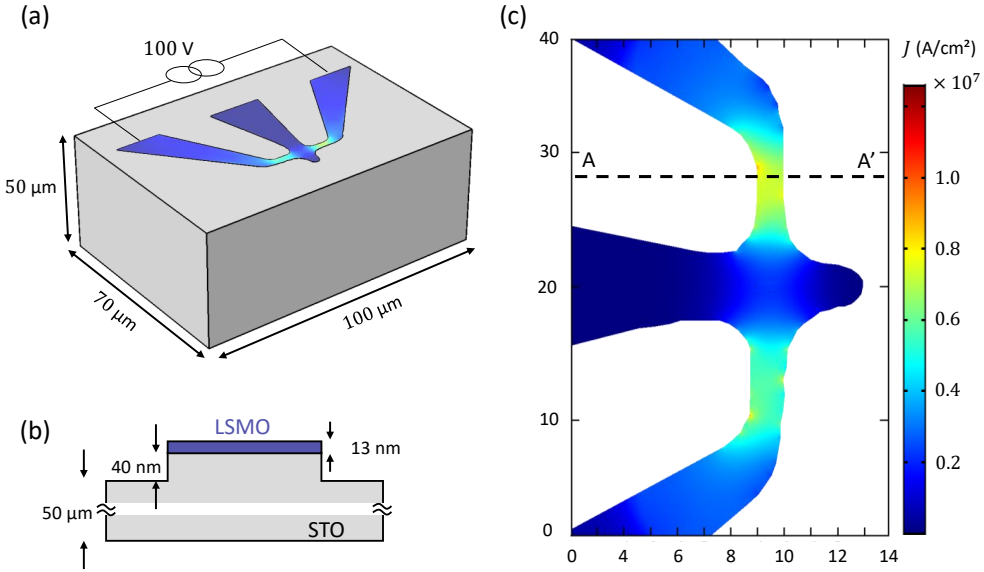


Figure C.1: (a) Sketch of simulation geometry with dimension details. The thickness of the STO substrate is set to $50 \mu\text{m}$ in order to minimize computation time. The LSMO layer is shaped based on a SEM picture. (b) Cut view of the modeled device consisting of a 13 nm-thick layer of LSMO on a 40 nm-thick layer of STO representing the step in the substrate generated by the etching process. (c) Current density distribution in the LSMO layer for a voltage bias of 100 V. A complete mapping is displayed on the sketch of panel (a).

A tilted view of the layout used for FEM simulations is shown in Fig.C.1(a) and a side-view is shown in Fig.C.1(b). We assume perfect transparent LSMO/STO interface for the phonon flow. The bottom surface of the STO substrate is set to a constant temperature of 110 K, as in the experiments. The values of the thermal coefficients are listed in Table C.1.

	ρ_m [kg/m ³]	C [J/(kg K)]	κ [W/(Km)]	ϵ/ϵ_0
STO	5170 [270]	544 [270]	12 [270]	300 [271]
LSMO	6600 [270]	568 [270]	2.46 [270]	$2 \cdot 10^4$ [272]

Table C.1: Thermal and dielectric coefficients used as input parameters in FEM simulations.

Fig.C.1(c) shows the current density map for the case when a bias voltage

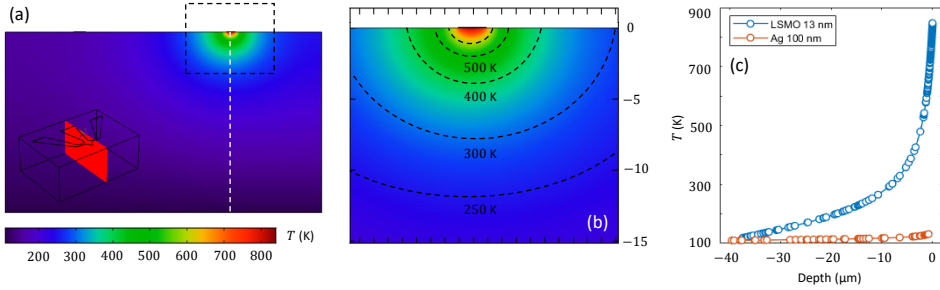


Figure C.2: (a) Cross-section of the temperature distribution in the plane indicated in the inset. (b) Zoom in the vicinity of the LSMO constriction where Joule heating occurs. The black dashed lines correspond to isothermal curves. The vertical scale indicates the spatial dimensions in μm . (c) Exponential decrease of the temperature with the depth penetration in the STO substrate along the vertical white dashed line shown in panel (a) for a 13 nm-thick LSMO sample (blue dots) and a 100 nm-thick Ag sample (red dots).

of 100 V is applied as indicated in Fig.C.1(a). As expected, this map reveals a higher current density along the narrowest bridges, precisely where the surface scars are initiated (see Fig. 6 of the main text). The resulting temperature map in the plane containing the A-A' line indicated in Fig.C.1(c) and perpendicular to the LSMO film, is presented in Fig.C.2(a). Temperatures as high as 800 K can be reached at the LSMO sample, although still far from the melting point at 2353 K. This local temperature rise spreads into the STO substrate as shown in the zoomed region presented in panel (b) in which some isothermal lines have been indicated. Note that the temperature decreases exponentially with distance as shown in Fig.C.2(c) with a characteristic length of few micrometers. It is interesting to point out that the (101) structural defects penetrate into the STO substrate down to a depth of about $3 \mu\text{m}$, similar to the thermal healing length. It is hence possible that the substantial temperature gradient imposed on the substrate induces stress due to the thermal expansion giving rise to the proliferation of structural defects as a natural way to relieve such stress. As a consequence, some atoms may find their way to the surface simply by edge dislocation glide thus producing the observed surface steps. Panel (c) also shows the spatial decay of temperature obtained for a Ag sample with the same layout as for LSMO at a circulating current of 44 mA, corresponding to the electromigration regime. In this case, the local temperature rise is minor thus likely explaining the fact that no surface scars are triggered in Ag bridges on STO.

Although the above scenario implying thermally induced strain is plausi-

ble, we cannot ignore the role played by the electric field as demonstrated in Ref.[190]. To that end, we have calculated the electric field generated around the narrow constriction submitted to a 100 V bias. The results are summarized in Fig.C.3. In panel (a) a map of the magnitude of the electric field in logarithmic scale is shown for the red plane indicated in the inset. Panel (b) shows a blow up around the region of interest with dark-dotted lines corresponding to a constant electric field magnitude. The electric field points mainly out of the plane along these lines. In panel (c) the decrease of electric field along the vertical white dotted line in (a), is shown. It is worth noting that the electric field remains moderate in all cases, with maximum values around 8 MV/m, five times smaller than the threshold for dielectric breakdown. We are inclined to believe that these low values of electric field support the scenario described above in which thermal stress is dominant.

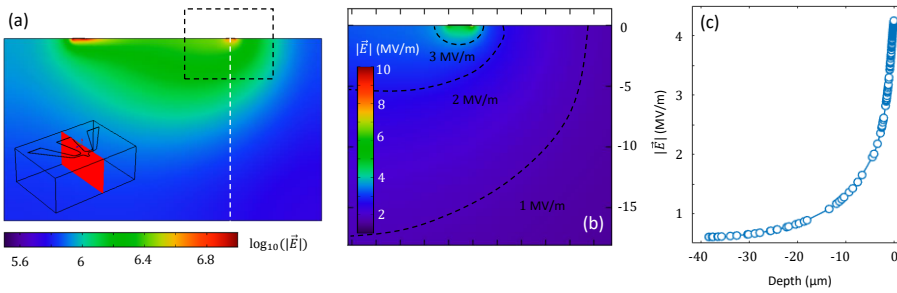


Figure C.3: (a) Cross-section of the electric field distribution in the same plane as in Fig.C.2(a). The color bar represents the logarithm of the magnitude of the electric field. (b) Zoom in the vicinity of the LSMO constriction with electric field indicated in linear scale. Dashed lines correspond to constant electric field curves. (c) Variation of the electric field with the depth penetration in the STO substrate along the white dashed line shown in panel (a).

C.2 Realtime tracking of the electromigration process

An animation of the LSMO oxygen electromigration experiment is available with Ref.[73]. It shows the time evolution of the pulsed electromigration process at the current indicated in the top panel, evidenced by bright field optical microscopy imaging (right vertical panels, image subtractions indicated on screen), while monitoring the individual bridge resistances (left vertical panels, measurement terminals indicated in indices). These measurements have been acquired at 110 K.

C.3 STEM images

Scanning Transmission Electron Microscopy investigation has been carried out in a JEOL-200-ARM at 200 kV acceleration voltage in a lamella cut out via Focused Ion Beam which location includes two surface scars as indicated in Fig.7(a) of the main text. Fig.C.4 shows a low magnification image of the

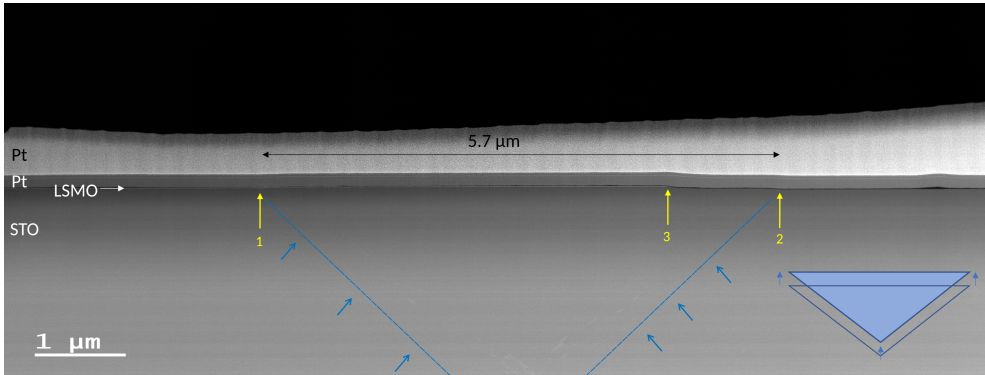


Figure C.4: Low magnification Scanning Transmission Electron Microscopy in a region including two surface scars as indicated in Fig.7(a) of the main text. The yellow arrows mark three steps. The arrows labeled #1 and #3 mark 14 nm-thick steps corresponding to the triggered surface scars. The LSMO is indicated with an horizontal white arrow, and runs from left to right till the yellow arrow #3. Extended defects indicated with blue arrows are observed within the STO substrate in the vicinity of the blue dashed lines. The inset shows a sketch illustrating the upward shifting of a region with triangular cross section resulting from the thermal stress.

cross section of the lamella. In this image the intensity scales with Z^2 , being Z the atomic number. Thus, regions with heavier atoms or more densely packed are seen brighter. Before FIB cutting, the LSMO/STO sample has been capped for protection with two Pt layers deposited by different evaporation techniques and therefore having different mean density (with the thicker Pt top layer being more dense). In this Z -contrast image, the LSMO layer appears brighter than the STO substrate because it contains a heavier cation (La). The yellow arrows mark three steps. The arrow labeled 1 marks a step up of 14 nm in height corresponding to one of the triggered surface scars. The LSMO is indicated with an horizontal white arrow, and runs from left to right till the yellow arrow #3. From that point to the right, there is only bare substrate. The yellow arrow #2 marks a step down in the STO substrate of the same height as in point #1 and corresponds to another surface scar. The

distance between arrow #1 and #2 is $5.7 \mu\text{m}$. Extended defects indicated with blue arrows are observed within the STO substrate in the vicinity of the blue dashed lines. The inset shows a sketch illustrating the upward shifting of a region with triangular cross section resulting from the thermal stress.

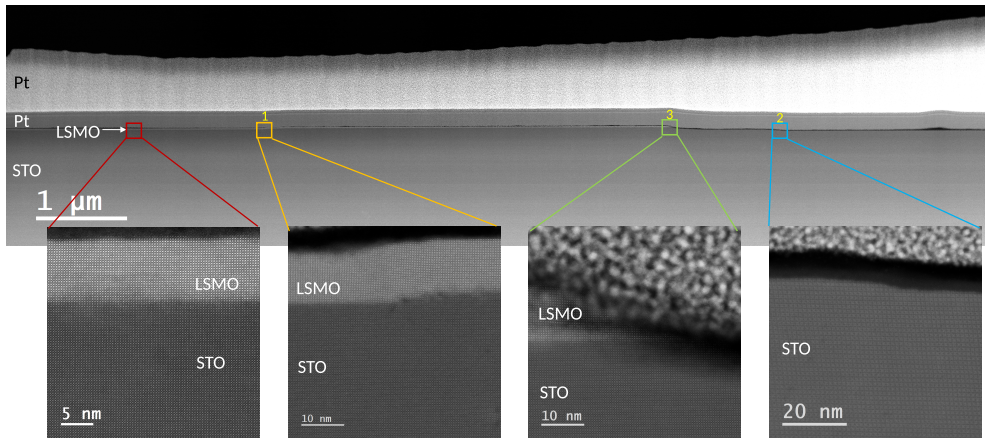


Figure C.5: High-magnification Z-contrast images of the regions marked in the upper low-magnification STEM image. The red framed image corresponds to the unaffected region. The yellow frame includes step #1. Region #3 (green frame) shows an edge of the LSMO layer resulting from the ion milling process. The step #2 (blue frame) at the bare STO substrate results from the thermal stress.

Fig.C.5 shows higher-magnification Z-contrast images of the regions marked in the upper low-magnification image. The red-framed image in the unaffected region shows that the LSMO layer exhibits a cube-on-cube epitaxial relationship with STO substrate with a coherent and sharp interface, i.e. no defects are observed at the interface. However, in step #1 (yellow frame) the interface exhibits defects and the nearby LSMO planes are highly tilted. Region #3 (green frame) shows an edge of the LSMO layer resulting from the ion milling process. The darkish contrast is suggestive of amorphisation due to the nanofabrication (likely oxygen vacancies generation) with an affected distance of 20 nm from the etched edge. The step #2 (blue frame) at the bare STO substrate shows atomic-scale steps at the surface.

Thanks to the particular geometry of the STEM, it is possible to characterize the electronic structure of a compound with sub-nanometer resolution using electron energy loss (EEL) spectroscopy, which gives information about the energy that the transmitted electrons lose when they interact with the core electrons of the atoms, providing information of the electronic energy

states that remain empty, being above the Fermi energy. Fig. C.6 shows electron energy loss spectra of the Ti L-edge in STO (a), O K-edge in STO (b), Mn L-edge in LSMO (c) and O K-edge in LSMO (d). In perovskites, the O $2p$ - and transition metal $3d$ -states are strongly hybridized and have similar energy close to the Fermi level, which helps to probe the metal-oxygen bond. The O K-near-edge structure arises from the excitations of the O $1s$ -electrons to the O $2p$ -states, whereas the metal L-edge results from the excitation of the $2p$ -electrons into the empty $3d$ -states. Thus, any change in the electronic structure can be probed by studying the variations in the fine structure of both edges. In our particular case, no changes in the fine structure of the Ti and Mn L-edges and the O K-edges of both the LSMO layer and the STO substrate are observed when comparing regions at the steps and far from them. This finding suggests no substantial proliferation of oxygen vacancies in the structure. In particular, the two satellite peaks observed in (a) are characteristic of Ti^{4+} whereas in oxygen vacancy-rich zones these satellite peaks should be less pronounced, due to the presence of Ti^{3+} .

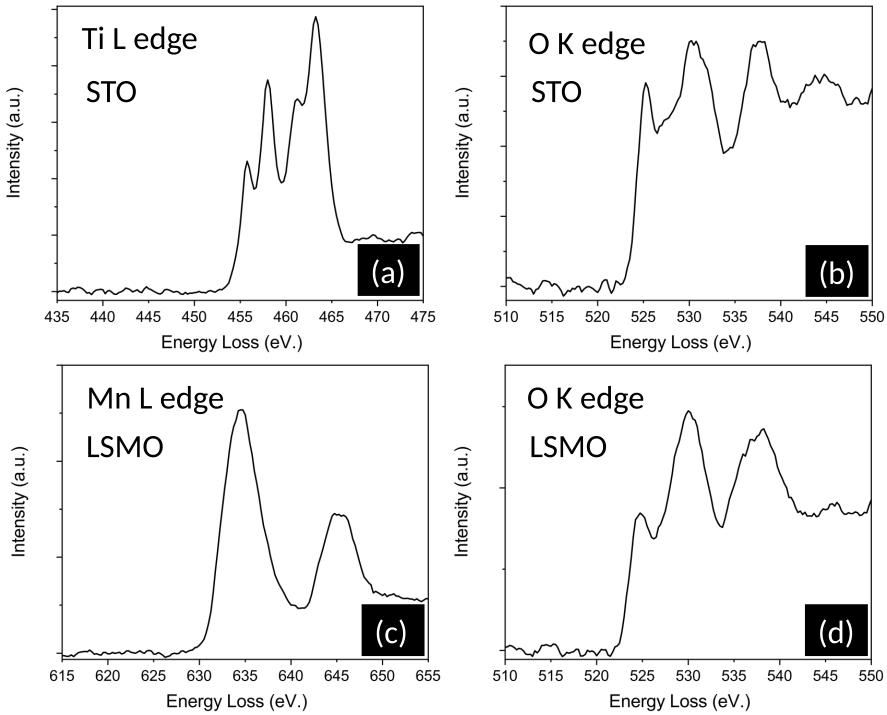


Figure C.6: (a,b) EEL spectra after background subtraction of Ti L-edge and O K-edge from the STO substrate, respectively. (c,d) EEL spectra after background subtraction of Mn L-edge and O K-edge from the LSMO, respectively. All the spectra were acquired in the step #1 region. The energy dispersion used for the EEL spectra acquisition was 0.25 eV.



Annex to Ch.7

D.1 Initial Thermalization Phase

The micrometric constrictions investigated in Ch.7 are exposed to high current densities during extended periods of time and, therefore, undergo substantial Joule heating. In the initial phase, the sample takes some time before stabilizing at the final temperature. The data presented in Ch.7 corresponds to the measurements acquired at thermal equilibrium (i.e. under isothermal conditions) whereas the initial thermalization phase is removed. In order to estimate the characteristic time-scale necessary to achieve the thermal equilibrium, we wired a second device 3.5 mm away from the sample under high bias (7.5 mA) and used this second device as a thermometer, i.e. its resistance is monitored with a low DC current (10 μ A). The sketch in Fig.D.1(d) shows the sample-thermometer in gray colour and the high-biased device with RGB colour code associated with each of the three bridges in series. The corresponding resistance evolution as a function of time is displayed using the same colour code in panels (a-c). These experiments suggest that for the utilized 5×5 mm² LAO substrates, the thermalization occurs on the order of minutes after turning on the high-current bias.

The resistance of the bridges (Fig.D.1(a-c)) and that of the thermometer (Fig.D.1(e)) asymptotically approach their final values R_f roughly following an exponential dependence as demonstrated by the semi-log plots shown in the insets of these panels. A fit to this data using the equation,

$$R(t) = R(0) + (R_f - R_0)(1 - e^{-t/\tau}), \quad (\text{D.1})$$

allow us to extract a relaxation time $\tau \approx 2$ min. In addition, by extracting the

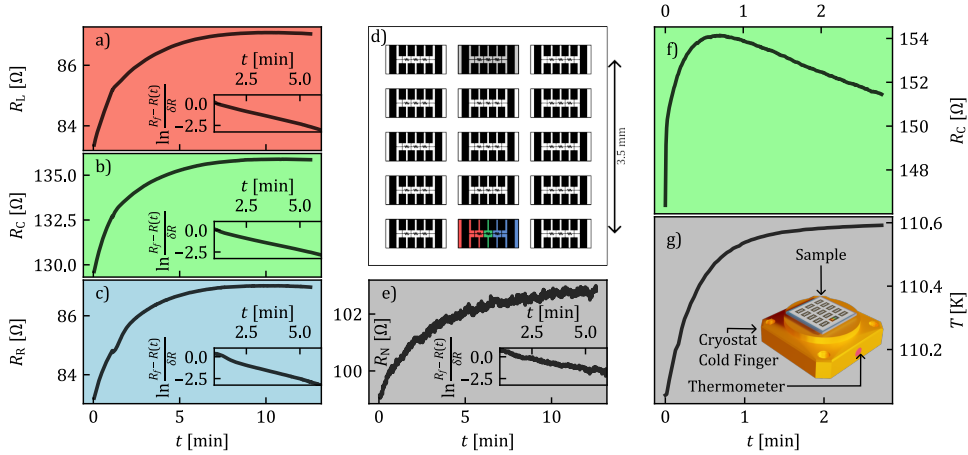


Figure D.1: Demonstration of the heating power effected by a device under experiment conditions. The three plots in the left column (red-green-blue) a)-c) show the measured 4-point resistance of a triple constriction device conducting 7.5 mA of DC current, with the panels representing the left, center and right constrictions, respectively. The measured resistances increased in all three bridges before settling to stable values at around 6 min after starting, implying that Joule-heating caused the thermalization of the chip. To confirm this heating effect, another device on the opposite side of the chip is wired, and its central constrictions' 4-point resistance is recorded with a low DC current (10 μ A) simultaneously with the high-current measurement in the device under test. The resulting measurement is shown in panel e) with a grey background. The two devices are positioned as shown in the illustration in panel d), the devices being colored as in the other panels. The central constrictions of the devices are ~ 3.5 mm apart. The identical shape of the resistance curves serves well to illustrate that the heating of the high-current device is enough to affect the whole chip. Measurement of the heating of the cryostat cold finger due to Joule heating in a YBCO microconstriction passing 7.5 mA DC current at 110 K are shown in panels f) and g). f) shows the resistance evolution of the central constriction R_C with the characteristic dome shape discussed in the main text, while panel g) shows the temperature read at the cryostat cold finger with a copper thermometer. Note the temperature increase of ~ 500 mK due to the heat generated in the sample. The inset in the grey panel shows a rendition of the mounted sample on the gold base of the cold finger, illustrating the distance from a working device to the thermometer.

temperature coefficient of resistance α from fits to $R(T) = R_0(1 - \alpha(T - T_0))$, we can estimate the temperature of the sample once the thermal equilibrium is reached ($T \approx 390$ K) and the temperature of the substrate 3.5 mm away from that hot spot, which rises to about 11 K above the room temperature. The fact that the temperature of the constriction during the switching process remains relatively low, is consistent with the observation of no loss of oxygen out of the sample. An additional manifestation of the thermalization process has been obtained directly from the thermometer attached to the bulky cold finger of the cryostat as schematically shown in the inset of Figure D.1(g). Panel (f) of this figure shows the evolution of the resistance of the central constriction at 110 K and panel (g) shows the evolution of the temperature simultaneously picked up by the thermometer in the cold finger.

D.2 Simulated Time Evolution of the Resistance, Doping and Temperature

Two animated overviews are presented to the reader to illustrate the time-dependent parameter change during the measurement. Resistance values are measured as voltages between points on the bottom ends of the vertical terminals, and the square-wave current of 5.8 mA amplitude is applied from the left and right mesh edges with the ground being on the left side. Current polarity reversal is executed upon reaching the preset value of $R_0 = 240 \Omega$ on the downward section of the R_C dome.

The animations are available on request and will be published with the article.

D.2.1 Symmetric Mesh

The animation applied to the symmetric mesh reproduces all major features of the experimental data. A stable section of this simulation is highlighted in Fig.7.3 and discussed in the main text. Data from this simulation was used to generate Fig.7.4, presenting an in-depth look at the parameter profiles in a single R_C dome during switching.

While the amplitude of the observed changes varies with time, they settle at an intermediate value for both δt and R_{max} (90 s and 242 Ω respectively). The oscillations in both T and x remain spatially symmetrical between left and right constrictions.

D.2.2 Asymmetric Mesh

In order to elucidate the origin of the alternating R_{max} values in the steady section of the experiment as seen in Fig.7.2, we have applied the finite element model to an asymmetric mesh where the right constriction is $1 \mu\text{m}$ wider than the left one. The applied model is otherwise the same as the one applied in the symmetric mesh.

The animated time evolution of the parameters of interest shows a periodicity of $2\delta t$ in the value of R_{max} which evolves to the state discussed in Fig.7.5 . We observe that the narrower constriction experiences persistently higher temperatures and accumulates higher amounts of oxygen. The right (wider) constriction, in turn, is persistently deoxygenated compared to the left, which is explained by the lower resistance and better heat evacuation experienced on this side making it into a vacancy trap.

One should note that the observed double periodicity only fits the experimental data after settling, as the early part of the simulation shows R_{max} stay fixed for positive polarity sections and decrease for negative ones. The experiment had a polarity-dependent alternation of R_{max} from very early in the process. Upon settling, we recreate the experimental behavior leading us to the conclusion that imperfections in sample geometry are the culprits in the alternating dome heights.

List of Figures

- 1 Comic by Kris Wilson, taken from <https://explosm.net/comics/kris-same> 8

- 1.1 Characteristic *IV* behavior in devices displaying resistive switching. Bipolar resistive switching (a) is shown in devices where the polarity of the electrical stimulation is important, while devices where the effect is primarily thermally driven show unipolar resistive switching (b). Both of these cases (a,b) are shown as having an initial forming step in which the given switching mechanism is set (gray dash-dotted line), e.g. the initial crystallization of phase-change material or the formation of the filament channels in a metallization cell. These devices are binary switches that only have one ON and one OFF state accessible in operation. (c) An idealized switching oxide[20–23] *IV*, where the positively charged oxygen vacancies V_O^{2+} move in response to an electric field and control the resistance in the material. The dark-to-bright shadings show the effect of sweeping rate or temperature on the *IV*. [24, 25] The vacancy diffusion switching mechanism allows for multi-state memory in these devices, presumably allowing one to select different states as a function of electrical control, as shown by the various dashed lines in the *VI* curve in (d). [26] 23

1.2 Illustration of common switching mechanisms. a) Phase-change materials undergo a glassy transition between an ordered (ON) and a disordered (OFF) state. b) Metallization cell systems function by intercalating metal ions in an insulating matrix, the device is in the ON state when the filament is connected. Metal ions can come from an active electrode (olive green) or from impurities/dopants (as in doped oxide switches). c) Metal oxides switch as their doping is controlled by oxygen vacancy distribution in the film - the device is ON when doped, i.e. when vacancies connect both electrodes. Shared color code: Magenta spheres are passive electrodes, yellow is phase-change material, green is active metal electrode, bronze is an insulator matrix, green and gold are the oxide. d) Schematic radar graph showing important characteristics for switching devices in computing. The lines and circles indicate the characteristics for the four main computing applications being studied - RAM memory, long term storage, neuromorphic (analog) computing and logic circuits. The shaded areas represent the current standards of the three families of switching materials in a-c). Radar graph and device demands based on Ref.[19], switch behavior adapted from Ref.[38]. 25

1.3 Illustration of the relative thermal and/or electrical influences on the free energy of diffusion G . x is the position of an ion. [19, 70] 30

1.4 Generic oxide phase diagram in terms of atomic percentage of oxygen. The phase diagram includes an eutectic point and a melting line is indicated. The Me-O segment with the gradual coloring represents the metal-oxygen solid solution. Recreated from Ref.[19]. 33

1.5 Switching oxides distributed across the periodic system. Alkaline metals and non-metals of little relevance are grayed out. Metals that have binary switching oxides are indicated by red vertical lines. A-site cations in perovskite oxides are indicated by the green horizontal zig-zag lines, while B-site cations are shown with golden waves. Additional symbols indicate the functionalities present in a any given family of perovskites based on their B-site cations.[80] The parent structure of the perovskite family is shown in the bottom left, the sizes represent ionic radii. 35

- 1.6 Generic perovskite oxide phase diagrams. a) LSMO phase diagram as shown in Ref.[139] as a function of x , indicative of hole doping in the material. PI is paramagnetic insulator, PM is paramagnetic metal, CNI marks the spin-canted insulator phase, FI the ferromagnetic insulator and FM the ferromagnetic metal. b) Idealized YBCO phase diagram, as presented in Ref.[42], as a function of hole doping, a function of the deoxygenation δ . AF is antiferromagnetic insulator, PG is the pseudogap phase, SM is the strange metal phase, FL represents Fermi liquid and SC is the superconducting phase. The insets represent the respective crystal structures. 38
- 2.1 Simplified working principle of thin film deposition by pulsed laser. The chamber is vacuum sealed and pumped to low pressure, and the oxide film properties are controlled by substrate heater temperature and oxygen partial pressure. Deposition thickness is calibrated in laser pulses per nm. A piezoelectric scale (not shown) is used to measure the real film thickness. 52
- 2.2 Schematic representation of compressive and tensile strain induced in a perovskite thin film by substrate lattice dimension mismatch. The axis in the bottom shows approximate values of lattice parameters for a number of common perovskites. On the example of LSMO, compressive strain may be induced by growing the film on LAO and tensile by growing on STO, while the best match is provided by $(\text{LaAlO}_3)_{0.3}(\text{Sr}_2\text{TaAlO}_6)_{0.7}$ (LSAT). 56

- 2.3 Schematic representation of thin film patterning and metallization processes used in this work. Starting sample consists of an unpatterned perovskite film covered with a photoresist. Using laser photolithography, the desired pattern is written into the photoresist (a). Areas exposed to the laser light become more soluble and dissolve in the development step when exposed proper solvents (2% $C_4H_{12}N^+$ in water), creating the pattern in the photoresist (b). If the patterning is being performed on the perovskite film itself, the stack is etched either via chemical (H_3PO_4) or Ar plasma etching (c). The photoresist in this setup protects the perovskite film underneath from the etch and can be freely lifted with organic solvents (like acetone) revealing the patterned perovskite underneath (d). A procedure without etching is used for metallization as the metal films are reserved for electrodes and have a larger thickness and less demand for precision film edges. Here the developed substrate-film-resist stack is metallized via PLD (e) and the final metal pattern is remnant after chemical lift-off (f). 57
- 2.4 Illustration of the sample designs used in the context of this thesis. Color code is same as in Fig.2.3 and Fig.2.2: substrate is orange and thin film is yellow, metallized sections are dark gray. The important distinction between the sample designs in a,b) and d) is the number of resistances individually accessible, as shown in the panels c) and e). We will stick to the colors indicated on the voltmeters in e) for the remainder of the thesis to indicate the left-center-right constrictions by red-green-blue, and define positive current polarity as having the positive arm of the circuit on the right. A single device will have the source/drain lines (horizontal) connected to large metallized electrodes and the voltmeter terminals (vertical) to smaller ones, as shown in f). Single chips are patterned in a matrix of identical devices, commonly in a 3×5 array. Every device is individually accessible by wire bonding, as shown in g). . . . 59

2.5 a) Sample under optical microscope. b) Sample chip glued to a gold-plated oxygen-free copper base with silver paste, mounted in a PCB with vertical metallic connectors. The sample is bonded to the gold pads of the PCB with fine wire, and the pads themselves feed through to the vertical connectors. c) Individual sample testing stage (red square), the sample PCB envelope is visible in the center (blue square), while the BNC coaxial connectors are visible on the sides. The stage includes a 240Ω resistance between the connectors and the pins of the PCB board and is grounded. d) Probe station for bondless testing, with low magnification microscope. 61

2.6 PID algorithm and the resulting $R(t)$ dependence. Red rounded rectangles are terminators, green parallelograms are inputs/outputs, orange squares are decisions and blue rectangles are processes. I is starting current, U is starting voltage, G^{thr} is the threshold conductance, $e(t)$ is the process variable, k is a constant, $\epsilon(t)$ is the root-mean-square noise, N is an iterator. The functions f_{nl} and f_{PID} are the non-linear and PID response, addressed in the main text body. 63

2.7 65

2.7 Pulsed-excitation protocol algorithm and the resulting $R(I)$ dependence. Same illustration convention as in Fig.2.6. I_{probe} and t_{probe} are the current and duration values in the low I part ("probe") of the protocol which produces R_{min} , i.e. the resistance isolated from the influence of Joule heating. I_{pulse} and t_{pulse} are the current and duration of the high I regime ("pulse"), where only the starting value of I_{pulse} is directly controlled by the user and is then linearly increased for every cycle. R^{thr} is the threshold resistance which triggers the algorithm to stop, in order to prevent sample destruction. We calculate the mean resistance \bar{R}_{min} measured for positive and negative I_{probe} during t_{probe} , and correlate the value to the previous R_{max} , i.e. the resistance measured during the pulse. Additionally, we may employ optical or other imaging techniques during the probe phase to track the visible changes in the system. Note that the R_{min} curve is flat until a threshold value of current is reached. We denote this as the electromigration threshold current I_{EM} 66

2.8 67

- 2.8 Continuous switching protocols and the resulting $R(t)$ curve. Same illustration convention as in Fig.2.6. The left-hand side of the diagram represents switching with a fixed period for the polarity flips (time-logic) and the right-hand side is switching at a predetermined threshold resistance (resistance logic). Both are executed using a fixed current amplitude I_{app} , but also take their respective control variables as inputs. The two-step decision process in the resistance-logic algorithm prevents unwanted polarity switches due to small fluctuations at the polarity inversion. Note the characteristic domed resistance curves in the bottom panel, every dome corresponds to one current polarity, two domes together make a whole period. 68
- 2.9 Schematic illustration of the tabletop cryogenic chamber of the Montana Instruments Cryostation used at EPNM. The sample assembly, which consists of the sample on top of a PCB envelope with a metallic base is mounted on top of an oxygen-free copper cold finger. The finger is mounted on the platform from which the heat extraction is performed. The chamber has two layers of shielding, an outer vacuum housing and a radiation shield. The key feature of this assembly is the optical access and the configurable electrical access via wiring. 68
- 2.10 Schematic illustration of the Olympus BXFM modular microscope assembly at EPNM. The light from the source passes through a condenser lens to parallelize the light rays, before passing through configurable apertures. The light is filtered with a green filter and passed through a polarizer and a quarter-wave plate. Image magnification is controlled by the objective. After reflection the light passes through an adjustable analyzer. The analyzer operates like a second polarizer to select the polarization of the collected light. The analyzer is mounted in a Bertrand lens. 70
- 2.11 Cryostat cold finger - sample - indicator stack for Faraday-effect based magneto optical imaging. The change in the light polarization is illustrated on the right hand side. 71

- 2.12 Schematic illustration of working principle of a SEM. The electron beam originates from a hot tungsten filament of the electron gun, by means of hot field effect. The extractor anode is mounted below it. A part of the emitted electrons passes the aperture and enter the acceleration column where condenser lenses form the beam and provide acceleration set by the operator. The beam passes through an electrostatic lens and a set of deflection coils for scanning the sample surface before entering the sample chamber. The sample is mounted on a stage with very fine mechanical controls for positioning. The InLens detector is positioned in the objective lens, and the Everhart-Thornley detector is mounted on the side of the sample chamber. The interaction of the impinging electrons and the sample volume is shown on the right. Electrons are only transmitted in very thin samples by very energetic electrons, usually in STEM setups. 74
- 2.13 Simplified view of AFM. The deflection of the oscillating tip changes as a function of an unspecified interaction as it is driven across the surface. The measured response is produced on the right. 76
- 2.14 Representation of a finite element mesh, S used for modeling the electrically driven oxygen diffusion. δS_L and δS_R are domain boundaries used to define the electrical control, with δS_L usually being the ground. Both are given fixed values for oxygen content. δS_0 is the model edge. The mesh geometry is taken from SEM images of a real device. 77
- 3.1 Scanning electron microscopy images of a single YBCO constriction (a) and a symmetric three-bridges structure (b). Electromigration takes place in between voltage contacts where the current density reaches its maximum value. In (a) the narrowest point of the bow-tie structure is $1 \mu\text{m}$ wide. In (b) the central bridge is $0.8 \mu\text{m}$ wide and the two symmetrical arranged side bridges are $3 \mu\text{m}$ wide. Panel (c) shows an optical microscopy image of the entire device. Inset: cross-section at the voltage pad showing the epitaxial $\text{YBa}_2\text{Cu}_3\text{O}_{7-\delta}$ film grown on a LaAlO_3 single crystal substrate and Ag electrodes. In panel (d) a magneto-optical image obtained at $T = 4.5 \text{ K}$ and $\mu_0 H = 0.95 \text{ mT}$ for the device in panel (c) is shown. . . . 84

- 3.2 (a) Resistance of a YBCO device similar to the one in Figure 3.1(a) as a function of the circulating current during an electromigration process. The time evolution of the measurement is indicated by the black arrows. The initial temperature in the pristine state is 105 K and increases up to ~ 525 K at point A. Controlled feedback operates from point A on avoiding thermal runaway. Inset: current circulating through the sample as a function of time during the electromigration process shown in the main panel. (b) Differential images showing the evolution of the front of the affected region for an applied current running from right to left as indicated in panel (a). Positively charged oxygen vacancies move towards the cathode (-) and negatively charged oxygen atoms move towards the anode (+). The labels correspond to the points indicated in panel (a). The superposed white curve delineates the borders of the transport bridge and the vertical black arrows indicate the mean position of the propagating front. 86
- 3.3 Normalized resistance $R(T)/R(200\text{ K})$ as a function of temperature for the central bridge (green), left bridge (red), and right bridge (blue) for the sample in the pristine state (a) and after electromigration (b). The inset in panel (a) shows a scanning electron microscopy image of the three bridges connected in series, indicating the color code of the voltage signal acquired and the polarity of the current source. In panel (b), the universal response for the pristine sample is replotted with black open circles. Inset in panel (b): optical microscopy image obtained after electromigration process. The affected area on the cathode side is clearly visible as a bright region starting from the central bridge and extending deep into the current leads to the left. Evolution of the critical temperature T_c (c) and the carrier density, n (d) at different regions of the YBCO constriction. The color code of the data points corresponds to the signal picked up at the colored regions in the insets. For the sake of clarity the numbering indicates the voltage contacts addressed in each measurement. 87
- 3.4 Superconducting critical temperature as function of the carrier density and hole doping estimated from the current-induced oxygen migration (filled squares). For the sake of comparison, we reproduce the data from Ref. [162] (empty squares). . . . 89

- 3.5 O(4) phonon mode frequency measured along the linear scan displayed in panel (a), for the pristine state and after reaching two different EM states (applied current 16 mA), together with the extracted oxygen content. The center of the constriction is marked with a dotted line. The error bar in the phonon frequency is 2 cm^{-1} and displayed only for the pristine sample. 90
- 3.6 Normalized resistance $R(T)/R(200 \text{ K})$ for the left (a), central (b), and right (c) bridges before (black) and after (white) illumination. Note the different vertical scale range in each panel. Panel (d) shows the percentage change of the central bridge resistance with respect to the initial value as a function of time. The pristine sample exhibits no resistance change during illumination at 200 K (empty squares) whereas after electromigration clear photodoping is observed (green circles). Inset: At room temperature and switching off the illumination, the photoexcited sample can relax back to the original state in a much longer time scale. 92
- 3.7 (a-f) Optical microscopy images showing the progression of the oxygen depleted zones (bright) during the anti-electromigration process. The time elapsed between consecutive images is about 15 minutes. (g) Resistance of the central bridge of a YBCO device as a function of the circulating current during the anti-electromigration process. The labels (R, I) in panels (a-f) correspond to the coordinates along the $R(I)$ curve shown in panel (g). (h-i) Differential images illustrating the partial healing (black spots) due to anti-electromigration on a previously affected area by electromigration. The gray curve is a guide to the eye delineating the transport bridge. Panel (j) shows simulation images of the evolution of the oxygen concentration starting from the pristine state, as the voltage is ramped up with time. 93
- 4.1 Optical microscopy image of the entire device after electromigration. The inset shows a scanning electron microscopy image of the three central bridges. 100

- 4.2 Experimental evolution of the resistance as a function of time under continuous electrical stress for the left, central, and right bridges. The inset in the left panel shows the polarity of the current source and the color code associated to each bridge. An optical microscopy image of the electromigrated YBCO device is shown as inset of the central panel. Higher reflectivity (brighter zone) reveals the region with oxygen deficiency. Measurements performed at room temperature and in ambient conditions. 101
- 4.3 Evolution of the resistance as a function of time under continuous electrical stress for the left, central, and right bridges as obtained by finite-element modeling with $E_a = 0.7$ eV, $x_0 = 0.76$, $x_{min} = 0.5$, $x_{max} = 0.95$ and $\delta x_0 = 5$ %. Inset in the middle panel shows a mapping of the oxygen distribution (yellow / green color indicates the oxygen depleted zone and red color the oxygen rich zone). 102
- 4.4 See next page. 104
- 4.4 (a) A bipolar I_{probe} pulsed current is used to monitor the sample resistance whereas a $I_{PLS} \gg I_{probe}$ of variable amplitude triggers the electromigration process. Optical microscopy images are acquired after each probe pulse. (b) The total sample resistance picked up by the external electrodes is monitored before and during the I_{PLS} excitation. The panel (c) shows the evolution of I_{PLS} and the panel (d) the resulting evolution of sample resistance before (black points, left axis) and during (white points, right axis) the application of I_{PLS} . Representative optical microscopy images at different stages of the electromigration process are shown in (e). Images labeled A-E acquired at the corresponding yellow points in panel (c), provide direct optical contrast of the affected areas. Images labeled A'-G' acquired at the corresponding green points in panel (c), provide differential optical contrast of the affected areas. 105
- 4.5 Finite element modeling of the resistance and oxygen cartography evolution as a function of an oscillating current pulse I_{PLS} . For the sake of convenience, the I_{PLS} as a function of pulse number already shown in Figure 4.4(c) is replotted here. The simulated R_{max} , R_{min} , oxygen concentration, and differential concentration mappings are to be directly compared with the experimental data presented in Figure 4.4. 107

- 4.6 (a) Amplitude of the current pulse I_{PLS} as a function of pulse number. (b) Optical microscopy images corresponding to the points labeled in panel (a). The brighter yellowish zones correspond to oxygen depleted areas. (c) Resistance vs temperature showing the superconducting transition at the left (salmon panel), central (green panel), and right (blue panel) bridges, respectively. The response of the pristine sample is shown with white points, after reaching maximum current amplitude is shown with gray data points, and after reaching maximum current of opposite polarity is shown with black points. . . . 109
- 4.7 Panel (a) shows the simulated oxygen maps for the same points A \rightarrow F as shown in Figure 4.6(a) except for the fourth point (formerly D) which is now taken after D. The red and yellow colors correspond to oxygen-rich and oxygen-poor areas respectively. (b) $R(T)$ curves for the left, center and right bridges. The color convention used is the same as in Figure 4.6(c). The parameters for these simulations are $E_a = 0.7$ eV, $x_0 = 0.76$, $x_{min} = 0.5$, $x_{max} = 0.9$ and $\delta x_0 = 5$ %. 110
- 4.8 The evolution of R_{min} and R_{max} for different activation energies are given in panels (a) and (b) respectively (E_a is given in eV). The other parameters remain unchanged: $x_0 = 0.76$, $x_{min} = 0.5$, $x_{max} = 0.95$ and $\delta x_0 = 5$ %. Panels (c) and (d) show R_{min} and R_{max} for several x_{min} and constant activation energy $E_a = 0.4$ eV. The snapshots on the right show the oxygen distribution for the corresponding points A - I indicated in panels (b) and (d). The maximum attained temperatures are shown in panels (b) and (d). 111
- 4.9 Panel (a) shows the temporal evolution of R_{min} for the different $E_a(x)$ profiles given in panel (b). The observed correlation between the irreversibility parameter $\Delta R = R_{final} - R_{init}$ and the lowest value of the activation energy is given as the inset of panel (b). The others parameters are $x_0 = 0.76$, $x_{min} = 0.5$, $x_{max} = 0.95$ and $\delta x_0 = 5$ %. The value of the applied current corresponds to the first 80 pulses of the Figure 4.5. 112

- 4.10 (a) Linear interpolation of $\rho(x, T)$ data extracted from Ref.[156]. For values of T above 300 K, a single α value is derived from an $R(T)$ curve for all oxygen concentrations. (b) Top view of the layout and the mesh used for FEM simulations. The positive (red) terminal is simulated as a current source while the negative (blue) terminal is connected to ground. The value of the current injected at each time step of the simulation is dictated by the experimental values. 115
- 5.1 Low magnification and high magnification false-colored scanning electron microscopy images of transport bridges along the crystallographic directions a (left), 45° from a (top central panel) and b (rightmost panel). The lower row shows the associated resistivity vs temperature curves obtained at zero applied magnetic field. The inset in the lower central panel shows the ratio ρ_a/ρ_b in the whole temperature range. 120
- 5.2 (a) Evolution of the sample resistivity as a function of the applied pulsed current density for bridges oriented along three crystallographic axes. The power dissipated in the bridges at the onset of the resistivity decrease (∇) and increase (Δ), is indicated with black arrows. The inset shows the measurement protocol using pump-probe current pulses and intercalated optical microscopy snapshots. (b) Schematic representation of the anisotropic $\rho(\theta)$ following an elliptic angular dependence (upper panel). The lower panel shows the experimentally determined onset of the sample resistivity decrease (∇) and the increase (Δ). The gray shadow covers a zone limited by the fittings to Eq. (5.1) for the extreme (minimum and maximum) power p_0 inferred from the experimental data points. 122
- 5.3 Bright field optical microscopy images for the bridges oriented along the a , 45° , and b crystallographic directions after (EM1) mild electromigration with $\sim 3\%$ increase in resistance, (EM2) severe electromigration with $\sim 30\%$ increase in resistance, and (Anti-EM) reversing the current polarity, so called anti-electromigration. All the images were acquired on the same sample in chronological order EM1, EM2, and finally Anti-EM under ambient conditions. The black arrows indicate the current direction. 123

- 5.4 (a) Numerical simulation of the sample resistance for ρ varying from 185 to 365 $\mu\Omega\text{cm}$ in steps of 20 $\mu\Omega\text{cm}$. The following parameters have been used for these simulations: $E_a = 0.55$ eV, $\alpha = 5 \times 10^{-3}$ K $^{-1}$, $x_0 = 0.9$, $\delta x_0 = 5\%$, $x_{min} = 0.5$, and $x_{max} = 0.95$. (b) Electromigration current determined using a criterion of 1 % increase on resistance, as a function of the resistivity extracted from the numerical simulation (blue) and the experiments (orange). The inset shows the power density (left ordinate) and maximum temperature (right ordinate) at the onset of electromigration for samples of different resistivity. 124
- 5.5 (a) Zoom in showing the numerically calculated initial change of resistance with current (blue line) of one of the curves in Fig.5.4(a) together with the evolution of the residual function r (orange line). (b) Evolution of the local resistance minima as a function of the degree of oxygen concentration disorder δx_0 . (c) Evolution of the local resistance minima as a function of the activation energy E_a 126
- 5.6 Numerical simulations reproducing the oxygen vacancy distribution of Fig.5.3 using the anisotropic model of section 5.4 with $E_{a_a} = 0.55$ eV, $E_{a_b} = 0.5$ eV. 127
- 6.1 Normalized magnetization (a) and resistance (b) as a function of temperature for a 20 nm thick plain film of LSMO. The ferromagnetic-paramagnetic transition takes place at a Curie temperature $T_C \approx 370$ K and is accompanied by a metal-insulator transition. The inset in panel (a) shows a 5 K magneto-optical image of the stray field generated by the sample shown in panel (c) with an in-plane magnetic field $H = 3$ mT. The inset in panel (b) corresponds to the X-ray diffraction spectra of a plain LSMO film deposited on STO substrate. SEM images of the two investigated sample layouts (continuous and discontinuous) are shown in panels (c) and (d), respectively. The zoom-in in panel (c) with a magnifying glass shows an optical microscopy image of the three bridges, the central one being $1 \times 3 \mu\text{m}^2$. In panel (d) the gap separating the two mirror symmetric structures is $3 \mu\text{m}$ 137

- 6.2 Relative change of resistance $\Delta R = R_i - R_0$, with R_i obtained after i -th current pulse and R_0 the resistance in the pristine state, as a function of temperature. The first three pulses are of same amplitude 0.5 mA whereas the fourth and last pulse increases to 1 mA. The background color of each panel indicates the corresponding transport bridge as illustrated in the sketch of panel (b). 138
- 6.3 (a) A bipolar I_{probe} pulsed current is used to monitor the sample resistance whereas a $I_{PLS} \gg I_{probe}$ of variable amplitude resulting from linearly increasing voltage pulses (b) triggers the oxygen migration process. Resistance of the left (c), central (d), and right (e) bridges after the voltage pulse as a function of the pulse number. The lower two rows show optical microscopy images acquired after the pulse number indicated in the frame. Electric transport and microscopy imaging are acquired at a bath temperature of 110 K. 139
- 6.4 Bright-field optical microscopy images of the LSMO/STO sample in the pristine state (a) and after applying a high electro-thermic stress (b) at bath temperature of 110 K. In (b) the appearance of dark vertical and horizontal lines in the substrate are indicated with white and black arrows, respectively. In (c) a scanning electron microscopy image of the central and left bridges is shown. Atomic force microscopy images of the same sample are shown in panels (d), (e) and (h). The line profiles indicated by the segments **A-A'** and **B-B'** are shown in panel (f) and (g), respectively. 141
- 6.5 Upper left panel: Optical microscopy image of the measured device and the polarity of the sweeping voltage ranging from 0 to 200 V at ambient conditions. The narrowest gap between the two electrodes is 3 μm . Yellowish background panels show differential images for which the image of the pristine sample has been subtracted to that of the indicated voltage. An area of electrolyzed LSMO can be observed developing above 154 V. 142

- 6.6 Upper left panel: Optical microscopy image of the measured device and the connection circuit used to sweep the voltage ranging from 0 to 200 V at ambient conditions. The narrowest gap between the two electrodes is 3 μm . Yellowish background panels show differential images for which the image of the pristine sample has been subtracted to that of the indicated voltage. A singular linear crystallographic defect develops and grows in the system above 138 V, before the device is electrically damaged at 158 V. 143
- 6.7 (a) Scanning electron microscopy of a LSMO/STO device evidencing several steps after severe electrothermal stress. Step-height along the x_1 (b) and along the x_2 (c) directions indicated in panel (a). Note that the profile along x_1 crosses two LSMO bridges, the one shown in (a) and one opposing it across the gap as shown in Fig.6.6. (d) Atomic force microscopy image of a device comparable to the one in (a) after triggering surface scars by applying electro-thermal stress. A zoom-in of the AFM images of the device in (b) at a crossing point of several lines is shown in panel (e). The rectangular box in panel (a) indicates the lamella cut-out by focused ion beam for subsequent STEM investigation presented in Fig.6.8 and Fig.6.9. 145
- 6.8 (a) Low magnification Z-contrast image of the FIB-cut lamella obtained from the zone indicated in Fig.6.7(a) around the step labeled 1. (b) Higher-magnification Z-contrast image of the red framed region marked in panel (a). (c) Atomic resolution image of the yellow framed region marked in panel (b). 146
- 6.9 (a) Low magnification Z-contrast image of the FIB-cut lamella obtained from the zone indicated in Fig.6.7(a) around the step labeled 2. (b,c) Higher-magnification Z-contrast image of the red and blue framed regions marked in panel (a), respectively. Inset in (b) shows an enlarged image at the surface of the bare STO. Scale bar is 2 nm long. 147
- 7.1 Sample layout in the form of a triple-constriction where each of the three bridge resistances can be accessed using two of the perpendicular terminals. The color code associated with the three bridges will be respected throughout the manuscript. The battery indicates what is defined as a positive voltage configuration. 155

- 7.2 Reversible resistive switching in a micropatterned YBCO film via square wave current of 5.8 mA amplitude and varying period. The red, green and blue panels correspond to the negative electrode (left), center and positive electrode (right constriction) resistance vs time measurements, while the gray panel shows the applied current. The switching resistance criterion (R_0) is set manually after a short initialization phase and is shown with the dashed horizontal line. This criterion is only checked in the middle constriction and determines the position at which the current polarity is switched. Note that the resistances of the left and right constrictions follow opposing trends, while the central constriction has a dome-shaped $R(t)$ curve. This is explained by an oxygen-vacancy counterflow following the current direction where the deoxygenation front repeatedly passes through the central constriction during switching. The insets are zooms on the highlighted sections of the data set. Experiments are performed in ambient conditions. (e) Evolution of the half-period δt (see definition in panel (d)) for a sample switching in a bipolar square wave current bias for ~ 7000 switching cycles. Polarity is switched whenever R_C returns to a preset R_0 , corresponding to 1% increase of resistance from pristine state. (f) Evolution of δt for three different current amplitudes performed on the same sample, the corresponding R_{\max} evolution is shown in (g). These measurements were performed in the same device in chronological order starting from the lowest current and progressively increasing the current. 156
- 7.3 Finite element modeling of the experimentally observed switching behavior in YBCO thin film constrictions. The numerical model captures both the regular dome shape of R_C (b) and the opposite trends in R_L (a) and R_R (c), as well as the decreasing values of δt (e) and R_{\max} (f). 157
- 7.4 Close up of the evolution of a single dome $R(t)$ from the finite element model. Oxygen distribution maps (in x) are shown in the upper row, oxygen distribution differential maps (dx) are depicted to the right and temperature profiles (T) are shown in the lower row, for the points indicated by the yellow circles. The highlighted section corresponds to a positive current polarity pulse. 159

- 7.5 Section of a finite element modeling simulation on a symmetric (upper panel) and an asymmetric (lower panel) mesh where the right constriction is $1 \mu\text{m}$ wider than the left one (see inset). The asymmetry induces an alternating trend in the evolution of R_C where positive polarity periods show higher R_{max} . The low observed amplitude results from the relatively long time needed for the system to settle. 160
- A.1 (a) Non-monotonous resistance rise as a function of current during the first electromigration process. The continuous blue line represent the experimental data and square symbols connected by a dashed line correspond to finite element simulations. (b) Simulated temperature distribution of the bridge for an applied current of 12 mA. 172
- A.2 Resistance $R(T)$ for the left (red), central (green), and right (blue) bridges, normalized by the $R(200 \text{ K})$ of the pristine sample. For the sake of comparison, the universal response for the pristine sample (shown in Fig.3.3) is replotted here with a black line. The inset shows an optical image of the final state after the electromigration process. 172
- A.3 (a-d) Typical room temperature μRaman spectra obtained at different spots along the transport bridge as indicated by the colored circles in panel (e). Panels (a'-d') show a zoom in the data presented in panels (a-d). The spectrum in panel (a) corresponds to the pristine sample whereas those in panels (b-d) correspond to the electromigrated sample. (f) Optically active Raman modes along the crystallographic c-axis for YBCO. The apical $\text{O}(4)$ Ag phonon mode occurs at 500 cm^{-1} 173
- A.4 Dark field (a) and bright field (b) optical microscopy images. Scanning electron microscopy images collected by InLens secondary electron detector (c) and Everhart-Thornley detector (d). For the SEM images an acceleration voltage 5 kV, aperture size $30 \mu\text{m}$, and working distance 6 mm has been used. 174
- B.1 Experimental evolution of the resistance as a function of time under DC stress of 5.8 mA of periodically switching polarity. The inset shows the polarity of the positive current and the color code associated to each bridge. These measurements were performed at room temperature and under ambient conditions. 178

- B.2 Panels (a) and (b), (c) and (d), (e) and (f) show the evolution of R_{min} and R_{max} for different values of x_{max} , x_0 and δx_0 respectively. Unless otherwise stated, the values of the parameters are given by : $E_a = 0.4$ eV, $x_0 = 0.76$, $x_{min} = 0.5$, $x_{max} = 0.95$ and $\delta x_0 = 5$ %. 180
- C.1 (a) Sketch of simulation geometry with dimension details. The thickness of the STO substrate is set to $50 \mu\text{m}$ in order to minimize computation time. The LSMO layer is shaped based on a SEM picture. (b) Cut view of the modeled device consisting of a 13 nm-thick layer of LSMO on a 40 nm-thick layer of STO representing the step in the substrate generated by the etching process. (c) Current density distribution in the LSMO layer for a voltage bias of 100 V. A complete mapping is displayed on the sketch of panel (a). 182
- C.2 (a) Cross-section of the temperature distribution in the plane indicated in the inset. (b) Zoom in the vicinity of the LSMO constriction where Joule heating occurs. The black dashed lines correspond to isothermal curves. The vertical scale indicates the spatial dimensions in μm . (c) Exponential decrease of the temperature with the depth penetration in the STO substrate along the vertical white dashed line shown in panel (a) for a 13 nm-thick LSMO sample (blue dots) and a 100 nm-thick Ag sample (red dots). 183
- C.3 (a) Cross-section of the electric field distribution in the same plane as in Fig.C.2(a). The color bar represents the logarithm of the magnitude of the electric field. (b) Zoom in the vicinity of the LSMO constriction with electric field indicated in linear scale. Dashed lines correspond to constant electric field curves. (c) Variation of the electric field with the depth penetration in the STO substrate along the white dashed line shown in panel (a). 184

- C.4 Low magnification Scanning Transmission Electron Microscopy in a region including two surface scars as indicated in Fig.7(a) of the main text. The yellow arrows mark three steps. The arrows labeled #1 and #3 mark 14 nm-thick steps corresponding to the triggered surface scars. The LSMO is indicated with an horizontal white arrow, and runs from left to right till the yellow arrow #3. Extended defects indicated with blue arrows are observed within the STO substrate in the vicinity of the blue dashed lines. The inset shows a sketch illustrating the upward shifting of a region with triangular cross section resulting from the thermal stress. 185
- C.5 High-magnification Z-contrast images of the regions marked in the upper low-magnification STEM image. The red framed image corresponds to the unaffected region. The yellow frame includes step #1. Region #3 (green frame) shows an edge of the LSMO layer resulting from the ion milling process. The step #2 (blue frame) at the bare STO substrate results from the thermal stress. 186
- C.6 (a,b) EEL spectra after background subtraction of of Ti L-edge and O K-edge from the STO substrate, respectively. (c,d) EEL spectra after background subtraction of Mn L-edge and O K-edge from the LSMO, respectively. All the spectra were acquired in the step #1 region. The energy dispersion used for the EEL spectra acquisition was 0.25 eV. 188

- D.1 Demonstration of the heating power effected by a device under experiment conditions. The three plots in the left column (red-green-blue) a)-c) show the measured 4-point resistance of a triple constriction device conducting 7.5 mA of DC current, with the panels representing the left, center and right constrictions, respectively. The measured resistances increased in all three bridges before settling to stable values at around 6 min after starting, implying that Joule-heating caused the thermalization of the chip. To confirm this heating effect, another device on the opposite side of the chip is wired, and its central constrictions' 4-point resistance is recorded with a low DC current (10 μ A) simultaneously with the high-current measurement in the device under test. The resulting measurement is shown in panel e) with a grey background. The two devices are positioned as shown in the illustration in panel d), the devices being colored as in the other panels. The central constrictions of the devices are ~ 3.5 mm apart. The identical shape of the resistance curves serves well to illustrate that the heating of the high-current device is enough to affect the whole chip. Measurement of the heating of the cryostat cold finger due to Joule heating in a YBCO microconstriction passing 7.5 mA DC current at 110 K are shown in panels f) and g). f) shows the resistance evolution of the central constriction R_C with the characteristic dome shape discussed in the main text, while panel g) shows the temperature read at the cryostat cold finger with a copper thermometer. Note the temperature increase of ~ 500 mK due to the heat generated in the sample. The inset in the grey panel shows a rendition of the mounted sample on the gold base of the cold finger, illustrating the distance from a working device to the thermometer. 190

Bibliography

- [1] T. S. Kuhn, *The structure of scientific revolutions*, en, 3rd ed. (Univ. of Chicago Press, Chicago, 1996).
- [2] H. K. Onnes, "Further experiments with liquid helium. C. on the change of electric resistance of pure metals at very low temperatures etc. IV. the resistance of pure mercury at helium temperatures", en, in *Through Measurement to Knowledge*, Vol. 124, edited by R. S. Cohen, K. Gavroglu, and Y. Goudaroulis (Springer Netherlands, 1911), pp. 261–263, 10.1007/978-94-009-2079-8_14.
- [3] J. G. Bednorz and K. A. Müller, "Possible high T_c superconductivity in the Ba-La-Cu-O system", *Zeitschrift für Physik B - Condensed Matter* **64**, 189–193 (1986) 10.1007/BF01303701.
- [4] M. Lorenz, M. S. R. Rao, T. Venkatesan, E. Fortunato, et al., "The 2016 oxide electronic materials and oxide interfaces roadmap", *Journal of Physics D: Applied Physics* **49** (2016), 10.1088/0022-3727/49/43/433001.
- [5] S. R. Ovshinsky, "Reversible electrical switching phenomena in disordered structures", *Physical Review Letters* **21**, 1450–1454 (1960) 10.1103/PhysRevLett.21.1450.
- [6] K. L. Chopra, "Avalanche-induced negative resistance in thin oxide films", *Journal of Applied Physics* **36**, 184–187 (1965) 10.1063/1.1713870.

- [7] G Dearnaley, A. M. Stoneham, and D. V. Morgan, "Electrical phenomena in amorphous oxide films", *Reports on Progress in Physics* **33**, 1129–1191 (1970) 10.1088/0034-4885/33/3/306.
- [8] D. Adler, M. S. Shur, M. Silver, and S. R. Ovshinsky, "Threshold switching in chalcogenide-glass thin films", *Journal of Applied Physics* **51**, 3289–3309 (1980) 10.1063/1.328036.
- [9] J. J. Yang, J. Borghetti, D. Murphy, D. R. Stewart, and R. S. Williams, "A family of electronically reconfigurable nanodevices", *Advanced Materials* **21**, 3754–3758 (2009) 10.1002/adma.200900822.
- [10] Y. V. Pershin and M. D. Ventra, "Memory effects in complex materials and nanoscale systems", *Advances in Physics* **60**, 145–227 (2011) 10.1080/00018732.2010.544961.
- [11] G. I. Meijer, "Who wins the nonvolatile memory race?", *Science* **319**, 1625–1626 (2008) 10.1126/science.1153909.
- [12] A. Sebastian, M. Le Gallo, R. Khaddam-Aljameh, and E. Eleftheriou, "Memory devices and applications for in-memory computing", *Nature Nanotechnology* **15**, Publisher: Nature Research, 529–544 (2020) 10.1038/s41565-020-0655-z.
- [13] A. Yoshihito and S.-S. Hokkaido, "Information processing using intelligent materials — information-processing architectures for material processors", *Journal of Intelligent Material Systems and Structures* **5**, 418–422 (1994) 10.1177/1045389X9400500315.
- [14] Y. Li, Z. Wang, R. Midya, Q. Xia, and J. J. Yang, "Review of memristor devices in neuromorphic computing: materials sciences and device challenges", *Journal of Physics D: Applied Physics* **51** (2018), 10.1088/1361-6463/aade3f.
- [15] E. Qiu, Y. H. Zhang, M. D. Ventra, and I. K. Schuller, "Reconfigurable cascaded thermal neuristors for neuromorphic computing", *Advanced Materials* **36**, 6 (2023), 10.1002/adma.202306818.
- [16] C. Metz, "Google built its very own chips to power its AI bots", *Wired*, Accessed Jan. 29th 2024 (2016), www.wired.com/2016/05/google-tpu-custom-chips/.
- [17] C. Kaspar, B. J. Ravoo, W. G. van der Wiel, S. V. Wegner, and W. H. Pernice, "The rise of intelligent matter", *Nature* **594**, 345–355 (2021) 10.1038/s41586-021-03453-y.

- [18] D. S. Jeong, R. Thomas, R. S. Katiyar, J. F. Scott, H. Kohlstedt, A. Petraru, and C. S. Hwang, "Emerging memories: resistive switching mechanisms and current status", *Reports on Progress in Physics* **75** (2012), 10.1088/0034-4885/75/7/076502.
- [19] J. J. Yang, D. B. Strukov, and D. R. Stewart, "Memristive devices for computing", *Nature Nanotechnology* **8**, 13–24 (2013) 10.1038/nano.2012.240.
- [20] A. Beck, J. G. Bednorz, C. Gerber, C. Rossel, and D. Widmer, "Reproducible switching effect in thin oxide films for memory applications", *Applied Physics Letters* **77**, 139–141 (2000) 10.1063/1.126902.
- [21] Y. Watanabe, J. G. Bednorz, A. Bietsch, C. Gerber, D. Widmer, A. Beck, and S. J. Wind, "Current-driven insulator-conductor transition and nonvolatile memory in chromium-doped srtio₃ single crystals", *Applied Physics Letters* **78**, 3738–3740 (2001) 10.1063/1.1377617.
- [22] R. Waser and M. Aono, "Nanoionics-based resistive switching memories", *Nature Materials* **6**, 833–840 (2007) 10.1038/nmat2023.
- [23] D. J. Wouters, S. Menzel, J. A. Rupp, T. Hennen, and R. Waser, "On the universality of the: I - V switching characteristics in non-volatile and volatile resistive switching oxides", *Faraday Discussions* **213**, 183–196 (2019) 10.1039/c8fd00116b.
- [24] J. C. Gonzalez-Rosillo, R. Ortega-Hernandez, J. Jareño-Cerulla, E. Miranda, J. Suñe, X. Granados, X. Obradors, A. Palau, and T. Puig, "Volume resistive switching in metallic perovskite oxides driven by the metal-insulator transition", in *Resistive switching: oxide materials, mechanisms, devices and operations*, edited by J. Rupp, D. Ielmini, and I. Valov (Springer, 2022).
- [25] D. Ielmini, "Resistive switching memories based on metal oxides: mechanisms, reliability and scaling", *Semiconductor Science and Technology* **31**, 10.1088/0268-1242/31/6/063002 (2016) 10.1088/0268-1242/31/6/063002.
- [26] I. Riess, "Review of mechanisms proposed for redox based resistive switching structures", in *Resistive switching: oxide materials, mechanisms, devices and operations*, edited by J. Rupp, D. Ielmini, and I. Valov (Springer, 2022).
- [27] I. H. Inoue and A. Sawa, "Resistive switchings in transition-metal oxides", *Functional Metal Oxides: New Science and Novel Applications* **11**, 443–463 (2013) 10.1002/9783527654864.ch16.

- [28] V. S. Zharinov, X. D. Baumans, A. V. Silhanek, E. Janssens, and J. V. D. Vondel, "Controlled electromigration protocol revised", *Review of Scientific Instruments* **89** (2018), 10.1063/1.5011953.
- [29] X. D. A. Baumans, A. Fernandez-Rodriguez, N Mestres, S Collienne, J. V. de Vondel, A Palau, and A. V. Silhanek, "Electromigration in the dissipative state of high-temperature superconducting bridges", *Applied Physics Letters* **114**, 012601 (2019) 10.1063/1.5063797.
- [30] P. Noé, C. Vallée, F. Hippert, F. Fillot, and J.-Y. Raty, "Phase-change materials for non-volatile memory devices: from technological challenges to materials science issues", *Semiconductor Science and Technology* **33**, 013002 10.1088/1361-6641/aa7c25.
- [31] W. Zhang, R. Mazzarello, M. Wuttig, and E. Ma, "Designing crystallization in phase-change materials for universal memory and neuro-inspired computing", *Nature Reviews Materials* **4**, 150–168 (2019) 10.1038/s41578-018-0076-x.
- [32] P. Noé, A. Verdy, F. d'Acapito, J.-B. Dory, M. Bernard, G. Navarro, J.-B. Jager, J. Gaudin, and J.-Y. Raty, "Toward ultimate nonvolatile resistive memories: The mechanism behind ovonic threshold switching revealed", en, *Science Advances* **6**, eaay2830 (2020) 10.1126/sciadv.aay2830.
- [33] I. Valov, R. Waser, J. R. Jameson, and M. N. Kozicki, "Electrochemical metallization memories - fundamentals, applications, prospects", *Nanotechnology* **22**, 254003 (2011) 10.1088/0957-4484/22/28/289502.
- [34] Z. B. Yan and J. M. Liu, "Resistance switching memory in perovskite oxides", *Annals of Physics* **358**, 206–224 (2015) 10.1016/j.aop.2015.03.028.
- [35] Z Li, C. L. Bauer, S Mahajan, and A. G. Milnes, "Degradation and subsequent healing by electromigration in Al-1wt% Si thin films", *Journal of Applied Physics* **72**, 1821–1832 (1992) 10.1063/1.351653.
- [36] C. F. Hong, M. Togo, and K. Hoh, "Repair of electromigration-induced voids in aluminum interconnection by current reversal", *Japanese Journal of Applied Physics* **32**, 624–627 (1993) 10.1143/JJAP.32.L624.
- [37] J. Lombardo, Željko L. Jelić, X. D. Baumans, J. E. Scheerder, J. P. Nacenta, V. V. Moshchalkov, J. V. D. Vondel, R. B. Kramer, M. V. Milošević, and A. V. Silhanek, "In situ tailoring of superconducting junctions via electro-annealing", *Nanoscale* **10**, 1987–1996 (2018) 10.1039/c7nr08571k.

- [38] M. A. Zidan, A. Chen, G. Indiveri, and W. D. Lu, "Memristive computing devices and applications", in *Resistive switching: oxide materials, mechanisms, devices and operations*, edited by J. Rupp, D. Ielmini, and I. Valov (Springer, 2022).
- [39] M. A. Peña and J. L. Fierro, "Chemical structures and performance of perovskite oxides", *Chemical Reviews* **101**, 1981–2017 (2001) 10.1021/cr980129f.
- [40] M. B. Salamon and M. Jaime, "The physics of manganites: structure and transport", *Reviews of Modern Physics* **73**, 583–628 (2001) 10.1103/RevModPhys.73.583.
- [41] S. V. Kalinin and N. A. Spaldin, "Functional ion defects in transition metal oxides", *Science* **341**, 858–859 (2013) 10.1126/science.1243098.
- [42] B. Keimer, S. A. Kivelson, M. R. Norman, S. Uchida, and J. Zaanen, "From quantum matter to high-temperature superconductivity in copper oxides", *Nature* **518**, 179–186 (2015) 10.1038/nature14165.
- [43] R. A. D. Souza, "Oxygen diffusion in SrTiO₃ and related perovskite oxides", *Advanced Functional Materials* **25**, 6326–6342 (2015) 10.1002/adfm.201500827.
- [44] K. Szot, W. Speier, G. Bihlmayer, and R. Waser, "Switching the electrical resistance of individual dislocations in single-crystalline SrTiO₃", *Nature Materials* **5**, 312–320 (2006) 10.1038/nmat1614.
- [45] R. Waser, R. Dittmann, C. Staikov, and K. Szot, "Redox-based resistive switching memories nanoionic mechanisms, prospects, and challenges", *Advanced Materials* **21**, 2632–2663 (2009) 10.1002/adma.200900375.
- [46] J.-P. Locquet, C. Marchiori, M. Sousa, J. Fompeyrine, and J. W. Seo, "High-K dielectrics for the gate stack", *Journal of Applied Physics* **100**, 051610 (2006) 10.1063/1.2336996.
- [47] M. Coll, J. Fontcuberta, M. Althammer, M. Bibes, et al., "Towards oxide electronics: a roadmap", *Applied Surface Science* **482**, 1–93 (2019) 10.1016/j.apsusc.2019.03.312.
- [48] J. R. Lloyd, "Electromigration in thin film conductors", *Semiconductor Science and Technology*. **12** **12**, 1661–1672 (1997) 10.1088/0268-1242/12/10/002.
- [49] Y. Kim, C. H. Ang, K. Ang, and S. W. Chang, "Electromigrated nanogaps: a review on the fabrications and applications", *Journal of Vacuum Science and Technology B* **39** (2021), 10.1116/6.0000866.

- [50] C. Xiang, J. Y. Kim, and R. M. Penner, "Reconnectable sub-5 nm nanogaps in ultralong gold nanowires", *Nano Letters* **9**, 2133–2138 (2009) 10.1021/nl900698s.
- [51] X. D. A. Baumans, D. Cerbu, O. A. Adami, V. S. Zharinov, N. Verellen, G. Papari, J. E. Scheerder, G. Zhang, V. V. Moshchalkov, A. V. Silhanek, and J. V. D. Vondel, "Thermal and quantum depletion of superconductivity in narrow junctions created by controlled electromigration", *Nature Communications* **7**, 3–10 (2016) 10.1038/ncomms10560.
- [52] T. Kozlova, M. Rudneva, and H. W. Zandbergen, "In situ TEM and STEM studies of reversible electromigration in thin palladium-platinum bridges", *Nanotechnology* **24**, 1–18 (2013) 10.1088/0957-4484/24/50/505708.
- [53] R Hoffmann-Vogel, "Electromigration and the structure of metallic nanocontacts", *Applied Physics Reviews* **4** (2017), 10.1063/1.4994691.
- [54] P. M. Chowdhury, "Oxygen diffusion study in manganite films near room temperature", *Materials Research Bulletin* **131** (2020), 10.1016/j.materresbull.2020.110976.
- [55] H. Gao, S. Sahu, C. A. Randall, and L. J. Brillson, "Direct , spatially resolved observation of defect states with electromigration and degradation of single crystal strtio 3 direct , spatially resolved observation of defect states with electromigration and degradation of single crystal strtio 3", *Journal of Applied Physics* **127** (2020), 10.1063/1.5130892.
- [56] K. Jin, R. Suchoski, S. Fackler, Y. Zhang, X. Pan, R. L. Greene, and I. Takeuchi, "Combinatorial search of superconductivity in fe-b composition spreads", *APL Materials* **1**, 042101 (2013) 10.1063/1.4822435.
- [57] G. He, Z. Wei, Z. Feng, X. Yu, B. Zhu, L. Liu, K. Jin, J. Yuan, and Q. Huan, "Combinatorial laser molecular beam epitaxy system integrated with specialized low-temperature scanning tunneling microscopy", *Review of Scientific Instruments* **91**, 013904 (2020) <https://doi.org/10.1063/1.5119686>, 10.1063/1.5119686.
- [58] T. Jacobs, Y. Simsek, Y. Koval, P. Müller, and V. M. Krasnov, "Sequence of quantum phase transitions in $\text{Bi}_2\text{Sr}_2\text{CaCu}_2\text{O}_{8+\delta}$ cuprates revealed by in situ electrical doping of one and the same sample", *Physical Review Letters* **116**, 1–6 (2016) 10.1103/PhysRevLett.116.067001.

- [59] E. Trabaldo, A. Kalaboukhov, R. Arpaia, E. Wahlberg, F. Lombardi, and T. Bauch, "Mapping the phase diagram of a $\text{YBa}_2\text{Cu}_3\text{O}_{7-\delta}$ nanowire through electromigration", *Physical Review Applied* **17**, 024021 (2022) 10.1103/PhysRevApplied.17.024021.
- [60] Y. B. Nian, J. Strozier, N. J. Wu, X. Chen, and A. Ignatiev, "Evidence for an oxygen diffusion model for the electric pulse induced resistance change effect in transition-metal oxides", *Physical Review Letters* **98**, 3–6 (2007) 10.1103/PhysRevLett.98.146403.
- [61] C. H. Ahn, S. Gariglio, P. Paruch, T. Tybell, L. Antognazza, and J. M. Triscone, "Electrostatic modulation of superconductivity in ultrathin $\text{GdBa}_2\text{Cu}_3\text{O}_{7-x}$ films", *Science* **284**, 1152–1155 (1999) 10.1126/science.284.5417.1152.
- [62] P. Gao, Z. Kang, W. Fu, W. Wang, X. Bai, and E. Wang, "Electrically driven redox process in cerium oxides", *Journal of the American Chemical Society* **132**, 4197–4201 (2010) 10.1021/ja9086616.
- [63] D. Gupta, ed., *Diffusion processes in advanced technological materials* (Springer, 2005).
- [64] J. R. Black, "Electromigration—a brief survey and some recent results", *IEEE Transactions on Electron Devices* **16**, 338–347 (1969) 10.1109/T-ED.1969.16754.
- [65] R. S. Sorbello, "Theory of direct force in electromigration", *Physical Review B* **31** (1985), 10.1103/PhysRevB.31.798.
- [66] R. P. Gupta, Y. Serruys, G. Brebec, and Y. Adda, "Calculation of the effective valence for electromigration in niobium", *Physical Review B* **27**, 672–677 (1983) 10.1103/PhysRevB.27.672.
- [67] D. Gupta, "Diffusion in bulk solids and thin films: some phenomenological examples", in *Diffusion processes in advanced technological materials*, edited by D. Gupta (Springer, 2005).
- [68] R. L. de Orió, H. Ceric, and S. Selberherr, "Physically based models of electromigration: from Black's equation to modern tcad models", **50**, Publisher: Elsevier Ltd, 775–789 10.1016/j.microrel.2010.01.007.
- [69] H. B. Huntington, "Electromigration in metals", in *Diffusion in solids*, edited by A. S. Nowick and J. Burton (Elsevier, 1975), pp. 303–349, 10.1016/B978-0-12-522660-8.50011-8.

- [70] D. Gupta, W. R. Donaldson, K. Koitkamp, and A. M. Kadin, "Optically triggered switching of optically thick YBCO films", *IEEE Transactions on Applied Superconductivity* **3**, 2895–2898 (1993) 10.1109/77.234005.
- [71] A. Palau, A. Fernandez-Rodriguez, J. C. Gonzalez-Rosillo, X. Granados, M. Coll, B. Bozzo, R. Ortega-Hernandez, J. Suñé, N. Mestres, X. Obradors, and T. Puig, "Electrochemical tuning of metal insulator transition and nonvolatile resistive switching in superconducting films", *ACS Applied Materials and Interfaces* **10**, 30522–30531 (2018) 10.1021/acsami.8b08042.
- [72] S. Marinković, A. Fernández-Rodríguez, S. Collienne, S. B. Alvarez, S. Melinte, B. Maiorov, G. Rius, X. Granados, N. Mestres, A. Palau, and A. V. Silhanek, "Direct visualization of current-stimulated oxygen migration in $\text{YBa}_2\text{Cu}_3\text{O}_{7-\delta}$ thin films", *ACS Nano* **14**, 11765–11774 (2020) 10.1021/acsnano.0c04492.
- [73] S. Marinković, A. Fernández-Rodríguez, E. Fourneau, M. Cabero, H. Wang, N. D. Nguyen, J. Gazquez, N. Mestres, A. Palau, and A. V. Silhanek, "From electric doping control to thermal defect nucleation in perovskites", *Advanced Materials Interfaces* **9** (2022), 10.1002/admi.202200953.
- [74] S. Collienne, S. Marinković, A. Fernández-Rodríguez, N. Mestres, A. Palau, and A. V. Silhanek, "Electrically-driven oxygen vacancy aggregation and displacement in $\text{YBa}_2\text{Cu}_3\text{O}_{7-\delta}$ films", *Advanced Electronic Materials* **8** (2022), 10.1002/aelm.202101290.
- [75] F. Gunkel, D. V. Christensen, Y. Z. Chen, and N. Pryds, "Oxygen vacancies: the (in)visible friend of oxide electronics", *Applied Physics Letters* **116** (2020), 10.1063/1.5143309.
- [76] M. J. Rozenberg, M. J. Sánchez, R. Weht, C. Acha, F. Gomez-Marlasca, and P. Levy, "Mechanism for bipolar resistive switching in transition-metal oxides", *Physical Review B* **81** (2010), 10.1103/PhysRevB.81.115101.
- [77] H. H. Barrett, "Dielectric breakdown of single-crystal strontium titanate", *Journal of Applied Physics* **35**, 1420–1425 (1964) 10.1063/1.1713643.

- [78] W. Jiang, R. J. Kamaladasa, Y. M. Lu, A. Vicari, R. Berekman, P. A. Salvador, J. A. Bain, Y. N. Picard, and M. Skowronski, "Local heating-induced plastic deformation in resistive switching devices", *J. App. Phys.* **110** (2011), 10.1063/1.3633271.
- [79] A. Kushima and B. Yildiz, "Oxygen ion diffusivity in strained yttria stabilized zirconia: where is the fastest strain?", *Journal of Materials Chemistry* **20**, 4809–4819 (2010) 10.1039/c000259c.
- [80] C. P. Poole Jr., H. A. Farach, R. J. Creswick, and R. Prozorov, *Superconductivity* (Academic Press, 2007), p. 670.
- [81] M. Imada, A. Fujimori, and Y. Tokura, "Metal-insulator transitions", *Reviews of Modern Physics* **70** (1998), 10.1103/RevModPhys.70.1039.
- [82] J. H. D. Boer and E. J. W. Verwey, "Semi-conductors with partially and with completely filled 3d-lattice bands", *Proceedings of the Physical Society* **49** (1937), 10.1088/0959-5309/49/4S/307.
- [83] G. Kotliar, S. Y. Savrasov, K. Haule, V. S. Oudovenko, O. Parcollet, and C. A. Marianetti, "Electronic structure calculations with dynamical mean-field theory", *Reviews of Modern Physics* **78**, 865–951 (2006) 10.1103/RevModPhys.78.865.
- [84] N. F. Mott, "The basis of the electron theory of metals, with special reference to the transition metals", *Proceedings of the Physical Society. Section A* **62**, 416–422 (1949) 10.1088/0370-1298/62/7/303.
- [85] J. Hubbard, "Electron correlations in narrow energy bands. iv. the atomic representation", *Proceedings of the Royal Society of London. Series A* **285**, 542–560 (1965) 10.1098/rspa.1965.0124.
- [86] V. I. Anisimov, J. Zaanen, and O. K. Andersen, "Band theory and Mott insulators: Hubbard U instead of Stoner I", *Physical Review B* **44**, 943–954 (1991) 10.1103/PhysRevB.44.943.
- [87] Y. Kohsaka, K. Iwaya, S. Satow, T. Hanaguri, M. Azuma, M. Takano, and H. Takagi, "Imaging nanoscale electronic inhomogeneity in the lightly doped mott insulator $\text{Ca}_{2-x}\text{Na}_x\text{CuO}_2\text{Cl}_2$ ", *Physical Review Letters* **93** (2004), 10.1103/PhysRevLett.93.097004.
- [88] M. V. Sadovskii, I. A. Nekrasov, E. Z. Kuchinskii, T. Pruschke, and V. I. Anisimov, "Pseudogaps in strongly correlated metals: a generalized dynamical mean-field theory approach", *Physical Review B* **72** (2005), 10.1103/PhysRevB.72.155105.

- [89] G. Kotliar and J. Liu, "Superexchange mechanism and d -wave superconductivity", *Physical Review B* **38**, 5142–5145 (1988) 10.1103/PhysRevB.38.5142.
- [90] T. Maier, M Jarrell, T. Pruschke, and J Keller, " d -Wave superconductivity in the Hubbard model", *Physical Review Letters* **85**, 1524–1527 (2000) 10.1103/PhysRevLett.85.1524.
- [91] F. J. Morin, "Oxides which show a metal-to-insulator transition at the Néel temperature", *Physical Review Letters* **3**, 34–36 (1959) 10.1103/PhysRevLett.3.34.
- [92] Y. Feng, K. J. Jin, L. Gu, X. He, C. Ge, Q. H. Zhang, M. He, Q. L. Guo, Q. Wan, M. He, H. B. Lu, and G. Yang, "Insulating phase at low temperature in ultrathin $\text{La}_{0.8}\text{Sr}_{0.2}\text{MnO}_3$ films", *Scientific Reports* **6**, 1–9 (2016) 10.1038/srep22382.
- [93] B. Kim, D. Kwon, J. H. Song, Y. Hikita, B. G. Kim, and H. Y. Hwang, "Finite size effect and phase diagram of ultra-thin $\text{La}_{0.7}\text{Sr}_{0.3}\text{MnO}_3$ ", *Solid State Communications* **150**, 598–601 (2010) 10.1016/j.ssc.2009.12.041.
- [94] J.-P. Locquet, J. Perret, J. Fompeyrine, E. Mächler, J. W. Seo, and G. Van Tendeloo, "Doubling the critical temperature of $\text{La}_{1.9}\text{Sr}_{0.1}\text{CuO}_4$ using epitaxial strain", *Nature* **394**, 453–456 (1998) 10.1038/28810.
- [95] G. Khadzhai, S. Kamchatnaya, M. Korobkov, Y. Necheporenko, R. Vovk, and O. Dobrovolskiy, "High-pressure effects on basal-plane conductivity of YPrBCO single crystals", *Current Applied Physics* **39**, 311–316 (2022) 10.1016/j.cap.2022.05.015.
- [96] B. Kyung, S. S. Kancharla, D. Sénéchal, A. M. Tremblay, M. Civelli, and G. Kotliar, "Pseudogap induced by short-range spin correlations in a doped Mott insulator", *Physical Review B* **73** (2006), 10.1103/PhysRevB.73.165114.
- [97] G. Nieva, E. Osquiguil, J. Guimpel, M. Maenhoudt, B. Wuyts, Bruynseraede, M. B. Maple, and I. K. Scghuller, "Photoinduced enhancement of superconductivity", *Applied Physics Letters* **60**, 2159–2161 (1992) 10.1063/1.107069.
- [98] R. S. Decca, H. D. Drew, B. Maiorov, J. Guimpel, and E. Osquiguil, "Photoinduced superconducting nanowires in $\text{GdBa}_2\text{Cu}_3\text{O}_{6.5}$ films", *Applied Physics Letters* **73**, 120–122 (1998) 10.1063/1.121787.

- [99] H. S. Lee, S. G. Choi, H. H. Park, and M. J. Rozenberg, "A new route to the Mott-Hubbard metal-insulator transition: strong correlations effects in $\text{Pr}_{0.7}\text{Ca}_{0.3}\text{MnO}_3$ ", *Scientific Reports* **3**, 1–5 (2013) 10.1038/srep01704.
- [100] E. Janod, J. Tranchant, B. Corraze, M. Querré, P. Stoliar, M. Rozenberg, T. Cren, D. Roditchev, V. T. Phuoc, M. P. Besland, and L. Cario, "Resistive switching in mott insulators and correlated systems", *Advanced Functional Materials* **25**, 6287–6305 (2015) 10.1002/adfm.201500823.
- [101] T. W. Hickmott, "Low-frequency negative resistance in thin anodic oxide films", *Journal of Applied Physics* **33**, 2669–2682 (1962) 10.1063/1.1702530.
- [102] Z. Yang, C. Ko, and S. Ramanathan, "Oxide electronics utilizing ultra-fast metal-insulator transitions", *Annual Review of Materials Research* **41**, 337–367 (2011) 10.1146/annurev-matsci-062910-100347.
- [103] F. A. Chudnovskii, L. L. Odynets, A. L. Pergament, and G. B. Stefanovich, "Electroforming and switching in oxides of transition metals: the role of metal-insulator transition in the switching mechanism", *Journal of Solid State Chemistry* **122**, 95–99 (1996) 10.1006/jssc.1996.0087.
- [104] S. Bagdzevicius, K. Maas, M. Boudard, and M. Burriel, "Interface-type resistive switching in perovskite materials", in *Resistive switching: oxide materials, mechanisms, devices and operations*, edited by J. Rupp, D. Ielmini, and I. Valov (Springer, 2022).
- [105] H. G. Luo, Y. H. Su, and T. Xiang, "Scaling analysis of normal-state properties of high-temperature superconductors", *Physical Review B* **77** (2008), 10.1103/PhysRevB.77.014529.
- [106] J. Cao and J. Wu, "New opportunities on phase transitions of correlated electron nanostructures", in *Functional metal oxide nanostructures*, Vol. 149, edited by J. Wu, J. Cao, W. Han, A. Janotti, and H. Kim (Springer, 2012).
- [107] J. L. Musfeldt, "Optical properties of nanoscale transition metal oxides", in *Functional metal oxide nanostructures*, Vol. 149, edited by J. Wu, J. Cao, W. Han, A. Janotti, and H. Kim (Springer, 2012).
- [108] I. D. Brown and R. D. Shannon, "Empirical bond-strength-bond-length curves for oxides", *Acta Cryst* **29**, 266 (1973) 10.1107/S0567739473000689.

- [109] K. Liu, S. Lee, S. Yang, O. Delaire, and J. Wu, "Recent progresses on physics and applications of vanadium dioxide", *Materials Today* **21**, 875–896 (2018) 10.1016/j.mattod.2018.03.029.
- [110] Z. Zhang, F. Zuo, C. Wan, A. Dutta, J. Kim, J. Rensberg, R. Nawrodt, H. H. Park, T. J. Larrabee, X. Guan, Y. Zhou, S. M. Prokes, C. Ronning, V. M. Shalaev, A. Boltasseva, M. A. Kats, and S. Ramanathan, "Evolution of metallicity in vanadium dioxide by creation of oxygen vacancies", *Physical Review Applied* **7** (2017), 10.1103/PhysRevApplied.7.034008.
- [111] O. T. Sørensen, *Nonstoichiometric oxides* (Academic Press, 1981), p. 441.
- [112] S. Andersson, B. Collén, U. Kuylenstierna, and A. Magnéli, "Phase analysis studies on the titanium-oxygen system", *Acta Chemica Scandinavica* **11**, 1641–1652 (1957) <https://doi.org/10.3891/acta.chem.scand.11-1641>.
- [113] A. Magnéli, "Non-stoichiometry and structural disorder in some families of inorganic compounds", *Pure and Applied Chemistry* **50**, 1261–1271 (1978) 10.1351/pac197850111261.
- [114] M. D. Pickett, J. Borghetti, J. J. Yang, G. Medeiros-Ribeiro, and R. S. Williams, "Coexistence of memristance and negative differential resistance in a nanoscale metal-oxide-metal system", *Advanced Materials* **23**, 1730–1733 (2011) 10.1002/adma.201004497.
- [115] K. M. Kim, D. S. Jeong, and C. S. Hwang, "Nanofilamentary resistive switching in binary oxide system; a review on the present status and outlook", *Nanotechnology* **22** (2011), 10.1088/0957-4484/22/25/254002.
- [116] K. Nagashima, T. Yanagida, K. Oka, M. Kanai, A. Klamchuen, J. S. Kim, B. H. Park, and T. Kawai, "Intrinsic mechanisms of memristive switching", *Nano Letters* **11**, 2114–2118 (2011) 10.1021/nl200707n.
- [117] F. Nardi, S. Balatti, S. Larentis, D. C. Gilmer, and D. Ielmini, "Complementary switching in oxide-based bipolar resistive-switching random memory", *IEEE Transactions on Electron Devices* **60**, 70–77 (2013) 10.1109/TED.2012.2226728.
- [118] J. Rupp, D. Ielmini, and I. Valov, eds., *Resistive switching: oxide materials, mechanisms, devices and operations* (Springer, 2022).
- [119] C. H. Ahn, J. M. Triscone, and J. Mannhart, "Electric field effect in correlated oxide systems", *Nature* **424**, 1015–1018 (2003) 10.1038/nature01878.

- [120] R. J. Cava, "Structural chemistry and the local charge picture of copper oxide superconductors", *Science* **247**, 656–662 (1990) 10.1126/science.247.4943.656.
- [121] J. D. Jorgensen, B. W. Veal, A. P. Paulikas, L. J. Nowicki, G. W. Crabtree, H. Claus, and W. K. Kwok, "Structural properties of oxygen-deficient $\text{YBa}_2\text{Cu}_3\text{O}_{7-\delta}$ ", *Physical Review B* **41**, 1863–1877 (1990) 10.1103/PhysRevB.41.1863.
- [122] W. M. Temmerman, H. Winter, Z. Szotek, and A. Svane, "Cu valency change induced by O doping in YBCO", *Physical Review Letters* **86**, 2435–2438 (2001) 10.1103/PhysRevLett.86.2435.
- [123] T. Ishihara, J. A. Kilner, M. Honda, N. Sakai, H. Yokokawa, and Y. Takita, "Oxygen surface exchange and diffusion in La-based 3 perovskite type oxides", *Solid State Ionics*, 593–600 (1998) 10.1016/S0167-2738(98)00390-7.
- [124] S. Menzel, M. Waters, A. Marchewka, U. Böttger, R. Dittmann, and R. Waser, "Origin of the ultra-nonlinear switching kinetics in oxide-based resistive switches", *Advanced Functional Materials* **21**, 4487–4492 (2011) 10.1002/adfm.201101117.
- [125] C. Zener, "Interaction between the d-shells in the transition metals. ii. ferromagnetic compounds of manganese with perovskite structure", *Physical Review* **82**, 403–405 (1951) 10.1103/PhysRev.82.403.
- [126] U. Staub, G. I. Meijer, F. Fauth, R. Allenspach, J. G. Bednorz, J. Karpinski, S. M. Kazakov, L. Paolasini, and F. d'Acapito, "Direct observation of charge order in an epitaxial NdNiO_3 film", *Physical Review Letters* **88**, 4 (2002) 10.1103/PhysRevLett.88.126402.
- [127] R. Ramesh and D. G. Schlom, "Creating emergent phenomena in oxide superlattices", *Nature Reviews Materials* **4**, 257–268 (2019) 10.1038/s41578-019-0095-2.
- [128] D. J. Werder, C. H. Chen, R. J. Cava, and B. Batlogg, "Oxygen-vacancy ordering and microstructure in annealed $\text{Ba}_2\text{YCu}_3\text{O}_{7-\delta}$ superconductors", *Physical Review B* **38**, 5130–5133 (1988) 10.1103/PhysRevB.38.5130.
- [129] R. D. King-Smith and D. Vanderbilt, "First-principles investigation of ferroelectricity in perovskite compounds", *Physical Review B* **49**, 5828–5844 (1994) 10.1103/PhysRevB.49.5828.

- [130] E. Dagotto, T. Hotta, and A. Moreo, "Colossal magnetoresistant materials: the key role of phase separation", *Physics Report* **344**, 1–153 (2001) 10.1016/S0370-1573(00)00121-6.
- [131] N. Nuraje and K. Su, "Perovskite ferroelectric nanomaterials", *Nanoscale* **5**, 8752–8780 (2013) 10.1039/c3nr02543h.
- [132] D. E. Gupp and A. M. Goldman, "Giant piezoelectric effect in strontium titanate at cryogenic temperatures", *Science* **276**, 392–394 (1997) 10.1126/science.276.5311.392.
- [133] F. Sun, H. Khassaf, and S. P. Alpay, "Strain engineering of piezoelectric properties of strontium titanate thin films", *Journal of Materials Science* **49**, 5978–5985 (2014) 10.1007/s10853-014-8316-y.
- [134] D. A. Muller, N. Nakagawa, A. Ohtomo, J. L. Grazul, and H. Y. Hwang, "Atomic-scale imaging of nanoengineered oxygen vacancy profiles in SrTiO₃", *Nature* **430**, 657–661 (2004) 10.1038/nature02756.
- [135] D. C. Meyer, A. A. Levin, T. Leisegang, E. Gutmann, P. Paufler, M. Reibold, and W. Pompe, "Reversible tuning of a series of intergrowth phases of the ruddlesden - popper type SrO(SrTiO₃)_n in an (001) SrTiO₃ single-crystalline plate by an external electric field and its potential use for adaptive X-ray optics", *Applied Physics A*: **84**, 31–35 (2006) 10.1007/s00339-006-3584-2.
- [136] V. Metlenko, A. H. H. Ramadan, F. Funkel, H. Du, H. Schraknepper, S. Hoffmann-Eifert, R. Dittmann, R. Waser, and R. A. De Souza, "Do dislocations act as atomic autobahns for oxygen in the perovskite oxide SrTiO₃?", *Nanoscale* **6**, 12864 (2014) 10.1039/c4nr04083j.
- [137] D. Marrocchelli, L. Sun, and B. Yildiz, "Dislocations in SrTiO₃: easy to reduce but not so fast for oxygen transport", *Journal of the American Chemical Society* **137**, 4735–4748 (2015) 10.1021/ja513176u.
- [138] M. Janousch, G. I. Meijer, U. Staub, B. Delley, S. E. Karg, and B. P. Andreasson, "Role of oxygen vacancies in Cr-doped SrTiO₃ for resistance-change memory", *Advanced Materials* **19**, 2232–2235 (2007) 10.1002/adma.200602915.
- [139] A. Urushibara, Y. Moritomo, T. Arima, A. Asamitsu, G. Kido, and Y. Tokura, "Insulator-metal transition and giant magnetoresistance in La_{1-x}Sr_xMnO₃", *Physical Review B* **51**, 14103–14109 (1995) 10.1103/PhysRevB.51.14103.

- [140] H. L. Ju, J. Gopalakrishnan, J. L. Peng, Q. Li, G. C. Xiong, T. Venkatesan, and R. L. Greene, "Dependence of giant magnetoresistance on oxygen stoichiometry and magnetization in polycrystalline $\text{La}_{0.67}\text{Sr}_{0.33}\text{MnO}_3$ ", *Physical Review B* **51**, 6143–6146 (1995) 10.1103/PhysRevB.51.6143.
- [141] M. Nord, P. E. Vullum, M. Moreau, J. E. Boschker, S. M. Selbach, R. Holmestad, and T. Tybell, "Structural phases driven by oxygen vacancies at the $\text{La}_{0.7}\text{Sr}_{0.3}\text{MnO}_3/\text{SrTiO}_3$ hetero-interface", *Applied Physics Letters* **106**, 0–4 (2015) 10.1063/1.4906920.
- [142] B. Vertruyen, R. Cloots, A. Rulmont, G. Dhahlenne, M. Ausloos, and P. Vanderbemden, "Magnetotransport properties of a single grain boundary in a bulk La–Ca–Mn–O material", *Journal of Applied Physics* **90**, 5692–5697 (2001) 10.1063/1.1410885.
- [143] T. G. Parsons, H. D'Hondt, J. Hadermann, and M. A. Hayward, "Synthesis and structural characterization of $\text{La}_{1-x}\text{A}_x\text{MnO}_{2.5}$ (A = Ba, Sr, Ca) phases: mapping the variants of the brownmillerite structure", *Chemistry of Materials* **21**, 5527–5538 (2009) 10.1021/cm902535m.
- [144] D. C. Johnston, H. Prakash, W. H. Zachariasen, and R. Viswanathan, "High temperature superconductivity in Li-Ti-O ternary system", *Materials Research Bulletin* **8**, 777–784 (1973) [https://doi.org/10.1016/0025-5408\(73\)90183-9](https://doi.org/10.1016/0025-5408(73)90183-9).
- [145] C. W. Chu, P. H. Hor, R. L. Meng, Z. J. Gao, Z. J. Huang, and Y. Q. Wang, "Evidence for superconductivity above 40 K in the La-Ba-Cu-O compound system", *Physical Review Letters* **58**, 405 (1987) 10.1103/PhysRevLett.58.405.
- [146] C. W. Chu, "Superconductivity above 90 K", *Proceedings of the National Academy of Sciences of the USA* **84**, 4681–4682 (1987) 10.1073/pnas.84.14.4681.
- [147] K. M. Lang, V. Madhavan, J. E. Hoffman, E. W. Hudson, H. Eisaki, S. Uchida, and J. C. Davis, "Imaging the granular structure of high- T_c superconductivity in underdoped BSCCO", *Nature* **415**, 412–416 (2002) 10.1038/415412a.
- [148] A. Schilling, M. Cantoni, J. Guo, and H. R. Ott, "Superconductivity above 130 K in the Hg-Ba-Ca-Cu-O system", *Nature* **363**, 56–58 (1993) 10.1038/363056a0.

- [149] A. L. Solovjov, E. V. Petrenko, L. V. Omelchenko, R. V. Vovk, I. L. Goulatis, and A. Chroneos, "Effect of annealing on a pseudogap state in untwinned $\text{YBa}_2\text{Cu}_3\text{O}_{7-\delta}$ single crystals", *Scientific Reports* **9** (2019), 10.1038/s41598-019-45286-w.
- [150] M. A. Obolenskii, R. V. Vovk, A. V. Bondarenko, and N. N. Chebotaev, "Localization effects and pseudogap state in $\text{YBa}_2\text{Cu}_3\text{O}_{7-\delta}$ single crystals with different oxygen content", *Low Temperature Physics* **32**, 571–575 (2006) 10.1063/1.2215373.
- [151] R. Beyers and T. M. Shaw, "The structure of $\text{YBa}_2\text{Cu}_3\text{O}_{7-\delta}$ and its derivatives", *Solid State Physics* **42**, 136–212 (1989) 10.1016/S0081-1947(08)60081-8.
- [152] J. Ye and K. Nakamura, "Quantitative structure analyses of YBCO thin films: determination of oxygen content from X-ray-diffraction patterns", *Physical Review B* **48**, 7554–7564 (1993) 10.1103/PhysRevB.48.7554.
- [153] W. K. Kwok, G. W. Crabtree, A. Umezawa, B. W. Veal, J. D. Jorgensen, S. K. Malik, L. J. Nowicki, A. P. Paulikas, and L. Nunez, "Electronic behaviour of oxygen-deficient $\text{YBa}_2\text{Cu}_3\text{O}_{7-\delta}$ ", *Physical Review B* **37**, 106–110 (1988) 10.1103/PhysRevB.37.106.
- [154] B. W. Veal and A. P. Paulikas, "Dependence of hole concentration on oxygen vacancy order in $\text{YBa}_2\text{Cu}_3\text{O}_{7-\delta}$. a chemical valence model", *Physica C: Superconductivity* **184**, 321 (1991) 10.1016/0921-4534(91)90398-I.
- [155] J. R. LaGraff and D. A. Payne, "Chemical diffusion of oxygen in single-crystal and polycrystalline $\text{YBa}_2\text{Cu}_3\text{O}_{6+x}$ determined by electrical-resistance measurements", *Physical Review B* **47**, 3380–3391 (1993) 10.1103/PhysRevB.47.3380.
- [156] K. Semba and A. Matsuda, "Superconductor-to-insulator transition and transport properties of underdoped $\text{YBa}_2\text{Cu}_3\text{O}_y$ crystals", *Physical Review Letters* **86**, 496–499 (2001) 10.1103/PhysRevLett.86.496.
- [157] E. Osquiguil, M. Maenhoudt, B. Wuyts, Y. Bruynseraede, D. Lederer, and I. K. Schuller, "Photoexcitation and oxygen ordering in $\text{YBa}_2\text{Cu}_3\text{O}_{7-\delta}$ ", *Physical Review B* **49**, 3675–3678 (1994) 10.1103/PhysRevB.49.3675.

- [158] F. Federici, D. Chew, B. Welker, W. Savin, J. Gutierrez-Solana, T. Fink, and W. Wilber, "Defect mechanism of photoinduced superconductivity in $\text{YBa}_2\text{Cu}_3\text{O}_{6+x}$ ", *Physical Review B* **52**, 592–597 (1995) 10.1103/PhysRevB.52.15592.
- [159] W. Markowitsch, W. Lang, J. D. Pedarnig, and D. Bäuerle, "Persistent photoconductivity in oxygen-deficient and ion-irradiated $\text{YBa}_2\text{Cu}_3\text{O}_x$ ", *Superconductor Science and Technology* **22**, 034011 (2009) 10.1088/0953-2048/22/3/034011.
- [160] J. Guimpel, B. Maiorov, E. Osquiguil, G. Nieva, and F. Pardo, "Interrelation between persistent photoconductivity and oxygen order in thin films", *Physical Review B* **56**, 3552–3555 (1997) 10.1103/PhysRevB.56.3552.
- [161] S. Bahrs, A. R. Goñi, B. Maiorov, G. Nieva, A. Fainstein, and C. Thomsen, "Raman-study of photoinduced chain-oxygen ordering in $\text{RBa}_2\text{Cu}_3\text{O}_{7-\delta}$ ", *IEEE Transactions on Applied Superconductivity* **13**, 3192–3195 (2003) 10.1109/TASC.2003.812193.
- [162] R. Liang, D. A. Bonn, and W. N. Hardy, "Evaluation of CuO_2 plane hole doping in $\text{YBa}_2\text{Cu}_3\text{O}_{6+x}$ single crystals", *Physical Review B* **73**, 1–4 (2006) 10.1103/PhysRevB.73.180505.
- [163] T. A. Friedmann, M. W. Rabin, J. Giapintzakis, J. P. Rice, and D. M. Ginsberg, "Direct measurement of the anisotropy of the resistivity in the $a - b$ plane of twin-free, single-crystal, superconducting $\text{YBa}_2\text{Cu}_3\text{O}_{7-\delta}$ ", *Physical Review B* **42**, 6217–6221 (1990) <https://doi.org/10.1103/PhysRevB.42.6217>.
- [164] M. Ikebe, H. Fujishiro, T. Naito, M. Matsukawa, and K. Noto, "Anisotropic thermal diffusivity and conductivity of YBCO(123) and YBCO(211) mixed crystals", *Japanese Journal of Applied Physics* **33**, 615–619 (1994) 10.1143/JJAP.33.4965.
- [165] Y. Ando, K. Segawa, S. Komiya, and A. N. Lavrov, "Electrical resistivity anisotropy from self-organized one dimensionality in high-temperature superconductors", *Physical Review Letters* **88**, 4 (2002) 10.1103/PhysRevLett.88.137005.
- [166] B. P. Stojković and D. Pines, "Theory of the longitudinal and hall conductivities of the cuprate superconductors", *Physical Review B* **55**, 8567–8595 (1997) 10.1103/PhysRevB.55.8576.

- [167] G. Cannelli, R. Cantelli, F. Trequattrini, and F. Cordero, "Oxygen mobility in $\text{ReBa}_2\text{Cu}_3\text{O}_{6+x}$ by anelastic relaxation", *Journal of Advanced Science* **7**, 188–192 (1995) 10.2978/j.sas.7.188.
- [168] D. Gupta, "Diffusion in some perovskites", in *Diffusion processes in advanced technological materials*, edited by D. Gupta (Springer, 2005).
- [169] H. I. Yoo and D. K. Lee, "Chemical diffusion in complex oxides with an emphasis on BaTiO_3 ", *Physical Chemistry Chemical Physics* **5**, 2212–2218 (2003) 10.1039/b300169p.
- [170] S. J. Rothman, J. L. Routbort, and J. E. Baker, "Tracer diffusion of oxygen in $\text{YBa}_2\text{Cu}_3\text{O}_{7-y}$ ", *Physical Review B* **64**, 8852–8860 (1989) 10.1103/PhysRevB.44.2326.
- [171] I. L. Goulatis, R. V. Vovk, and A. I. Chroneos, "Oxygen diffusion in $\text{RBa}_2\text{Cu}_3\text{O}_{7-\delta}$ superconductors: a brief review", *Fizika Nizkikh Temperatur* **49**, 1397–1403 (2023) 10.1063/10.0021373.
- [172] T. G. Wang, J. J. Cao, and X. F. Gou, "Activation energy of oxygen diffusion: a possible indicator of supercurrents through $\text{YBa}_2\text{Cu}_3\text{O}_{7-\delta}$ grain boundaries", *Applied Surface Science* **480**, 765–769 (2019) 10.1016/j.apsusc.2019.02.208.
- [173] S. J. Rothman, J. L. Routbort, U. Welp, and J. E. Baker, "Anisotropy of oxygen tracer diffusion in single-crystal $\text{YBa}_2\text{Cu}_3\text{O}_{7-\delta}$.", *Phys. Rev. B* **44**, 2326–2333 (1991).
- [174] M. Ronay and P. Nordlander, "Anisotropy of oxygen transport $\text{YBa}_2\text{Cu}_3\text{O}_7$: the role of the $[\frac{1}{2}, b, O]$ tunnels", *Physica C* **153-155**, 834–835 (1988) 10.1016/S0921-4534(88)80112-6.
- [175] R. V. Vovk, Y. I. Boiko, V. V. Bogdanov, S. N. Kamchatnaya, I. L. Goulatis, and A. Chroneos, "Different diffusion mechanisms of oxygen in $\text{ReBa}_2\text{Cu}_3\text{O}_{7-x}$ (Re = Y, Ho) single crystals", *Physica C: Superconductivity and its Applications* **536**, 26–29 (2017) 10.1016/j.physc.2017.04.001.
- [176] T. Mayeshiba and D. Morgan, "Strain effects on oxygen migration in perovskites", *Physical Chemistry Chemical Physics* **17**, 2715–2721 (2015) 10.1039/c4cp05554c.
- [177] R. Arpaia, E. Andersson, A. Kalaboukhov, E. Schröder, E. Trbaldo, R. Ciancio, G. Dražić, P. Orgiani, T. Bauch, and F. Lombardi, "Untwinned $\text{YBa}_2\text{Cu}_3\text{O}_{7-\delta}$ thin films on MgO substrates: a platform to study strain effects on the local orders in cuprates", *Physical Review Materials* **3**, 114804 (2019) 10.1103/PhysRevMaterials.3.114804.

- [178] X. T. Zhang, Q. X. Yu, Y. P. Yao, and X. G. Li, "Ultrafast resistive switching in SrTiO₃:Nb single crystal", *Applied Physics Letters* **97** (2010), 10.1063/1.3524216.
- [179] G. L. Yuan and J. Wang, "Evidences for the depletion region induced by the polarization of ferroelectric semiconductors", *Applied Physics Letters* **95** (2009), 10.1063/1.3268783.
- [180] M. A. Lampert, "Theory of space-charge-limited currents in an insulator with traps", *Physical Review* **103** (1956), 10.1103/PhysRev.103.1648.
- [181] M. Y. Song, Y. Seo, Y. S. Kim, H. D. Kim, H. M. An, B. H. Park, Y. M. Sung, and T. G. Kim, "Realization of one-diode-type resistive-switching memory with Cr-SrTiO₃ film", *Applied Physics Express* **5** (2012), 10.1143/APEX.5.091202.
- [182] Z. Yan, Y. Guo, G. Zhang, and J. M. Liu, "High-performance programmable memory devices based on Co-doped BaTiO₃", *Advanced Materials* **23**, 1351–1355 (2011) 10.1002/adma.201004306.
- [183] A. Chanthbouala, A. Crassous, V. Garcia, K. Bouzehouane, S. Fusil, X. Moya, J. Allibe, B. Dlubak, J. Grollier, S. Xavier, C. Deranlot, A. Moshar, R. Proksch, N. D. Mathur, M. Bibes, and A. Barthélémy, "Solid-state memories based on ferroelectric tunnel junctions", *Nature Nanotechnology* **7**, 101–104 (2012) 10.1038/nnano.2011.213.
- [184] M. Dawber, K. M. Rabe, and J. F. Scott, "Physics of thin-film ferroelectric oxides", *Reviews of Modern Physics* **77**, 1083–1130 (2005) 10.1103/RevModPhys.77.1083.
- [185] C. Moreno, C. Munuera, S. Valencia, F. Kronast, X. Obradors, and C. Ocal, "Reversible resistive switching and multilevel recording in La_{0.7}Sr_{0.3}MnO₃ thin films for low cost nonvolatile memories", *Nano Letters* **10**, 3828–3835 (2010) 10.1021/nl1008162.
- [186] M. Hasan, R. Dong, H. J. Choi, D. S. Lee, D. J. Seong, M. B. Pyun, and H. Hwang, "Uniform resistive switching with a thin reactive metal interface layer in metal- La_{0.7}Ca_{0.3}MnO₃ -metal heterostructures", *Applied Physics Letters* **92**, 10.1063/1.2932148 (2008) 10.1063/1.2932148.
- [187] M. Bobeth, N. Farag, A. A. Levin, D. C. Meyer, W. Pompe, and A. E. Romanov, "Reversible electric field-induced structure changes in the near-surface region of strontium titanate", *Journal of the Ceramic Society of Japan* **114**, 1029–1037 (2006) 10.2109/jcersj.114.1029.

- [188] T. Leisegang, H. Stöcker, A. A. Levin, T. Weissbach, M. Zschornak, E. Gutmann, K. Rickers, S. Gemming, and D. C. Meyer, "Switching trivalence in SrTiO_3 by a dc electric field", *Physical Review Letters* **102**, 1–4 (2009) 10.1103/PhysRevLett.102.087601.
- [189] C. Rodenbücher, S. Menzel, D. Wrana, T. Gensch, C. Korte, F. Krok, and K. Szot, "Current channeling along extended defects during electroreduction of SrTiO_3 ", *Scientific Reports* **9**, 1–9 (2019) 10.1038/s41598-019-39372-2.
- [190] D. M. Evans, D. Ren, T. S. Holstad, P. E. Vullum, A. B. Mosberg, Z. Yan, E. Bourret, A. T. J. V. Helvoort, S. M. Selbach, and D. Meier, "Observation of electric-field-induced structural dislocations in a ferroelectric oxide", *Nano Letters* **21**, 3386–3392 (2021) 10.1021/acs.nanolett.0c04816.
- [191] A. Schulman and C. Acha, "Cyclic electric field stress on bipolar resistive switching devices", *Journal of Applied Physics* **114**, 243706 (2013) 10.1063/1.4859475.
- [192] A. Lagarrigue, "Electrical and spin switching effects in high-temperature superconducting devices", PhD thesis (Université Paris-Saclay, 2023), <http://www.theses.fr/2023UPASP058>.
- [193] A. S. Dhoot, S. C. Wimbush, T. Benseman, J. L. MacManus-Driscoll, J. R. Cooper, and R. H. Friend, "Increased T_c in electrolyte-gated cuprates", *Adv. Mater.* **22**, 2529–2533 (2010) 10.1002/adma.200904024.
- [194] L. Bégon-Lours, V. Rouco, A. Sander, J. Trastoy, R. Bernard, E. Jacquet, K. Bouzehouane, S. Fusil, V. Garcia, A. Barthélémy, M. Bibes, J. Santamaría, and J. E. Villegas, "High-temperature-superconducting weak link defined by the ferroelectric field effect", *Physical Review Applied* **7**, 064015 (2017) 10.1103/PhysRevApplied.7.064015.
- [195] Z. Zhang, W. Sigle, and M. Rühle, "Atomic and electronic characterization of the [100] dislocation core in SrTiO_3 ", *Physical Review B* **66**, 094108 (2002) 10.1103/PhysRevB.66.094108.
- [196] A. M. Perez-Muñoz, P. Schio, R. Poloni, A. Fernandez-Martinez, A. Rivera-Calzada, J. C. Cezar, E. Salas-Colera, G. R. Castro, J. Kinney, C. Leon, J. Santamaria, J. Garcia-Barriocanal, and A. M. Goldman, "In operando evidence of deoxygenation in ionic liquid gating of $\text{YBa}_2\text{Cu}_3\text{O}_{7-x}$ ", *Proceedings of the National Academy of Sciences of the United States of America* **114**, 215–220 (2017) 10.1073/pnas.1613006114.

- [197] J. Alcalà, A. Fernández-Rodríguez, T. Günkel, A. Barrera, M. Cabero, J. Gazquez, L. Balcells, N. Mestres, and A. Palau, "Tuning the superconducting performance of $\text{YBa}_2\text{Cu}_3\text{O}_{7-\delta}$ films through field-induced oxygen doping", *Scientific Reports* **14** (2024), 10.1038/s41598-024-52051-1.
- [198] B. H. Moeckly, D. K. Lathrop, and R. A. Buhrman, "Electromigration study of oxygen disorder and grain-boundary effects in $\text{YBa}_2\text{Cu}_3\text{O}_{7-\delta}$ thin films", *Physical Review B* **47**, 400–417 (1993) 10.1103/PhysRevB.47.400.
- [199] B. H. Moeckly, R. A. Buhrman, and P. E. Sulewski, "Micro-raman spectroscopy of electromigration-induced oxygen vacancy aggregation in $\text{YBa}_2\text{Cu}_3\text{O}_{7-\delta}$ ", *Applied Physics Letters* **64**, 1427–1429 (1994) 10.1063/1.111905.
- [200] S. H. Huerth, H. D. Hallen, and B. H. Moeckly, "Spectroscopy of voltage dependence of oxygen movement in $\text{YBa}_2\text{Cu}_3\text{O}_{7-\delta}$ ", *Physical Review B* **67**, 1–4 (2003) 10.1103/PhysRevB.67.180506.
- [201] S. Marinković, E. Trbaldo, S. Collienne, F. Lombardi, T. Bauch, and A. V. Silhanek, "Oxygen ordering in untwinned $\text{YBa}_2\text{Cu}_3\text{O}_{7-\delta}$ films driven by electrothermal stress", *Physical Review B* **107**, 10.1103/PhysRevB.107.014208 (2023) 10.1103/PhysRevB.107.014208.
- [202] E. Trbaldo, A. Garibaldi, F. Lombardi, and T. Bauch, "Electromigration tuning of the voltage modulation depth in $\text{YBa}_2\text{Cu}_3\text{O}_{7-\delta}$ nanowire-based SQUIDS", *Supercond. Sci. Technol.* **34**, 104001 (2021) 10.1088/1361-6668/ac1c15.
- [203] S. Collienne, B. Raes, W. Keijers, J. Linek, D. Koelle, R. Kleiner, R. B. Kramer, J. V. D. Vondel, and A. V. Silhanek, "Nb-based nanoscale SQUIDS tuned by electroannealing", *Physical Review Applied* **15**, 034016 (2021) 10.1103/PhysRevApplied.15.034016.
- [204] J. Li, J. Wang, H. Kuang, H. R. Zhang, Y. Y. Zhao, K. M. Qiao, F. Wang, W. Liu, W. Wang, L. C. Peng, Y. Zhang, R. C. Yu, F. X. Hu, J. R. Sun, and B. G. Shen, "Oxygen defect engineering by the current effect assisted with temperature cycling in a perovskite-type $\text{La}_{0.7}\text{Sr}_{0.3}\text{CoO}_3$ film", *Nanoscale* **9**, 13214–13221 (2017) 10.1039/c7nr03162a.
- [205] L. Balcells, L. Peña, R. Galceran, A. Pomar, B. Bozzo, Z. Konstantinovic, F. Sandiumenge, and B. Martinez, "Electroresistance and Joule heating effects in manganite thin films", *Journal of Applied Physics* **113**, 10.1063/1.4792222 (2013) 10.1063/1.4792222.

- [206] V. Ceriale, L. Pellegrino, N. Manca, and D. Marré, “Electro-thermal bistability in $\text{La}_{0.7}\text{Sr}_{0.3}\text{MnO}_3$ suspended microbridges: thermal characterization and transient analysis”, *Journal of Applied Physics* **115**, 0–8 (2014) 10.1063/1.4864222.
- [207] G. Lin, H. Wang, X. Cai, W. Tong, and H. Zhu, “Joule self-heating effects and controlling oxygen vacancy in $\text{La}_{0.8}\text{Ba}_{0.2}\text{MnO}_3$ ultrathin films with nano-sized labyrinth morphology”, *AIP Advances* **10**, 1–8 (2020) 10.1063/5.0009801.
- [208] A. Asamitsu, Y. Tomioka, H. Kuwahara, and Y. Tokura, “Current switching of resistive states in magnetoresistive manganites”, *Nature* **388**, 50–52 (1997) 10.1038/40363.
- [209] P. Salev, L. Fratino, D. Sasaki, R. Berkoun, J. Valle, Y. Kalcheim, Y. Takamura, M. Rozenberg, and I. K. Schuller, “Transverse barrier formation by electrical triggering of a metal-to-insulator transition”, *Nature Communications* **12**, 5499 (2021) 10.1038/s41467-021-25802-1.
- [210] X. D. A. Baumans, J. Lombardo, J. Brisbois, G. Shaw, V. S. Zharinov, G. He, H. Yu, J. Yuan, B. Zhu, K. Jin, R. B. G. Kramer, J. V. de Vondel, and A. V. Silhanek, “Healing effect of controlled anti-electromigration on conventional and high- T_c superconducting nanowires”, *Small* **13**, 1–8 (2017) 10.1002/smll.201700384.
- [211] K. K. Nanda, N. Routra, and D. Bhatta, “Synthesis conditions and superconductivity in 123-type superconductors”, *Journal of Superconductivity and Novel Magnetism* **11**, pure solid state, 649–652 (1998) 10.1023/A:1022612316767.
- [212] G. Khadzhai, R. Vovk, N. Vovk, S. Kamchatnaya, and O. Dobrovolskiy, “Room-temperature annealing effects on the basal-plane resistivity of optimally doped $\text{YBa}_2\text{Cu}_3\text{O}_{7-\delta}$ single crystals”, in *Physica C: Superconductivity and its Applications* **545**, 14–17 (2018) 10.1016/j.physc.2017.11.015.
- [213] R. Liang, P. Dosanjh, D. A. Bonn, D. J. Baar, J. F. Carolan, and W. N. Hardy, “Growth and properties of superconducting YBCO single crystals”, *Physica C: Superconductivity and its applications* **195**, 51–58 (1992) 10.1016/0921-4534(92)90073-L.
- [214] R. Cloots, T. Koutzarova, J.-P. Mathieu, and M. Ausloos, “From RE-211 to RE-123. How to control the final microstructure of superconducting single-domains”, in *Superconductor Science and Technology* **18**, R9–R23 (2005) 10.1088/0953-2048/18/3/R01.

- [215] P. M. Martin, *Handbook of deposition technologies for films and coatings: science, applications and technology*, 3rd ed. (Elsevier, 2010).
- [216] X. Obradors, T. Puig, A. Pomar, F. Sandiumenge, S. Piñol, N. Mestres, O. Castaño, M. Coll, A. Cavallaro, A. Palau, J. Gázquez, J. C. González, J. Gutiérrez, N. Romà, S. Ricart, J. M. Moretó, M. D. Rossell, and G. Van Tendeloo, "Chemical solution deposition: a path towards low cost coated conductors", *Superconductor Science and Technology* **17**, 1055–1064 (2004) 10.1088/0953-2048/17/8/020.
- [217] G. Hodes, *Chemical solution deposition of semiconductor films*, 1st ed. (CRC Press), 10.1201/9780203909096.
- [218] R. W. Schwartz, "Chemical solution deposition of perovskite thin films", **9**, 2325–2340 10.1021/cm970286f.
- [219] X. Obradors, T. Puig, S. Ricart, M. Coll, J. Gázquez, A. Palau, and X. Granados, "Growth, nanostructure and vortex pinning in superconducting $\text{YBa}_2\text{Cu}_3\text{O}_{7-\delta}$ thin films based on trifluoroacetate solutions", *Superconductor Science and Technology* **25**, 32 (2012) 10.1088/0953-2048/25/12/123001.
- [220] H. Wang, J. Gázquez, C. Frontera, M. F. Chisholm, A. Pomar, B. Martínez, and N. Mestres, "Spontaneous cationic ordering in chemical-solution-grown $\text{La}_2\text{CoMnO}_6$ double perovskite thin films", *NPG asia materials* **11**, 10.1038/s41427-019-0144-8 (2019) 10.1038/s41427-019-0144-8.
- [221] H. Wang, C. Frontera, J. Herrero-Martín, A. Pomar, P. Roura, B. Martínez, and N. Mestres, "Aqueous chemical solution deposition of functional double perovskite epitaxial thin films", *Chemistry - A European Journal* **26**, 9338–9347, 10.1002/chem.202000129.
- [222] J. Lombardo, S. Collienne, A. Petrillo, E. Fourneau, N. D. Nguyen, and A. V. Silhanek, "Electromigration-induced resistance switching in indented Al microstrips", *New Journal of Physics* **21**, 10.1088/1367-2630/ab5025 (2019) 10.1088/1367-2630/ab5025.
- [223] G. Shaw, J. Brisbois, L. B. Pinheiro, J. Müller, S. Blanco Alvarez, T. Devillers, N. M. Dempsey, J. E. Scheerder, J. Van De Vondel, S. Melinte, P. Vanderbenden, M. Motta, W. A. Ortiz, K. Hasselbach, R. B. Kramer, and A. V. Silhanek, "Quantitative magneto-optical investigation of superconductor/ferromagnet hybrid structures", *Review of Scientific Instruments* **89**, 1–21 (2018) 10.1063/1.5016293.
- [224] *COMSOL Multiphysics*© v. 5.4. COMSOL AB, Stockholm, Sweden.

- [225] F. Tair, L. Carreras, J. Camps, J. Farjas, P. Roura, A. Calleja, T. Puig, and X. Obradors, "Melting temperature of $\text{YBa}_2\text{Cu}_3\text{O}_{7-x}$ and $\text{GdBa}_2\text{Cu}_3\text{O}_{7-x}$ at subatmospheric partial pressure", *Journal of Alloys and Compounds* **692**, 787–792 (2017) 10.1016/j.jallcom.2016.08.072.
- [226] D. Q. Shi, R. K. Ko, K. J. Song, J. K. Chung, S. J. Choi, Y. M. Park, K. C. Shin, S. I. Yoo, and C. Park, "Effects of deposition rate and thickness on the properties of YBCO films deposited by pulsed laser deposition", *Superconductor Science and Technology* **17** (2004), 10.1088/0953-2048/17/2/059.
- [227] G. A. Farnan, M. P. McCurry, D. G. Walmsley, Z. Z. Li, and H. Raffy, "Doping and characterization of $\text{YBa}_2\text{Cu}_3\text{O}_{7-\delta}$ thin films prepared by pulsed laser deposition", *Superconductor Science and Technology* **14**, 160 (2001) 10.1088/0953-2048/14/3/307.
- [228] B. W. Veal, A. P. Paulikas, Y. Shi H. and Fang, and J. W. Downey, "Observation of temperature-dependent site disorder in $\text{YBa}_2\text{Cu}_3\text{O}_{7-\delta}$ below 150°C ", *Physical Review B* **42**, 6305–6316 (1990) 10.1103/PhysRevB.42.6305.
- [229] K. N. Tu, N. C. Yeh, S. I. Park, and C. C. Tsuei, "Diffusion of oxygen in superconducting $\text{YBa}_2\text{Cu}_3\text{O}_{7-\delta}$ ceramic oxides", *Physical Review B* **39**, 304–314 (1989) 10.1103/PhysRevB.39.304.
- [230] J. Kircher, M. Kelly, S. Rashkeev, M. Alouani, D. Fuchs, and M. Cardona, "Anisotropy and oxygen-stoichiometry dependence of the dielectric tensor of $\text{YBa}_2\text{Cu}_3\text{O}_{7-\delta}$ ($0 \leq \delta \leq 1$)", *Physical Review B* **44**, 217–224 (1991) 10.1103/PhysRevB.44.217.
- [231] P. E. Sulewski, T. W. Noh, J. T. McWrither, A. J. Sievers, S. E. Russek, R. A. Buhrman, C. S. Jee, J. E. Crow, R. E. Salomon, and G. Myer, "Free-carrier relaxation dynamics in the normal state of sintered $\text{YBa}_2\text{Cu}_3\text{O}_{7-y}$ ", *Physical Review B* **36**, 2357–2360 (1987) 10.1103/PhysRevB.36.2357.
- [232] G. L. Zhao, Y. Xu, W. Y. Ching, and K. W. Wong, "Theoretical calculation of optical properties of Y-Ba-Cu-O superconductors", *Physical Review Letters* **36**, 7203–7207 (1987) 10.1103/PhysRevB.36.7203.
- [233] K. Kamaras, C. D. Porter, M. G. Doss, S. L. Herr, D. B. Tanner, D. A. Bonn, J. E. Greedan, A. H. O'Reilly, C. V. Stager, and T. Timusk, "Excitonic absorption and superconductivity in $\text{YBa}_2\text{Cu}_3\text{O}_{7-y}$ ", *Physical Review Letters* **59**, 919–922 (1987) 10.1103/PhysRevLett.59.919.

- [234] C. Thomsen and G. Kaczmarczyk, "Vibrational raman spectroscopy of high-temperature superconductors", in *Handbook of vibrational spectroscopy*, edited by J. M. Chalmers and P. R. Griffiths (John Wiley and Sons, Chichester, 2002), p. 2651.
- [235] R. Feile, "Lattice vibrations in high- T_c superconductors: optical spectroscopy and lattice dynamics", *Physica C* **159**, 1–32 (1989) 10.1016/0921-4534(89)90099-3.
- [236] P. V. Huong, "Microstructure of high-temperature superconductor thin films as studied by micro-raman spectroscopy", *Physica C* **180**, 128–131 (1991) 10.1016/0921-4534(91)90651-E.
- [237] E. Osquiguil, M. Maenhoudt, B. Wuyts, Y. Bruyneseraede, D. Lederman, G. Nieva, J. Guimpel, and I. K. Schuller, "Photoexcitation effects in $\text{YBa}_2\text{Cu}_3\text{O}_x$ ", *Journal of Alloys and Compounds* **195**, 667–670 (1993) 10.1016/0925-8388(93)90826-9.
- [238] J. Lombardo, S. Collienne, A. Petrillo, E. Fourneau, N. D. Nguyen, and A. V. Silhanek, "Electromigration-induced resistance switching in indented al microstrips", *New J. Phys.* **21**, 113015 (2019) 10.1088/1367-2630/ab5025.
- [239] J. Choi, M. Sarikaya, I. A. Aksay, and R. Kikuchi, "Theory of oxygen diffusion in the $\text{YBa}_2\text{Cu}_3\text{O}_{7-x}$ superconducting compound", *Physical Review B* **42**, 4244 (1990) 10.1103/PhysRevB.42.4244.
- [240] C. Krauns and H. Krebs, "Comparison of the oxygen diffusion in $\text{Y}_1\text{Ba}_2\text{Cu}_3\text{O}_7$ bulk materials and thin films", *Zeitschrift für Physik B* **92**, 4346 (1993) 10.1007/BF01309165.
- [241] R. Baetzold, "Atomistic study of defects in $\text{YBa}_2\text{Cu}_3\text{O}_7$ ", *Physical Review B* **42**, 56 (1990) 10.1103/PhysRevB.42.56.
- [242] T. Wang, J. Cao, and X. Gou, "Activation energy of oxygen diffusion: a possible indicator of supercurrents through $\text{YBa}_2\text{Cu}_3\text{O}_7$ grain boundaries", *Appl. Surf. Sci.* **480**, 765–769 (2019).
- [243] C. You, I. Sung, and B. Joe, "Analytic expression for the temperature of the current-heated nanowire for the current-induced domain wall motion", *Applied Physics Letters* **89**, 222513 (2006) 10.1063/1.2399441.
- [244] H. Fangohr, D. Chernyshenko, M. Franchin, T. Fischbacher, and G. Meier, "Joule heating in nanowires", *Physical Review B* **84** (2011), 10.1103/PhysRevB.84.054437.

- [245] A. Paul, T. Laurila, V. Vuorinen, and S. V. Divinski, "Atomic mechanism of diffusion", in *Thermodynamics, Diffusion and the Kirkendall Effect in Solids* (Springer International Publishing, 2014), pp. 167–238.
- [246] V. Sadykov, N. N. Bulgakov, V. Muzykantov, T. Kuznetsova, G. Alikina, A. Lukashevich, Y. V. Potapova, V. Rogov, E. Burgina, V. Zaikovskii, E. Moroz, G. S. Litvak, I. S. Yakovleva, L. Isupova, V. Zyryanov, E. Kemnitz, and S. Neophytides, "Mobility and reactivity of the surface and lattice oxygen of some complex oxides with perovskite structure", in *Mixed Ionic Electronic Conducting Perovskites for Advanced Energy Systems* (Springer Netherlands, 2004), pp. 53–74.
- [247] G. Cannelli, R. Cantelli, F. Cordero, and F. Trequattrini, "Dynamics of oxygen and phase transitions in the 123 ceramic superconductors by anelastic relaxation measurements", *Superconductor Science and Technology* **5**, 247–257 (1992) 10.1088/0953-2048/5/4/009.
- [248] M. Nahum, S. Verghese, P. L. Richards, and K. Char, "Thermal boundary resistance for $\text{YBa}_2\text{Cu}_3\text{O}_{7-\delta}$ films", *Appl. Phys. Lett.* **59**, 2034–2036 (1991) 10.1063/1.106123.
- [249] S. K. Gupta, P. Berdahl, R. E. Russo, G. Briceño, and A. Zettl, "Pulse I-V characteristics measurement to study the dissipation mechanism in epitaxial $\text{YBa}_2\text{Cu}_3\text{O}_x$ thin films at high current densities", *Physica C: Supercond.* **206**, 335–344 (1993) 10.1016/0921-4534(93)90533-V.
- [250] P. C. Michael, J. U. Trefny, and B. Yarar, "Thermal transport properties of single crystal lanthanum aluminate", in *Journal of Applied Physics* **72**, 107–109 (1992) 10.1063/1.352166.
- [251] A. Knizhnik, G. E. Shter, G. S. Grader, G. M. Reisner, and Y. Eckstein, "Interrelation of preparation conditions, morphology, chemical reactivity and homogeneity of ceramic YBCO", *Physica C: Supercond.* **400**, 25–35 (2003) 10.1016/S0921-4534(03)01311-X.
- [252] I. Grekhov, L. Delimova, I. Liniichuk, A. Lyublinsky, I. Veselovsky, A. Titkov, M. Dunaevsky, and V. Sakharov, "Growth mode study of ultrathin HTSC YBCO films on YBaCuNbO buffer", *Physica C: Supercond.* **324**, 39–46 (1999) 10.1016/S0921-4534(99)00423-2.
- [253] N. E. Phillips, J. P. Emerson, R. A. Fisher, J. E. Gordon, B. F. Woodfield, and D. A. Wright, "Specific heat of $\text{YBa}_2\text{Cu}_3\text{O}_7$ ", *J. Supercond.* **7**, 251–255 (1994) 10.1007/BF00730406.

- [254] S. Nawaz, R. Arpaia, F. Lombardi, and T. Bauch, "Microwave response of superconducting $\text{YBa}_2\text{Cu}_3\text{O}_{7-\delta}$ nanowire bridges sustaining the critical depairing current: evidence of Josephson-like behavior", *Phys. Rev. Lett.* **110**, 167004 (2013) 10.1103/PhysRevLett.110.167004.
- [255] S. Nawaz, R. Arpaia, T. Bauch, and F. Lombardi, "Approaching the theoretical depairing current in $\text{YBa}_2\text{Cu}_3\text{O}_{7-x}$ nanowires", *Phys. C: Supercond. Appl.* **495**, 33–38 (2013) 10.1016/j.physc.2013.07.011.
- [256] A. M. Hofmeister, "Thermal diffusivity and thermal conductivity of single-crystal MgO and Al_2O_3 and related compounds as a function of temperature", *Physics and Chemistry of Minerals* **41**, 361–371 (2014) 10.1007/s00269-014-0655-3.
- [257] J. C. Gonzalez-Rosillo, S. Catalano, I. Maggio-Aprile, M. Gibert, X. Obradors, A. Palau, and T. Puig, "Nanoscale correlations between metal–insulator transition and resistive switching effect in metallic perovskite oxides", *Small* **16**, 2001307 (2020) 10.1002/smll.202001307.
- [258] P. M. Chowdhury and A. K. Raychaudhuri, "Electromigration of oxygen and resistive state transitions in sub-micron width long strip of $\text{La}_{0.85}\text{Sr}_{0.15}\text{MnO}_3$ connected to an engineered oxygen source", *Materials Research Bulletin* **137** (2021), 10.1016/j.materresbull.2020.111160.
- [259] L. Yao, S. Inkinen, and S. V. Dijken, "Direct observation of oxygen vacancy-driven structural and resistive phase transitions in LSMO", *Nature Communications* **8**, 1–9 (2017) 10.1038/ncomms14544.
- [260] J. Hanzig, M. Zschornak, F. Hanzig, E. Mehner, H. Stöcker, B. Abendroth, C. Röder, A. Talkenberger, G. Schreiber, D. Rafaja, S. Gemming, and D. C. Meyer, "Migration-induced field-stabilized polar phase in strontium titanate single crystals at room temperature", *Physical Review B - Condens. Matter Mater. Phys.* **88**, 1–10 (2013) 10.1103/PhysRevB.88.024104.
- [261] S. Koohfar, A. S. Disa, M. S. J. Marshall, F. J. Walker, C. H. Ahn, and D. P. Kumah, "Structural distortions at polar manganite interfaces", *Physical Review B* **024108**, 6–11 (2017) 10.1103/PhysRevB.96.024108.
- [262] M. D. Armstrong, K. W. Lan, Y. Guo, and N. H. Perry, "Dislocation-mediated conductivity in oxides: progress, challenges, and opportunities", *ACS Nano* **15**, 9211–9221 (2021) 10.1021/acsnano.1c01557.

- [263] S. Marinković, D. Stoffels, S. Collienne, N. Mestres, A. Palau, and A. V. Silhanek, "Electromigration-driven weak resistance switching in high-temperature superconducting devices", unpublished.
- [264] S. Collienne, D. Majidi, J. Van de Vondel, C. B. Winkelmann, and A. V. Silhanek, "Targeted modifications of monolithic multiterminal superconducting weak-links", *Nanoscale* **14**, 5425–5429 (2022) 10.1039/D2NR00026A.
- [265] M Aravind and P. C. W. Fung, "Thermal parameter measurements of bulk YBCO superconductor using PVDF transducer", en, *Measurement Science and Technology* **10**, 979–985 (1999) 10.1088/0957-0233/10/11/301.
- [266] B. Friedl, C. Thomsen, H. U. Habermeier, and M. Cardona, "Intensity anomalies of Raman-active phonons in the superconducting state of $\text{YBa}_2\text{Cu}_3\text{O}_{7-\delta}$ ", *Solid State Commun.* **78**, 291–294 (1991) 10.1016/0038-1098(91)90199-6.
- [267] K. H. Kim, Z. Akase, T. Suzuki, and D. Shindo, "Charging effects on SEM/SIM contrast of metal/insulator system in various metallic coating conditions", *Materials Transactions* **51**, 1080–1083 (2010) 10.2320/matertrans.M2010034.
- [268] A. K. W. Chee, R. F. Broom, C. J. Humphreys, and E. Bosch, "A quantitative model for doping contrast in the scanning electron microscope using calculated potential distributions and Monte Carlo simulations", *Journal of Applied Physics* **109**, 013109 (2011) 10.1063/1.3524186.
- [269] A. Bhogra, A. Masarrat, R. Meena, D. Hasina, M. Bala, C.-L. Dong, C.-L. Chen, T. Som, A. Kumar, and A. Kandasami, "Tuning the electrical and thermoelectric properties of N ion implanted SrTiO_3 thin films and their conduction mechanisms", *Scientific Reports* **9**, 14486 (2019) 10.1038/s41598-019-51079-y.
- [270] A. Aryan, B. Guillet, J. Routoure, C. Fur, P. Langlois, and L. Méchin, "Measurement of thermal conductance of $\text{La}_{0.7}\text{Sr}_{0.3}\text{MnO}_3$ thin films deposited on SrTiO_3 and MgO substrates", *Applied Surface Science* **326**, 204–210 (2015) 10.1016/j.apsusc.2014.11.119.
- [271] *Strontium titanate (SrTiO_3) - properties and applications*, <https://www.azom.com/article.aspx?ArticleID=2362>, Accessed: 2021-12-06.

- [272] S. Majumdar, H. Huhtinen, P. Paturi, and H. S. Majumdar, "Effect of strain and grain boundaries on dielectric properties in $\text{La}_{0.7}\text{Sr}_{0.3}\text{MnO}_3$ thin films", *Journal of Materials Science* **48**, 2115–2122 (2013) 10.1007/s10853-012-6986-x.

Part VII

Curriculum Vitae and Publication List

Stefan Marinković, M.Sc.

- ✉ smarinkovic@uliege.be
- ✉ marinkovicstefan@outlook.com
- 📧 @Stefan-Marinkovic-2
- 🆔 ORCID: 0000-0001-8302-4777
- 🌐 <http://www.mate.ulg.ac.be/members-of-the-group>
- 🇷🇵 Nationality: Bosnian-Herzegovinian, Croatian (EU)
- 🎂 Date of Birth: 29th of December, 1994



Education

- 2020 – 2024 **Ph.D., Experimental Physics of Nanostructured Materials, Department of Physics, Faculty of Science, University of Liège, Belgium**
Thesis: *All-electrical oxygen doping in perovskites.*
Thesis defense: 29th of August 2024.
- 2019 – 2020 **M.Sc. Physics, Faculty of Science, University of Liège, Belgium**
Functionalized Advanced Materials and Engineering (FAME+) - an ERASMUS MUNDUS JOINT masters programme
Thesis title: *Direct visualization of current stimulated oxygen migration in YBCO.*
- 2018 – 2019 **M.Sc. Material Science, PHELMA school of engineering, Grenoble Polytechnic Institute (INP), France**
Functionalized Advanced Materials and Engineering (FAME+) - an ERASMUS MUNDUS JOINT masters programme
Thesis title: *Nanofabrication of Bismuth Hall probes for Scanning Hall Probe Microscopy..*
- 2013 – 2018 **B.Sc. Chemistry, Faculty of Natural Sciences, University of Sarajevo, Bosnia and Herzegovina**
Thesis title: *A Zn/rGO (reduced Graphene Oxide) hybrid supercapacitor with aqueous electrolyte.*
- 2009 – 2013 **High School Diploma, Gymnasium Nikola Tesla, Šamac, Bosnia and Herzegovina**

Employment History






- 2020 – 09/2024 **Research Fellow**, Experimental Physics of Nanostructured Materials, Department of Physics, University of Liège, Liège, Belgium. Supported by Fonds de la Recherche Scientifique (FNRS).
- 06/2019 – 08/2019 **M1 Internship in Nanofabrication**, Institute Néel, Grenoble, France. Supported by Centre national de la recherche scientifique (CNRS).
- 2016 – 2019 **Tour Guide**, Sarajevo Insider Tourist Agency, Sarajevo, Bosnia and Herzegovina.
- 2016 – 2017 **Project Coordinator**, Association for Media and Civil Society Development, Sarajevo, Bosnia and Herzegovina.
- Writer (Political Satire)**, Šatro info (satro.info), Sarajevo, Bosnia and Herzegovina.
- 2014 – 2015 **Educator/Regional Coordinator (Bundesfreiwilligendienst-Volunteer Service)**, Schüler Helfen Leben e.V. (Charity), Neumünster, Germany.
- 2013 – 2017 **Journalist**, Karike, youth magazine (magazinkarike.com); Crna Ovca, cultural web magazine (defunct); sova.ba, cultural web magazine (defunct), freelance work for press agencies, Sarajevo, Bosnia and Herzegovina.

Publications

Journal Articles

- 1 Badía-Majós, A., Martínez, E., Angurel, L. A., Fuente, G. F. D. L., Fourneau, E., **Marinković, S.**, & Silhanek, A. V. (2023). Laser nanostructured metasurfaces in Nb superconducting thin films. *Applied Surface Science*, 649. <https://doi.org/10.5281/zenodo.1>
- 2 **Marinković, S.**, Abbey, E. A., Chaves, D. A. D., Collienne, S., Fourneau, E., Jiang, L., Xue, C., Zhou, Y. H., Ortiz, W. A., Motta, M., Nguyen, N. D., Volodin, A., de Vondel, J. V., & Silhanek, A. V. (2023). Effect of moderate electropulsing on Nb multiterminal transport bridges. *Physical Review Applied*, 19. <https://doi.org/10.1103/PhysRevApplied.19.054009>
- 3 **Marinković, S.**, Trabeldo, E., Collienne, S., Lombardi, F., Bauch, T., & Silhanek, A. V. (2023). Oxygen ordering in untwinned $\text{YBa}_2\text{Cu}_3\text{O}_{7-\delta}$ films driven by electrothermal stress. *Physical Review B*, 107. <https://doi.org/10.1103/PhysRevB.107.014208>
- 4 Nulens, L., Lejeune, N., Caeyers, J., **Marinković, S.**, Cools, I., Dausy, H., Basov, S., Raes, B., Bael, M. J. V., Geresdi, A., Silhanek, A. V., & de Vondel, J. V. (2023). Catastrophic magnetic flux avalanches in NbTiN superconducting resonators. *Communications Physics*, 6. <https://doi.org/10.1038/s42005-023-01386-8>
- 5 Collienne, S., **Marinković, S.**, Fernández-Rodríguez, A., Mestres, N., Palau, A., & Silhanek, A. V. (2022). Electrically-driven oxygen vacancy aggregation and displacement in $\text{YBa}_2\text{Cu}_3\text{O}_{7-\delta}$ films. *Advanced Electronic Materials*, 8. [10.1002/aelm.202101290](https://doi.org/10.1002/aelm.202101290).
- 6 Jiang, L., Xue, C., **Marinković, S.**, Fourneau, E., Xu, T. Q., Cai, X. W., Nguyen, N. D., Silhanek, A. V., & Zhou, Y. H. (2022). Tunable domino effect of thermomagnetic instabilities in superconducting films with multiply-connected topological structures. *New Journal of Physics*, 24. <https://doi.org/10.1088/1367-2630/ac83e3>
- 7 **Marinković, S.**, Fernández-Rodríguez, A., Fourneau, E., Cabero, M., Wang, H., Nguyen, N. D., Gazquez, J., Mestres, N., Palau, A., & Silhanek, A. V. (2022). From electric doping control to thermal defect nucleation in perovskites. *Advanced Materials Interfaces*, 9. [10.1002/admi.202200953](https://doi.org/10.1002/admi.202200953).
- 8 **Marinković, S.**, Fernández-Rodríguez, A., Collienne, S., Alvarez, S. B., Melinte, S., Maiorov, B., Rius, G., Granados, X., Mestres, N., Palau, A., & Silhanek, A. V. (2020). Direct visualization of current-stimulated oxygen migration in $\text{YBa}_2\text{Cu}_3\text{O}_{7-\delta}$ thin films. *ACS Nano*, 14. <https://doi.org/10.1021/acsnano.0c04492>

Awards and Achievements

- 2021  **Best Young Speaker at Online Summer School 2021**, Arab-German Young Academy of Sciences and Humanities (AGYA).
-  **Best Master Thesis 2021**, Belgian Physical Society.
-  **Prix de Physique (Best Master Thesis 2020)**, Université de Liège.
- 2020  **Fonds de la Recherche Scientifique (FNRS) - ASPIRANTS PhD studies grant**, FNRS.
- 2018  **FAME+ Erasmus Mundus Joint Scholarship, Master studies grant**, FAME+ Consortium.


Conference Talks

- Invited Talks
- **"Electronic Erosion in Perovskites,"** FAME+ Summer School 2023, July the 19rd 2023, Louvain-La-Neuve, Belgium. Organized by Functionalized Advanced Materials Engineering (FAME+) Consortium.
 - **"Oxygen Ordering in Untwinned YBCO Films Driven by Electrothermal Stress,"** International Meeting on Superconducting Quantum Materials and Nanodevices - MonteSuper, April 17th - 21st 2023, Budva, Montenegro. Organized by European Cooperation in Science and Technology (COST).
 - **"Electronic Erosion in Complex Oxides,"** BPS Meeting 2021, November 30th 2021, Hasselt, Belgium. Organized by Belgian Physical Society (BPS).
 - **"Ionotronic Memristors: Non-Volatile Doping Control by Electric Current,"** Online Summer School 'Materials for Energy and Quantum Technology', October 16th - 20th 2021, Online. Organized by Arab-German Young Academy of Sciences and Humanities (AGYA).
 - **"Direct Visualization of Current-Stimulated Oxygen Migration in YBCO Thin Films,"** Superconducting Hybrids @ Extreme, June 28th - July 2nd 2021, Tatry, Slovakia (Online). Organized by European Cooperation in Science and Technology (COST).
- Contributed Talks
- **"Electromigration-driven weak resistance switching in HTS devices"** 9th International Conference on Superconductivity and Magnetism (ICSM), April 27th - May 4th 2024, Fethiye, Türkiye.
 - **"Electronic Erosion in Perovskites,"** Micro- and Nanoengineering - Euroensors - MNE Euroensors 2022, September 19th - 23rd 2022, Leuven, Belgium.
 - **"Direct Visualization of Current-Stimulated Oxygen Migration in YBCO Thin Films,"** Condensed Matter Division 2020 (CMD-GEFES), August 31st - September 4th 2020, Online. Organized by European Physical Society and the Spanish Royal Physical Society.

Skills

- Languages
- Strong reading, writing and speaking competencies for English (C1), German (C2) and French (B2). Native Bosnian/Croatian/Serbian proficiency.
- Instruments
- Scanning Electron Microscope, High Magnification Optical Microscope, Atomic Force Microscope, Electronic Test Equipment (Source Measurement Units, Nanovoltmeters, Signal Generators, Oscilloscopes, ...), Lock-in Amplifier, Vector Network Analyzer (passing), μ Raman Microscope (passing),...
- Maintenance
- Scanning Electron Microscope, Optical Microscope, CCD Cameras, Wirebonding and Probe Systems, Anti-Vibration Tables, Electronic Test Equipment, Instrument-Computer Interfaces (GPIB),...
- Techniques
- Electromigration, Transport Measurements, Cryogenic Measurements, Magneto-Optics (Faraday and Kerr-effect based), Electron-Beam and Optical Lithography, Presurized Vapor Deposition (PVD), Electron-Beam Evaporation (passing), Magnetron Sputtering Deposition (passing), Chemical Solution Deposition (passing),...
- Software
- Python (instrument control, experiment automation, data handling, data processing, image processing, application design), MATLAB (finite element modeling, COMSOL interfacing), LabVIEW (instrument control, image processing, data handling), COMSOL, \LaTeX , bash, Blender (3D modeling), Godot Game Engine, Inkscape (vector graphics), GIMP (raster graphics), ImageJ (microscopy image processing),...


Skills (continued)

Misc.  Academic research, teaching, training, consultation, \LaTeX typesetting and publishing. Simultaneous translation. Linux system administration. Drivers licence (B1)

References


Alejandro V. Silhanek, PhD

Professor, Principal Investigator at Experimental Physics of Nanostructured Materials (EPNM)
Université de Liège,
Sart Tilman B-4000, Belgium.

 asilhanek@uliege.be

Anna Palau, PhD

Tenured Scientist - CT, Superconducting Materials and Nanostructure at Large Scale,
Institut de Ciència de Materials de Barcelona (ICMAB-CSIC),
Campus UAB, 08193, Bellaterra.

 palau@icmab.es

